

AD-A166 087

ON THE DEVELOPMENT OF CONSTITUTIVE RELATIONS FOR PLAIN
AND REINFORCED CONCRETE(U) S-CUBED LA JOLLA CA

1/4

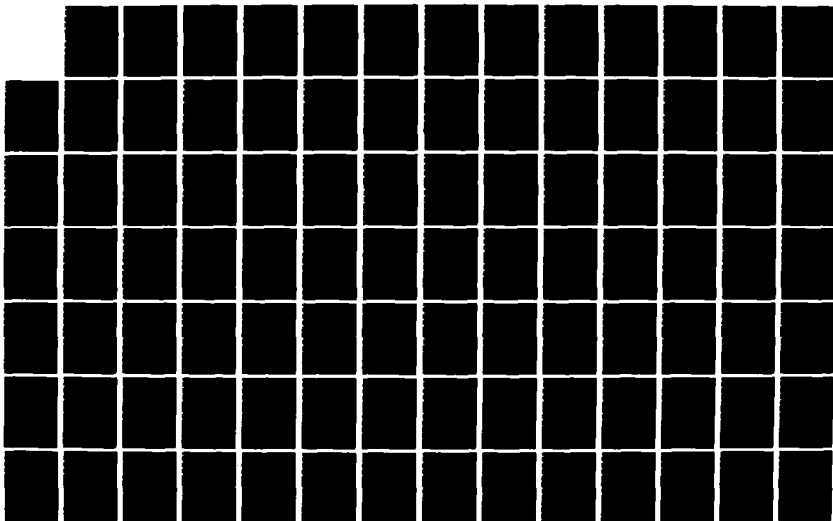
G A HEGEMIER ET AL 09 APR 82 SSS-R-82-5495

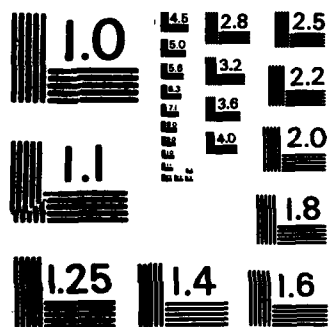
UNCLASSIFIED

DNA-TR-81-65 DNA001-81-C-0181

F/G 11/2

NL





MICROCOPY RESOLUTION TEST CHART
NATIONAL BUREAU OF STANDARDS-1963-A

AD-A166 087

DNA-TR-81-65

ON THE DEVELOPMENT OF CONSTITUTIVE RELATIONS FOR PLAIN AND REINFORCED CONCRETE

G. A. Hegemier
K. J. Cheverton
L. J. Hagerman
P. V. Lade
S-CUBED
A Division of Maxwell Laboratories, Inc
P.O. Box 1620
La Jolla, CA 92038-1620

9 April 1982

Technical Report

CONTRACT No. DNA 001-81-C-0181

Approved for public release;
distribution is unlimited.

THIS WORK WAS SPONSORED BY THE DEFENSE NUCLEAR AGENCY
UNDER RDT&E RMSS CODE B344080464 Y99QAXSC37802 H2590D.

Prepared for
Director
DEFENSE NUCLEAR AGENCY
Washington, DC 20305-1000

DTIC
SELECTE
APR 10 1986
S A D

DTIC FILE COPY

86 3 19 003

DISTRIBUTION LIST UPDATE

This mailer is provided to enable DNA to maintain current distribution lists for reports. We would appreciate your providing the requested information.

- ☐ Add the individual listed to your distribution list.
- ☐ Delete the cited organization/individual.
- ☐ Change of address.

NAME: _____

ORGANIZATION: _____

OLD ADDRESS

CURRENT ADDRESS

TELEPHONE NUMBER: () _____

SUBJECT AREA(s) OF INTEREST:

DNA OR OTHER GOVERNMENT CONTRACT NUMBER: _____

CERTIFICATION OF NEED-TO-KNOW BY GOVERNMENT SPONSOR (if other than DNA):

SPONSORING ORGANIZATION: _____

CONTRACTING OFFICER OR REPRESENTATIVE: _____

SIGNATURE: _____

AD-A166087

REPORT DOCUMENTATION PAGE				Form Approved OMB No. 0704-0188 Exp. Date: Jun 30, 1986	
1a. REPORT SECURITY CLASSIFICATION UNCLASSIFIED			1b. RESTRICTIVE MARKINGS		
2a. SECURITY CLASSIFICATION AUTHORITY			3. DISTRIBUTION / AVAILABILITY OF REPORT Approved for public release; distribution is unlimited.		
2b. DECLASSIFICATION / DOWNGRADING SCHEDULE N/A since UNCLASSIFIED					
4. PERFORMING ORGANIZATION REPORT NUMBER(S) SSS-R-82-5495			5. MONITORING ORGANIZATION REPORT NUMBER(S) DNA-TR-81-65		
6a. NAME OF PERFORMING ORGANIZATION S-CUBED, A Div. of Maxwell Laboratories, Inc		6b. OFFICE SYMBOL (if applicable)	7a. NAME OF MONITORING ORGANIZATION Director Defense Nuclear Agency		
6c. ADDRESS (City, State, and ZIP Code) P.O. Box 1620 La Jolla, CA 92038-1620			7b. ADDRESS (City, State, and ZIP Code) Washington, DC 20305-1000		
8a. NAME OF FUNDING / SPONSORING ORGANIZATION		8b. OFFICE SYMBOL (if applicable)	9. PROCUREMENT INSTRUMENT IDENTIFICATION NUMBER DNA 001-81-C-0181		
8c. ADDRESS (City, State, and ZIP Code)			10. SOURCE OF FUNDING NUMBERS		
PROGRAM ELEMENT NO		PROJECT NO	TASK NO	WORK UNIT ACCESSION NO.	
62715H		Y99QAXS	C	DH004788	
11. TITLE (Include Security Classification) ON THE DEVELOPMENT OF CONSTITUTIVE RELATIONS FOR PLAIN AND REINFORCED CONCRETE					
12. PERSONAL AUTHOR(S) G.A. Hegemier K.J. Cheverton L.J. Hageman P.V. Lade					
13a. TYPE OF REPORT Technical		13b. TIME COVERED FROM 800218 TO 810418		14. DATE OF REPORT (Year, Month, Day) 820409	
15. PAGE COUNT 324					
16. SUPPLEMENTARY NOTATION This work was sponsored by the Defense Nuclear Agency under RDT&E RMSS Code B344080464 Y99QAXSC37802 H2590D.					
17. COSATI CODES			18. SUBJECT TERMS (Continue on reverse if necessary and identify by block number)		
FIELD	GROUP	SUB-GROUP	Constitutive Models; Mixture Theories; Plasticity.		
11	2		Plain Concrete; Inelastic Response;		
20	11		Reinforced Concrete Large Deformation;		
19. ABSTRACT (Continue on reverse if necessary and identify by block number) The report presents progress made to-date on the construction of improved constitutive relations for plain and reinforced concrete. The report contains: (1) a comprehensive survey and assessment of the experimental and theoretical literature pertaining to plain concrete and steel-concrete interaction; (2) a new failure criterion for plain concrete that accurately reflects material behavior; and (3) a new theoretical framework for reinforced concrete that provides excellent simulation capability. Model validations are conducted for a certain class of plain and reinforced concrete problems. Key words:					
20. DISTRIBUTION / AVAILABILITY OF ABSTRACT <input type="checkbox"/> UNCLASSIFIED/UNLIMITED <input type="checkbox"/> SAME AS RPT <input checked="" type="checkbox"/> DTIC USERS			21. ABSTRACT SECURITY CLASSIFICATION UNCLASSIFIED		
22a. NAME OF RESPONSIBLE INDIVIDUAL Betty L. Fox			22b. TELEPHONE (Include Area Code) (202) 325-7042		22c. OFFICE SYMBOL DNA/STTJ

NOTED FOR	
NTIS GRA&I	<input checked="" type="checkbox"/>
DTIC TAB	<input type="checkbox"/>
Unannounced	<input type="checkbox"/>
Justification	
By	
Distribution/	
Availability Codes	
Dist	Avail and/or Special
A-1	

PREFACE

This report was completed in late 1981. In view of the long delay of publication (1985), it is appropriate to note that considerable progress has since been made in some of the subject areas discussed herein. For updated information the reader is referred to the following papers and reports:



Modeling of Plain Concrete

Valanis, K. C. and H. E. Read, "An Endochronic Plasticity Theory for Concrete," Proc. Second Symp. on the Interaction of Non-Nuclear Munitions with Structures, Panama City Beach, Florida, April 1985.

Valanis, K. C., and H. E. Read, "An Endochronic Plasticity Theory for Concrete," Mechanics of Materials, Vol. 4, No. 2, 1985.

Lade, P. V., "Three-Parameter Failure Criterion for Concrete," J. Engng. Mech. Div., ASCE, Vol. 108 (EM5), 1982.

Modeling of Reinforced Concrete

Hegemier, G. A., and H. Murakami, "A Nonlinear Theory for Reinforced Concrete," Proc. Second Symp. on the Interaction of Non-Nuclear Munitions with Structures, Panama City Beach, Florida, April 1985.

Hegemier, G. A., H. E. Read, H. Murakami, L. J. Hageman, and R. G. Herrmann, "Development of Advanced Constitutive Model for Reinforced Concrete," S-CUBED Second Annual Report to the AFOSR, SSS-R-83-6112, April 1983.

Hegemier, G. A., H. E. Read and H. Murakami, "Development of Advanced Constitutive Model for Reinforced Concrete," S-CUBED Final Report to the AFOSR, SSS-R-84-6684, April 1984.

Hegemier, G. A., H. Murakami, and L. J. Hageman, "On Tension Stiffening in Reinforced Concrete," Mechanics of Materials, Vol. 4, No. 2, 1984.

Murakami, H. and G. A. Hegemier, "On Simulating Steel-Concrete Interaction in Reinforced Concrete, Part 1: Theoretical Development," Mechanics of Materials, 1985 (to appear).

Hagemann, L. J., H. Murakami, and G. A. Hegemier, "On Simulating Steel-Concrete Interaction in Reinforced Concrete, Part II: Validation Studies," Mechanics of Materials, 1985 (to appear).

Strain Rate Effects

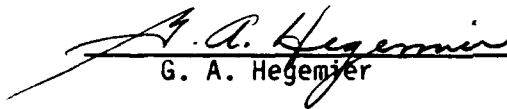
Read, H. E., "Strain Rate Effects in Concrete: A Review of Experimental Methods," S-CUBED Report SSS-R-85-6081, January 1985.

Strain Softening

Read, H. E. and G. A. Hegemier, "Strain Softening of Rock, Soil and Concrete -- A Review Article," Mechanics of Materials, Vol. 3, No. 4, 1984.

Survey Articles

Hegemier, G. A. and H. E. Read, "On Deformation and Failure of Brittle Solids: Some Outstanding Issues," Mechanics of Materials, Vol. 4, No. 3, 1985.


G. A. Hegemier

1 July 1985
Date

TABLE OF CONTENTS

<u>Section</u>	<u>Page</u>
PREFACE	i
LIST OF ILLUSTRATIONS	4
LIST OF TABLES	12
1. INTRODUCTION	13
1.1 OBJECTIVE	13
1.2 APPROACH	14
1.3 SINGLE VERSUS TWO-PHASE MODELS	16
1.4 SCOPE	17
1.5 PRESENTATION	17
1.6 RELEVANCE	18
2. EXPERIMENTAL DATA BASE: PLAIN CONCRETE	19
2.1 REMARKS	19
2.2 UNIAXIAL RESPONSE	19
2.2.1 Testing Machine Considerations	20
2.2.2 Specimen Considerations	25
2.2.3 Concrete Stress and Strain Rate Sensitivity	29
2.2.4 Monotonic Response in Compression	39
2.2.5 Cyclic Response in Compression	45
2.2.6 Tensile Response	48
2.3 BIAXIAL RESPONSE	52
2.3.1 Remarks	52
2.3.2 Biaxial Test Specimens	53
2.3.3 Biaxial Testing Machine Considerations	55
2.3.4 Stress-Strain Results	60
2.3.5 Biaxial Strength Results	67
2.3.6 Experimental Support for Plasticity Theories of Biaxial Response	78
2.3.7 Issues	83
2.4 TRIAXIAL RESPONSE OF PLAIN CONCRETE	83
2.4.1 Remarks on Micromechanics, Variability	84
2.4.2 Triaxial Test Specimens	88
2.4.3 Triaxial Testing Machine Considerations	88
2.4.4 Triaxial Test Procedures	90
2.4.5 Triaxial Testing Results	93
2.4.6 Outstanding Issues	102
3. EXPERIMENTAL DATA BASE: STEEL-CONCRETE INTERACTION	104
3.1 REMARKS	104
3.2 MECHANICS OF THE STEEL-CONCRETE BOND	105
3.2.1 Steel-Concrete Bond Mechanisms	105
3.2.2 Bond Failure Mechanism	109
3.2.3 Experimental Procedures for Bond Stress-Bond Slip Determination	110
3.2.4 Parameters Influencing Bond Slip and Attainable Bond Stress	113

TABLE OF CONTENTS (continued)

<u>Section</u>	<u>Page</u>
3.2.5 Bond Stress Distribution.	122
3.2.6 Attainable Levels of Bond Stress.	124
3.2.7 Cyclic Loading Effects.	126
3.2.8 Multiaxial Loading.	136
3.2.9 Issues.	136
3.3 AGGREGATE INTERLOCK, DOWEL ACTION.	139
3.3.1 Aggregate Interlock	139
3.3.2 Dowel Action, Combined IST and Dowel Action	147
3.3.3 Issues.	156
 4. PREVIOUS CONSTITUTIVE MODELS: PLAIN CONCRETE	 157
4.1 UNIAXIAL CONSTITUTIVE MODELS	157
4.2 BIAXIAL CONSTITUTIVE MODELS.	159
4.2.1 Nonlinear Elasticity Models	159
4.2.2 Plasticity Models	161
4.2.3 Biaxial, Cyclic Response Models	177
4.3 TRIAXIAL CONSTITUTIVE MODELS	183
4.3.1 Variable Modulus Models	183
4.3.2 Hypoelastic Models.	185
4.3.3 Elastic Plastic Models.	186
4.3.4 Plastic-Fracturing Models	188
4.3.5 Endochronic Models.	192
4.3.6 Constitutive Theory Conclusions and Recommendations	 194
 5. DEVELOPMENT OF IMPROVED CONSTITUTIVE MODEL OF PLAIN . . CONCRETE.	 196
5.1 GENERAL THEORY	196
5.1.1 The Progressively-Fracturing Solid.	196
5.1.2 The Plastic Solid	204
5.1.3 The Plastic-Fracturing Solid.	205
5.3 SPECIFICATION OF FAILURE SURFACE FOR PLAIN CONCRETE	207
5.3.1 Failure Criterion	208
5.3.2 Determination of Material Parameters.	212
5.3.3 Material Parameter Values	215
5.3.4 Evaluation of Failure Criterion	218
5.3.5 Conclusions	227
 6. DEVELOPMENT OF IMPROVED CONSTITUTIVE MODEL OF REIN- FORCED CONCRETE	 228
6.1 APPROACH AND SCOPE	228
6.2 DEVELOPMENT OF TWO-PHASE MIXTURE RELATIONS	232

TABLE OF CONTENTS (concluded)

<u>Section</u>	<u>Page</u>
6.2.1 Equilibrium Relations.	232
6.2.2 Constitutive Relations	232
6.2.3 Interface Relations.	234
6.2.4 Microcoordinates	235
6.2.5 Basic Relations: Asymptotic Form.	235
6.2.6 Periodicity Condition.	236
6.2.7 Smoothing Operation.	236
6.2.8 Two-Phase Mixture Equations: Equilibrium and Constitutive	237
6.2.9 Interaction Terms and Closure	238
6.3 VALIDATION OF TWO-PHASE MIXTURE RELATIONS FOR STEEL-CONCRETE BOND PROBLEM.	241
6.3.1 Basic Mixture Relations	242
6.3.2 Monotonic Extension	248
6.3.3 Hysteretic Extension.	261
6.3.4 Influence of Basic Parameters	267
6.3.5 Recovery of Microstructure.	275
6.4 REMARKS.	275
6.5 ON SINGLE-PHASE MODELS	280
7. CONCLUDING REMARKS.	297
LIST OF REFERENCES.	299

LIST OF ILLUSTRATIONS

<u>Figure</u>		<u>Page</u>
2-1	Typical uniaxial monotonic response of concrete. . .	21
2-2	Typical uniaxial compressive cyclic response of concrete (a) pre-peak response (b) post-peak response .	21
2-3	Sensitivity of concrete behavior to testing machine stiffness.	23
2-4	Influence of the specimen size and shape on the complete stress-strain curve for marble loaded in uniaxial compression.	28
2-5	Sensitivity of concrete compressive strength to loading rate	31
2-6	Sensitivity of concrete compressive stress-strain curves to stress rate.	32
2-7	Concrete strength rate sensitivity	34
2-8	Stress and strain rate controlled concrete compression experiments	34
2-9	Stress-strain curves for several strain rates. . . .	35
2-10	Effect of strain rate on softening response	37
2-11	Typical stress-strain curve for concrete uniaxial, monotonic, compressive response	40
2-12	Typical stress-strain curves for concretes.	40
2-13	Volumetric strain ϵ_v for uniaxial, monotonic, compression test	42
2-14	Typical compressive stress - Volumetric strain results	43
2-15	Isochronous stress-strain curves for a typical concrete	44
2-16	Uniaxial, compressive cyclic stress-strain curve. .	47
2-17	Monotonic and cyclic compressive stress-strain response.	47

LIST OF ILLUSTRATIONS (continued)

<u>Figure</u>		<u>Page</u>
2-18	Typical uniaxial stress-strain curves	50
2-19	Isochronous tension stress-strain curves.	51
2-20	Uniaxial and biaxial compressive strengths versus prism thickness.. . . .	56
2-21	Comparison of failure surfaces for biaxial compression.	56
2-22	Failure surfaces for biaxial compression (a) brush bearing platen, (b) unlubricated steel platen . . .	59
2-23	Failure surfaces for biaxial compression using fluid cushion and unlubricated steel platens.	59
2-24	Biaxial failure surface	61
2-25	Experimental results from Weigler and Becker: (a) uniaxial compression, (b) equi-biaxial compression.	62
2-26	Biaxial compression data.	64
2-27	Biaxial compression response for model concrete . .	68
2-28	Biaxial compression-tension response.	69
2-29	Biaxial tension response.	70
2-30	Typical biaxial strengths of plain concrete	71
2-31	Load platen types used in experimental program. . .	73
2-32	Strength envelopes obtained using different load platen designs.	74
2-33	Strength envelopes obtained using different load platen designs and normalized to f'_c	75
2-34	Failure surface for biaxial compression-tension . .	76
2-35	Failure surface for biaxial compression-tension and tension	76
2-36	Failure surface for biaxial compression-tension . .	77

LIST OF ILLUSTRATIONS (continued)

<u>Figure</u>		<u>Page</u>
2-37	Sensitivity of biaxial failure surface to load path: dry specimens.	79
2-38	Sensitivity of biaxial failure surface to load path: wet specimens.	79
2-39	Curves of constant secant modulus plotted in principal stress space.	81
2-40	Ultimate and discontinuity curves for biaxial compression and compression-tension.	82
2-41	Crack length and ultrasonic wave speed reduction as a function of lateral stress.	86
2-42	Failure stresses on the octahedral plane $\sigma_n = 5$ ksi	94
2-43	Intersection of failure surface with octahedral planes $\sigma_n = 3\alpha/\sigma_0$, σ_0 = uniaxial compressive strength	95
2-44	Intersection of failure surface with the plane $\sigma_1 = \sigma_2$	97
2-45	Failure stresses obtained by Chinn and Zimmerman. .	98
2-46	Failure stress data from various authors.	98
2-47	Triaxial stress-strain results for same concrete under different levels of hydrostatic pre-stress. .	100
2-48	Cyclic stress-strain data from a conventional triaxial test.	101
3-1	Bond stress - the interfacial shear stress between rebar and concrete.	106
3-2	Aggregate interlock - the transfer of shear load across a crack by aggregate contact	107
3-3	Dowel action - the transfer of shear load across a concrete crack by a rebar	108
3-4	Pull out test specimen.	112
3-5	Tension test specimen	112

LIST OF ILLUSTRATIONS (continued)

<u>Figure</u>		<u>Page</u>
3-6	(a) Differential bar element, showing uniaxial bar stress σ equilibrated by bond shear stress τ (b) Definition of A and p as bar cross-section area and perimeter	114
3-7	Average bond stress versus loaded end slip.	117
3-8	Bar end load as a function of end slip for different covers and concrete strengths	119
3-9	Migration of bond stress distribution and increase in maximum bond stress with rebar end load.	123
3-10	Migration of bond stress distribution and increase in maximum bond stress with rebar end load.	123
3-11	Tension specimen showing added concrete at ends of cylinder to increase bar confinement.	125
3-12	Bond stress distribution along rebar for different load cycles	129
3-13	Strain distribution along rebar for different cycles and for the load histories in Table 2-10.	130
3-14	Bond stress as function of slip for cyclic history between fixed load limits	133
3-15	Bond stress as function of slip for cyclic history with increasing load amplitude.	133
3-16	Bond stress versus slip for fully reversed cyclic histories (a) fix slip limits, (b) increasing slip limits.	134
3-17	Stabilized cyclic bond stress-slip curve for testing between fixed slip limits	135
3-18	Average bond stress as a function of end slip showing effect of external lateral pressure	137
3-19	Bond stress as a function of external lateral pressure for fixed bond slip and different bar sizes.	138
3-20	Fenwick's aggregate interlock test specimen	141

LIST OF ILLUSTRATIONS (continued)

<u>Figure</u>		<u>Page</u>
3-21	Displacement curve for Fenwick's tests.	141
3-22	Loeber's test specimen.	142
3-23	Displacement curve for Loeber's tests	142
3-24	Typical displacement curve from Houde	144
3-25	Test specimen configuration from work performed by White and Holley.	145
3-26	Typical response for IST transfer from tests performed by White and Holley.	146
3-27	Typical shear stress versus shear slip results for IST tests performed by Laible	148
3-28	Block type test specimens performed by Jimenez. . .	149
3-29	Typical load-slip behavior of combined mechanism (IST and dowel)	151
3-30	First cycle load-displacement curve for dowel action	152
3-31	Details of test specimen construction	154
3-32	Dowel shear force-slip relationship	155
4-1	Initial and subsequent yield surfaces and failure surface proposed by Chen and Chen	167
4-2	Equivalent stress versus equivalent strain curves .	168
4-3	Averaged equivalent stress versus equivalent strain curves.	169
4-4	Strain based failure criterion.	171
4-5	Initial yield, subsequent yield and failure curves.	173
4-6	Comparison between theory of Murray et al, and data of Kupfer, Hilsdorf and Rusch: (a) Biaxial compression, (b) compression-tension	175
4-7	Uniaxial, cyclic, compressive stress-strain history showing envelope curve.	181

LIST OF ILLUSTRATIONS (continued)

<u>Figure</u>		<u>Page</u>
4-8	Uniaxial, cyclic, compressive stress-strain history showing loop closure on or below common point curve	181
4-9	Piecewise linear description of stress-strain cycle	182
4-10	Comparison of Darwin and Pecknold proposed model results with experimental data of Karsan and Jirsa	182
4-11	Comparison of cyclic panel response predicted by proposed model of Darwin and Pecknold with experimental data of Cervanka and Gerstle	184
5-1	Uniaxial tensile behavior	202
5-2	Biaxial example of instability surface.	203
5-3	Characteristics of proposed failure surfaces shown in principal stress space	210
5-4	Translation of principal stress space along hydrostatic axis to include effect of tensile strength in failure criterion	211
5-5	Determination of material parameters involved in failure criterion for Mix A concrete tested by Mills and Zimmerman	214
5-6	Comparison of proposed failure criterion in biaxial planes with results of biaxial tests performed by Kupfer, Hilsdorf, and Rusch in (a) biaxial plane, and (b) enlarged tension-tension region	220
5-7	Comparison of proposed failure criterion in biaxial planes with results of biaxial tests performed by (a) Mills and Zimmerman on Mix A concrete, and by Tasuji, Slate, and Nilson	221
5-8	Comparison of proposed failure criterion in triaxial planes with results of triaxial compression and extension tests	222
5-9	Comparison of proposed failure criterion in octahedral planes with results of tests on concrete	224
5-10	Comparison of proposed failure criterion with results of torsion shear tests.	226

LIST OF ILLUSTRATIONS (continued)

<u>Figure</u>		<u>Page</u>
6-1	Single and Two-Phase model concepts	230
6-2	Dense mesh, hexagonal layout.	231
6-3	Dense mesh, rectangular layout.	231
6-4	Sparse mesh, non-periodic (beam cross-section). . .	231
6-5	Typical cell and coordinate system.	233
6-6	Reinforced concrete (masonry) under cyclic tensile loading	243
6-7	Stiffness degradation in a reinforced concrete (masonry) specimen.	244
6-8	Behavior of constituents and steel-concrete interface for monotonic extension example	245
6-9	Typical cell cracking sequence: (a) physical, (b) mathematical.	249
6-10	Typical stress distributions prior to and after concrete cracking	253
6-11a,b	Effective stress versus effective strain for monotonic extension	256
6-11c,d	Stiffness degradation	257
6-12a,b	Response of wire-reinforced test specimen under monotonic extension	259
6-13	Specimen details.	260
6-14	Theory versus experiment for monotonic extension. .	262
6-15a	Bond slip law for unloading to zero effective stress	264
6-15b	Bond slip law for cyclic deformation.	264
6-16	Mixture model response under cyclic loading	265
6-17	Single cycle of deformation for mixture model . . .	266
6-18	Single cycle of deformation for R/C test specimen .	266

LIST OF ILLUSTRATIONS (concluded)

<u>Figure</u>		<u>Page</u>
6-19	Comparison of theory and experiment for cyclic deformation	268
6-20	Comparison of theoretical and experimental stiffness degradation for cyclic deformation	269
6-21	Effect of initial crack spacing on stiffness degradation	271
6-22	Smoothing of the stiffness degradation.	272
6-23	Influence of bond strength on stiffness degradation	273
6-24	Variation of monotonic response with bond strength	274
6-25	Influence of steel volume fraction on stiffness degradation	276
6-26	Influence of steel volume fraction on monotonic response.	277
6-27a	Local axial displacements in steel and concrete a distance 2.4 in. from crack face. Axial displacements normalized on cross-sectional average in concrete	278
6-27b	Variation of local axial stress in steel and concrete a distance 2.5 in. from crack face	279
6-28	R/C stiffness behavior in (a) tension, (b) compression.	281
6-29	Initial and subsequent biaxial fracture surfaces in strain space.	284
6-30	Initial biaxial fracture surface in stress space. .	285
6-31	Principal coordinates and reference coordinates . .	286
6-32	Influence of initial normal strain on shear modulus	289
6-33	Initial and subsequent biaxial fracture surfaces in strain space.	290
6-34	Single-phase model simulation of stress versus strain	293
6-35	Single-phase model simulation of stiffness degradation	294
6-36	Normalized dissipation function	295

LIST OF TABLES

<u>Table</u>		<u>Page</u>
2-1	Experimental Variables in Concrete Uniaxial Testing	20
2-2	Specimen Types used in Biaxial Tests.	54
2-3	Coefficients of Friction Between Load Platens and Specimens for Various Lubricants.	57
2-4	Geometric Data for Specimens Used in Triaxial Tests	89
2-5	Lubrication Schemes for Reducing Friction at the Specimen Platen Interface	91
2-6	Effect of Lubrication Scheme on True Triaxial Failure Stress.	91
3-1	Variables in the Design of Steel-Concrete Interaction Experiment	115
3-2	Restraint on Rebar Slip Increases with Cover. . . .	120
3-3	Bond Strength for Plain Bars.	126
3-4	Average Bond Strength for Deformed Bars	127
3-5	Load Histories Corresponding to Figure 3-13	131
5-1	Strength Parameters for Concrete and Mortar	216

SECTION 1 INTRODUCTION

1.1 OBJECTIVE

The primary objective of this research program is to initiate the construction and validation of an advanced continuum model of reinforced concrete that simulates real material behavior in the highly nonlinear range of material response.

A secondary objective is to identify experimental and theoretical problem areas associated with model development and validation, and to recommend remedial research where necessary.

It is intended that the continuum constitutive model of reinforced concrete under development be, when completed:

- Nonphenomenological
- Multiaxial
- Applicable to both dense and sparse steel layouts.
- Valid for arbitrary time histories

It is also intended that the model properly describe:

- Failure surface geometry
- Strain hardening, softening
- Stiffness degradation
- Anisotropy due to steel
- Anisotropy due to cracking
- Stress, deformation path dependence
- Strain-rate effects

The term "nonphenomenological" above denotes a model that will synthesize the global behavior of reinforced concrete from a description of the concrete and steel properties, the concrete-steel interface properties, and the steel geometry. The purpose of such a model is to minimize the number and size of tests necessary to evaluate the model parameters, and to allow immediate identification of the physical significance of each model parameter.

The term "multiaxial" above has the usual connotation: arbitrary stress (deformation) states and stress (deformation) paths.

Both "dense" and "sparse" steel layouts occur in practice, although the former is more common in the defense community. Consequently, it is important that a model of reinforced concrete be applicable to a practical range of steel layouts.

The loading conditions associated with reinforced concrete structures in a defense environment envelop a wide range of strain rates. Of particular importance is the high strain-rate regime. Consequently, a complete constitutive model of reinforced concrete should incorporate time history or strain-rate effects.

The second group of terms noted above refer to the basic measures of material response: strength, stiffness, and ductility, and to the changes in these measures due to progressive cracking and degradation of the steel-concrete bond, and stress-rate.

1.2 APPROACH

The task of constructing a viable constitutive model of reinforced concrete can be partitioned into several basic subtasks. The first such subtask consists of formulating sufficiently accurate models of the constituents: steel and concrete. The former does not present a problem; the latter does. Consequently, the first subtask consists of formulating an improved model of plain concrete. In what follows, this effort is further partitioned into: (1) rate-independent models and (2) rate-dependent models.

The second subtask consists of mathematically describing the behavior of the steel-concrete interfaces.

The third subtask consists of formulating a procedure for analytically mixing the steel and concrete. This must be defined such that the steel-concrete interaction, which plays a critical role in the global response of reinforced concrete, is adequately modeled. Further, the mixing procedure must synthesize the global properties of reinforced concrete from the properties of plain

concrete, steel, interfaces, and the steel geometry. In what follows, this effort is further partitioned into four important problems areas: (1) the steel-concrete bond problem, (2) the steel-concrete dowel problem, (3) the concrete aggregate interlock problem, and (4) the steel-buckling-concrete-spallation problem. Problem (1) plays a dominant role in the bending and nonlinear stretching (associated with membrane action) of R/C beams, plates and shells (e.g., the "late-time" bending and nonlinear stretching of R/C protective box-type structure roofs). Problem (2) plays a major role in the transverse shear deformation of R/C beams, and the transverse and in-plane shear deformation of R/C plates and shells (e.g., the "early-time" response of R/C protective box-type structure roofs and the protective cover "punch-out" problem). Problem (3) plays an important role in those cases wherein relative motion occurs across existing cracks (e.g., hysteretic in-plane shear deformation of R/C plates). Problem (4), which concerns containment of the concrete by the rebar mesh, spallation of the concrete, and subsequent buckling of rebar, plays an important role in direct compression of R/C structural elements (e.g., impact loading of a R/C liner in the axial direction).

The final task consists of validating the resulting models of plain and reinforced concrete by experimental versus theoretical data comparisons.

To accomplish the task of modeling plain concrete, the use of a plastic-fracturing theory is explored herein. This formulation allows simulation of both progressive fracture and "plastic" slip, and it includes elasto-fracture coupling (i.e., stiffness degradation). A major advantage of this approach is that the constitutive relation is linear in the stress and strain increments.

To accomplish the task of analytically mixing the steel and concrete, a mixture-theory-with-microstructure approach is explored herein. This procedure has been previously used with considerable success to model fibrous composite materials. The technique, which must be expanded to cover problems peculiar to reinforced concrete,

allows one to directly synthesize the global composite material properties from the component properties.

1.3 SINGLE VERSUS TWO-PHASE MODELS

Both 'two-phase' and 'single-phase' mixture models of reinforced concrete are discussed in this report. The two-phase model retains the identity of the individual constituents (steel and concrete) while the single-phase theory represents a single, new composite material in which the steel and concrete are completely homogenized.

The advantage of a two-phase model is increased (over a single-phase model) simulation capability and accuracy. In addition, the role of each constituent is easily identified. The disadvantage is increased (over a single-phase model) complexity: roughly twice the dependent variables associated with a single-phase model.

The advantage of a single-phase model is its simplicity. This simplicity, however, is obtained at the price of reduced simulation capability and reduced accuracy. Nevertheless, for many practical applications these reductions are not serious. A single-phase model also has the advantage that it can be readily incorporated into current finite element codes. This is in contrast to the two-phase formulation which requires special numerical treatment.

It is noted that development of a two-phase theory has progressed under AFOSR support** while development of a single phase theory has progressed under DNA support.* It is emphasized, however, that one must derive a two-phase model before a single-phase model can be constructed. Consequently, there has been considerable overlap in these two programs in the area of two-phase

* DNA-001-80-C-0181

** AFOSR - F49620-81-C-0033.

model development. On the other hand, a major difference in these two programs is the use of an endochronic theory to model plain concrete in the case of AFOSR and the use of a plastic-fracturing theory in the case of DNA.

1.4 SCOPE

Although considerable progress toward achievement of the stated objectives has occurred under the current contract, the complete development and validation of either a single-phase or a two-phase theory of reinforced concrete is beyond the scope of a single twelve-month research effort. Indeed, such a task requires a period of focused and sustained research covering several years.

In order to render the research effort systematic and manageable, attention was focused during the above mentioned twelve-month research period on a subset of the tasks outlined in subsection 1.2. In particular, model development was confined to: (1) strain-rate independent plain concrete theories and (2) the steel-concrete bond problem. Data collection and assessment, which are critical to model validation, and also serves as a precursor to model development covered, on the other hand, most of the task areas outlined in subsection 1.2, including strain-rate effects.

1.5 PRESENTATION

The report presentation is divided into seven sections. Sections 2,3 document the relevant experimental data base for plain concrete and steel-concrete interaction. As was noted previously, these are items critical to both model construction and validation. Section 4 reviews previous constitutive models for plain concrete. Development and validation of an improved model of plain concrete is presented in Section 5. Section 6 presents the construction and validation of an improved model of reinforced concrete. This section also reviews some additional important experimental data concerning the direct testing of reinforced concrete. Conclusions and recommendations are furnished in Section 7.

1.6 RELEVANCE

This research program attempts to fulfill a critical need in the defense community for more accurate theoretical descriptions of reinforced concrete in the inelastic, nonlinear range of material response. Such descriptions are essential components of numerical simulations of structural response. Simulations are, in turn, important elements in system design and evaluation, fragility studies, and cost trade-off studies for protective facilities.

SECTION 2

EXPERIMENTAL DATA BASE: PLAIN CONCRETE

2.1 REMARKS

In this section a comprehensive survey is made of the current data on the behavior of plain concrete. Such information is vital for model validation purposes. The discussion is partitioned into uniaxial response (subsection 2.2), biaxial response (subsection 2.3), and triaxial response (subsection 2.4). A substantial portion of this information is used in the validation of the improved model of plain concrete presented in Section 5.

2.2 UNIAXIAL RESPONSE

The preponderance of experimental data on plain concrete has been obtained from uniaxial tests. Much of the data is of little use for constitutive theory development and verification tasks because either experimental procedures were not adequately documented or the generated data base was too small. For example, many researchers make no mention of testing speeds or specimen end conditions while much of the data is little more than a list of observed compressive strengths.

For experimental data to be useful in constitutive theory research the data must be the result of a carefully executed suite of experiments. Care is needed because of the large number of variables involved, Table 2-1. Additionally, concrete response is extremely complicated. Typical uniaxial compressive monotonic response is shown in Figure 2-1. Concrete has little strength in tension. In compression the response is initially elastic and then becomes progressively nonlinear as internal microcracks propagate. At a maximum compressive stress, f'_c , concrete can start softening and the stress continuously decrease until, at some ultimate strain ϵ_{L-t} , complete specimen disintegration occurs. Typical cyclic stress-strain curves are shown in Figure 2-2. Little hysteresis occurs so long as the stress has never reached f'_c . On the softening branch, Figure 2-2b, hysteresis appears more pronounced

and possibly variable. Currently no well designed and executed series of experiments has been executed on a set of identical specimens over the entire uniaxial response spectrum.

Table 2-1

Experimental variables in concrete uniaxial testing

Testing Machine and Procedure	Machine Stiffness Strain versus Load Control Testing Speed Servo Controls Feedback Signal
Specimen	Size and Shape Aggregate Type and Content Aggregate Size Distribution Water/Cement Ratio Curing/Storage History
Machine/Specimen Interface	Load Platen Stiffness Interfacial Friction

In the following subsections, equipment and experimental procedures are first reviewed. The objectives here are (1) identify problem areas in concrete uniaxial testing, (2) recommend techniques that will produce reliable stress-strain data, and (3) suggest why there is so much scatter in the reported data. Subsequently the experimental data bases for concrete uniaxial monotonic and cyclic, compression and tension response are reviewed.

2.2.1 Testing Machine Considerations

It has been very difficult for experimentalists to design testing machines that load (or deform) concrete test specimens to desired stress (or strain) time histories. The principal problems have been

- inadequate testing machine stiffness
- unintentional constraining of specimen deformations.

A. Testing Machine Stiffness.

Figure 2-1 shows that under displacement controlled conditions, concrete exhibits a long softening branch. This branch

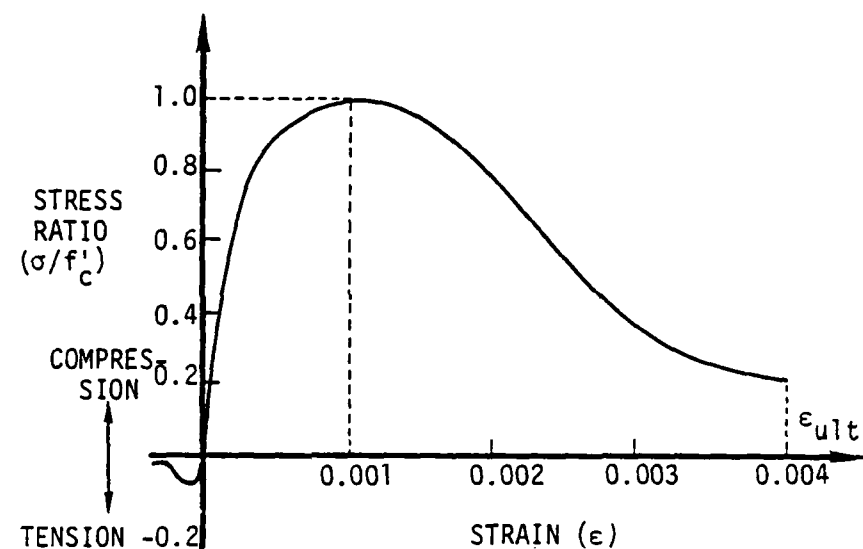


Figure 2-1. Typical uniaxial monotonic response of concrete.

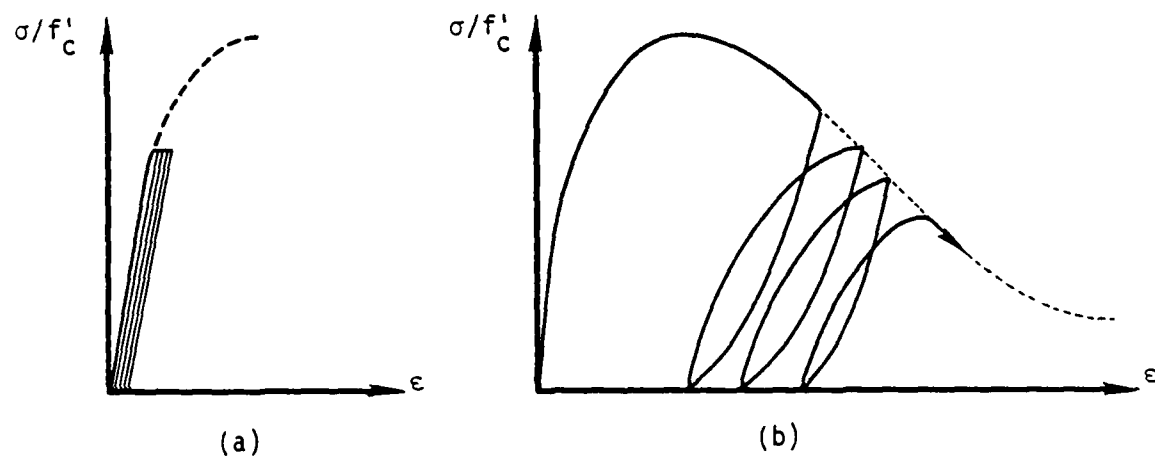


Figure 2-2. Typical uniaxial compressive cyclic response of concrete
(a) pre-peak response (b) post-peak response.

implies that concrete does not necessarily fail catastrophically when the stress reaches f'_c . Indeed current ACI guidelines for structural design account for concrete softening. Also most of the energy dissipation and material damping in concrete occurs on the softening branch. However, reliable data on concrete softening is difficult to obtain because sudden, even explosive, specimen failures frequently occur when the stress reaches f'_c . Figure 2-3 shows data obtained by Whitney⁽¹⁾ on three different concretes. The results indicated that uncontrolled specimen failure occurred when the magnitude of stiffness associated with the concrete specimen softening branch just exceeded testing machine stiffness. Whitney suggested that such failures occurred because the testing machine was not stiff enough to absorb the energy released as the specimen softened. Hudson, Crouch and Fairhurst,⁽²⁾ using virtual work and stability arguments later repeated by Ahmad and Shah,⁽³⁾ gave a mathematical justification for this reasoning. Experimental verification was obtained by Sigvaldason⁽⁴⁾ who used two testing machines with stiffnesses of 0.1×10^7 lb/in and 2.0×10^7 lb/in to test identical specimens. Specimens in the softer machine failed explosively while those in the stiffer machine did not. Sigvaldason also noted that the failure stress was insensitive to machine stiffness.

Several researchers have sought to prevent uncontrolled specimen failures by artificially stiffening their test machines. Hsu, Slate, Sturman and Winter⁽⁵⁾ placed aluminum channels in parallel with their specimen so that they were simultaneously loaded along with the specimen. However the channels had too small a cross-section and the authors achieved only limited success. Ahmad and Shah⁽³⁾ placed a case hardened steel cylinder around but not in contact with their specimens. The cylinders responded elastically up to an axial strain of 0.006 and were of sufficient wall thickness that the composite steel-concrete stiffness was not sufficiently negative as to cause uncontrolled failure. Hughes and Chapman⁽⁶⁾ effectively increased the stiffness of their universal testing machine when they were performing tensile tests by

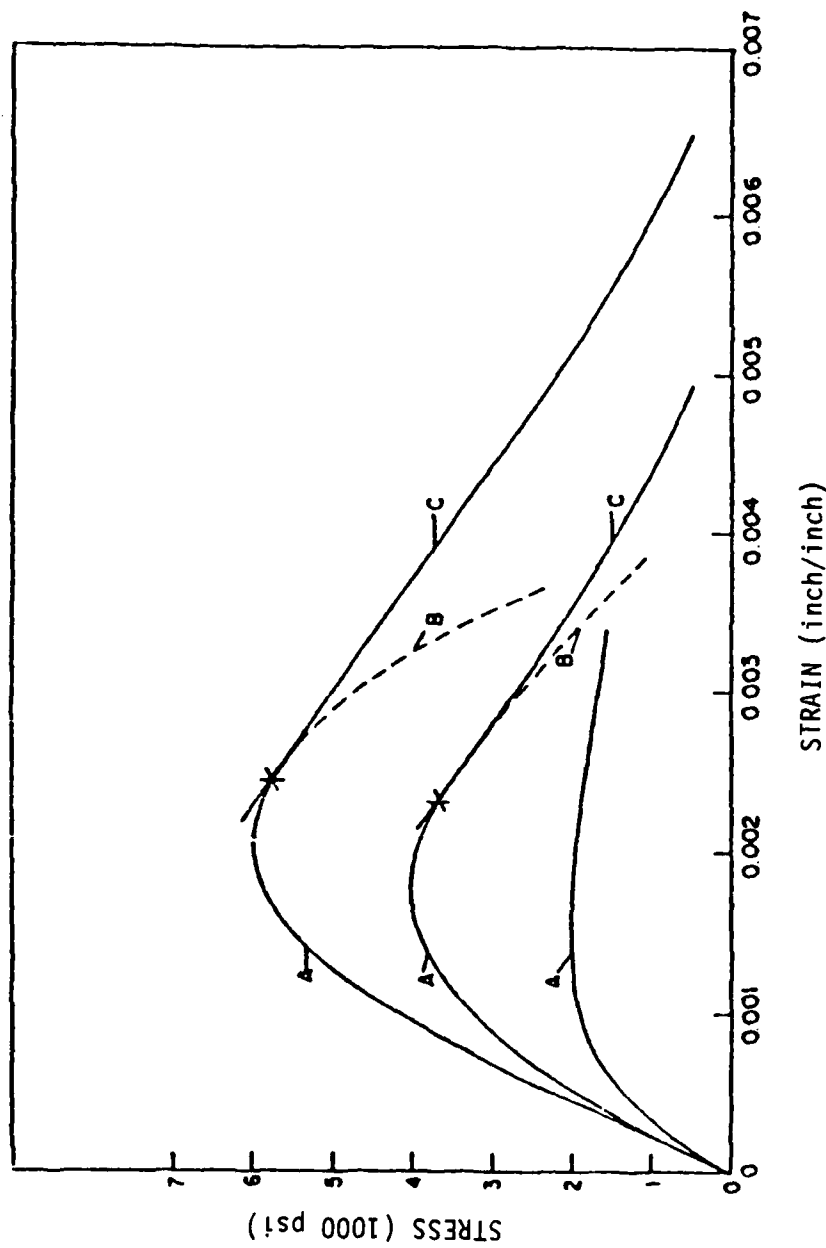


Figure 2-3. Sensitivity of concrete behavior to testing machine stiffness. Failure occurs at point X when specimen stiffness equals machine stiffness, curve C. Curve B is specimen response for very stiff machine.

simultaneously compressing a steel block placed in the compression compartment of the machine. From their experiments the authors showed that concrete can soften in tension.

Concrete post-peak response can also be controlled if closed-loop servo-controlled systems are used to apply the load. Hudson, Crouch and Fairhurst⁽²⁾ discussed such systems at length. In a closed-loop servo-controlled concrete testing system the feedback signal (a preselected varying deformation measure that is characteristic of the experiment) is continuously monitored and its value compared with that programmed into the system. If significant error is detected, the control system automatically adjusts load cell pressure so as to minimize the error. For maximum effectiveness system response time must be sufficiently fast and the feedback signal judiciously selected. For rock testing, a response time of 5 msec is adequate since then failure propagation will be slow; this is well within the capability of many systems and should hold for concrete also since the failure processes of the two materials are similar. The optimum feedback signal is that deformation measured which is most sensitive to the ongoing failure. In a compression test, where failure results from cracks parallel to the load, transverse displacement is the best choice while in a tension test tensile strains or displacements are best.

In summary, the steps necessary to construct an adequate testing machine and properly control it are known. However few such testing systems exist.

B. Specimen Constraint Reduction

In uniaxial tension and compression tests, load is transferred from load cell to specimen through steel load platens that are very stiff relative to the concrete. Particularly in compression tests interfacial friction between platen and specimen allows the steel to inhibit free transverse motion of the concrete and retard internal microcrack formation in the concrete parallel to the load. Consequently the specimen is artificially strengthened. This phenomenon is particularly noticeable in cubes where no point in the specimen is far from the load platens (Rüsch⁽⁷⁾).

The lateral constraint would not be objectionable if it were not so uncontrollable. However, as is shown in subsequent sections, frictional effects cause wide variations in observed failure stress. Thus platen-specimen friction should be minimized. A variety of materials have been interposed between platen and specimen to achieve this. Jones⁽⁸⁾ even tried plywood and rubber. Plywood had negligible effect but rubber induced premature failure because the rubber expanded laterally more than the concrete and induced lateral tension in the concrete. The usual technique for reducing friction, (Hsu et al.⁽⁵⁾, Hughes and Bahramian⁽⁹⁾), is to alternate layers of waxed paper, plastic, teflon or metallic foils with grease.

The latter authors, in comparing lubricated versus unlubricated interfaces noted that lubrication

- reduced differences in concrete strengths obtained from specimens of different shape
- resulted in compression specimens failing from longitudinal splitting, which was indicative of unconstrained deformation.

2.2.2 Specimen Considerations

The most serious source of scatter in concrete stress-strain data is the specimen itself. The large number of variables that describe a specimen are of two types -- concrete mix parameters and the rest. Sensitivity of experimental data to mix parameters will not be discussed since these, in essence, define a concrete's microstructure and thus fall outside the purview of continuum mechanics based constitutive theories. The remaining variables are specimen size, shape and curing history.

In uniaxial tests, specimens range from two inch cubes to 6 in. D x 12 in. L cylinders and larger. Concrete is subject to a certain randomness in its macroscopic stress-strain response because its behavior is governed by the initiation, propagation and final coalescence of internal microcracks. Thus specimen strength

decreases with increasing specimen volume since, from statistics, larger specimens will have a larger expected initial microcrack size. For example, Sigvaldason⁽⁴⁾ found that 4 in. cubes were 10 percent stronger than 6 in. cubes. Newman and Sigvaldason⁽¹⁰⁾ have noted a subtle way that large specimens can effect experimental results. An inhomogeneous distribution of aggregate and the accumulation of voids beneath pieces of aggregate close to the top, horizontal, free surface of the specimen, can result in a nonuniform specimen strength. This was verified by Cole⁽¹¹⁾ who tested the upper and lower halves of a 4 x 4 x 8 in. prism and found the upper half to be weaker by as much as 56 percent relative to the lower half. Consequently constitutive data obtained from test specimens will be most representative of in situ plain concrete when the test specimens are large; small specimens will tend to overestimate strength, Sabnis and Aroni⁽¹²⁾, Newman⁽¹³⁾.

Three specimen shapes have been commonly used:

- Cubes
- Rectangular prisms
- Cylinders.

The most important specimen shape parameter is the specimen longitudinal-to-transverse dimension ratio L/T . Extensive experiments indicate that results are insensitive to L/T when L/T is greater than two; this is reflected in the dimensions of the common 6 in. ϕ x 12 in. L cylinder specimen. (Newman and Lachance⁽¹⁴⁾ recommended taking $L/T > 2.5$).

Thus the cube specimen is least desirable because it is overly sensitive to platen induced end constraints. For example Newman and Lachance⁽¹⁴⁾ found cube compressive strength to be 30 percent greater than that of cylinders with $L/T = 2.5$. Sigvaldason⁽⁴⁾ found 4 in. cubes were 20 percent stronger than cylinders with $L/T = 2$; Hughes and Bahramian⁽⁹⁾, using unlubricated platens found 4 in. cubes were up to 50 percent stronger than rectangular prisms with $L/T = 2.5$

The effects of specimen size and shape are particularly noticeable in the determination of the compressive softening branch. Figure 2-4 shows results for a series of tests on marble specimens and it is clear that for short specimens, where $L/D < 0.5$, almost no softening is observed because of platen constraints. When $L/T > 2$ response curves are fairly close together. When specimen dimensions were scaled keeping L/T fixed, changes in specimen response were not as dramatic, indicating that L/T is more important than absolute dimensions. Of course large specimens are more difficult to control on the softening branch because they release more energy than smaller specimens. Thus larger specimens will tend to failure more rapidly.

The final way that specimens can effect experimental results is through their curing history. Curing effects are complicated and are connected with the diffusion of moisture through the concrete microstructure. Large specimens cure slower and more non-uniformly than small specimens thus setting up moisture gradients which would make large specimens more prone to curing induced microcracking. Mirza, Hatzinikolas and MacGregor⁽¹⁵⁾ and Sabnis and Aroni⁽¹²⁾ noted that specimens cored from massive structures such as dams are not size sensitive when tested. This is because while the specimens were curing in situ they did not have large surface areas over which to lose moisture. Thus for the current application, where the structures are very large, it is best to make specimens by coring them from larger specimens. An alternative would be to seal the specimens against moisture loss/gain. This latter suggestion is motivated by the work of Sabnis and Aroni who found that sealed specimens also showed reduced sensitivity to size when tested.

Conclusions

The objectives of the discussion on specimen variables were to identify reasons why there is so much scatter in the current data base and to suggest how best to design a specimen that would be most useful in protective structure modeling. The reasons for the data scatter are clear:

SIZE EFFECT

SHAPE EFFECT

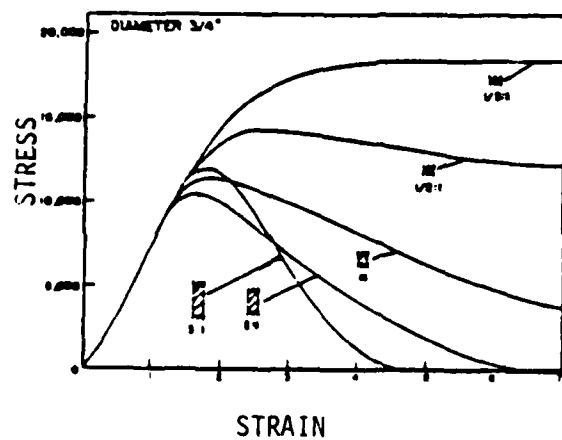
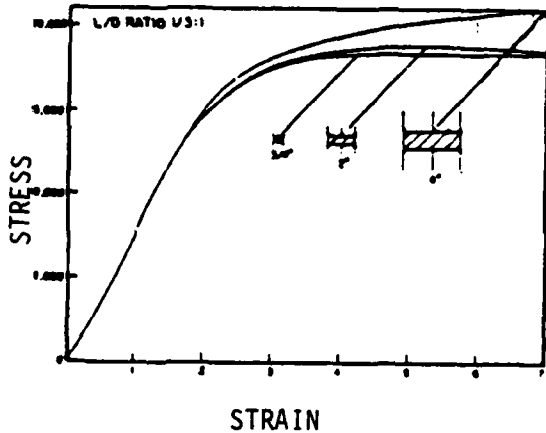
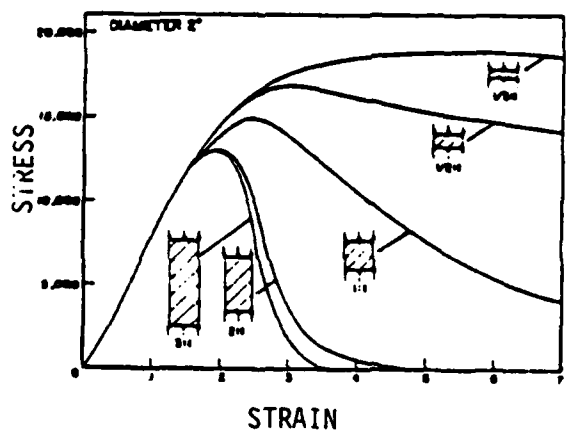
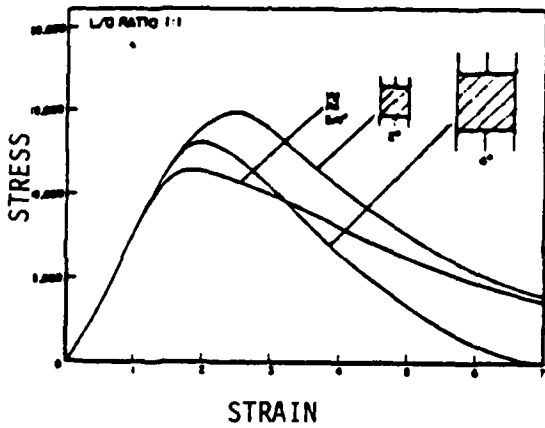
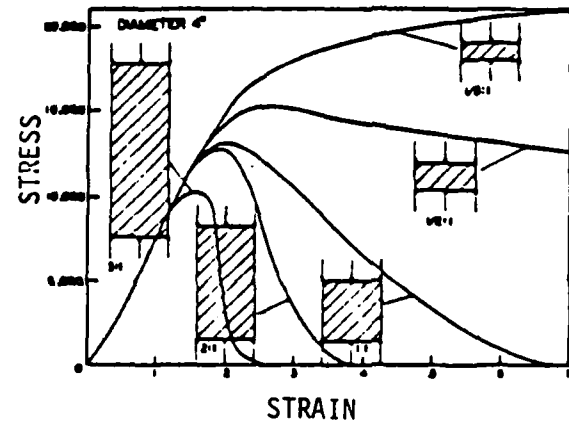
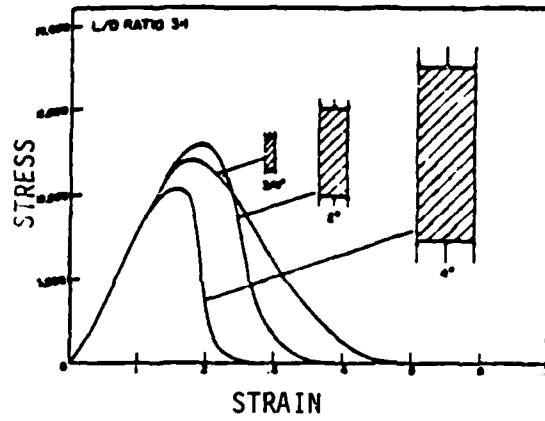


Figure 2-4. Influence of the specimen size and shape on the complete stress-strain curve for marble loaded in uniaxial compression.

- wide differences in mix (not discussed)
- large number of different specimen sizes and shapes
- non-uniformity in specimen curing history.

To overcome these problems it is recommended that:

- in modeling a particular structure, the constitutive parameters be for the concrete mix used to fabricate the structure,
- specimens should satisfy $L/T > 2$ but not be so large as to prevent controlled descent of the softening branch,
- specimens should ideally be cored from the structure being analyzed or else cured in an environment that simulates in situ curing.

2.2.3 Concrete Stress and Strain Rate Sensitivity

Discussion of concrete rate sensitivity can be divided into two parts depending on whether testing lasts long enough for significant concrete creep to occur. Typical uniaxial tests last only minutes and for longer tests, specimen creep or relaxation is possible while for shorter test time, concrete will exhibit a viscoplastic (i.e., rate enhanced strength) effect. Concrete strength increases monotonically with increasing strain rate. Standard tests are performed at a rate of 10^{-1} in/in/sec (or 35 psi/sec). Mirza, Hatzinikolas and MacGregor,⁽¹⁵⁾ using a modified form of an earlier result by Jones and Richart,⁽¹⁶⁾ stated that

$$f_{CR} = 0.89 f_{C35} (1 + 0.08 \log_{10} R) \quad (2-1)$$

represented the stress rate sensitivity of concrete strength. Here f_{C35} , f_{CR} were concrete strengths at stress rates 35 psi/sec and R psi/sec respectively. Eq. 2-1 was valid over the range $10^{-1} \leq R$ psi/sec $\leq 10^4$ and predicted that f_{c1} and f_{c1000} were 12 percent lower and higher than f_{C35} . (For $R = 1, 35, 1000$ psi/sec, $f_{C35} = 4200$ and initial Young's modulus $E = 3.6 \times 10^6$ psi, the corresponding strain rates and test durations are $\dot{\epsilon} = 2.8 \times 10^{-7}, 10^{-5}, 2.7 \times 10^{-4}$ in/in/sec and 7, 0.2, 0.07 min respectively.)

More recently Kaplan⁽¹⁷⁾ tested a 20 N/mm² (2900 psi) concrete at stress rates 10⁻³ - 10 N/mm²/sec (0.145 - 1450 psi/sec). Results for a 36-day concrete are shown in Figure 2-5. The data was found to fit the equation

$$f_{CR} = 0.84 f_{C35} (1 + 0.124 \log_{10} R) \quad (2-2)$$

which is similar to Eq. 2-1.

High stress rate data have been obtained by Ferrito⁽¹⁸⁾, Watstein⁽¹⁹⁾, Atchley and Furr⁽²⁰⁾ and Hughes and Watson⁽²¹⁾. Figure 2-6 shows data from the first paper. Stress rate range was 1.8 x 10³ - 1.8 x 10⁶ psi/sec which, for an initial Young's Modulus of 3.6 x 10⁶ psi, corresponded to a strain rate range of 5 x 10⁻⁴ - 5 x 10⁻¹/sec. Thus load rates were much more severe than in previously discussed papers. Indeed for the highest rate Ferrito found that strength was 30 percent greater than for the static loading case. Note that initial Young's modulus also increased (by 18 percent over static test value). Watstein⁽¹⁹⁾ obtained comparable results, Figure 2-7. He tested concretes with static strengths of 2800 psi and 6300 psi respectively and thus straddled Ferrito's 4000 psi static strength concrete. Watstein found concrete to be very rate sensitive with strength increases for the weaker (stronger) concrete of 55 percent (19 percent) over the strain rate range 5 x 10⁻⁴ - 5 x 10⁻¹/sec. Thus concrete strength under dynamic load increased more for the weaker concrete, a trend consistent with Ferrito's data.

Figure 2-7 also shows the data obtained by Atchley and Furr.⁽²⁰⁾ Their principal differences with Watstein are that they found weak concrete to be less strain rate sensitive than strong concrete and more importantly the rate of strength increase decreased with strain rate. However, over most of the explored strain rate range Watstein and Atcheley and Furr are in reasonable agreement.

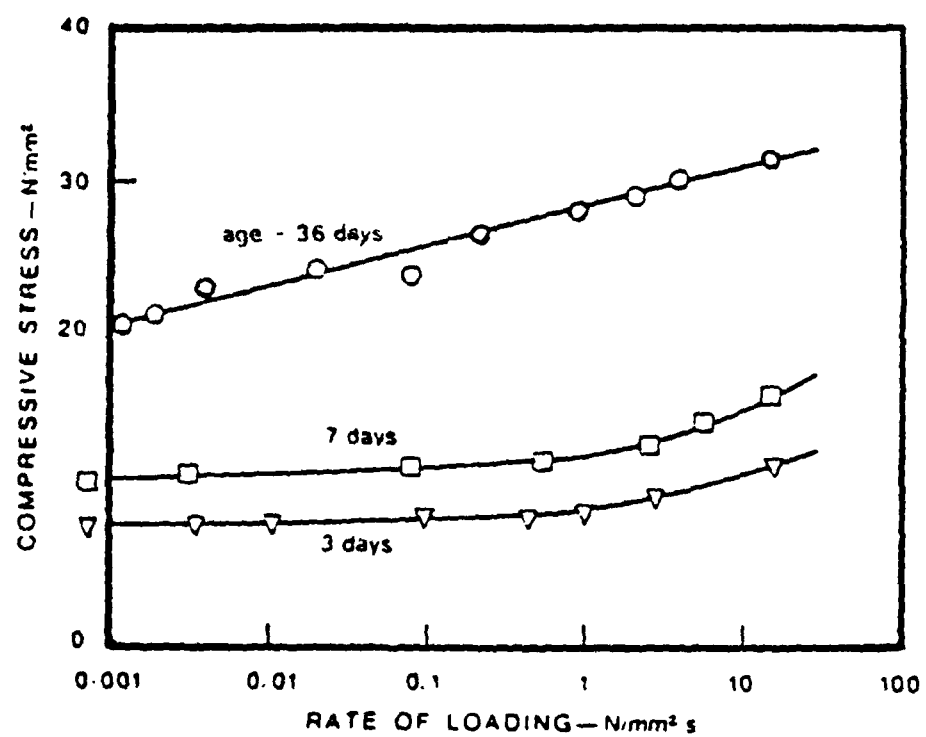


Figure 2-5. Sensitivity of concrete compressive strength to loading rate.

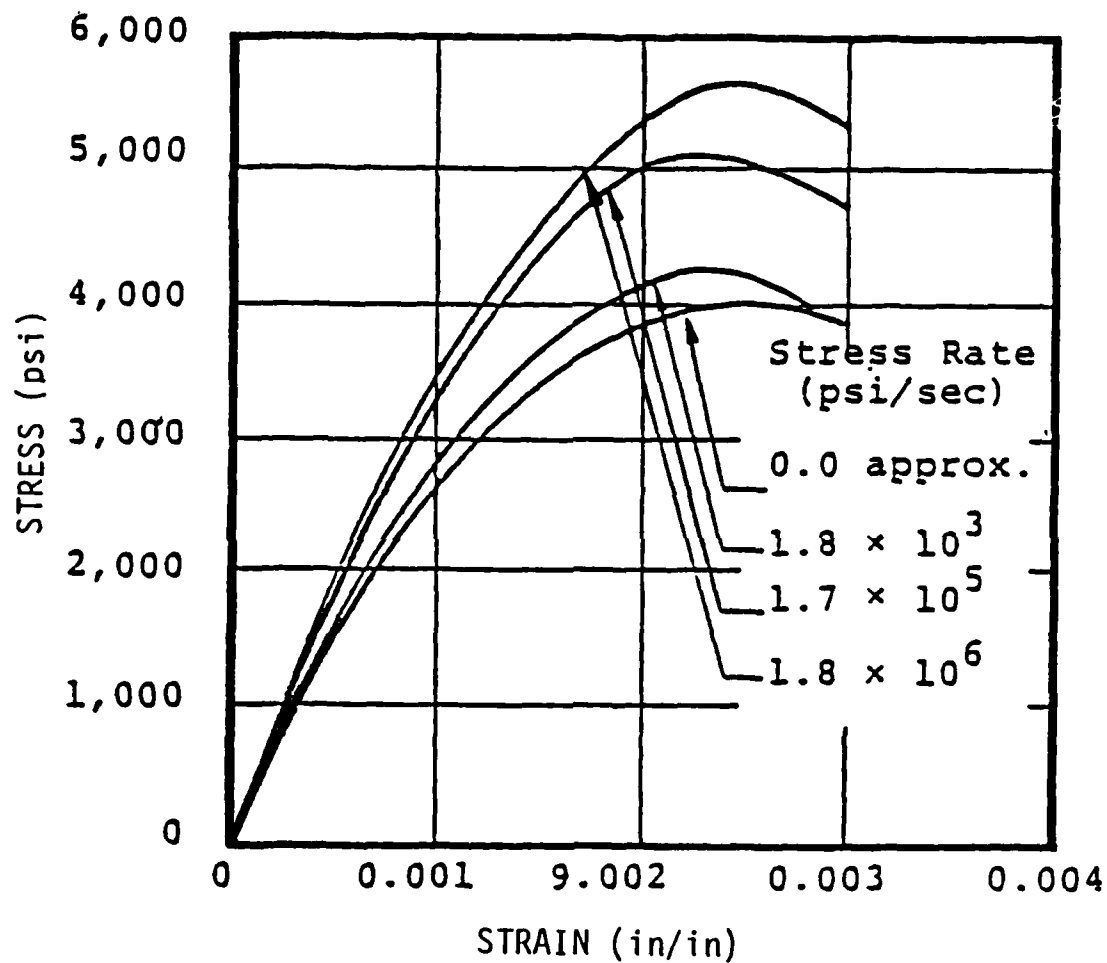


Figure 2-6. Sensitivity of concrete compressive stress-strain curves to stress rate.

The preceding authors concentrated on determining strength strain-rate sensitivity. Nelissen,⁽²²⁾ Figure 2-8, obtained data on both strength and softening branch rate sensitivity. Constant strain and stress rate experiments were performed in pairs with stress rate chosen to equal that initially induced by the constant strain-rate experiment.

The stress controlled experiments achieved the higher failure stress and ended in abrupt specimen failure. The strain controlled experiments allowed stress to relax once the maximum stress was achieved so that softening was observed. The data showed a 20 percent strength increase occurred between the slower and faster stress controlled experiments compared to a 18.7 percent increase predicted by Eq. 2-1. So Nelissen's results are consistent with those previously discussed.

The softening branches obtained by Nelissen were at constant strain rates of 1.7×10^{-7} /sec and 3.3×10^{-5} /sec. At a strain of approximately 0.0035 the two curves met. Rüschi⁽²³⁾ in his softening experiments, Figure 2-9, covered the strain rate range 10^{-10} /sec to 1.7×10^{-5} /sec and observed that stress-strain curves crossed at $\epsilon = 0.003$ with the faster loaded specimens showing faster softening.

In terms of initial stress rate, the Figure 2-9 curves correspond to 6.2×10^1 , $1, 4 \times 10^{-2}$ and 2×10^{-4} psi/sec. Thus the experiments were slow, taking from two minutes to two years. Strength asymptotically approached a limit for test times greater than 2 days.

It is reasonable to assume that in all but the fastest of Rusch's experiments creep and/or stress relaxation was continuously occurring. In concrete, creep need not be deleterious to structural integrity. Concrete behavior is governed by progressive microcracking. If microcracking occurs at a sufficiently slow rate then mortar creep will tend to close cracks, redistribute stress concentrations around cracks and generally retard crack growth. Therefore, as test time shortens, creep will be of lessening

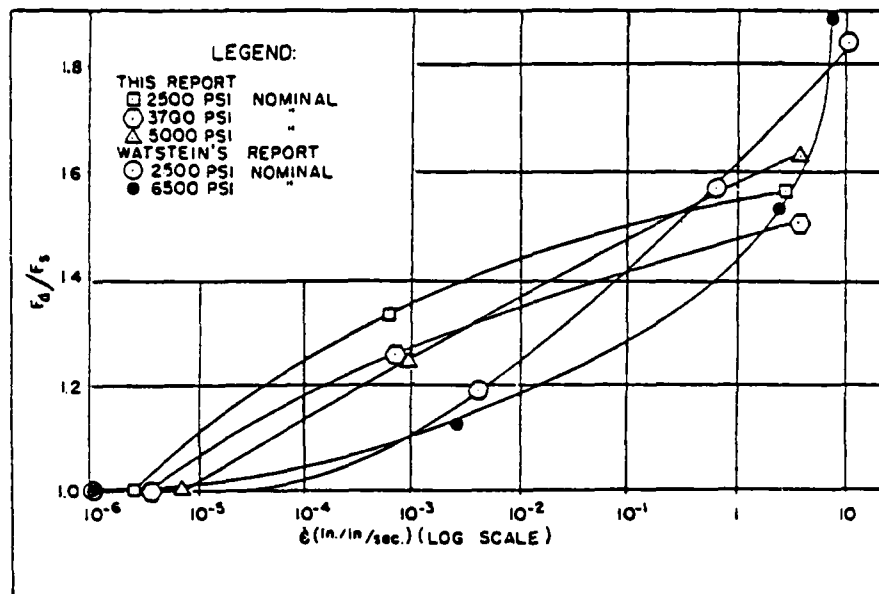


Figure 2-7. Concrete strength rate sensitivity. F_d and F_s are dynamic and static strengths.

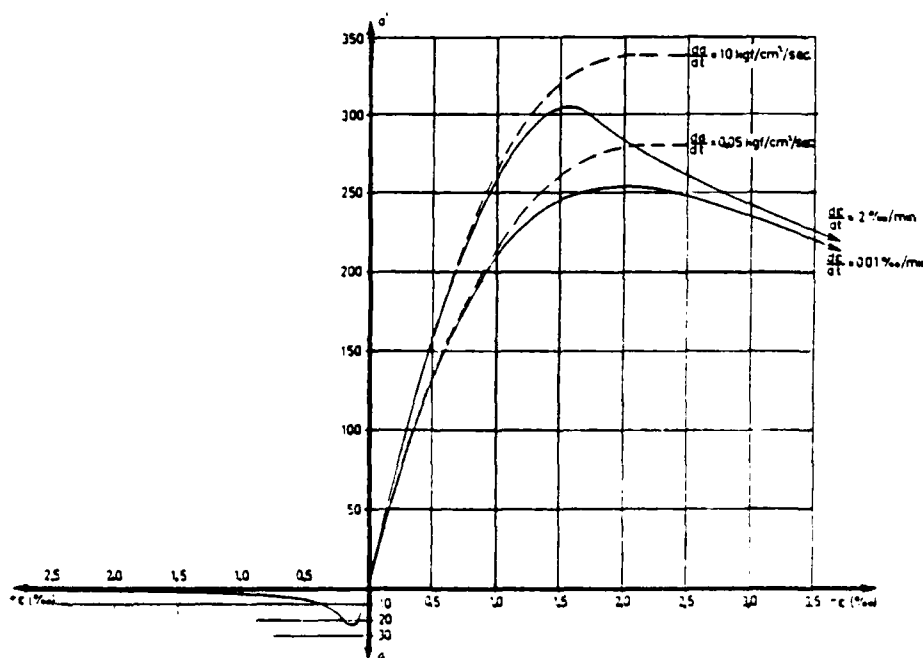


Figure 2-8. Stress and strain rate controlled concrete compression experiments.

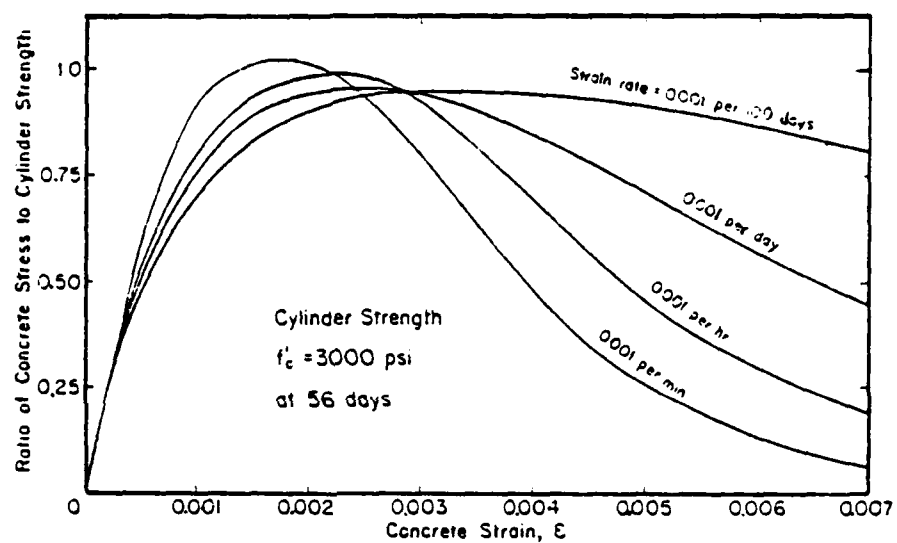


Figure 2-9. Stress-strain curves for several strain rates.

importance, cracks will not "heal," ultimate failure will occur at lower strains, and the softening branch will be steeper.

Experimental observation of this phenomena, while suggested by very slow rate tests, would be difficult to observe at higher rates because of equipment shortcomings. As strain rate increases, a specimen sheds load faster on the softening branch and thus has an increasing energy release rate. This energy is absorbed by the test equipment but because of inertia in testing machine and servo-controls, the system would find it increasingly difficult to accommodate the energy as the energy release rate grew until finally specimen unloading would become unstable. Figure 2-10 shows exactly this type of behavior. Cylinders were tested at two strain rates, $32 \times 10^{-6}/\text{sec}$ and $10^{-2}/\text{sec}$. A stable softening branch was observed for the lower strain rate while for the higher rate unloading was unstable. From the data it is unclear whether the behavior is the result of a machine inadequacy or actual material response.

Conclusions

Conclusions are divided into two categories; those pertaining to testing and those pertaining to structural analysis and constitutive theories.

Testing. The preceeding discussion showed that concrete is rate sensitive over its entire response spectrum. Thus data to be used in a structural analysis problem should be obtained over a strain rate range characteristic of the problem. Additionally in all concrete tests load rate or strain rate should be reported. If strain softening data is required then testing should be performed at several constant strain rates in a stiff, servo-controlled testing machine and, depending on equipment limitations, there will be a specimen-size/strain-rate envelope beyond which the testing machine will be unable to control softening.

Structural Analysis. For structural analyses to accurately simulate concrete response one must model

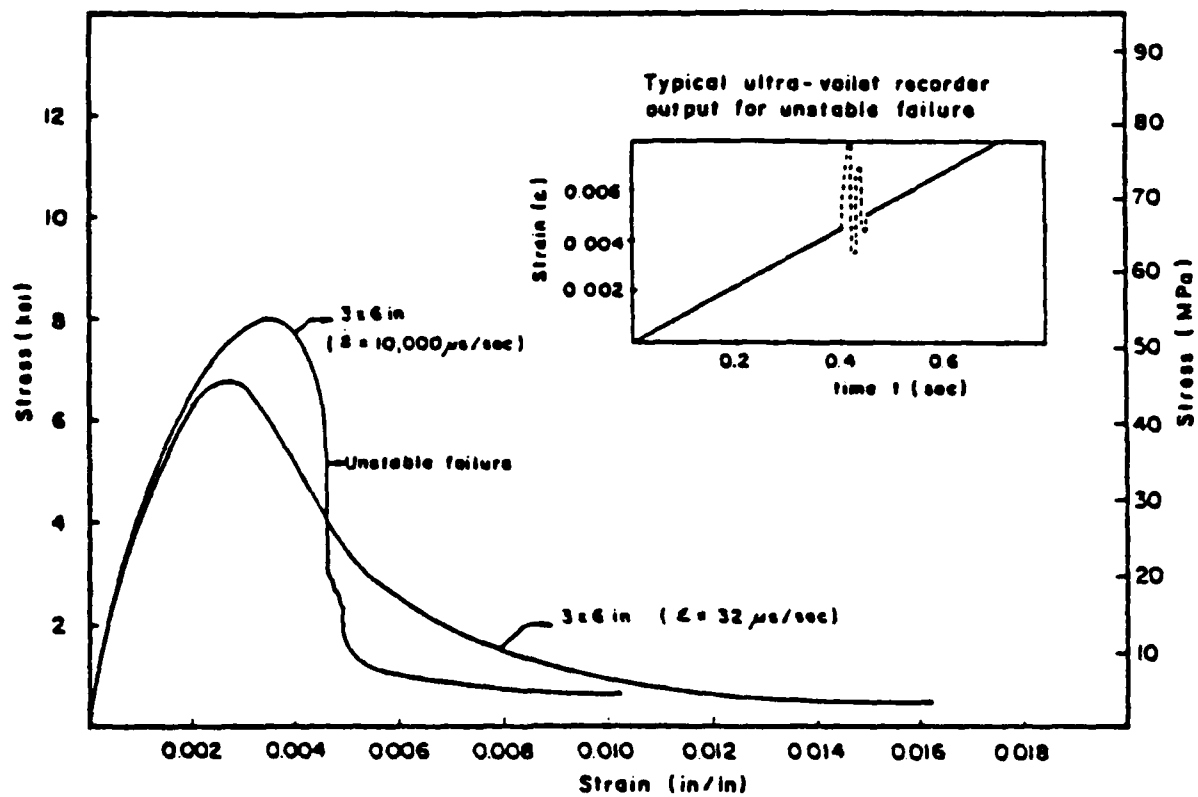


Figure 2-10. Effect of strain rate on softening response.

- strength strain rate sensitivity
- softening branch strain rate sensitivity.

No static structural analysis problem is completely time independent because loads are always applied over a finite time period. The loads and their application time will translate into some average strain rate and concrete is rate sensitive at all load rates. Thus to perform a conservative static analysis the selected, f'_c should be representative of the strain rates experienced during the loading.

For dynamic structural analyses strain rate effects can enhance concrete strength 50 percent or more beyond that attained in a static test. Thus a comprehensive analysis requires a strain-rate dependent strength model, e.g., viscoplasticity, where both Young's Modulus and the yield strength are rate sensitive. A conservative approach, i.e., one that would underpredict strength, would be to neglect rate effects and use data corresponding to a low strain rate test.

The most important conclusion concerns the softening branch. In Figure 2-9 the slope of the softening branch was shown to be very rate sensitive, even at rates corresponding to static analyses, because of creep. Physically, softening represents the gradual performance degradation that concrete can experience and implies that under suitable constraints concrete will experience controlled, progressive shedding of load from a failed region into its surroundings, i.e., failure need not be sudden and catastrophic. Modeling of softening in finite element codes would be advantageous since it would provide a physically based mechanism for gradual failure and would obviate the need for the usual artifices employed by modelers to simulate failure. If softening were not modeled then a rational approach to failure would be to reduce stress over a series of loads increments so as not to propagate a spurious failure through suddenly overloading neighboring regions. What are totally incorrect and unconservative are those models that maintain stresses at their failure level once that level is reached.

For dynamic analyses it appears that concrete may not soften under intense loading. Thus in impact analyses the impact zone would spall and crush rather than soften and it would only be farther away from the impact zone that softening would occur. In problems where the entire structure was impulsively loaded, softening would not need to be considered; concrete would just reach the failure stress and crush.

2.2.4 Monotonic Response in Compression

Figure 2-11 is a schematic of a typical uniaxial compressive stress-strain curve for a two-minute concrete test. Initially the response is linear elastic with tangent modulus of $2 - 4 \times 10^6$ psi and Poisson's Ratio $\nu = 0.2$. At $0.3 - 0.4 f'_c$ (f'_c being the uniaxial compressive strength) anelastic response starts and irreversible strains begin to accumulate. With a further stress increase the material strain hardens and the stress-strain curve starts to flatten until at the maximum stress f'_c the curve is horizontal. For typical concretes f'_c is in the range 2 - 10 ksi and the corresponding strain ϵ'_c is 0.002 - 0.004.

Any attempt to load concrete beyond f'_c results in explosive failure. However, in a strain controlled experiment the stress decreases as the strain increases beyond ϵ'_c and the material softens. The softening or descending branch at first steepens and then flattens out. At some final strain ϵ_{ult} , uncontrolled deformation occurs and failure ensues. Strain ϵ_{ult} is extremely sensitive to test and specimen conditions but for well controlled experiments is in the range 0.008 - 0.02. Figure 2-12 shows stress-strain curves for typical concretes and indicates that high strength concretes have a steeper softening branch and fail at a lower final strain. Stronger concretes are in a sense more brittle because softening is controlled by creep mechanisms and strong concretes creep less readily than weak concretes.

Figure 2-13 is a schematic of the stress versus volumetric strain curve that results during the ascending part of the Figure 2-11 history. The curve is linear up to about $0.6 f'_c$ at which

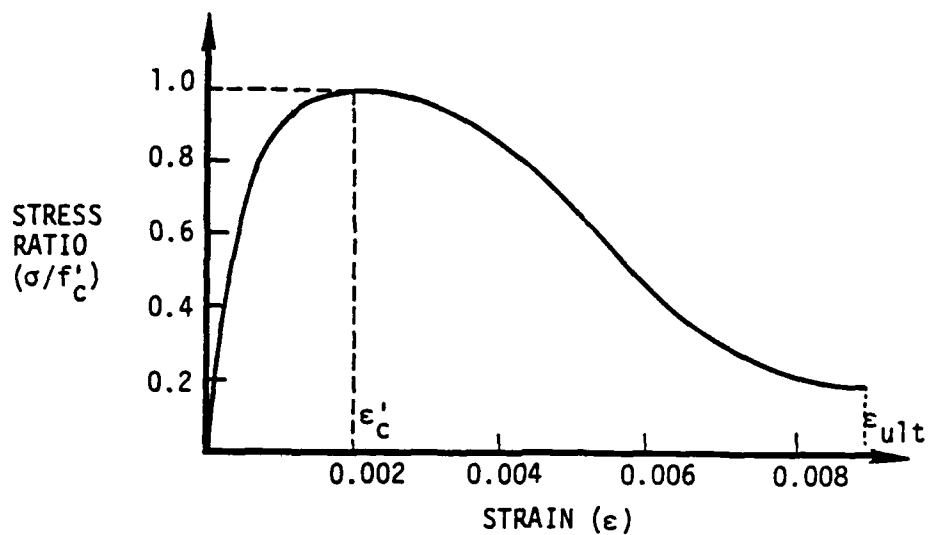


Figure 2-11. Typical stress-strain curve for concrete uniaxial, monotonic, compressive response.

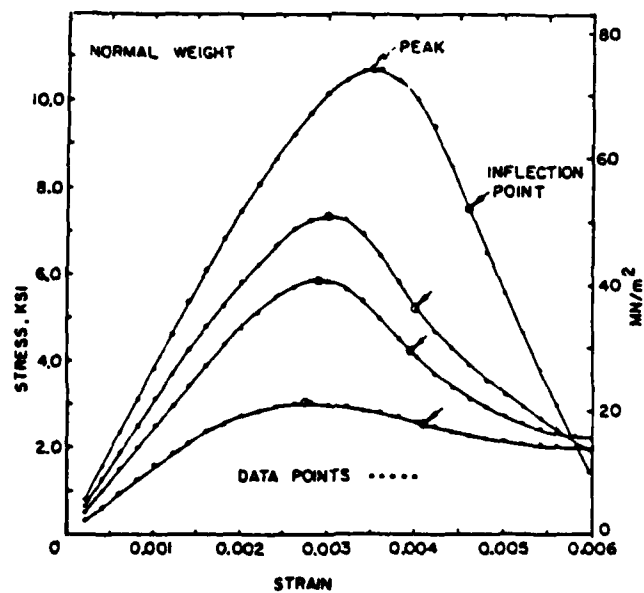


Figure 2-12. Typical stress-strain curves for concretes.

stress the rate of volume contraction decreases. At the critical stress σ_{cs} , between $0.7 - 0.9 f'_c$ the curve is vertical and dilatation or volume expansion commences. For many concretes when the stress reaches f'_c sufficient dilatation has occurred that the volume is greater than at the beginning of the experiment. At the critical stress the instantaneous Poisson's Ratio equals one half and increases as dilatation increases. Figure 2-14 shows two typical sets of data for volumetric strains.

Rüsch⁽²³⁾ showed, Figure 2-15, that the critical stress corresponded to the concrete sustained load strength. Rüsch preloaded specimens of the same concrete in compression and then recorded strain-time histories. In Figure 2-15 each curve is for a fixed elapsed time and gives accumulated strain in that time for a given stress. Stresses are normalized to the concrete strength determined from the usual two minute compression test. Rüsch found that concrete would support indefinitely any stress below σ_{cs} while for stresses above the critical value failure always occurred given enough time. Thus σ_{cs} represents the onset of an unstable progressive fracturing process which culminates in failure. For $\sigma < \sigma_{cs}$ concrete would creep and internal stresses would be redistributed until a final equilibrium configuration was achieved. From Figure 2-15 it can be concluded that for deformations lasting less than two minutes creep effects will be negligible and since, in this report, none of the extreme load environments involves extensive periods of time, creep phenomena are not explicitly considered.

Conclusions

- Concrete uniaxial monotonic compressive response is totally different from metals.
- The stress σ_{cs} at which dilatation starts is the sustained load strength. Stress σ_{cs} signals the onset of an internal instability which ultimately results in failure.
- If at the end of any structural analysis residual stresses are greater than $0.7 f'_c$,

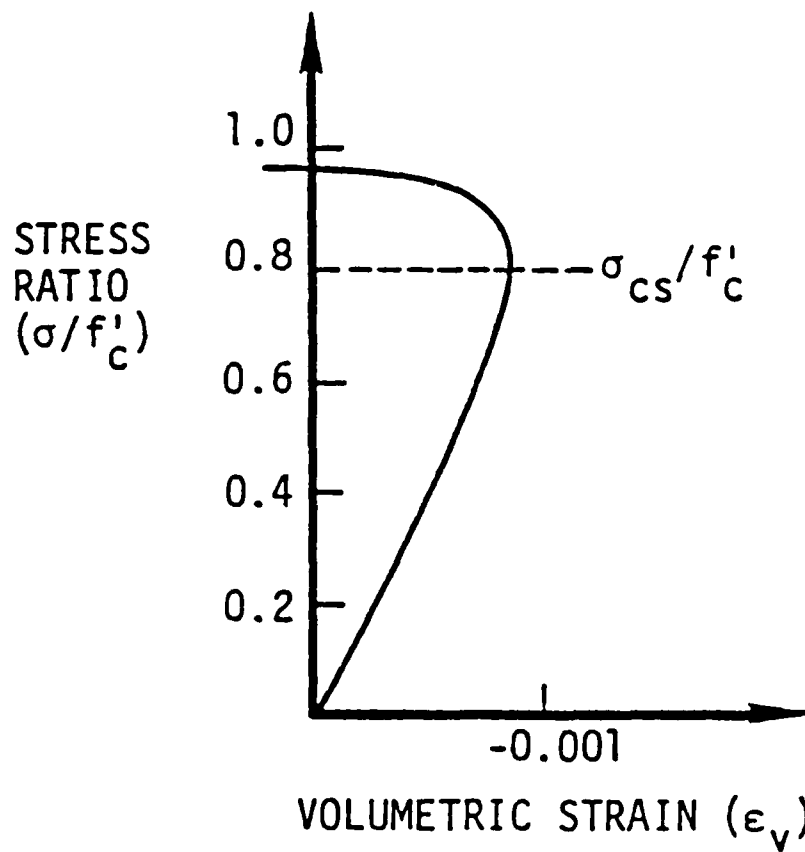
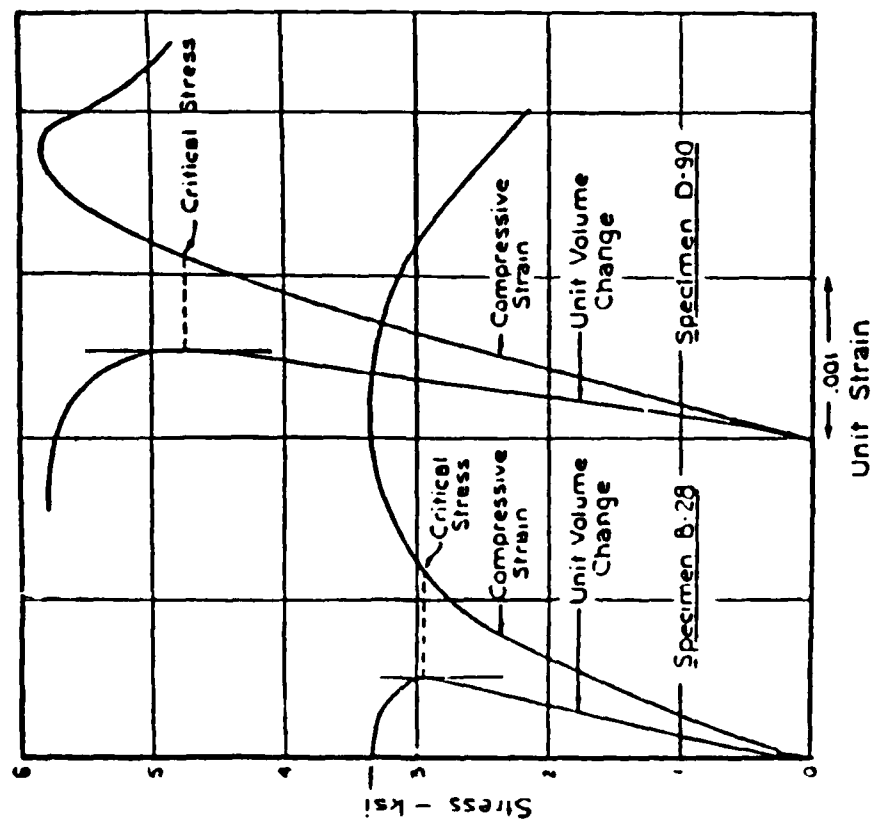
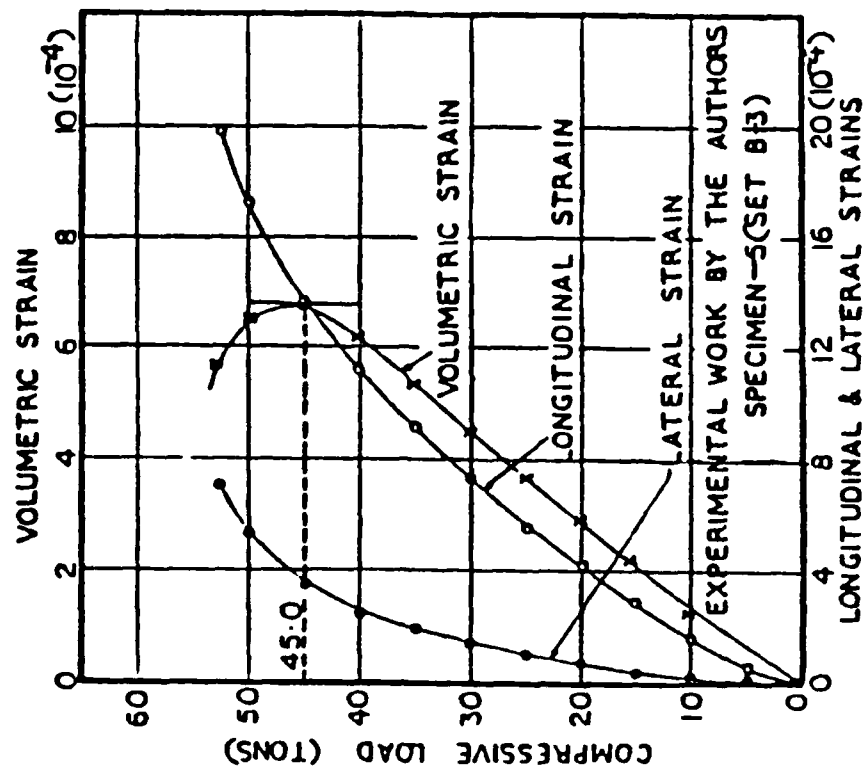


Figure 2-13. Volumetric strain ϵ_v for uniaxial, monotonic, compression test.



(a)



(b)

Figure 2-14. Typical compressive stress - Volumetric strain results.

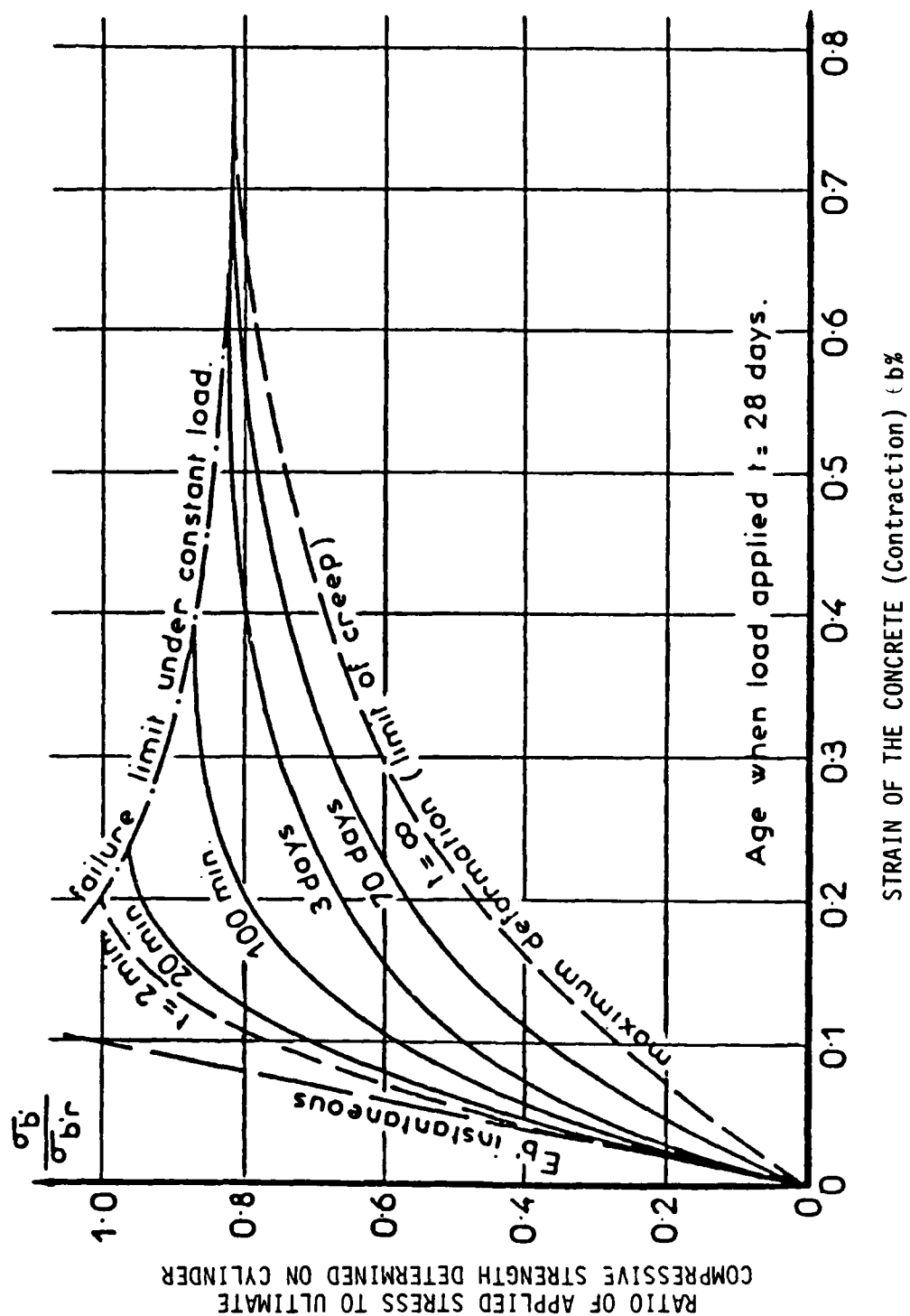


Figure 2-15. Isochronous stress-strain curves for a typical concrete.

then the structure must be assumed unstable and, if enough of the structure is highly stressed, in damage of collapse.

- Creep effects are unimportant for short time phenomena.

2.2.5 Cyclic Response in Compression

Protective structures may, under certain loading conditions, be subjected to several loading-unloading-reloading cycles. Consequently, in this subsection a critical evaluation is given of the current understanding of concrete uniaxial cyclic response.

Shah and Chandra⁽²⁷⁾ performed a fatigue study on plain concrete. Samples were cycled in uniaxial compression in the ranges $0.1 f'_c$ to $\alpha f'_c$ where α equalled 0.6, 0.7, 0.8 and 0.9. In order of decreasing cycle size the authors found the number of cycles to failure was 17, 82, 1000+, 1000 +. Thus within the framework of practical finite element analyses the possibility of a fatigue failure can be discarded since it is impractical to track stresses around more than a few loading-reloading cycles.

The pioneering work on compressive cyclic loading was performed by Sinha, Gerstle and Tulin⁽²⁸⁾ and typical results are shown in Figure 2-16.

The figure indicates that considerable creep was occurring at cycle peaks i.e., at the start of unloading strain continued to increase giving the cycles a rounded appearance. If there had been no significant creep or relaxation, the start of unloading would have made a sharp corner as the strain instantaneously changed from increasing to decreasing. The authors noted that spontaneous (i.e., uncontrolled) unloading and specimen cracking occurred at points of vertical tangency on the cycles. Two important finds were

- average stiffness over a cycle decreased as cycles accumulated.
- The envelope curve traced out by cycle peaks corresponded well with the monotonic stress strain curve.

Cycle-sensitive stiffness degradation implies that concrete exhibits elastic-plastic coupling i.e., the instantaneous elastic unload-reload modulus changes as the plastic strain increases. Coincidence of envelope and monotonic loading curves is an indication that the failure surface in multiaxial stress space might be unique and not sensitive to stress-strain history. Finally Figure 2-16 shows that concrete can exhibit considerable material hysteresis.

The findings of Sinha, Gerstle and Tulin have been qualitatively verified by Karsan and Jirsa⁽²⁹⁾ and more recently by Cook and Chindaprasirt.⁽³⁰⁾ Figure 2-17, from the latter authors, shows that maximum stresses under cyclic load do indeed follow the monotonic loading curve. Note that the authors achieved a sharp unloading and that for cyclic loading along the softening branch the unload-reload behavior is nonlinear.

Discussion

Under uniaxial compressive cyclic loading concrete is

- hysteretic
- stiffness-degrading
- nonlinear in its unload-reload behavior.

Uniaxial mathematical models, based on the above data, have been developed and do exhibit these features. However, the theories have not been implemented in the analysis of protective facility structural response. Thus, currently, no definitive conclusions can be drawn regarding the importance of including cyclic stress-strain effects in stress analyses. In typical structural analyses concrete is assumed to be

- nonhysteretic
- nonstiffness degrading
- linear in its unload-reload response.

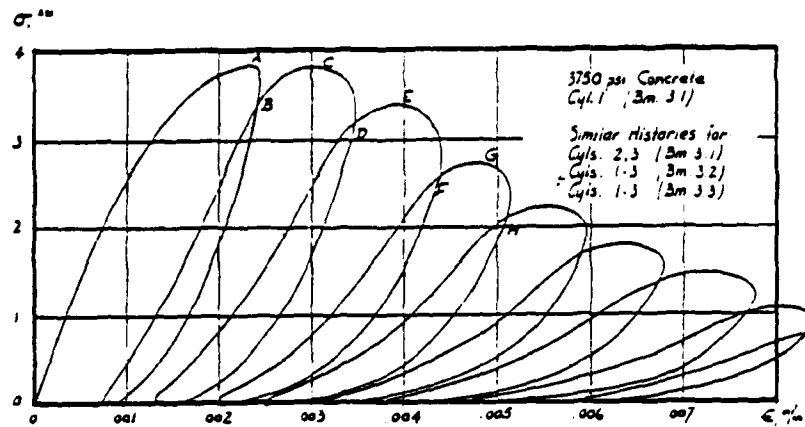


Figure 2-16. Uniaxial, compressive cyclic stress-strain curve.

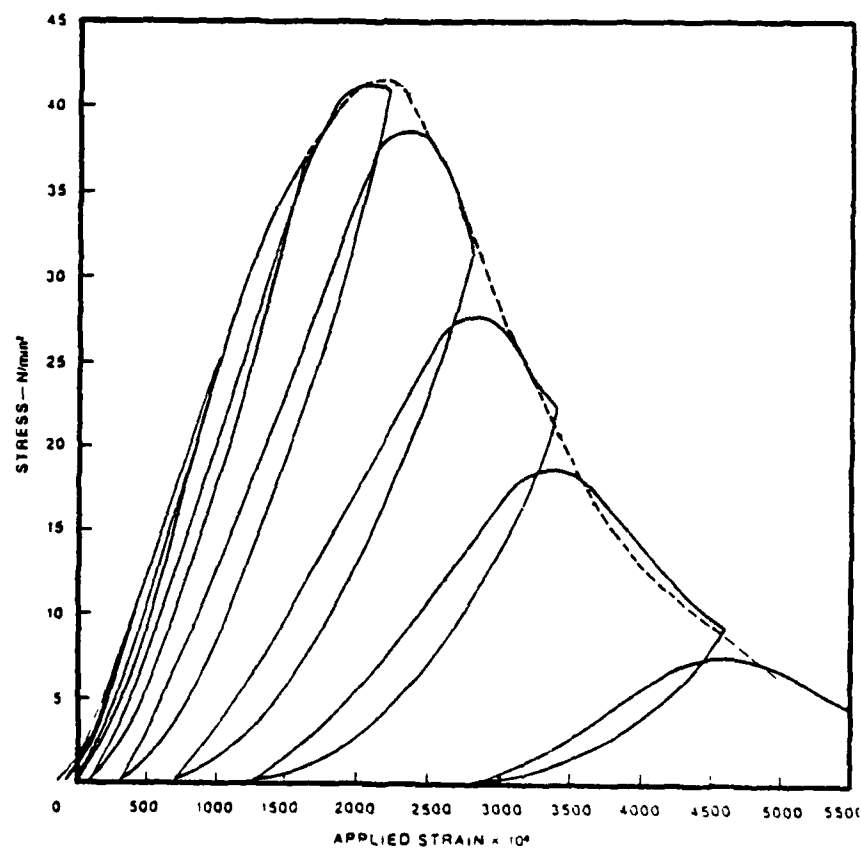


Figure 2-17. Monotonic (-----) and cyclic compressive stress-strain response.

The first assumption is conservative since it omits an energy dissipation mechanism and thus would lead to an overestimate of structural deflections and damage. The second assumption is unconservative since it results in models whose stiffness is never degraded. As a consequence predicted deflections are less than those that would be obtained if stiffness degradation was included.

The most important shortcoming of the data on which the above remarks are based is the strain rate at which the experiments were performed. Cycle times were on the order of minutes while the natural frequencies of concrete structures are approximately 1 - 10 Hz. Thus what is needed are cyclic tests which are an order of magnitude faster than those discussed here. Since concrete is strain rate sensitive, results from these tests might differ significantly from those presented here.

2.2.6 Tensile Response

The least explored region of concrete uniaxial stress-strain response is its behavior in tension. In structural design it is usual to assume that concrete has no tensile strength and that all tensile loads are carried by reinforcing steel. However, for large structures, such as protected facilities, damage will at first be localized and then subsequently propagate. Damage propagation will be in the form of cracking and tensile cracking will require a continuum understanding of concrete tensile response.

An accurate understanding of concrete tensile response can only come from the performance of carefully controlled and instrumented experiments. Thus the cylinder splitting or Brazilian test is not an appropriate test because an inhomogeneous stress state is induced in the specimen. Similar remarks hold for beam type tests. Acceptable data come only from specimens loaded in testing machines such that a gage section of the specimen is in a homogeneous state of stress and strain. The most comprehensive experimental study of this type was performed by Hughes and Chapman⁽⁶⁾ whose results are shown in Figure 2-18. The testing machine was discussed in subsection 2.2.1 and the tests were

performed at a constant strain rate of 6.7×10^{-8} /sec. The figure shows that concrete is extremely weak in tension. For most concretes, uniaxial tensile strength f'_t is in the range of 200 - 800 psi or 8 - 10 percent of f'_c . Strains at maximum stress are 5×10^{-5} - 2×10^{-4} . Surprisingly if concrete is sufficiently well constrained it will strain soften and, depending on the concrete, sustain loads until strains reach 0.0002.

Parallel to its compressive behavior, concrete has a sustained load strength in tension. Al-Kubaisy and Young⁽³¹⁾ and Domone⁽³²⁾ have shown that concrete will support loads less than $0.6 - 0.8 f'_t$ indefinitely but will finally fail under higher loads. Failure results from microcracking induced creep. Figure 2-19 shows isochronous tension stress-strain curves for a typical concrete. The curves are similar to those obtained by Rüschi for compressive response.

Discussion

The above data only describe the monotonic tensile response of concrete at essentially a single strain rate. Nothing is known about either the strain rate sensitivity or the cyclic behavior of concrete in tension. Although concrete has little capacity for supporting tensile loads, its tensile behavior cannot be ignored. Tensile failure and how concrete redistributes load after reaching the failure stress will control how fast cracks propagate and how fast a structure's load carrying capacity is destroyed. From the discussion on compressive behavior it is probable that concrete tensile response is strain rate sensitive and that strength is enhanced and softening branch steepened as strain rate increases. Current data are for very low strain rates and so no data exist on which to base constitutive models for dynamic structural analyses. Under strain control concrete in tension would probably exhibit cyclic behavior similar to that shown in Figure 2-17 for compression. This possibility has not been explored and its importance cannot be assessed.

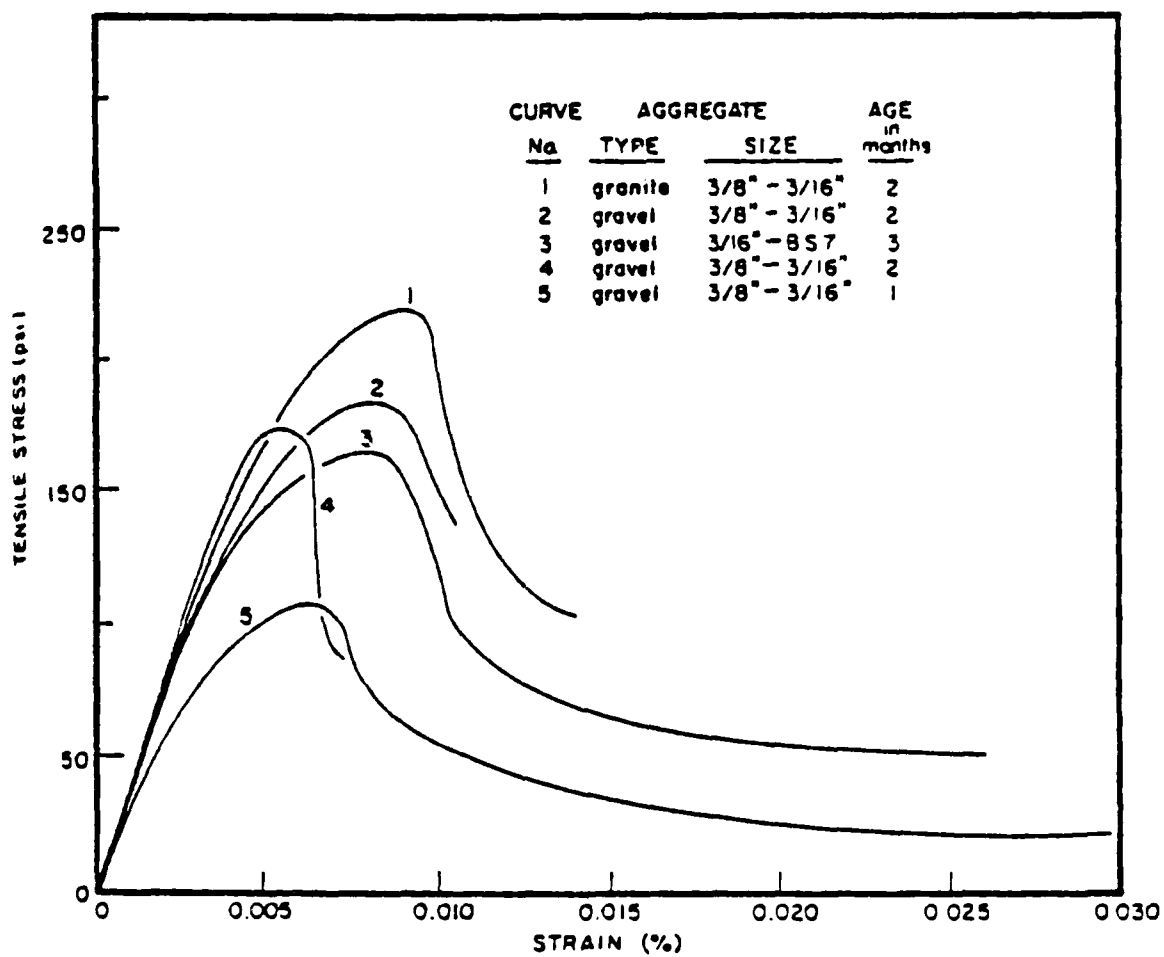


Figure 2-18. Typical uniaxial stress-strain curves

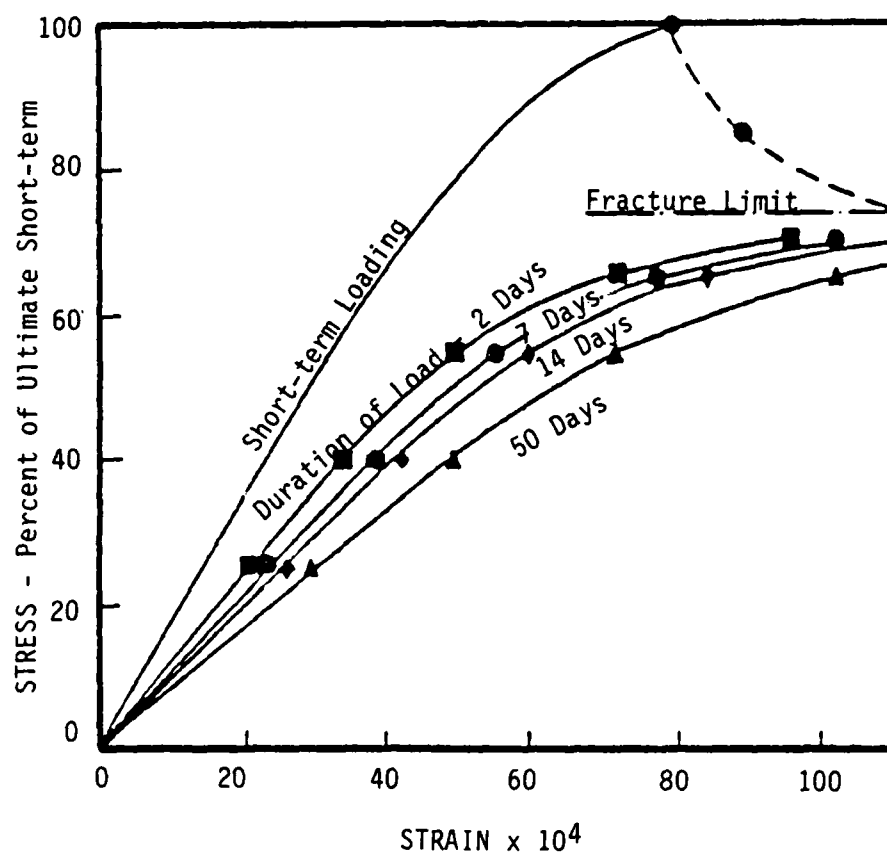


Figure 2-19. Isochronous tension stress-strain curves.

2.3 BIAXIAL RESPONSE

2.3.1 Remarks

Biaxial loading corresponds locally to a state of plane stress wherein only two principal stresses are non-zero. The biaxial stress state is called biaxial tension, biaxial compression or compression-tension accordingly as the principal stresses are both positive, both negative or of different signs, respectively.

Most biaxial experiments are performed on plate-like specimens where one dimension, the thickness, is much less than the other two. The specimen is loaded around the edges by forces in its plane. For biaxial tension failure is similar to uniaxial tension and occurs from a single thru-thickness crack perpendicular to the direction of the maximum principal stress. For biaxial compression failure occurs from a single crack in the mid-surface of the plate; the crack does not meet the free unloaded surfaces of the plate. Finally, for the case of compression-tension, the failure mode is a mixture of the two previous modes depending on the relative magnitudes of the compressive and tensile loads.

Slate and his co-workers⁽³³⁻³⁵⁾ believe that under biaxial compression failure is governed by tensile strain in the plate thru-thickness direction while Kupfer, Hilsdorf and Rüschi⁽³⁶⁾ believe that the biaxial failure modes imply that any realistic failure criterion must depend upon all three principal stresses and not just the two extreme stresses.

Multiaxial experiments on plain concrete were first performed around the beginning of the century but it has only been in the last thirty years that generally accepted data has been published. Many different shapes and sizes of specimens and many different testing machines have been used to obtain biaxial stress-strain data. The objectives of all tests have been to subject specimens to known homogeneous, stress histories and to then record failure loads and/or strain histories. However, occasionally, difficulties associated with experimental procedures and the complexity of plain

concrete response have resulted in researchers unknowingly not achieving their objectives. In the following is presented a discussion of specimen types, and testing machines and their affect on experimental results. Subsequently, data from biaxial experiments are presented.

2.3.2 Biaxial Test Specimens

One reason for the great difference in experimental results obtained by different researchers is the wide variety of test specimens used; this can be seen in Table 2-2. Biaxial test specimens fall into three main categories

- plates
- cubes
- hollow cylinders.

Plate specimens are by far the most popular because they are easy to fabricate and minimize frictional constraints between the specimen edges and the load platens. (Frictional effects reduction through platen design will be discussed in more detail in subsection 2.3.3.) Weigler and Becker^(41,42) tested a series of prisms whose dimensions varied from 10 x 10 x 10 cm to 10 x 10 x 2 cm in uniaxial and biaxial compression ($\sigma_1 = \sigma_2$) and found that specimen strength decreased with size because of reduced platen constraint, Figure 2-20. Similar findings have been reported by Fumagelli.⁽⁵⁰⁾ Iyengar, Chandrashekhara and Krishnaswamy⁽⁴⁴⁾ in their biaxial compression experiments used cubical specimens and, because of friction over the large contact area between the specimens and load platens obtained biaxial compression strengths three to four times what is now considered correct.

Hollow cylinders have been used in compression-tension and compression-torsion experiments. However, the specimens are difficult to fabricate with uniform wall thickness. Also, it is impossible to obtain a homogeneous stress field in the specimen. This is because cylinder wall thickness must be at least three times the maximum aggregate dimension to obtain a reasonably homogeneous

Table 2-2
Specimen types used in biaxial tests

Authors	Ref	Type	Specimen Dimensions		Aggregate (max)	
Atan and Slate	(37)	Plate	5x 5x0.5	in.	0.75	in.
Kotsovos and Newman	(38)	"	10x10x4	in.	0.5	in.
Kupfer, Hilsdorf + Rusch	(36)	"	20x20x5	cm	1.5	cm
Liu, Nilson + Slate	(35)	"	5x 5x0.5	in.	Model aggregate	
Robinson	(39)	"	10x10x4	in.	0.187	in.
Vile	(40)	"	10x10x4	in.	0.75	in.
Weigler + Becker	(41,42)	"	10x10x2.5	cm	0.7	cm
Andanaes, Gerstle + Ko	(43)	Cube	4	in.	----	
Bertacchi, Berlotti + Rocci	(38)	"	10	cm	1.25	cm
Iyengar, Chandrashekhara + Krishnaswamy	(44)	"	4 in. , 6	in.	0.375 to 0.75 in.	
Linse	(38)	"	10	cm	1.25	cm
Schickert	(38)	"	10	cm	1.25	cm
Taylor	(38)	"	2	in.	0.5	in.
Traina + Zimmerman	(38)	"	3	in.	0.5	in.
Bresler + Pister	(45,46)	Cylinder ^(a)	9x1.5x30	in.	0.5	in.
Goode + Helmy	(47)	"	8x1 x26	in.	0.375	in.
Isenberg	(48)	"	6.4x.84x10.2	cm	0.47	cm
Rosenthal + Glucklich	(49)	"	30.5x2.75x35	cm	1.25	cm

(a) Dimensions are outside diameter, wall thickness and gage length respectively.

specimen. Yet when wall thickness is greater than ten percent of the cylinder radius the stress state becomes significantly inhomogeneous thus making it impossible to accurately define stresses and strains in the specimen.

In summary the preferred biaxial test specimen is one which, in conjunction with its test machine, minimizes frictional effects and stress-strain inhomogeneities.

2.3.3 Biaxial Testing Machine Considerations

The objectives of all biaxial experiments to date have been to obtain data on concrete monotonic strength and stress-strain relationships. No data has been published on either cyclic response or post-peak softening behavior. Therefore, testing machine stiffness is not of primary concern. Rather, for cube and plate specimens attention has focused on transferring load to the specimen with a minimum of friction between the load platens and the specimen since friction induces lateral constraint on the specimen resulting in artificially high levels of concrete strength.

For cubes and plate-like specimens there are three major load platen designs:

- steel plate
- brush bearing
- fluid-cushion.

The steel plate platen is a steel plate thick enough not to be distorted during a test. When no lubricants are used between steel and concrete, high levels of friction are present. Friction has two effects on experimental results. First, it inhibits free lateral expansion and contraction in the plane of the platen face thus artificially stiffening the specimen. Secondly, in biaxial compression loads applied through platens in one direction are partially transferred to, and hence supported by, the load platens orthogonal to them. The combination of these effects can lead to totally erroneous results as can be seen in Figure 2-21. In Figure

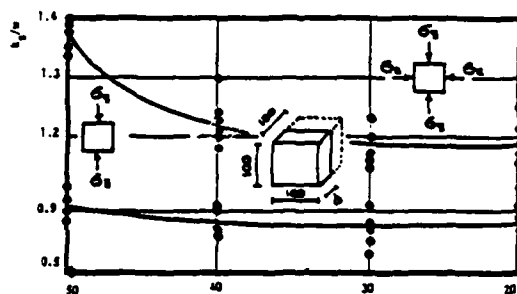


Figure 2-20. Uniaxial and biaxial compressive strengths versus prism thickness, $d \cdot W$ = uniaxial strength for $d = 100$ mm.

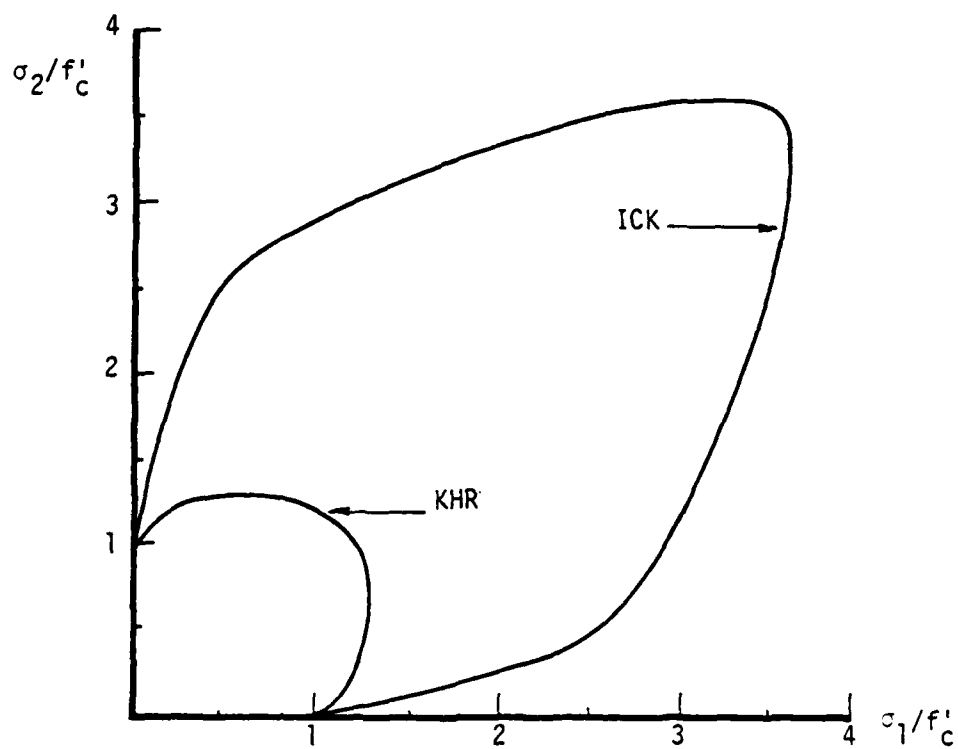


Figure 2-21. Comparison of failure surfaces for biaxial compression.

2-21 data obtained by Iyengar, Chandrashekhara and Krishnaswamy⁽⁴⁴⁾ using unlubricated steel plate platens are compared with data from Kupfer, Hilsdorf and Rüschi⁽³⁶⁾ who used the brush bearing platens described below. Friction can be reduced by interposing layers of material between the load platens and the specimen. Table 2-3 taken from Nelissen⁽⁵¹⁾ shows how different levels of lateral constraint can be obtained and that it is possible to practically eliminate friction. Thus acceptable plate platen arrangements can be designed for compression testing; however, the designs cannot be modified to transmit tension to a specimen.

Table 2-3
Coefficients of friction between load platens and
specimens for various lubricants
(Source: Nelissen⁽⁵¹⁾)

<u>Lubricant</u>	<u>Coefficient of Friction</u>
None	0.46 - 0.65
Graphite powder	0.28 - 0.31
Grease	0.15 - 0.24
0.05 mm teflon film and silicon grease	0.018 - 0.023
Rubber films and silicon grease	0.008 - 0.012

The brush bearing platen was first developed by Kijellmann⁽⁵²⁾ for soils testing and was later modified for concrete testing by Hilsdorf.⁽⁵³⁾ As its name suggests, the surface of the platen resembles a brush. The space between the "bristles" allows the specimen to expand and contract freely. Also, by bonding the bristles to the specimen, tensile loads can be applied. The brush platens used by Kupfer, Hilsdorf and Rüschi⁽³⁶⁾ were steel filaments of cross-section 3 x 5 mm and with 0.2 mm separation. The free length of the filaments varied from 65 mm to 105 mm with the shorter bristles being used on higher strength

concretes. The authors were able to maintain flatness of the brush bearing surface to within 2×10^{-3} mm and no filament buckling was observed during loading. More recently brush bearing platens have been used by Slate and his coworkers.^(33,35) Kupfer, Hilsdorf and Rüschi performed two series of biaxial compression experiments, on three different types of concrete. In one series brush bearing platens were used and in the other steel platens. Resulting average biaxial failure surfaces are shown in Figure 2-22 where strength enhancement arising from the steel platen's constraining action can be clearly seen.

The third type of load platen for cubes and plates is the fluid cushion pioneered by Ko and Sture⁽⁵⁴⁾ and applied to concrete by Andanaes, Gerstle and Ko.⁽⁴³⁾ Here load is applied to the specimen through fluid filled membranes pressed against the specimen. The membrane possesses little stiffness and thus does not constrain specimen lateral motion. By inserting a steel plate between the membranes and the specimens, the authors obtained higher biaxial compression strengths than were obtained without the plates, Figure 2-23. This again demonstrates how friction between specimen and stiff load platens increases measured strength. As with the steel load platens the fluid cushion cannot be modified to load specimens in tension.

For hollow cylindrical specimens frictional constraints have not usually been of concern since sufficiently long specimens have been used, so that the specimen central section was free of end effects. By applying compressive and torsional loads at the cylinder ends states of compression-tension have been achieved and reliable results obtained.

Rosenthal and Glucklich⁽⁴⁹⁾ attempted to obtain biaxial compression data using hollow circular cylinders whose axes were vertical. The cylinders were placed inside a rubber bladder which in turn was inside a thick steel tube. The clearance between concrete and steel was one inch. Biaxial loading was achieved by simultaneously pressurizing the bladder and applying vertical end

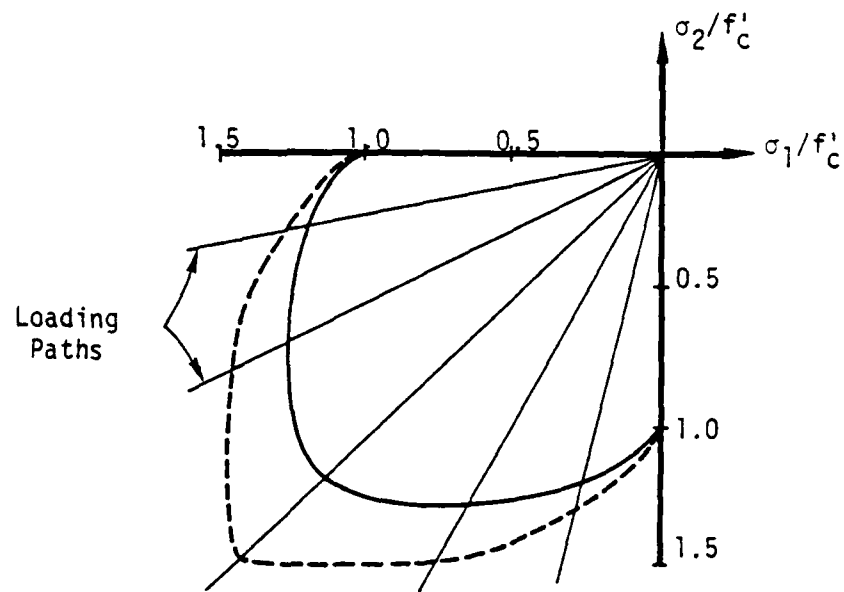


Figure 2-22. Failure surfaces for biaxial compression (a) — brush bearing platen, (b) ---- unlubricated steel platens.

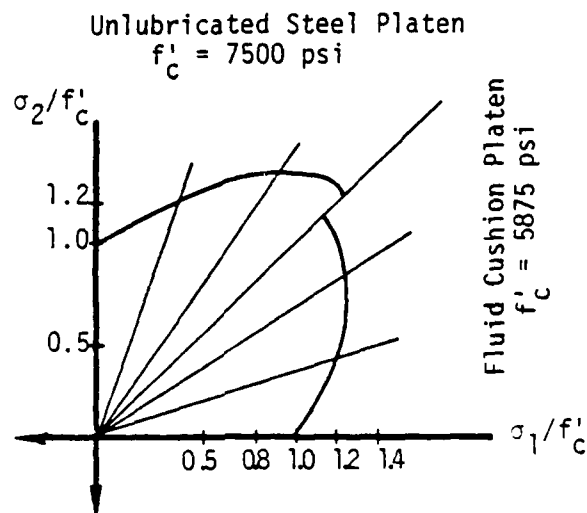


Figure 2-23. Failure surfaces for biaxial compression using fluid cushion and unlubricated steel platens.

loads. The biaxial, compression, failure envelope obtained is shown in Figure 2-24, and it can be seen that for equi-biaxial compression ($\sigma_1 = \sigma_2$) stress levels are twice the uniaxial compressive strength rather than the usual 1.2. The reasons for the increased strength level are not clear but are probably related to friction between the bladder and the specimen. As evidence of this it can be noted that without an applied vertical load the cylinder failed from a single horizontal circumferential crack, a failure mode usually related to vertical tension. Tension could have been introduced into the specimen if pressure induced membrane stresses in the top of the bladder were gradually transferred to the cylinder through friction so that away from the ends of the cylinder there were minimal membrane stresses in the bladder.

It is clear from the preceding discussion that great care must be taken to ensure no extraneous stresses are introduced that give spurious results. The most promising general purpose load platen appears to be the brush bearing type because it can be used in both tension and compression and is free of frictional effects.

2.3.4 Stress-Strain Results

The data for the stress-strain response under monotonic, biaxial loading up to failure appears to be reasonably complete for 'radial' or 'proportional' loading where the stress components are maintained at a constant ratio throughout the experiment. The discussion is divided into three parts corresponding to biaxial compression, compression-tension and biaxial tension.

A. Biaxial Compression

Figure 2-25 summarizes results for uniaxial and equi-biaxial compression obtained by Weigler and Becker⁽⁴¹⁾ in 1961 using plate-like specimens of dimensions 10 x 10 x 2.5 cm. All results are for the same concrete whose uniaxial compressive strength was 6700 psi. Compared to the uniaxial response the equi-biaxial response exhibited more nonlinearity and larger stresses and strain. However, both responses did have an increasing volumetric

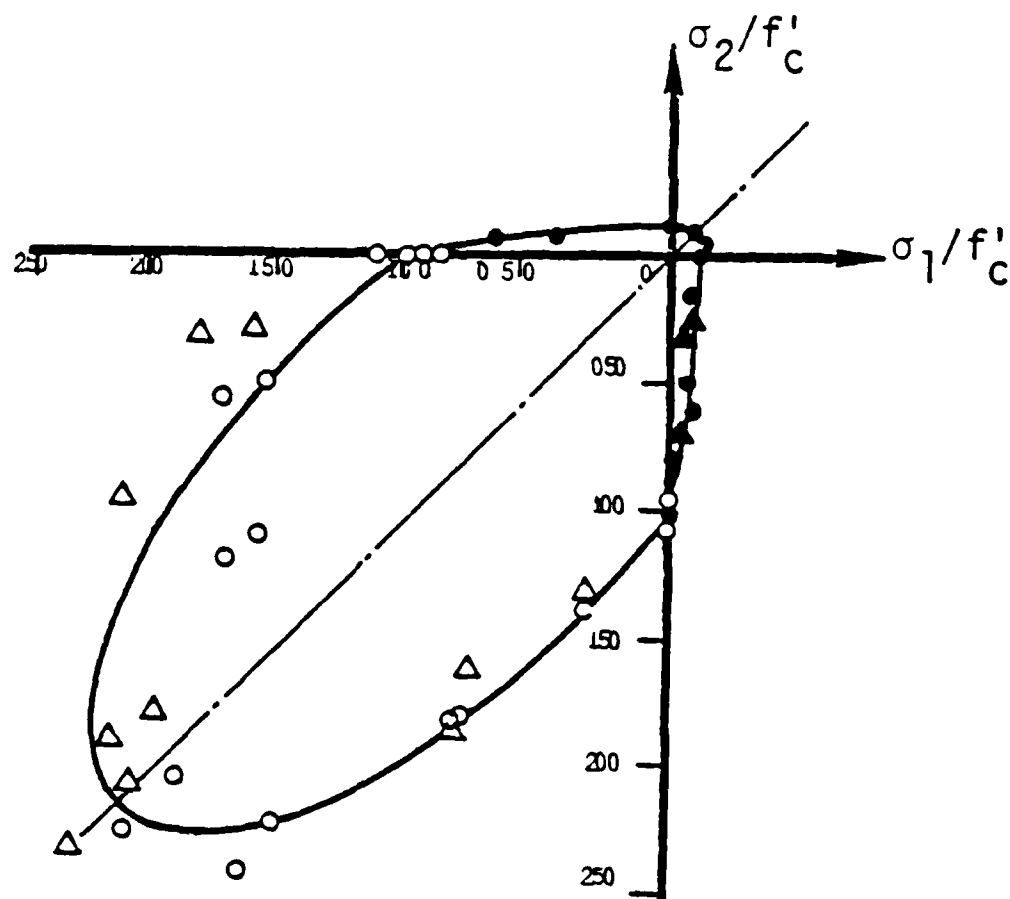


Figure 2-24. Biaxial failure surface.

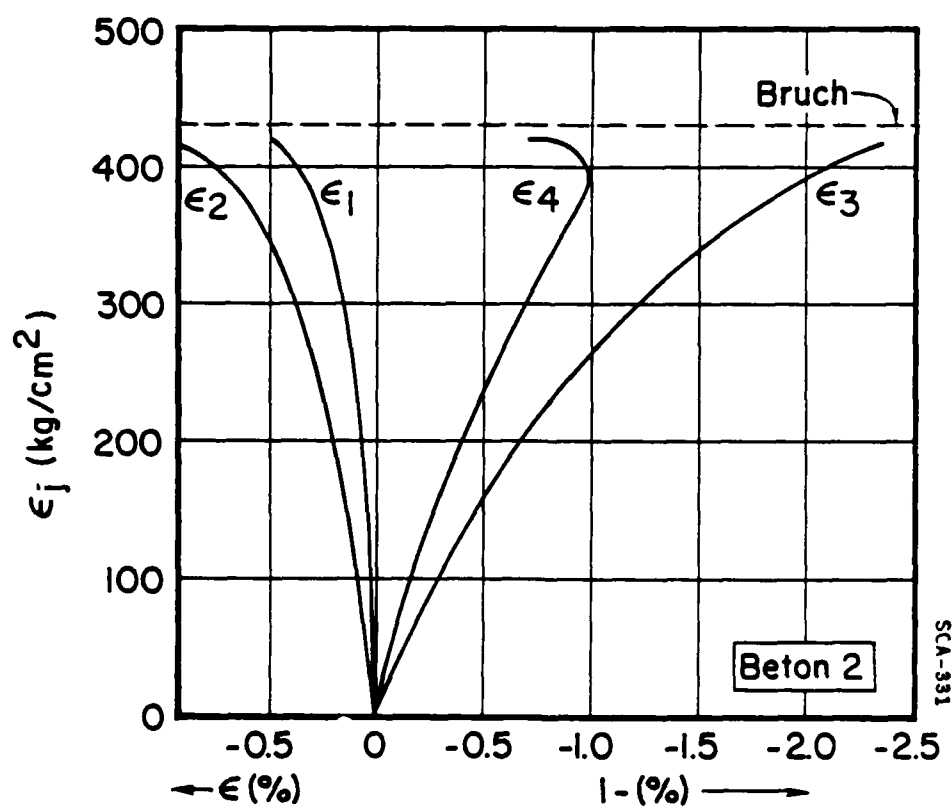
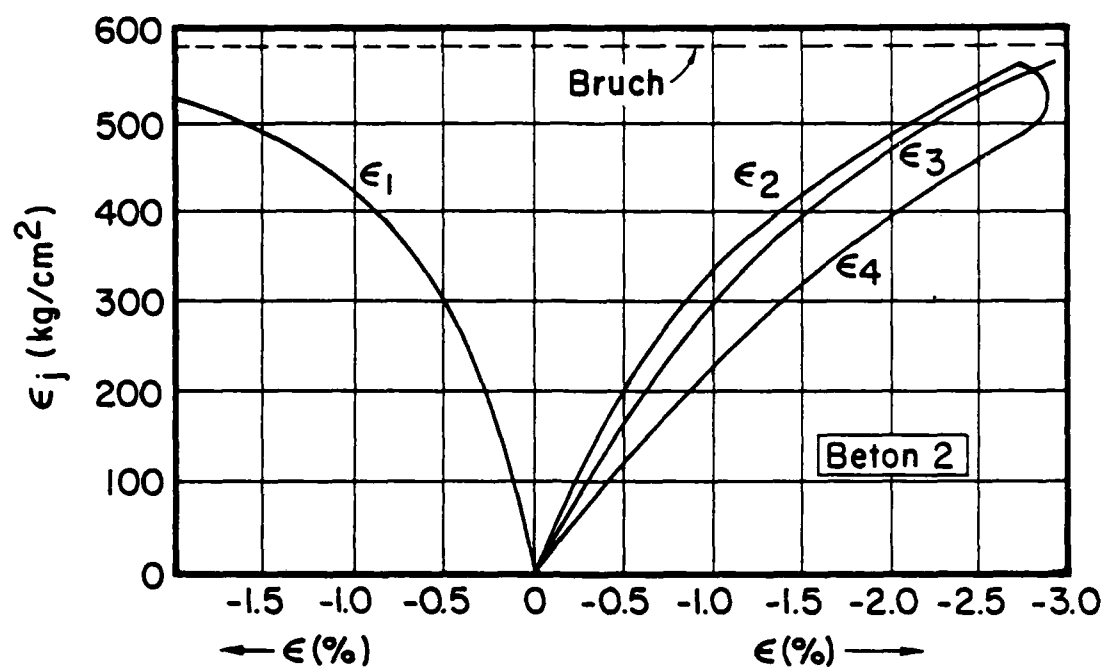
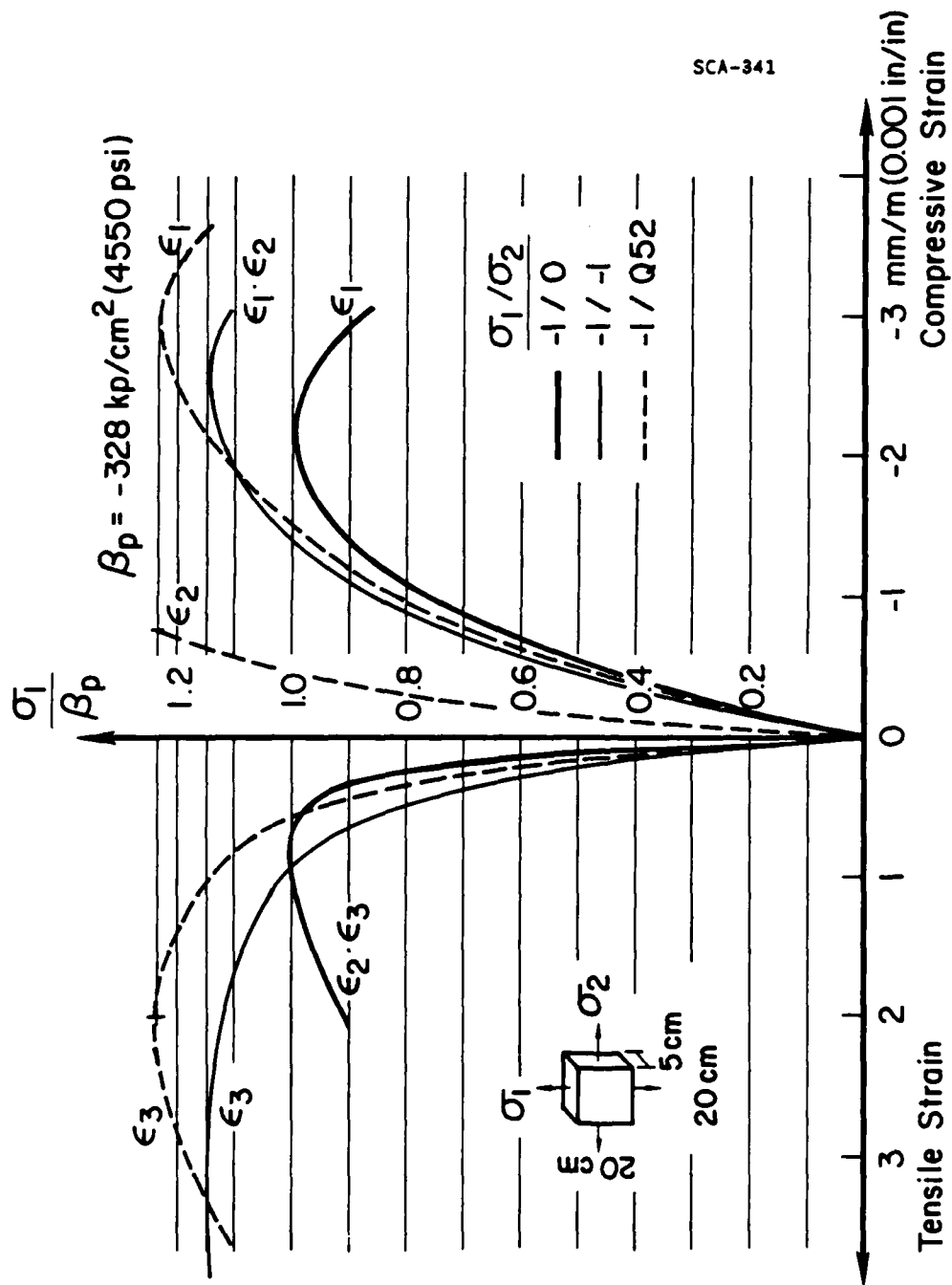


Figure 2-25. Experimental results from Weigler and Becker:
(a) uniaxial compression, (b) equi-biaxial compression.

strain prior to failure. Since concrete under biaxial compression does not exhibit surface cracking, and since concrete aggregate remains linear elastic, the nonlinearity arose from relative motion of the aggregate and mortar and possibly from nonlinearity in the mortar response. Larger obtainable stresses and strains relative to uniaxial response are to be expected for biaxial loading because the multiaxial stress state inhibits cracking which is the ultimate failure mode.

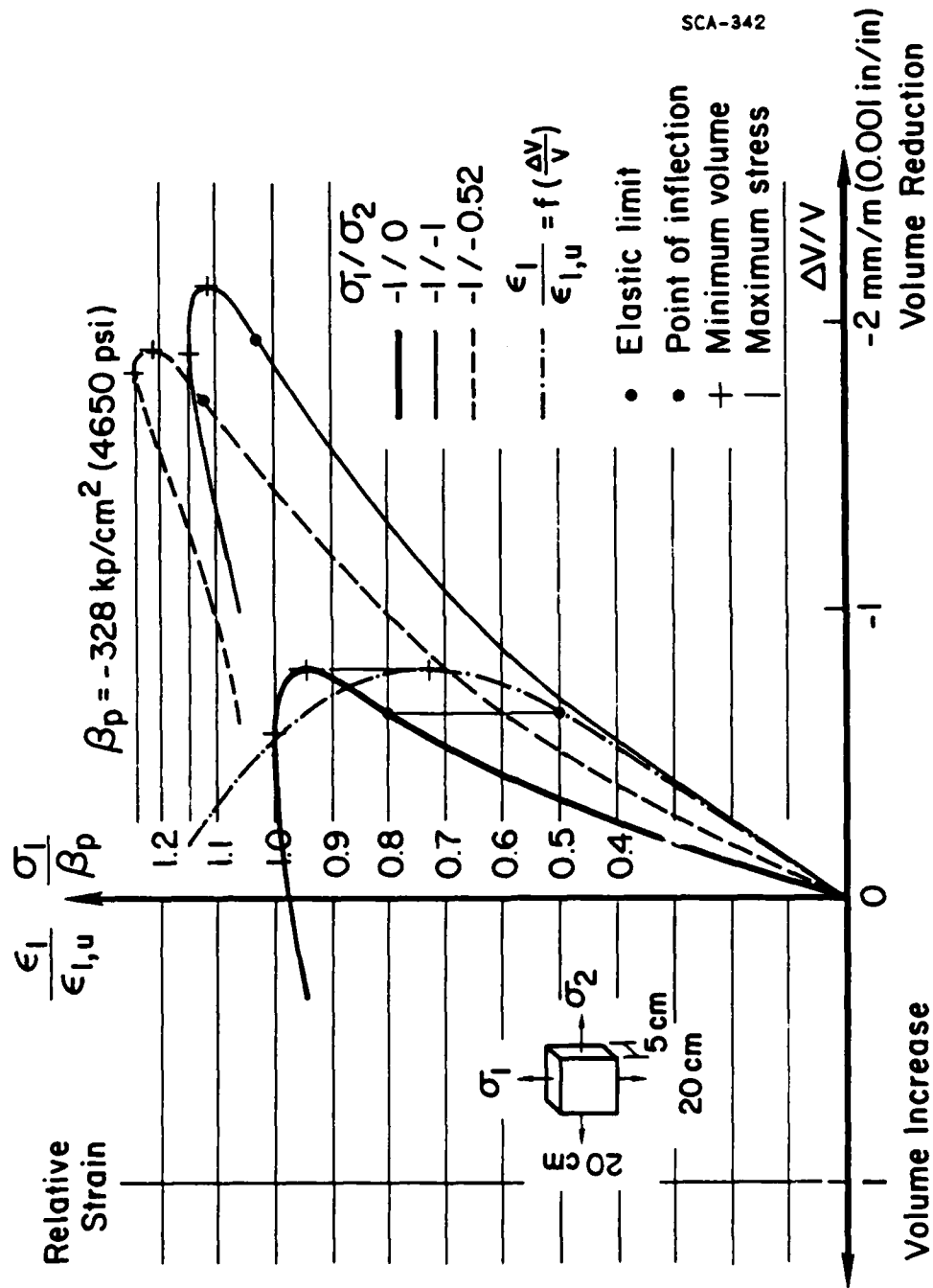
The most comprehensive study of concrete biaxial response was performed by Kupfer and his co-workers^(36,55-59) and is reviewed by Dei Poli.⁽⁶⁰⁾ Figure 2-26 shows typical results taken from Reference.⁽³⁶⁾ In Figure 2-26a are compared the stress-strain response for three proportional loadings. The most surprising result is that the maximum obtainable stress did not occur for equi-biaxial compression but instead for a stress ratio $\sigma_1/\sigma_2 = -1/-0.52$. Again it is clear that lateral expansion (ϵ_3) was greater for biaxial compression compared to uniaxial compression. Figure 2-26b shows that, in agreement with intuitive expectation, volumetric compression was greater for biaxial compression than for uniaxial and in agreement with Weigler and Becker⁽⁴¹⁾ the volumetric strains under biaxial compression started to increase just before failure.

On each curve in Figure 2-26 are marked four points. The elastic limit corresponded to the first deviation of response from linearity. As the degree of biaxiality of the compressive loading increased the linear elastic range increased, thus lending credence to the idea that biaxial load constraint inhibits initiation of additional microcracks. The inflection point corresponded to the stress-strain state where the volumetric strain rate changed sign and marked the beginning of the slowing down of volumetric shrinkage. At the inflection point a new deformation mechanism was introduced that grew as the load increased and counteracted the compressive actions of the applied loads. This new mechanism was major microcracking which occurred in the plane of the applied



(a). Biaxial stress-strain

Figure 2-26. Biaxial compression data.



(b) Stress versus volumetric strain

Figure 2-26 (continued) Biaxial compression data.

loads. The sustained load strength of concrete probably lies between the inflection point and the point of minimum volume. At the minimum volume point microcracking had become so wide spread that it swamped any tendency of the specimen to contract. The maximum stress point indicated that under biaxial loading concrete has a softening branch akin to the uniaxial response. However, Kupfer did not examine this possibility in detail.

Figure 2-27 is taken from a study by Liu, Nilson and Slate⁽³⁵⁾ who used a model concrete. Their specimens were 5 x 5 x 0.5 inch and contained circular inclusions of various diameters and randomly distributed. As the magnitude of σ_2 increased relative to σ_1 the corresponding strain ϵ_2 went from expansion to compression. At $\sigma_2 = 0.2\sigma_1$, ϵ_{23} was essentially null for most of the load history suggesting that for the concrete used, $\nu = 0.2$. In consonance with the findings of Kupfer, Hilsdorf and Rüschi⁽³⁶⁾ the maximum stress occurred for $\sigma_2/\sigma_1 = 0.5$.

B. Tension-Compression.

Kupfer and his co-workers^(36,55-59) used their brush bearing platen testing machine to obtain biaxial compression-tension data. Sample results are shown in Figure 2-28. It can be seen that as the tension component increased, attainable levels of stress and strain decreased and when the tensile stress had grown to twenty percent of the compressive stress, strength was only thirty percent of the uniaxial strength. Also, the response exhibited increasingly less nonlinearity as the tensile component increased, indicating a transition to a brittle, cleavage-type of fracture.

C. Biaxial Tension

There is very little data on biaxial tension. Figure 2-29 is taken from Kupfer, Hilsdorf and Rüschi⁽³⁶⁾ and shows that as the loading changed from uniaxial to equi-biaxial tension, the specimen stiffened and obtainable levels of strain decreased. Also, the maximum obtainable stress levels were essentially independent of the stress ratio σ_1/σ_2 implying that for biaxial tension, strength

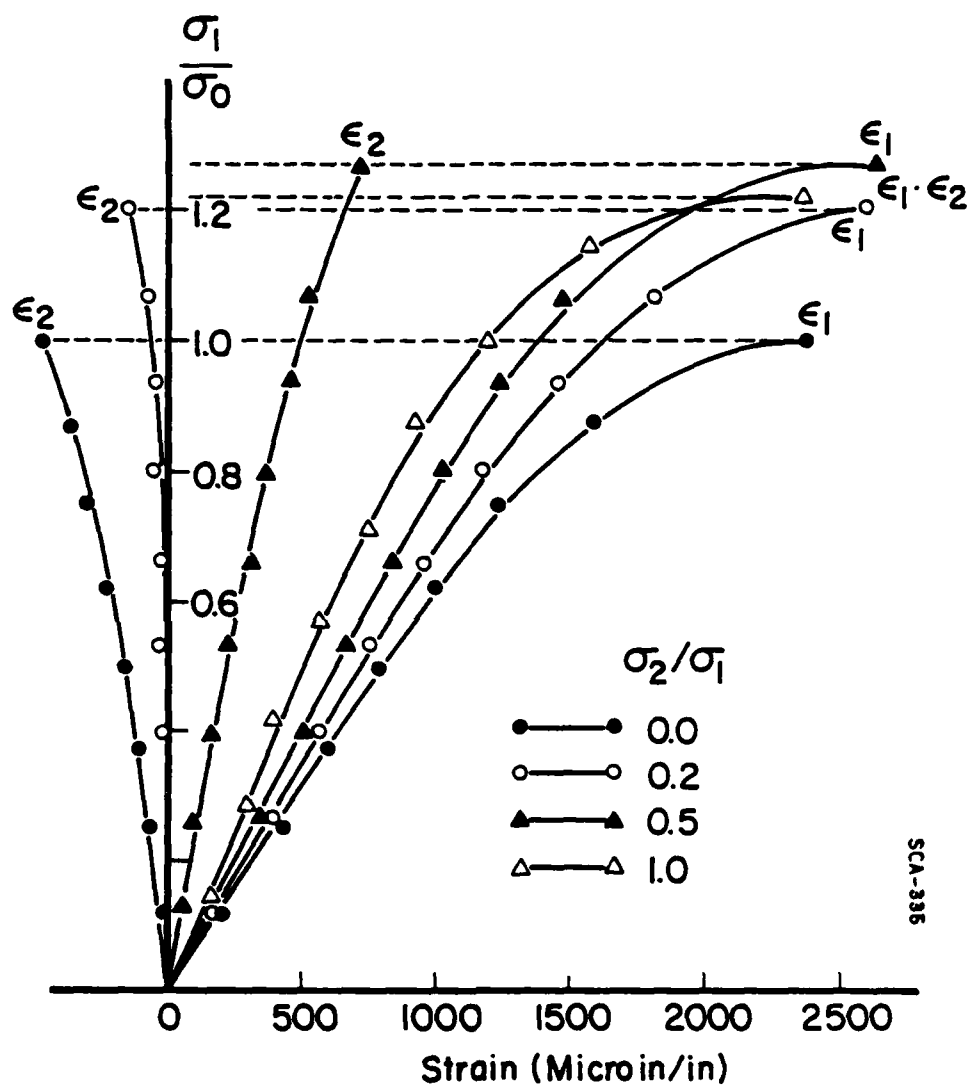
is governed by a maximum stress component criterion derivable from uniaxial test results. Finally note that the response up to failure was essentially linear elastic.

2.3.5 Biaxial Strength Results

Most biaxial experiments on concrete have attempted to determine the strength of concrete under biaxial loads and many results have been obtained. The objective of such tests was to determine biaxial stress levels necessary to cause concrete to fail. In principal stress space, biaxial stresses lie on planes where one principal stress is null. On such a plane, stress combinations at failure define a strength or failure envelope. In the following only data which is considered reliable is presented. Also, most results refer to short-term loading.

Kupfer, Hilsdorf and Rüsch⁽³⁶⁾ published results for three different concretes whose uniaxial compression strengths ranged from 2700 psi to 8350 psi. The data was obtained from proportional load histories using brush bearing platens so that frictional effects were minimized. Strength (i.e., failure) envelopes in terms of principal stresses σ_1, σ_2 are shown in Figure 2-30 where stresses have been normalized with respect to f'_c for each concrete. From Figure 2-30 it is clear that the normalized strength envelopes are essentially insensitive to concrete uniaxial strength. The authors found that biaxial compressive strengths were greater than uniaxial and that concrete could sustain only small tensile loads when biaxially stressed. For equi-biaxial compression failure occurred when $\sigma_1 = \sigma_2 = 1.16 f'_c$ while for the load trajectory $\sigma_1 = 2\sigma_2$ failure occurred at $\sigma_1 = 1.27 f'_c$.

Gerstle et al.,⁽³⁸⁾ conducted a comprehensive test program designed to identify the sensitivity of biaxial compression failure surface to test technique. Seven laboratories in four countries performed tests on specimens cast from the same concrete mix. The anticipated experimental variables were load platen design and specimen shape; specimen moisture loss was an uncontrolled variable which for standard 3 in. x 6 in. cylinders, varied from 0.2 to 2.7



SCA-335

Figure 2-27. Biaxial compression response for model concrete.

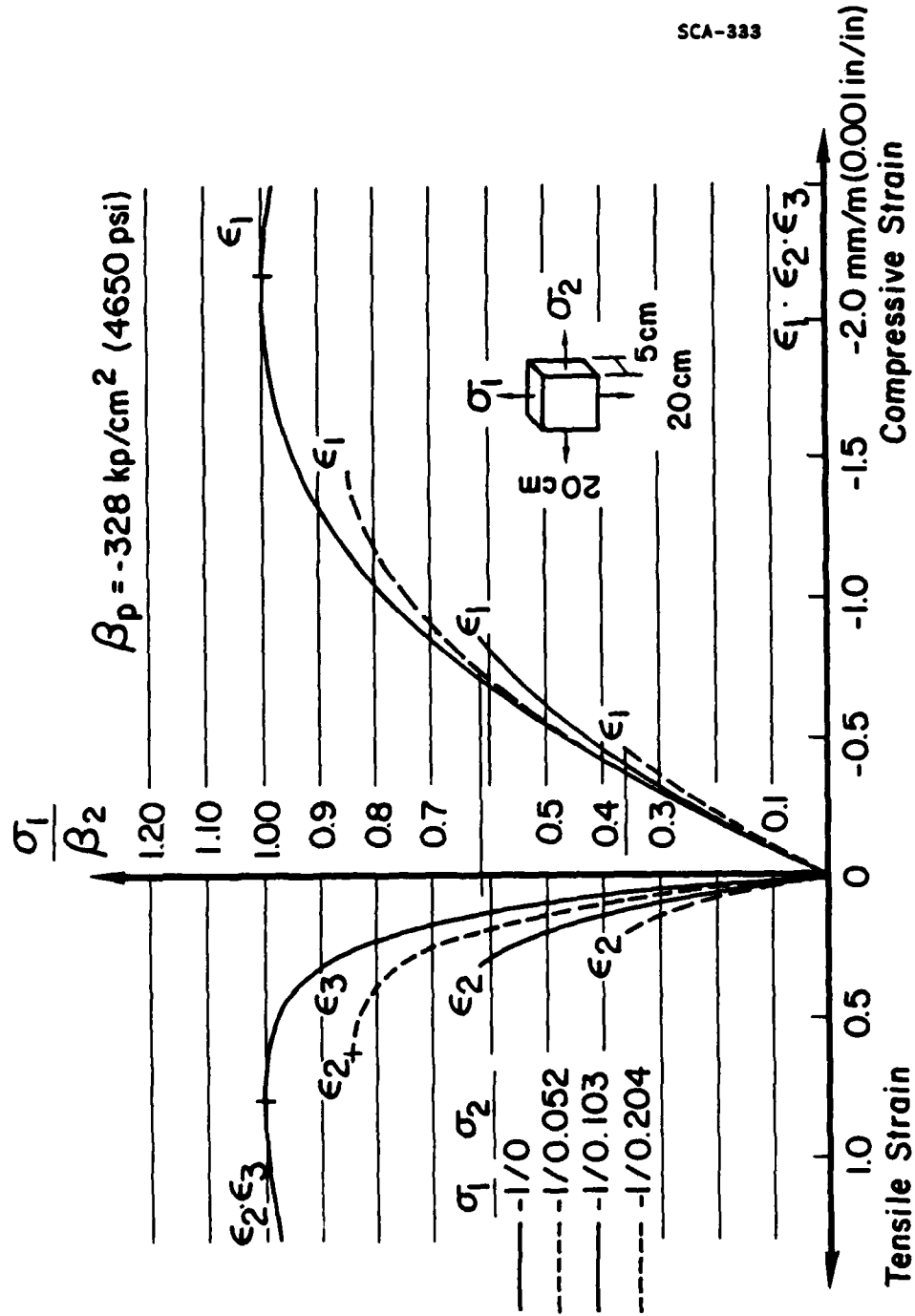


Figure 2-28. Biaxial compression-tension response.

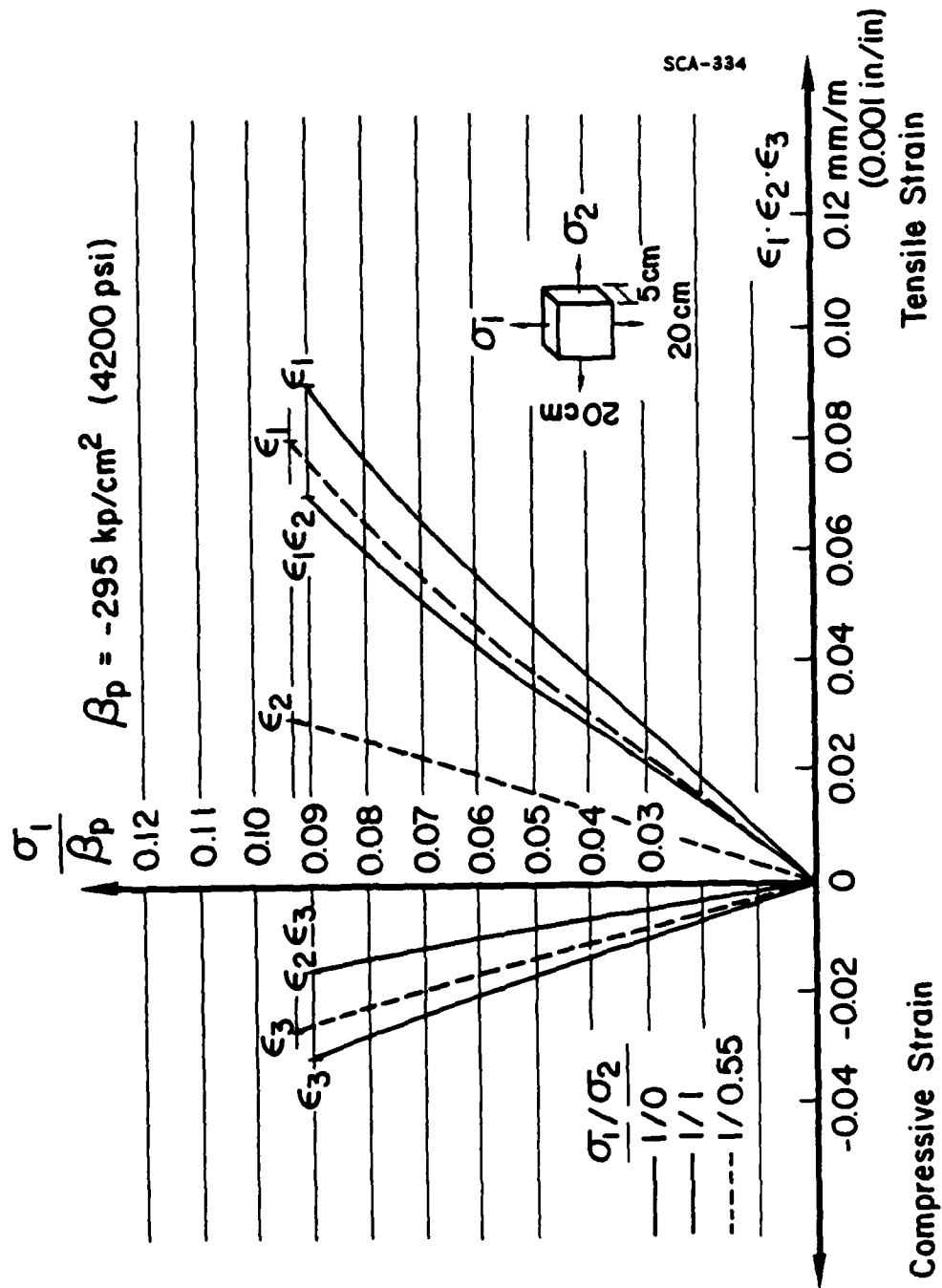


Figure 2-29. Biaxial tension response.

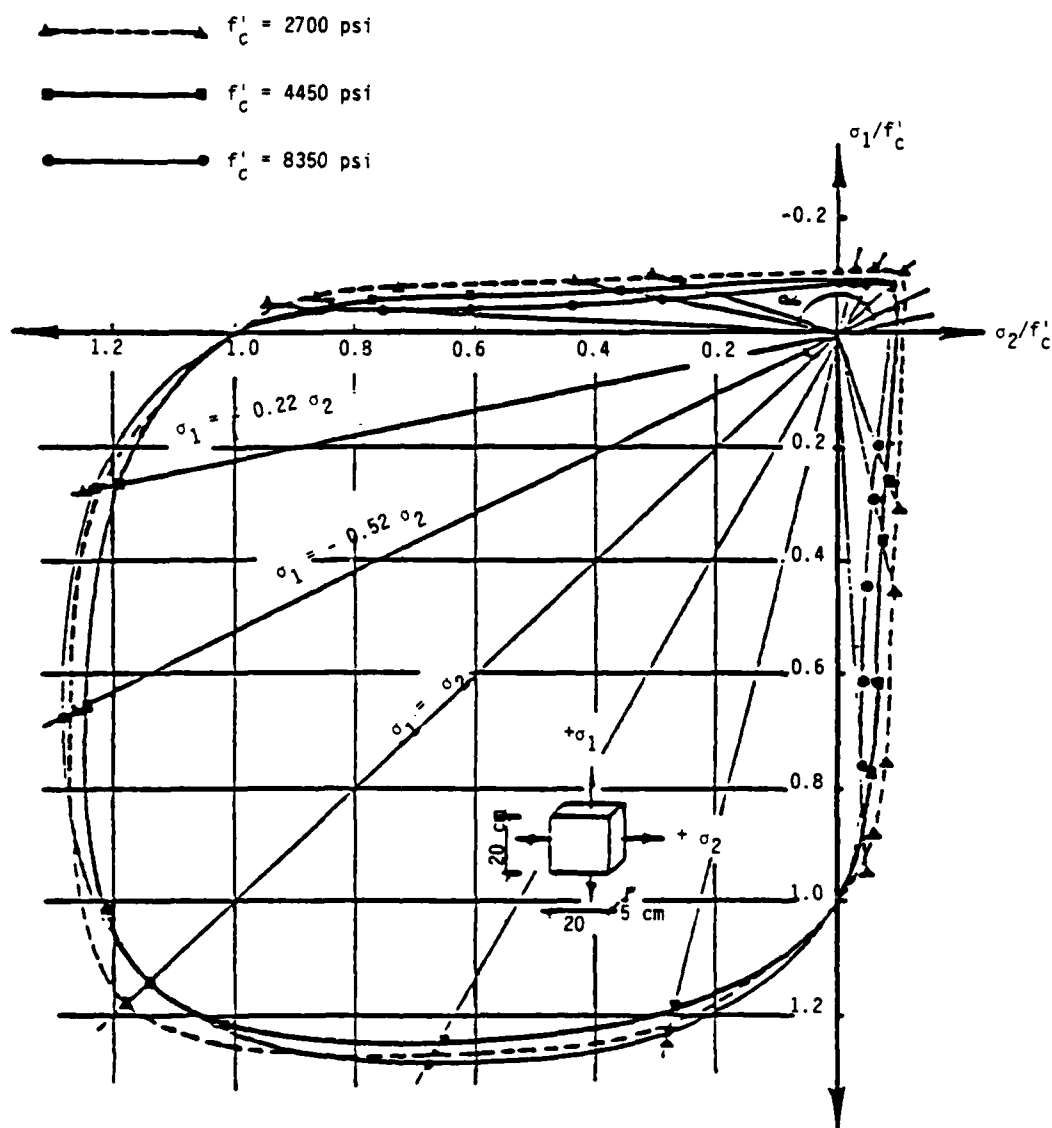


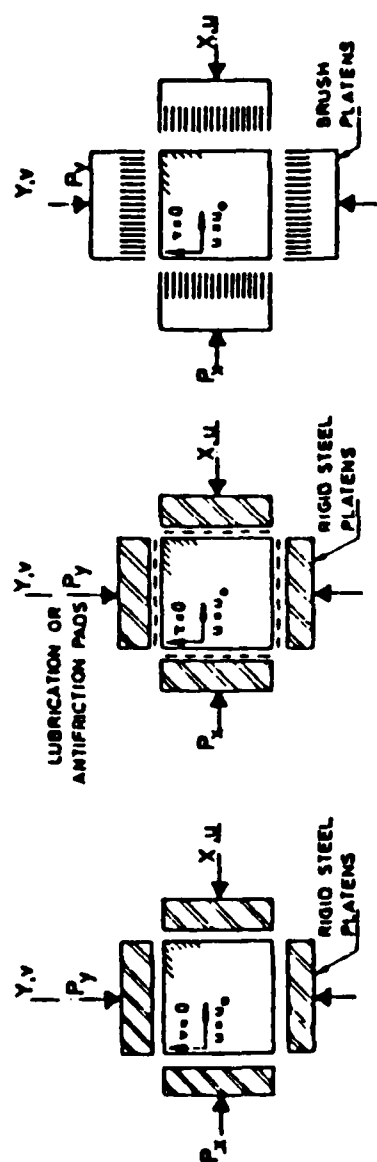
Figure 2-30. Typical biaxial strengths of plain concrete.

percent. The five types of load platens employed in the tests, (along with their two letter identifying codes), are shown in Figure 2-31. In Figures 2-32 and 2-33 are given the failure envelopes found by the various test techniques.* The principal observation is that specimens tested with unlubricated solid steel load platens (denoted by DP) gave higher strengths than specimens tested with fluid cushion (FC), lubricated (LP) and brush bearing (BR) platens. Also, there is much more scatter among the results obtained from dry platens than among the remaining results.

Several authors have focused their attention on the tension-compression quadrants of the biaxial stress plane. Bresler and Pister^(45,46) and Isenberg⁽⁴⁸⁾ performed compression-tension experiments on hollow circular cylindrical specimens. Isenberg's results have also been reported by Johnson and Lowe.⁽⁶¹⁾ Based on their experimental results Bresler and Pister proposed the failure surface shown in Figure 2-34. From the figure it can be seen that in the compression-tension region strength is primarily controlled by the tensile stress component. The slight increase in attainable tensile stresses indicated in Figure 2-34 for moderate levels of compressive stress levels is not necessarily real but may be only an artifact of the curve fit employed by Bresler and Pister.

The results in Figures 2-35 and 2-36 are also for the biaxial compression-tension failure surface normalized to f'_c . When the expanded tension scales are taken into account, the results are comparable to those of Bresler and Pister. In Figures 2-35 and 2-36 both sets of authors believed the slight 's' shape to the failure surface might be real and indicated that the compression-tension quadrants were transition zones between the gradual crushing failure of uniaxial compression and the sudden cleavage failure of uniaxial tension. Figure 2-35 is a magnification of the compression-tension

* Acronyms BAM, ENEL, ICL, TUM NMSU, UCD and CU, which identify the performing laboratories, are defined in Reference 38.

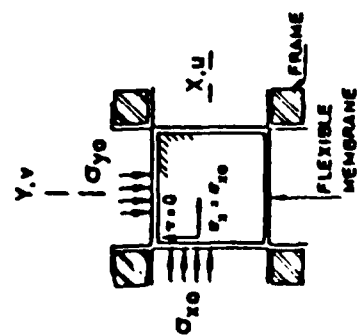


Dry Steel Platens (DP) Lubricated Steel Platens (LP) Brush Bearing Platens (BR)

DP

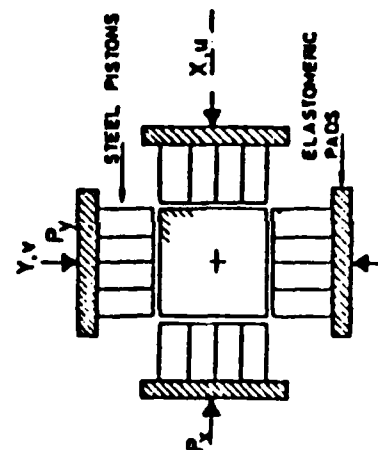
LP

BR



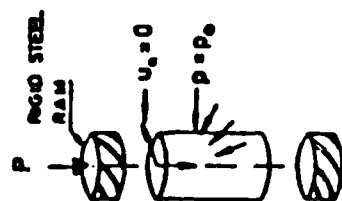
Fluid Cushion (FC)

FC



Flexible Platens (FP)

FP



Standard Triaxial Test (CYL)

CYL

Figure 2-31. Load platen types used in experimental program.

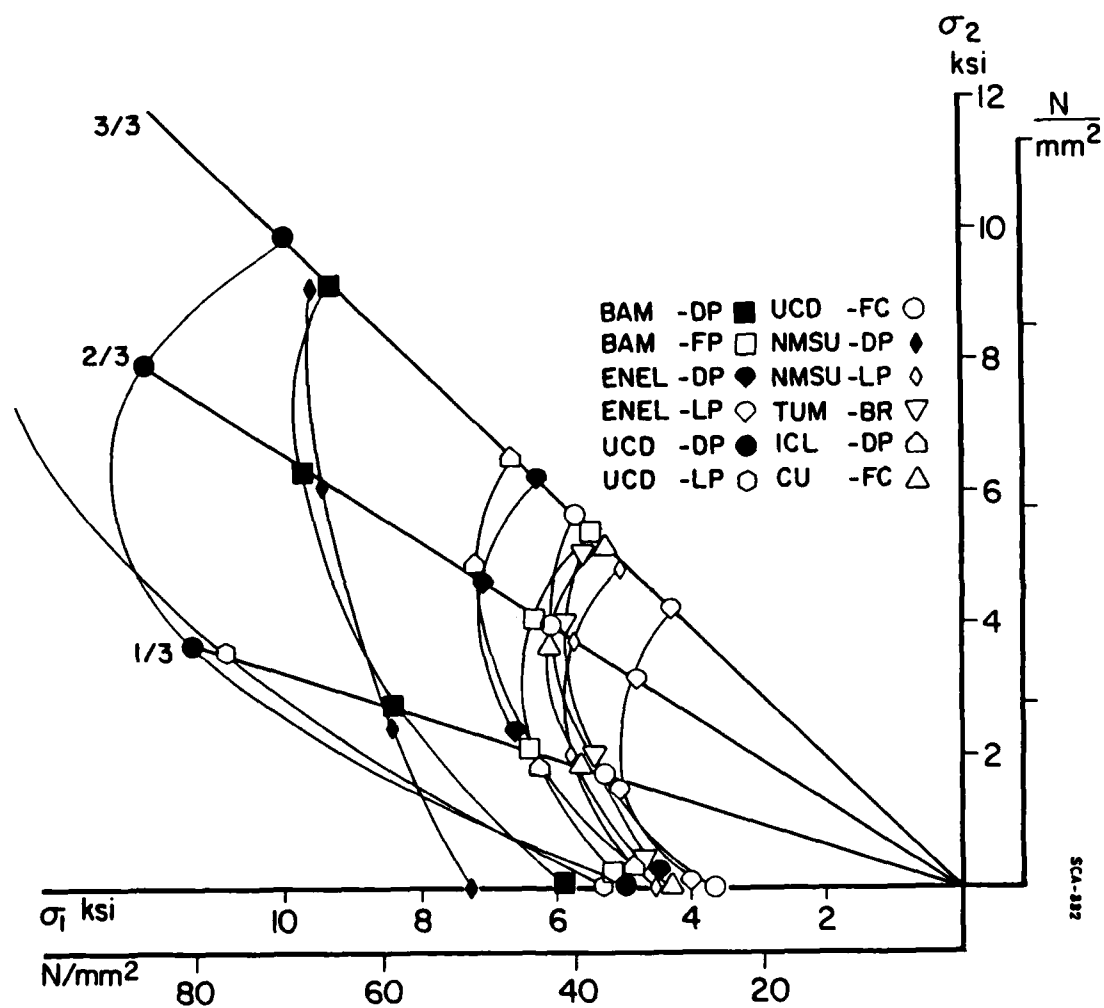


Figure 2-32. Strength envelopes obtained using different load platen designs (see Figure 2-31).

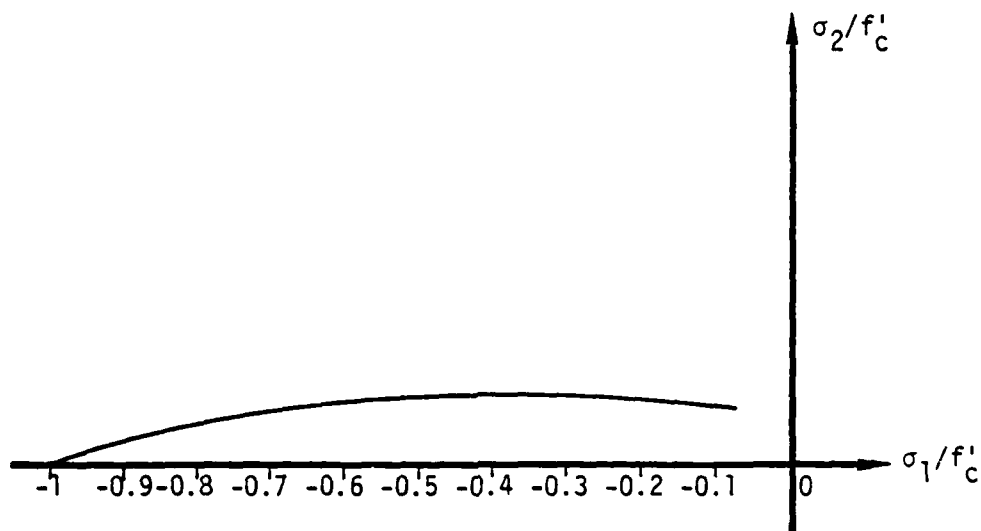


Figure 2-34. Failure surface for biaxial compression-tension.

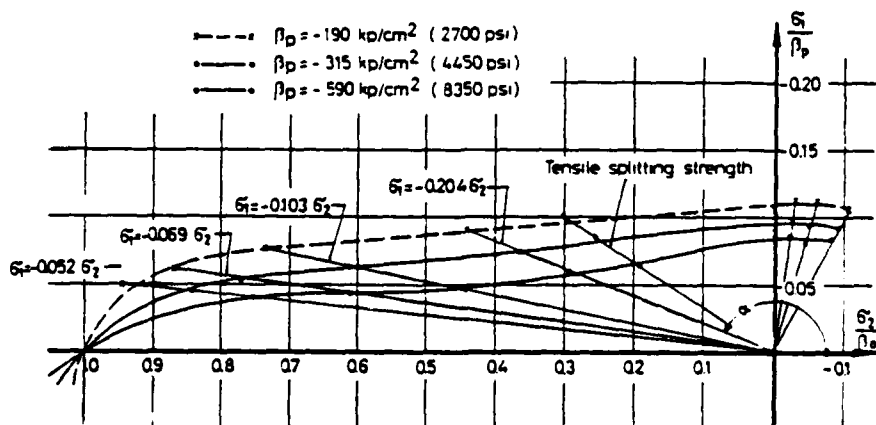


Figure 2-35. Failure surface for biaxial compression-tension and tension.

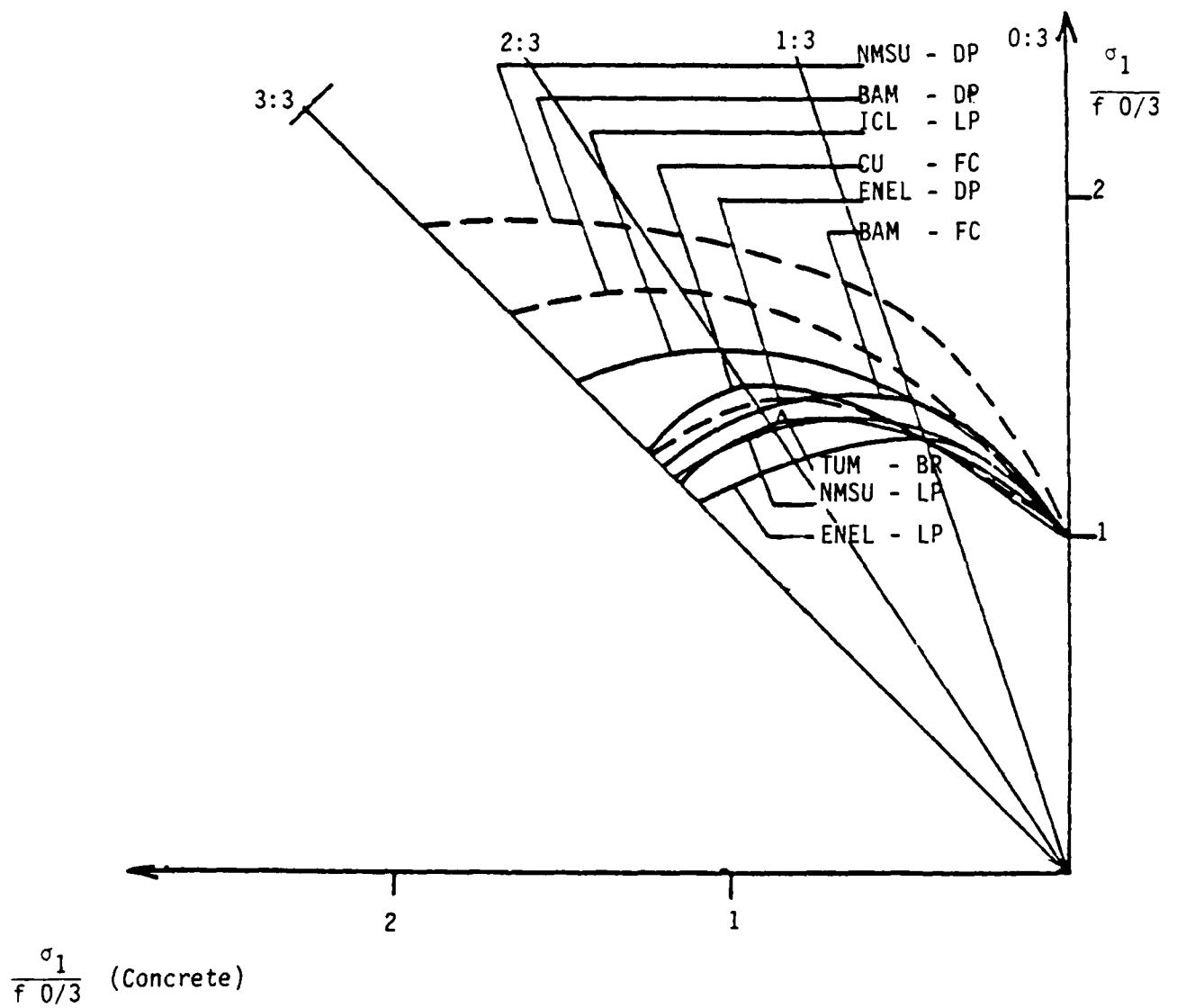


Figure 2-33. Strength envelopes obtained using different load platen designs and normalized to f'_c (see Figure 2-31).

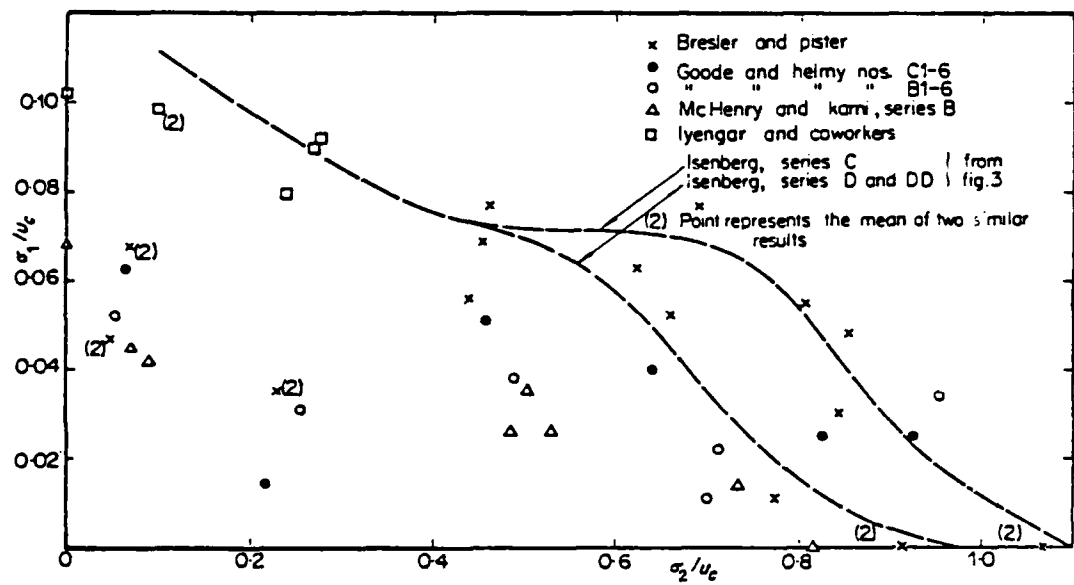


Figure 2-36. Failure surface for biaxial compression-tension.

and biaxial tension regions of Figure 2-30 and raises the possibility that the failure surface is sensitive to f'_c . In Figure 2-36 the wide scatter between data obtained by various authors is evident.

The only systematic determination of strength in the biaxial tension quadrant was performed by Kupfer, Hilsdorf and Rüschi.⁽³⁶⁾ Results are shown in Figure 2-35 and indicate that failure occurred whenever a stress component reached the uniaxial tension strength.

Very little data exist on the sensitivity of failure surface definition to differences in the path traversed in stress space from zero stress to failure. Taylor and Patel⁽⁶²⁾ subjected both wet and dry concrete cubical specimens to two types of stress history. For the first type radial loading was used. In the second type a sequential loading was employed where first one principal stress was incremented and then subsequently held fixed while the other principal stress was increased from zero until failure occurred. The wet specimens were cured in water and kept moist during tests by a damp cloth while the dry specimens were stored in a normal laboratory environment for two weeks before testing. Results obtained are shown in Figure 2-37 and 2-38. For wet specimens the average strength obtained by sequential loading was greater than that for proportional loading. For dry specimens average strength for proportional and sequential loading were approximately equal. Thus the evidence suggests that under the right conditions it might not be possible to define a unique failure surface for biaxial stress states.

2.3.6 Experimental Support for Plasticity Theories of Biaxial Response

Constitutive theories for concrete biaxial response are sometimes developed using the concepts of conventional plasticity. In these theories an initial yield surface in principal stress space is postulated. The yield surface is closed, contains the zero stress state and has a shape similar to the failure surface. For all stress states inside the initial yield surface, concrete response is elastic. As stress component magnitudes increase, the

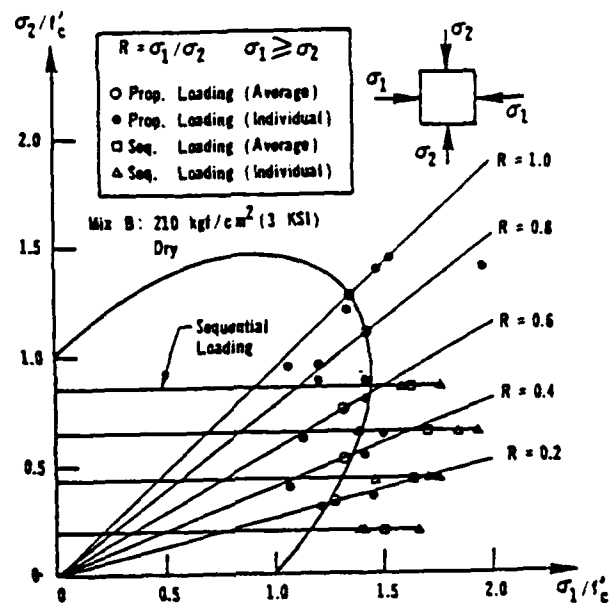


Figure 2-37. Sensitivity of biaxial failure surface to load path: dry specimens.

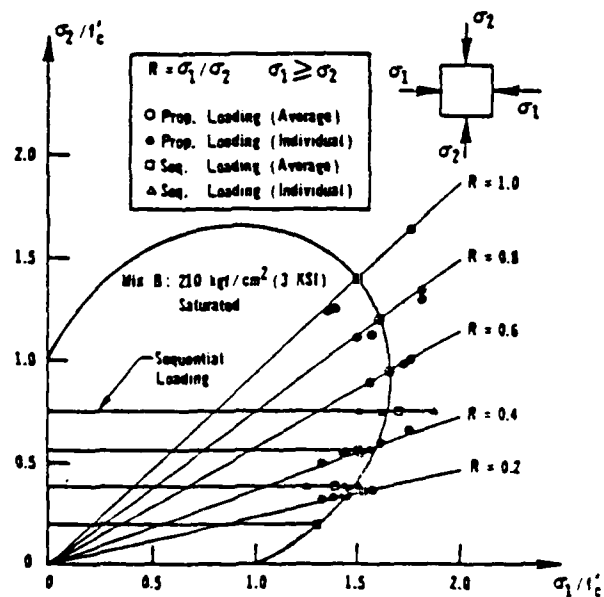


Figure 2-38. Sensitivity of biaxial failure surface to load path: wet specimens.

stress state reaches the initial yield surface and the constitutive model predicts that on further loading some irreversible damage occurs in the concrete. With continued loading the yield surface expands in all directions so that the increasing stress state is always on the yield surface. If the stress should subsequently decrease, the yield surface maintains its size and position and the unloading response is elastic as is the response along all stress trajectories inside the yield surface. Additional damage to the concrete occurs only if the stress again reaches the yield surface and expands the yield surface farther.

Conventional plasticity theories also require that for all points on a yield surface the material secant modulus be the same.

Experimental evidence to support plasticity models is limited. Dei Poli⁽⁶⁰⁾ has reported experiments by Kupfer and his co-workers, Figure 2-39. In the figure E_0 is the initial concrete secant modulus and the curves, plotted in principal stress space, are curves of constant secant modulus. As stress increases, the secant modulus decreases until at failure it is thirty percent of its initial value. The small shaded area represents an elastic region whose perimenter has similar shape to that of the failure surface and could serve as an initial yield surface. The remaining curves of constant secant modulus also are similar in shape to the failure surface and could serve as subsequent yield surfaces.

Additional biaxial test data have been published by Vile,⁽⁴⁰⁾ Figure 2-40. In the figure the failure or 'ultimate' surface is plotted in principal stress space along with a 'discontinuity' surface. The discontinuity surface, whose shape is similar to the failure surface, represents a 'critical point' where 'there is a marked change in the mechanical properties of the material and more severe cracking takes place which leads eventually to failure.' Thus the discontinuity surface does not represent initial yield but rather some subsequent level of damage. However

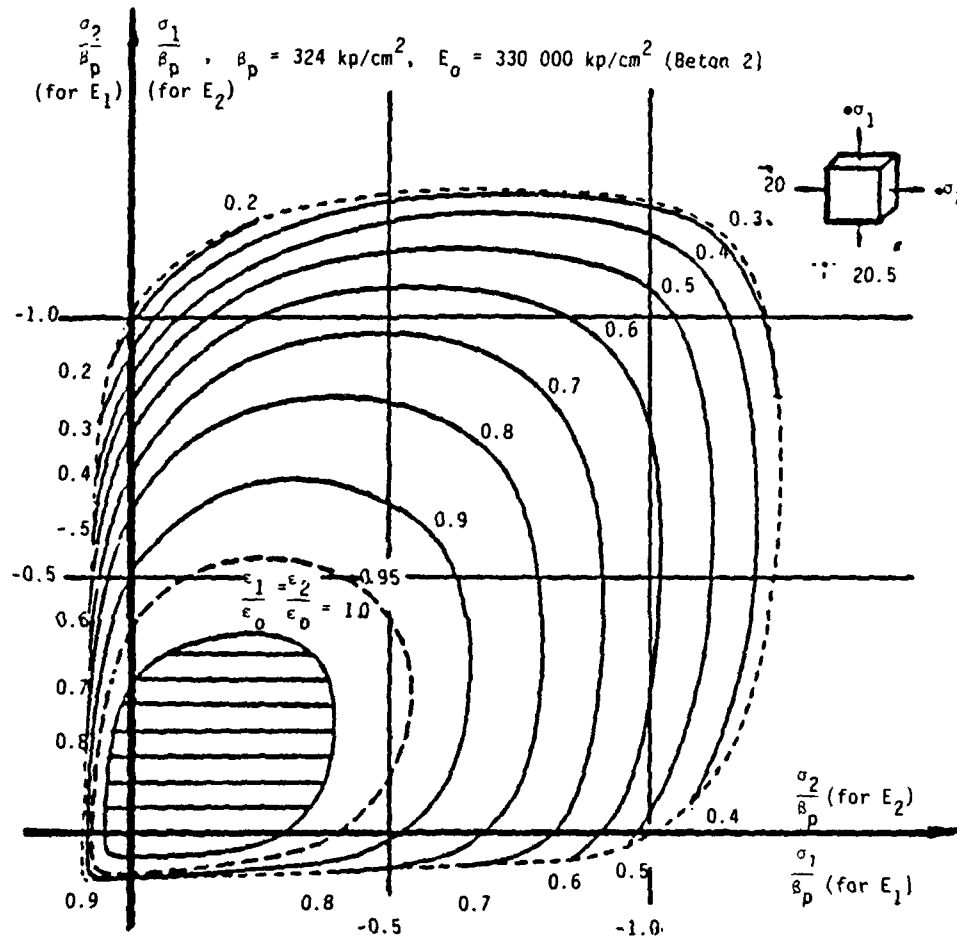


Figure 2-39. Curves of constant secant modulus plotted in principal stress space.

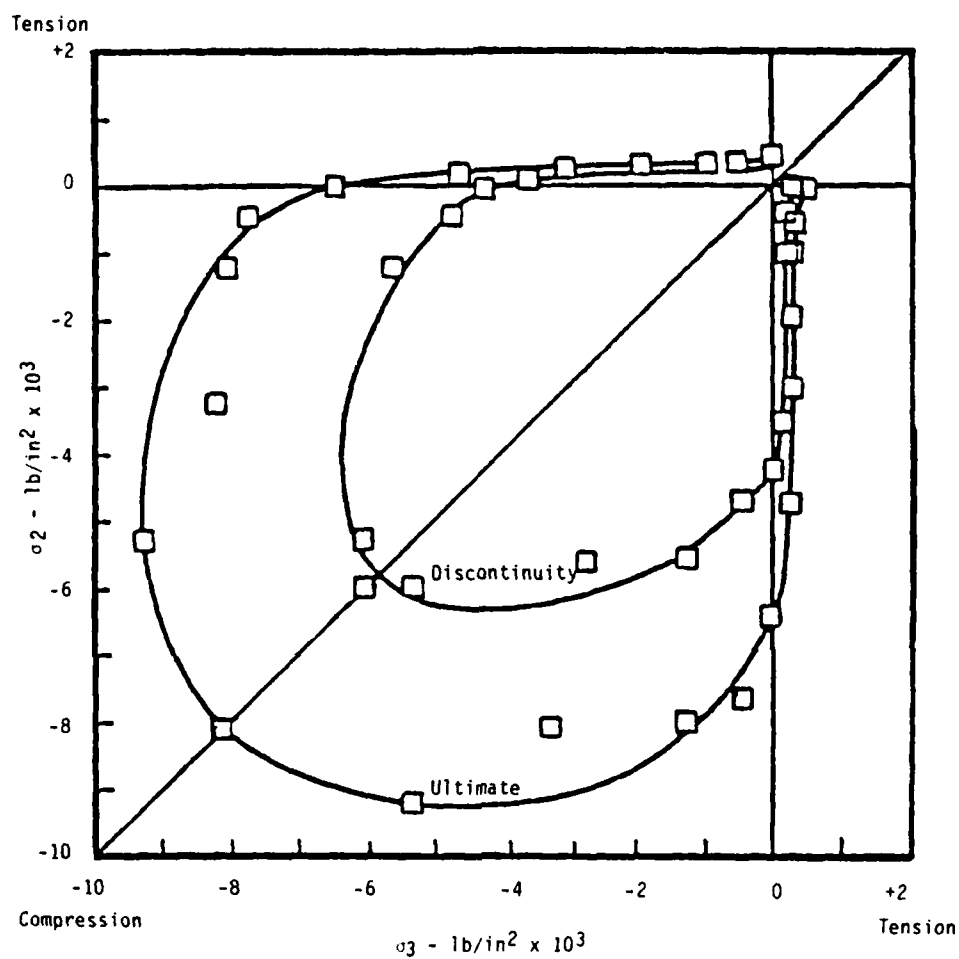


Figure 2-40. Ultimate and discontinuity curves for biaxial compression and compression-tension.

the surface is compatible with plasticity theory in that when the yield and discontinuity surfaces coincide, all points on the yield surface would experience the same 'marked change in material properties.'

2.3.7 Issues

The qualitative response of plain concrete under monotonic, biaxial loading up to failure is well understood. The principal shortcoming is the lack of agreed upon experimental procedures so that different laboratories performing the same tests on specimens fabricated from the same batch of concrete yield the same results. The international program reported by Gerstle *et al.*,⁽³⁸⁾ is a necessary first step and what are now required are efforts to reconcile differences in results followed by development of generally agreed upon testing procedures.

The most serious inadequacies in the experimental data base are results on

- biaxial cyclic stress-strain response
- biaxial post-peak softening behavior
- strain rate sensitivity
- microcracking induced anisotropy.

All sets of data are needed before it is possible to predict the response of reinforced concrete protective structures for load environments of interest to the defense community.

2.4 TRIAXIAL RESPONSE OF PLAIN CONCRETE

For most analyses of protective structures, three-dimensional constitutive theories of concrete are required. When a theory is first formulated the developer validates it by fitting the theory to existing data. The uniaxial and biaxial data discussed in Sections 2.2 and 2.3 have traditionally formed the major portion of that data base. However, in the last few years, reliable triaxial data has been published. The objective of this section is to review this

triaxial concrete data. As in the previous section presentation of triaxial data is prefaced by discussions of concrete micromechanics and experimental procedures so that greater insight into the data can be achieved.

2.4.1 Remarks on Micromechanics, Variability

Very little research has been done on the micromechanical behavior of plain concrete under triaxial loading and what data there are appear contradictory. Krishnaswamy,⁽⁶³⁾ subjected four-inch cubes to various levels of triaxial compression, sectioned the tested specimens and examined them for microcracking. Krishnaswamy's principal observation was that the presence of all around compression retarded microcrack growth. For example, under uniaxial compression, cracks at the aggregate-mortar interface started to grow at a compressive strain of approximately 0.0005, while for triaxial compression, with minor compressive stresses approximately ten percent of the major stress, interface cracking did not occur until the major compressive strain reached 0.0018. Krishnaswamy also noted that at failure the amount of microcracking induced by either uniaxial or triax compression was approximately the same.

Palaniswamy and Shah⁽⁶⁴⁾ tested 3 in. D x 9 in. L concrete cylinders. Most of their results were for moist concrete with a uniaxial compressive strength of 2.3 ksi. In their tests the authors applied axial and lateral stresses up to 24 ksi and 9 ksi respectively. The loading path was always one of hydrostatic loading followed by additional axial loading with the lateral pressure fixed.

The results of Palaniswamy and Shah fell into two distinct regimes according to whether the maximum lateral stress at failure satisfied either $\sigma_{lat} \leq 4$ ksi or $\sigma_{lat} \geq 6$ ksi. For low lateral pressures, post-test examination showed:

- surface bulging and cracking increased as σ_{lat} increased

- failure was of a splitting or tensile mode similar to uniaxial failure
- compressive deviatoric stress components were greater than the hydrostatic component
- maximum longitudinal strain increased with σ_{lat}
- bond cracking between aggregate and mortar increased with σ_{lat}
- ultrasonic pulse wave velocities in both the longitudinal and lateral directions were increasingly attenuated as σ_{lat} increased.

Figure 2-41 shows the sensitivity of pulse velocity and total bond crack length to maximum lateral confining pressure. For high maximum lateral pressures ($\sigma_{lat} \geq 6$ ksi) an entirely different behavior was exhibited:

- little or no post-test surface bulging or lateral surface distress
- failure was by mortar and aggregate crushing
- the hydrostatic stress was greater than the deviatoric components
- lateral strains were always compressive
- bond cracking diminished as σ_{lat} increased
- ultrasonic pulse wave velocity attenuation decreased as σ_{lat} increased.

Additionally the authors also tested specimens that had been previously loaded to a hydrostatic stress of 8 ksi and found no deterioration in either stiffness or strength.

The results of Palaniswamy and Shah clearly showed the sensitivity of concrete failure mode and load to the level of imposed hydrostatic stress, a result reflected by the entire triaxial data base. Whether the results of these authors are in agreement with those of Krishnaswamy is not clear since the two experimental programs used entirely different specimens and load paths. Both contributions indicate that triaxial stress states inhibit bond

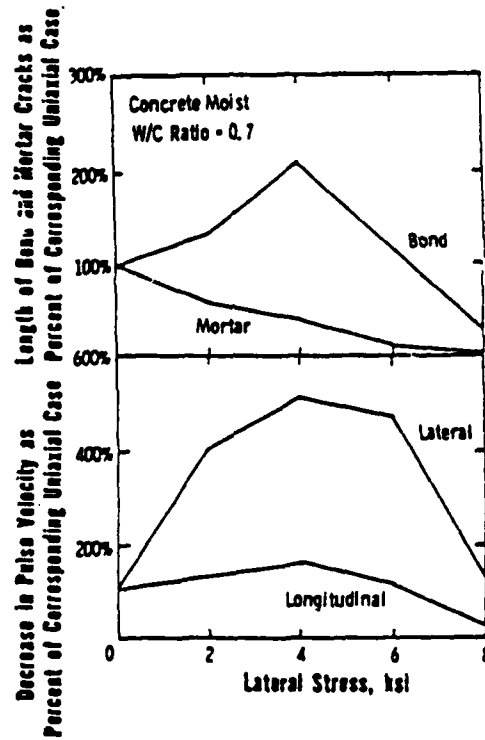


Figure 2-41. Crack length and ultrasonic wave speed reduction as a function of lateral stress.

crack initiation. However, the first paper concludes that at failure the amount of bond cracking is almost always the same while the second paper indicated bond cracking at failure first increased and then decreased as the magnitude of stress components increased.

The dual natures of concrete triaxial response and failure mode indicate the presence of competing influences. If the stress has a large deviatoric component then significant tensile-deviatoric stress exists thus encouraging a splitting failure. At low hydrostatic pressures, the pressure merely holds the specimen together longer thus permitting higher levels of cracking. At higher levels of pressure, pressure actively inhibits cracking thus lending credence to the idea that aggregate-mortar interface bond failure is in shear, the failure shear stress level being controlled by hydrostatic pressure.

Plain concrete strength is conventionally characterized by its uniaxial strength f'_c . For biaxial compressive stress states the maximum obtainable stress is approximately $1.3 f'_c$ and so f'_c still characterizes concrete strength and the size of the equipment used in biaxial tests is essentially unchanged from (though more complicated than) that used in uniaxial experiments. For triaxial testing the same is not true. Under triaxial compression concrete can support stresses larger than four times f'_c because of constraints imposed on the specimen by the hydrostatic component of loading. However, in most triaxial experiments maximum stresses are much smaller than this because of equipment size, and concomitant cost constraints. For example, to achieve stresses five to ten times f'_c on four-inch cube specimens of 5 ksi concrete would require 500,000 - 1,000 000 lb actuators and sufficiently strong frames to support them. Consequently it is usually practical to explore only a limited portion of the concrete, triaxial stress, failure envelope. The objective of the following subsections is to show the variability that exists in concrete triaxial testing techniques so that the scatter seen in data can be partially explained in terms of test parameter differences.

2.4.2 Triaxial Test Specimens

In triaxial tests two specimen types are used:

- solid cylinders
- cubes.

Cylinders are used in "conventional" triaxial testing where two of the three principal stresses are always equal. The axial or longitudinal stress is one principal stress while the other two principal stresses equal the lateral or radial load applied to the specimen's curved, lateral surface. All data from a conventional triaxial test can be plotted on a single plane, the Rendulic plane, in principal stress space. Further it is impossible to subject the lateral surface to tension. Thus only a limited amount of data can be obtained from cylinders.

The cube used in "true" triaxial tests, is a more versatile specimen since all three principal stresses can, potentially, be varied independently and tensile stress states can in principle, be induced by bonding the load platens to the specimen.

No established guidelines exist for desirable specimen size. To obtain an approximately homogeneous stress state in a specimen aggregate size (A) must be small relative to specimen minimum dimension (D). Typical values for D/A are shown in Table 2-4 where the minimum and average values were four and eight respectively. Johnson and Lowe⁽⁶⁸⁾ believed that concrete strength increased as D/A decreased. Bertacchi⁽⁷³⁾ found that strength results from 10 cm, 16 cm and 20 cm cubes were essentially identical while Dei Poli⁽⁷⁴⁾ reporting on the work of others, noted that 1 in. maximum aggregate concrete was seven percent stronger than 2 in. maximum aggregate concrete. Thus, based on a limited amount of data, triaxial strength appears sensitive to maximum aggregate size.

2.4.3 Triaxial Testing Machine Considerations

Machines for triaxial testing fall into two classes corresponding to the two specimen types. For cylindrical specimens an

Table 2-4

Geometric data for specimens used in triaxial tests

<u>Authors</u>	<u>Reference</u>	<u>Dimensions (in)</u>	<u>Maximum Aggregate Size (in)</u>	<u>Size Ratio (D/A)</u>
Krishnaswamy	(63)	4	≤ 0.75	5
Palaniswamy and Shah	(64)	3D x 9L	0.50	6
Chinn and Zimmerman	(65)	6D x 12L	≤ 0.50	12
Gardner	(66)	3D x 6L	0.75	4
Gerstle <u>et al</u>	(67)	2.5	0.50	5
		6.4D x 12.8L	0.5	13
		4D x 10L	0.5	8
		3	0.5	6
		2	0.5	4
		4	0.5	8
Johnson and Lowe	(68)	1.5D x 3L	0.93	16
Launay and Gachon	(69)	2.8 and 5.6	--	--
Mills and Zimmerman	(70)	2.25	0.375	6
Newman	(71)	4D x 10L	0.8	5
Richart, Brandtzaeg and Brown	(72)	4D x 8L	--	--

D and A are minimum specimen dimension and maximum aggregate size respectively.

oil filled chamber surrounds the specimen lateral surface which, in turn, is coated with a non-porous material such as neoprene to prevent oil from filling cylinder surface pores and inducing premature failure. Lateral surface loads are imposed by pressurizing the oil chamber. Axial loads are applied through a hydraulically actuated load platen.

For cubical specimen tests three different platen designs were used to minimize friction induced lateral movement constraints:

- brush bearing
- fluid cushion
- steel plate.

The brush bearing and fluid cushion platen designs were discussed in Section 2.3.3 and will not be reviewed further.

Table 2-5 shows lubrication schemes employed in conjunction with solid steel plate platens. Krishnaswamy⁽⁶⁵⁾ was the only author to study the effects of different lubrication schemes on compressive strength in a true triaxial test where all three stress components were varied independently. His results are summarized in Table 2-6 and it can be seen that as the amount of lubrication increased the maximum compressive stress at failure (σ_3/f'_c) decreased, thus suggesting that unlubricated load platens gave artificially high triaxial failure stresses.

2.4.4 Triaxial Test Procedures

While most authors provided details on specimen composition and curing, almost no description was given of testing procedures. In particular only Gerstle et al.,⁽⁶⁷⁾ Kotsovos⁽⁷⁵⁾ and Chinn and Zimmerman⁽⁶⁵⁾ noted specimen loading rate which varied over the range 0.2 ksi/min to 5 ksi/min. In addition, Green and Swanson⁽⁷⁶⁾ performed their experiments at a constant strain rate of 10^{-4} /sec. Specimen loading path in principal stress space also differed considerably between authors. Palaniswamy and Shah⁽⁶⁴⁾ initially loaded their cylinders hydrostatically then, holding the

Table 2-5
Lubrication schemes for reducing friction at the
specimen platen interface

<u>Author</u>	<u>Reference</u>	<u>Lubricating Scheme</u>
Gerstle <u>et al.</u>	(67)	4 polyethylene sheets with molybdenum sulphide grease
Gerstle <u>et al.</u>	(67)	2 polyethylene sheets 0.002 in. thick with axle grease
Gerstle <u>et al.</u>	(67)	1 layer of grease
Krishnaswamy	(63)	1 polyethylene sheet (0.006 in.) or
Krishnaswamy	(63)	2 polyethylene sheets with grease
Launay and Gachon	(69)	4 aluminum sheets (0.4 m) with talc
Mills and Zimmerman	(70)	2 sheets of 0.003 in. teflon with axle grease
Mills and Zimmerman	(70)	2 sheets of 0.004 in. polyethylene with grease.

Table 2-6
Effect of lubrication scheme on true triaxial
failure stress, Krishnaswamy⁽⁶³⁾

<u>Nonlubricated</u>		<u>1 Layer 0.006 in. Polyethylene</u>		<u>2 Layers 0.006 in. Polyethylene Plus Grease</u>	
$\sigma_2^{(a)}$	σ_3	σ_3	σ_3	σ_2	σ_3
0.25	2.35	0.20	1.79	0.26	1.68
0.5	2.31	0.50	1.85	0.52	1.73
1.0	2.41	1.0	2.00	1.00	1.79
1.0	2.40	1.5	2.05	--	--
--	--	--	--	2.00	1.89

(a) All stresses normalized to f_c , $\sigma_1/f_c = 0.20$.

AD-A166 087

ON THE DEVELOPMENT OF CONSTITUTIVE RELATIONS FOR PLAIN
AND REINFORCED CONCRETE(U) S-CUBED LA JOLLA CA
G A HEGEMIER ET AL 09 APR 82 555-R-82-5495

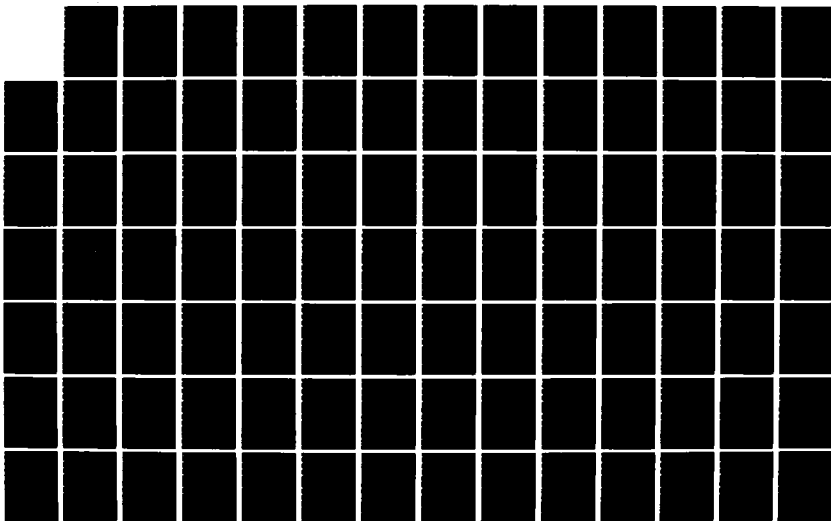
2/4

UNCLASSIFIED

DNA-TR-81-65 DNA001-81-C-0181

F/G 11/2

NL



lateral pressure fixed, increased axial pressure until specimen failure. Krishnaswamy⁽⁶³⁾ loaded his cube specimens in the three principal stress directions, sequentially. Chinn and Zimmerman⁽⁶⁵⁾ subjected cylinders to four different load paths. In their notation Type I loading coincided with that of Palaniswamy and Shah. Type II loading was initially hydrostatic followed by increased radial loading holding the axial load fixed. Type III loading was purely hydrostatic while for Type IV loading axial and radial stresses were increased at a fixed ratio. In the international cooperative research program, Gerstle et al.⁽⁶⁴⁾ first loaded specimens hydrostatically and then followed straight line trajectories in the octahedral shear plane. Finally Mills and Zimmerman⁽⁷⁰⁾ applied an initial hydrostatic load to their cube specimens, then increased two principal stresses to a prescribed level and finally increased one of these two stresses until failure occurred.

There was also a paucity of definitions of what constituted specimen failure perhaps because direct visual examination of the specimen was not possible during tests. Mills and Zimmerman⁽⁷⁰⁾ had little trouble recognizing failure since their specimens explosively disintegrated. Chinn and Zimmerman assumed failure had occurred when the stress in the specimen started to drop.

Dei Poli⁽⁷⁴⁾ in his review of experimental work noted that (i) Shickert and Winkler⁽⁷⁷⁾ assumed failure had occurred when one of the strain components started to experience abnormally large increases, (ii) Bertachhi and Belloti⁽⁷⁸⁾ used, as a failure criterion, a sudden increase in strain in one direction accompanied by a sudden decrease in strain in the other two directions and (iii) Bremer⁽⁷⁹⁾ used a loading criterion and assumed failure when one load component deviated abruptly from that programmed by remaining constant. Most other authors did not describe their definition of specimen failure.

2.4.5 TRIAXIAL TESTING RESULTS

Most triaxial test data concerns the definition of a failure surface under monotonic loading. In metals plasticity the yield surface in three-dimensional principal stress space is an infinitely long circular cylinder whose axis is the hydrostatic pressure line. From the discussion on biaxial stress states it is clear that the failure surface for concrete is not a cylinder because its intersection with a biaxial stress plane is not an ellipse. Alternatively said, concrete failure is pressure dependent. In addition, the intersection of the three-dimensional failure surfaces with planes of constant pressure is not circular. Consequently concrete failure cannot be accurately described in terms of stress invariants I_1 and J_2 alone. Gerstle et al.,⁽⁶⁷⁾ in a study that paralleled the biaxial investigation summarized in Section 2.3.5, reported results for seven laboratories that used the same concrete in all tests. Figure 2-42 shows failure stresses found in a typical 60° sector of the octahedral (i.e. constant hydrostatic stress) plane at a pressure σ_n of 5 ksi. Considerable scatter existed between the various sets of data with unlubricated platen machines giving the highest strengths. However, failure stress on path 1 was consistently farther from the hydrostat ($\sigma_1 = \sigma_2 = \sigma_3 = \sigma_n$) than the failure stress on path 3, where paths 1, 2, 3 were loadings up the hydrostat to $\sigma_n = 5$ ksi followed by loading in the octahedral plane. In the octahedral plane the σ_1 increment on path 1 was compressive while the σ_3 increment on path 3 was tensile.

Launay and Gachon⁽⁶⁹⁾ performed a more extensive study of failure surface shape. Figure 2-43, which gives their results, shows a 60° arc of the failure surface's intersection with various octahedral planes, $\sigma_n = 3\sigma_0\alpha$, where σ_0 was uniaxial compressive strength. The results in Figure 2-42 correspond to $\alpha = 3$ and appear to be comparable. From Figure 2-43 it is seen that as the amount of hydrostatic pressure increased the curves became more circular.

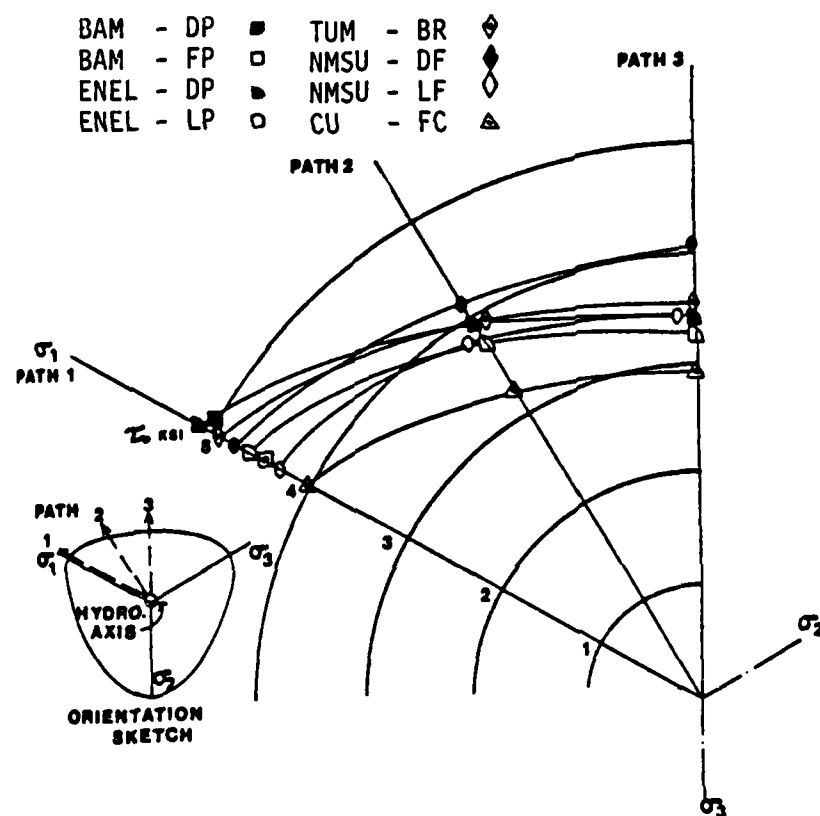


Figure 2-42. Failure stresses on the octahedral plane
 $\sigma_n = 5$ ksi.

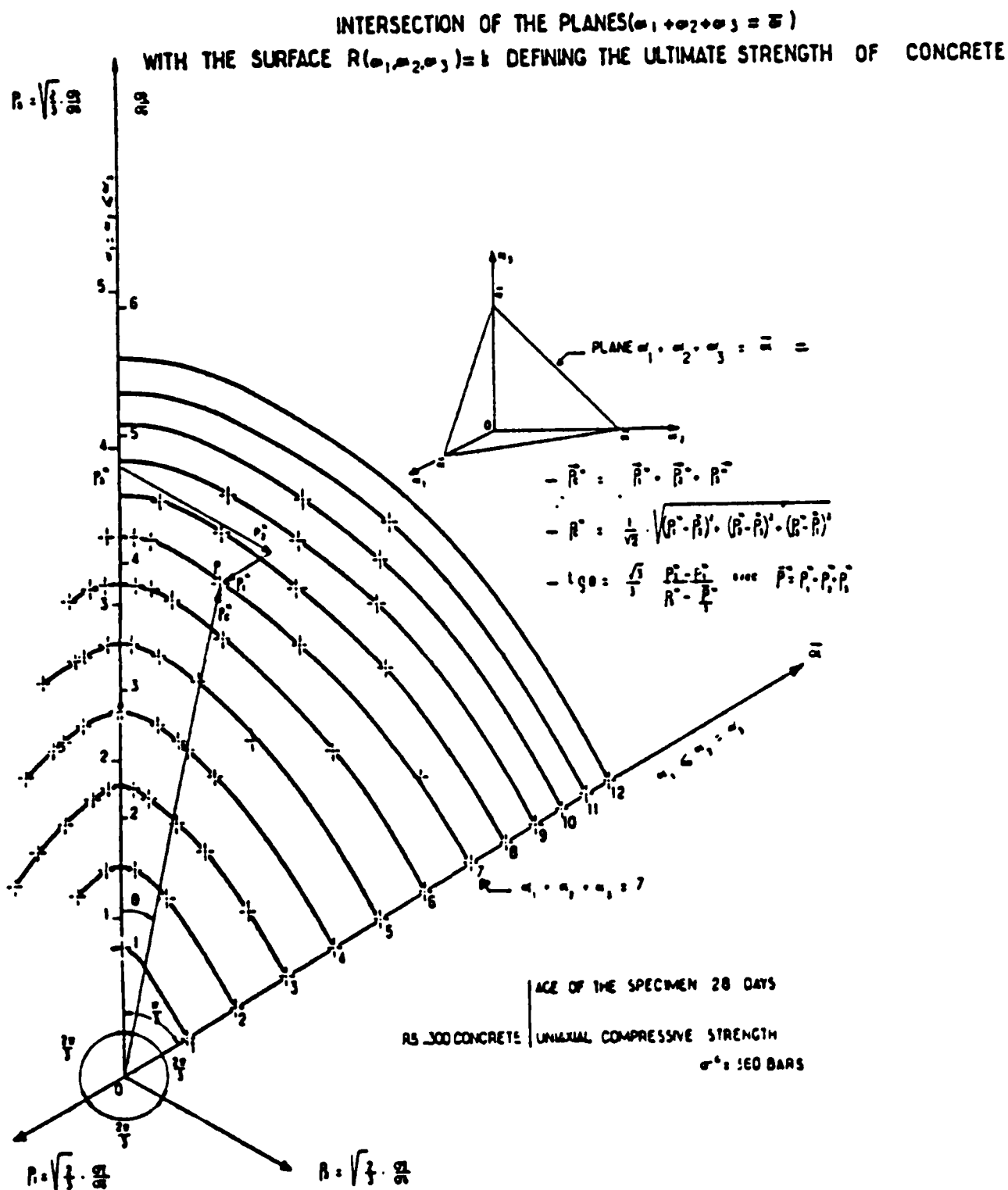


Figure 2-43. Intersection of failure surface with octahedral planes $\sigma_n = 3\sigma_0/3$, σ_0 = uniaxial compressive strength.

Launay and Gachon also plotted, Figure 2-44, the intersection of the failure surface with $\sigma_1 = \sigma_2$, which corresponds to the plane of data for conventional triaxial experiments. The inclined line marked σ_3/σ_0 is the principal stress axis σ_3 normalized to uniaxial axial strength σ_0 and the inclined line 90° anticlockwise from it is the stress trajectory $\sigma_1 = \sigma_2$, $\sigma_3 = 0$. Failure envelope expansion with increasing confining pressure (here parameterized as α) is clearly evident.

Figure 2-45 shows the results obtained by Chinn and Zimmerman⁽⁶⁵⁾. The authors probed the failure surface along several different stress trajectories and for confining pressures up to $20 f_c'$. Their data possessed some scatter particularly at higher pressures but, after allowing for a reversal of axes, the trends are identical to those in Figure 2-44. The results of the above authors are also in agreement with the data collated by Johnson and Lowe,⁽⁶⁸⁾ Figure 2-46, from various sources.

From the preceding five figures a clear definition of failure surface data can evolve. The failure surface is highly pressure dependent in compression, possesses a small tensile stress region which is pressure insensitive and, has noncircular cross-sections on octahedral planes. Finally the intersection of the failure surface with the plane $\sigma_2 = \sigma_3$ is two curved lines that straddle the hydrostat.

As part of the international cooperative research program coordinated by Gerstle,⁽⁶⁷⁾ Schickert and Winkler⁽⁷²⁾ performed a beautifully documented set of true triaxial (and biaxial) compression experiments. Stress-strain plots for every biaxial and triaxial test were separately reported together with average results and 99 percent confidence limit. Also both unlubricated and flexible steel platen designs were investigated. The principal findings and conclusions of the study, in addition to those stated in the previous paragraph are:

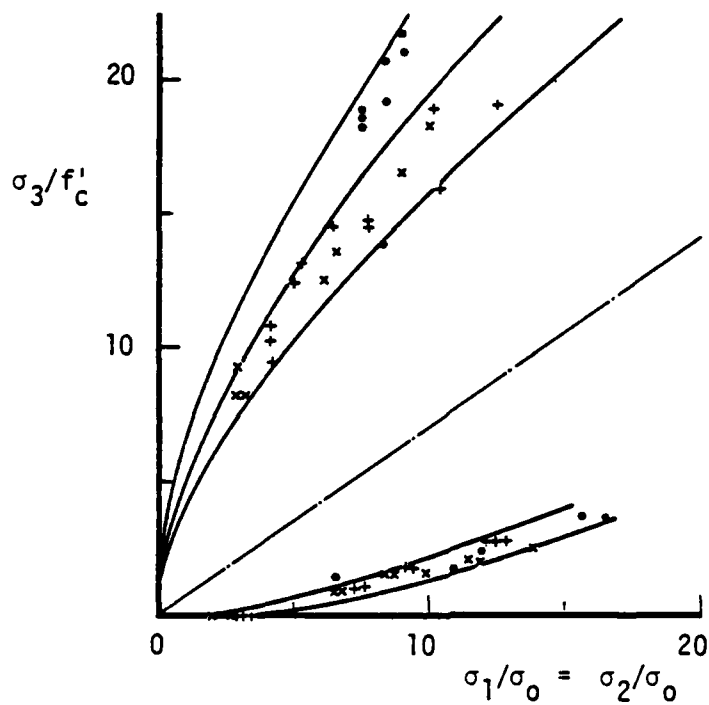


Figure 2-45. Failure stresses obtained by Chinn and Zimmerman^[65] plotted in plane $\sigma_1/\sigma_0 = \sigma_2/\sigma_0$.

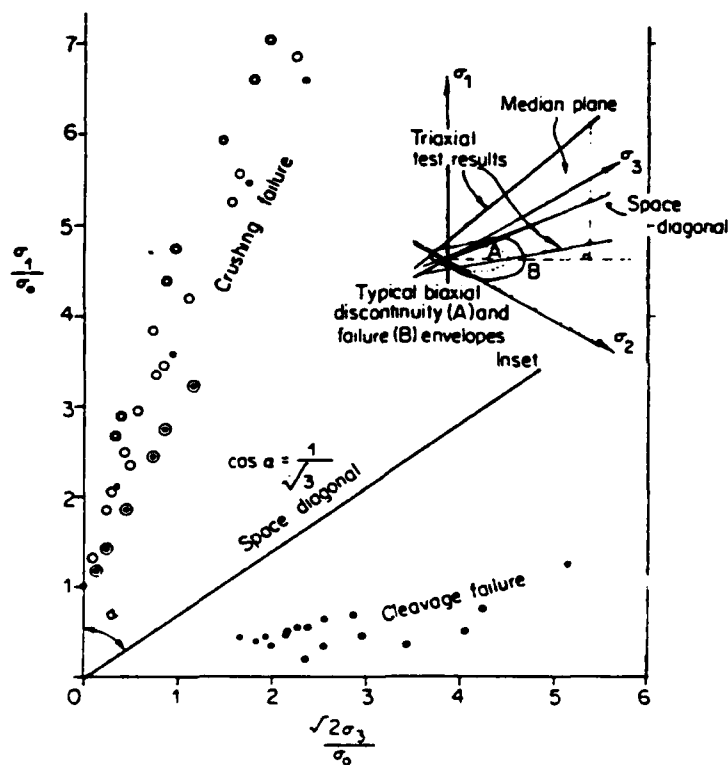


Figure 2-46. Failure stress data from various authors.

- unlubricated platens produce higher strengths than flexible platens
- unlubricated platens produce more scatter in data than flexible platens
- failure always occurs by extension in the direction of minimum principal stress.

Figure 2-47 shows stress-strain data on a 34 N/mm² uniaxial strength concrete. In Figures 2-47(a), and (b) hydrostatic stresses of $0.75 f'_c$ and $1.5 f'_c$ were first applied followed by loading in path 1 on the octahedral plane (i.e., $2\Delta\sigma_2 = 2\Delta\sigma_3 = -\Delta\sigma_1$). The two confining pressures increased σ_1 to $1.8 f'_c$ and $3.2 f'_c$ respectively at failure thus demonstrating the beneficial effect of confining concrete. Also compressive strain ϵ_1 at failure was 3-10 times greater than that in uniaxial tests with most of the strain occurring after departure from the hydrostat. Thus concrete is more ductile in triaxial compression than is predicted by a simple scaling of uniaxial strain at failure by the ratio at failure of triaxial stress to uniaxial stress. When the two cases in Figure 2-47 are compared it is seen that for low confinement, volumetric strain still retained the characteristics of its uniaxial response with a dilatational trend setting in just prior to failure. For the high confinement case no dilatation occurred and at failure all strains were still compressive.

Green and Swanson⁽⁷⁶⁾ briefly studied triaxial cyclic loading using cylindrical specimens of a 6 ksi uniaxial strength concrete. Results for a single test are shown in Figure 2-48, where symbols on the curves were used to indicate corresponding points in the load history. A 2 ksi hydrostatic preload was first applied and then the axial stress was cycled in compression. In Figures 2-48(a) negligible stiffness degradation is evident while some hysteresis in the second cycle is evident. The pressure-volumetric strain response was more complicated with dilatation occurring shortly after reloading to the point of previous unloading. The results in Figure 2-48 were for a low confining pressure and for only two load

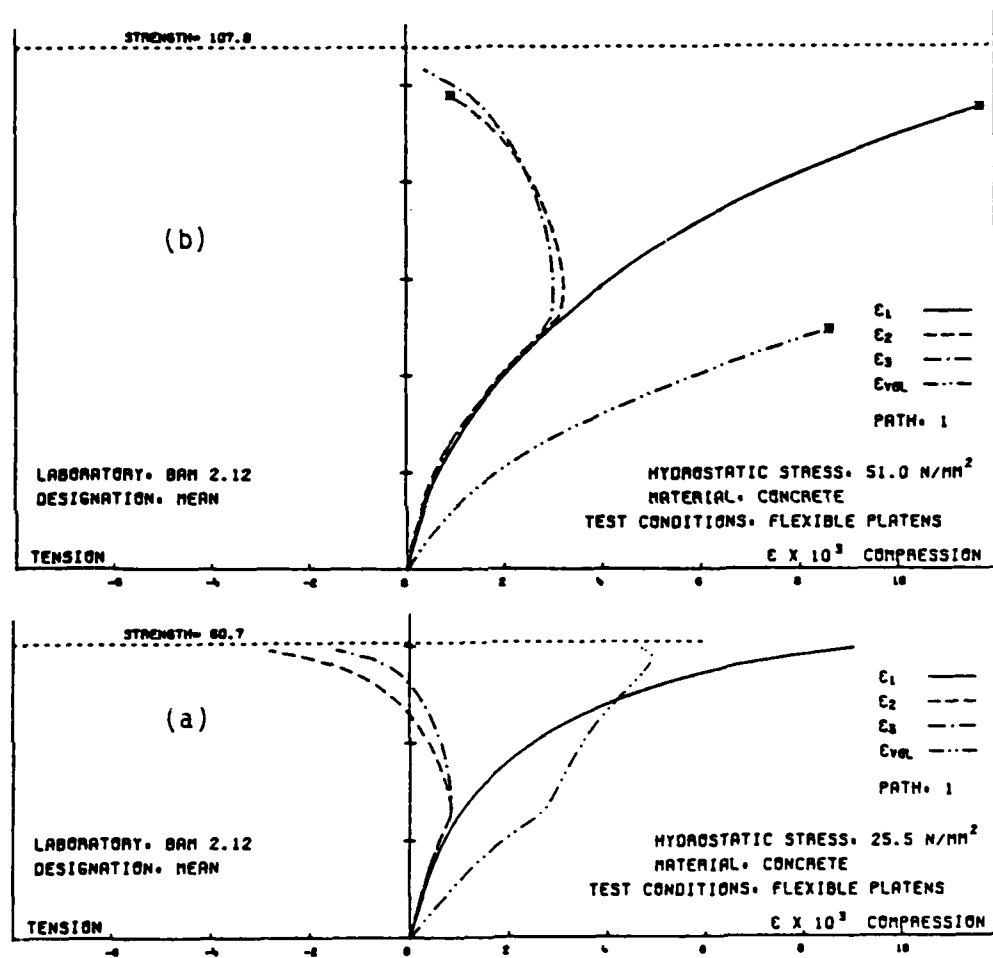


Figure 2-47. Triaxial stress-strain results for same concrete under different levels of hydrostatic prestress.

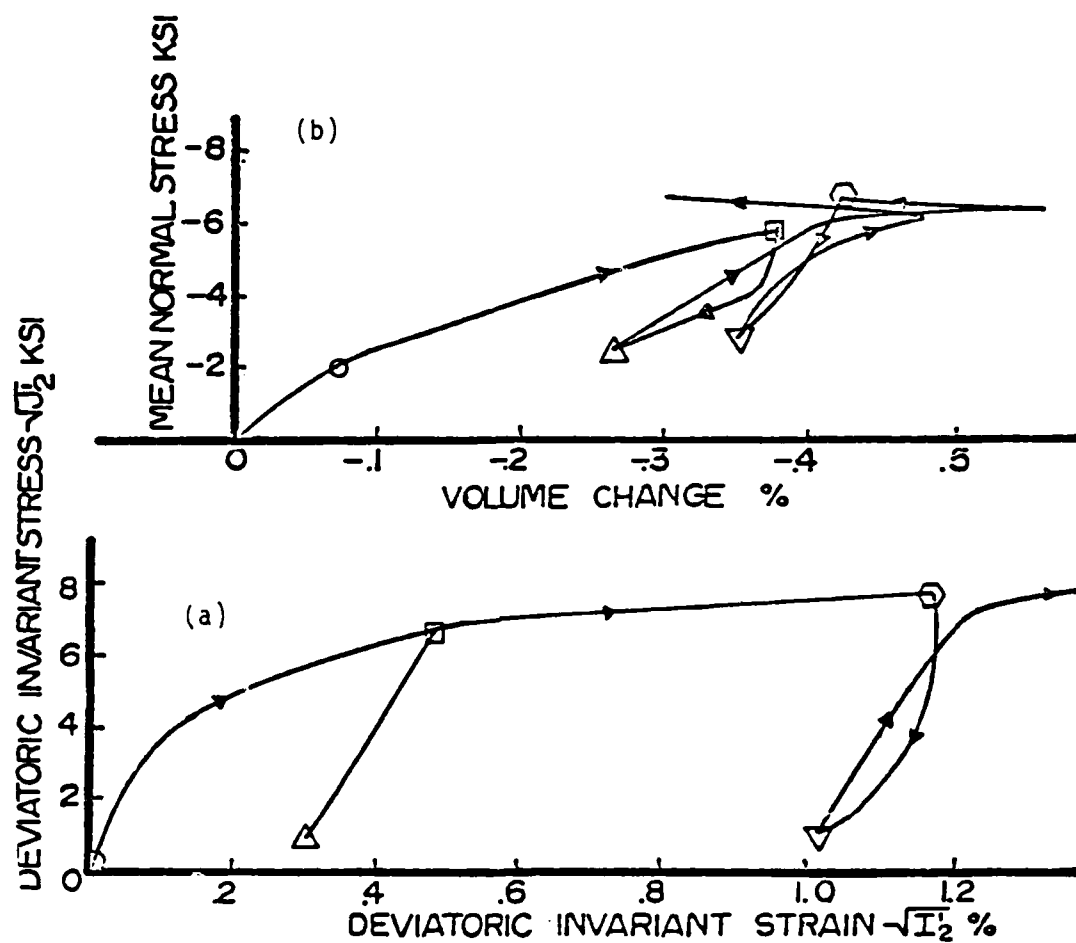


Figure 2-48. Cyclic stress-strain data from a conventional triaxial test.

cycles at or below the concrete monotonic loading strength. Clearly much more data are needed to fully represent concrete triaxial response under cyclic loading.

2.4.6 Outstanding Issues

Experimental data from concrete triaxial tests have mainly covered two facets of concrete response: (a) failure under monotonic loading and (b) stress-strain response under monotonic loading. For triaxial stress states limited or no data are available on the following possible response features:

- post-peak response - strain softening
- microcracking induced stiffness degradation
- microcracking induced anisotropy
- cyclic stress-strain response
- strain rate sensitivity.

Given the multiplicity of adverse load environments that protective facilities must survive, it is important that the existence and relative size of these response features be determined.

From the discussion of uniaxial results it is anticipated that concrete failure will not occur when the stress reaches the failure surface if the concrete is properly confined. Rather, the stresses will subsequently decrease as the strains increase and neighboring parts of a structure will be exposed to increased loads. If this is the case then constitutive theories that assume failure has occurred when the stress reaches the failure surface will be overly conservative while theories that maintain the stress at the value attained on the failure surface will be unconservative.

Qualitatively concrete response can be described in terms of microcracking. In the discussion on uniaxial and multiaxial experiments it was shown that microcracks propagate perpendicular to the direction of maximum deviatoric tensile stress. It is reasonable to

assume that microcracking in a particular direction will have two consequences. First stiffness perpendicular to the cracking will be decreased while that parallel to the cracks will not. Secondly the directionally dependent stiffness will imply that concrete has become anisotropic both in its incremental stress-strain law and in its failure strength. Currently the authors are aware of no published data on microcracking induced anisotropy.

The cyclic stress-strain response data obtained by Green and Swanson pointed to a complicated behavior even for the limited case of conventional triaxial experiments. The consequences of such deformation patterns in a protective structure are completely unknown. Triaxial strain rate sensitivity could be important and, in light of the demonstrated sensitivity of uniaxial data to strain rates, should be explored.

A final item -- relative directions of the stress and the inelastic strain increments -- should be added to the list. Such data would aid in constitutive model development. However, no data exist to suggest that constitutive model prediction errors are the result of incorrectly assuming an "associated flow rule."

SECTION 3

EXPERIMENTAL DATA BASE: STEEL-CONCRETE INTERACTION:

3.1 REMARKS

The least understood aspect of reinforced concrete response is the interaction (load transfer) that occurs between the plain concrete and the embedded reinforcing steel bars - rebars. Much time and money have been spent testing reinforced concrete structural elements. All such experiments can hope to achieve is a statement on how the particular element being tested responds to the loads being applied. Nothing can be concluded concerning steel-to-concrete load transfer. This is because in such experiments there is a multiplicity of active phenomena, few of which have been controlled enough to determine their individual contributions to steel-concrete interaction. Additionally, nonlinearity of reinforced concrete response precludes either scaling of results to predict stress and deformation of larger but similar structures or the prediction of the response of related structures. To understand steel-concrete interaction, specially designed and carefully controlled and instrumented tests must be performed. What follows is a discussion of such tests and the results obtained therefrom.

As long as a reinforced concrete structure has experienced no cracking there is negligible interaction between the steel and concrete. In this case satisfactory stress-strain equations for reinforced concrete can be obtained by modeling the steel and concrete as a homogeneous continuum whose material properties are a weighted volume average of those of steel and concrete. After cracking has occurred, three new load transfer mechanisms are active that are associated with:

- Steel-concrete bond
- Aggregate interlock
- Dowel action.

Thus, any useful reinforced concrete theory must adequately simulate these mechanisms. The steel-concrete bond transfers rebar tensile

stresses into the surrounding concrete. For modeling purposes this transfer mechanism is idealized as an interfacial shear or 'bond' stress, Figure 3-1, that is governed by a bond stress-bond slip law. Bond slip is the relative motion of a rebar and its surrounding concrete. Aggregate interlock or "interface shear transfer" is the locking up of aggregate asperities on opposite faces of a crack so as to provide a shear stress transfer mechanism across a crack face, Figure 3-2. Finally, dowel action is the resistance provided by reinforcing bars that span a crack, to sliding of the crack faces relative to each other, Figure 3-3. In the present research program emphasis was placed upon the steel-concrete bond. Further work is needed to understand the roles played by aggregate interlock and dowel action in transferring load from one area of a degraded reinforced concrete structure to another.

3.2 MECHANICS OF THE STEEL-CONCRETE BOND

3.2.1 Steel-Concrete Bond Mechanisms

The processes that contribute to the steel-concrete bond have been studied by Bresler and Bertero,⁽⁸²⁾ Dorr,⁽⁸³⁾ Edwards and Yannopoulos,⁽⁸⁴⁾ Ferguson et al.,⁽⁸⁵⁾ Lutz and Gergely⁽⁸⁶⁾ and it is generally accepted that there are three contributions:

- adhesion
- friction
- mechanical interlock.

Adhesion is the physical bonding of the concrete to the steel and is the result of chemical processes that occur when a reinforced concrete structure is curing. Friction is present because during the curing process the concrete shrinks around the reinforcing steel leaving the steel-concrete interface in a state of residual compressive stress. Finally, mechanical interlock arises from the lugs on the surface of a deformed rebar interlocking with the surrounding concrete. Of course, for plain rebars mechanical interlock is not present.

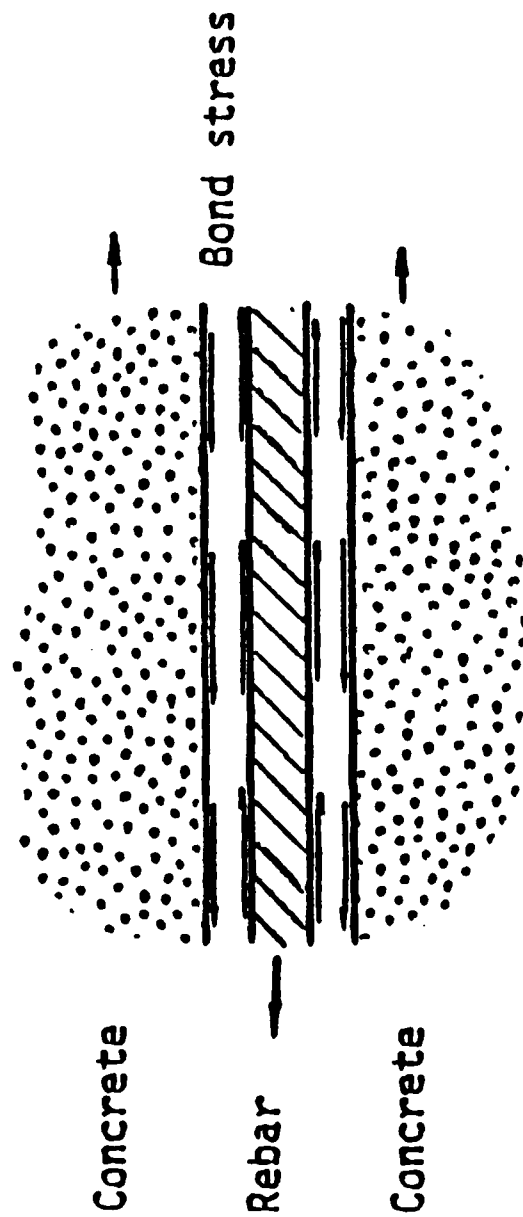


Figure 3-1. Bond stress - the interfacial shear stress between rebar and concrete.

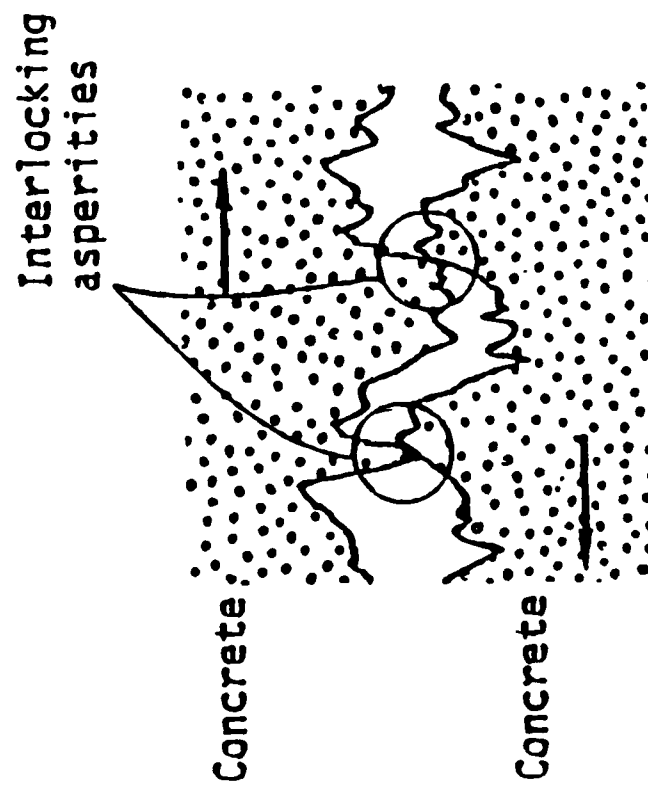


Figure 3-2. Aggregate interlock - the transfer of shear load across a crack by aggregate contact.

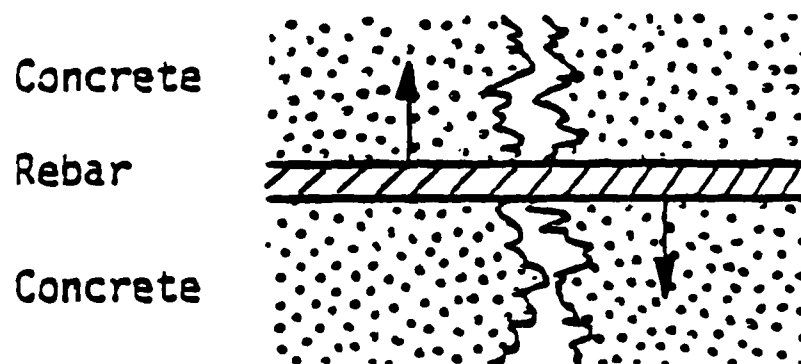


Figure 3-3. Dowel action - the transfer of shear load across a concrete crack by a rebar.

Of the three contributions, mechanical interlock is the most important contributing approximately half the strength of the steel-concrete bond. Lutz and Gergely⁽⁸⁶⁾ examined bond stress in detail using finite element analysis. Their principal conclusions were:

- Adhesive bond has a strength of 50-100 psi and is destroyed at low levels of bond slip.
- Compressive stresses arising from concrete shrinkage are approximately 100 psi.
- Shrinkage stresses are sufficient to keep steel and concrete in contact during the slip process, i.e., they dominate any tendency for the steel and concrete to separate because of a Poisson's ratio differential between steel and concrete.

3.2.2 Bond Failure Mechanism

Depending on the geometry, bar type, rebar configuration and stress history a reinforced concrete structure can exhibit a variety of failure modes. Here discussion is limited to experiments on a single rebar in which case the observed failure types are:

- pullout
- transverse cracking
- longitudinal cracking
- rebar yielding or fracture.

Edwards and Yannopoulos⁽⁸³⁾ and Mains⁽⁸⁷⁾ found that plain bars pulled out without visible surface cracking. Mathy and Watstein⁽⁸⁸⁾ noted that a similar pullout occurred when deformed bars were not embedded far enough into the concrete. Ferguson *et al.*,⁽⁸⁵⁾ and Bresler and Bertero⁽⁸²⁾ found transverse cracking occurred when the rebar had insufficient concrete cover. In this case small radial cracks initiated close to the rebar and propagated outwards in a plane transverse to the rebar. Goto⁽⁸⁹⁾ tracked growth of such cracks using a dyeing technique and theoretical evidence for transverse cracks was given by Mirza and Houde.⁽⁹⁰⁾

Transverse cracking failure results when tensile stresses in the concrete exceed concrete tensile strength and can be inhibited by using larger covers.

Longitudinal cracking occurs because large hoop stresses are induced in the concrete by the rebar lugs that push the concrete outwards as slip occurs. Untrauer and Henry⁽⁹¹⁾ and Tepfers⁽⁹²⁾ showed that longitudinal cracking occurs in beams and simple geometries under multiaxial loading. Many researchers delayed splitting by surrounding the rebar with stirrups (Mains,⁽⁸⁷⁾ Kemp and Wilhelm⁽⁹³⁾) or wire cages (Ferguson et al.,⁽⁹⁴⁾ Mathey and Watstein⁽⁸⁸⁾)). Presently, no criterion exists for when longitudinal rather than transverse cracking should occur although Lutz and Gergely⁽⁸⁶⁾ suggested a necessary condition is that the bond stress be greater than the rebar stress.

Rebar yielding and fracture occur when rebar embedment length is sufficient to preclude pullout, and cover is sufficient to suppress cracking.

3.2.3 Experimental Procedures for Bond Stress-Bond Slip Determination

Specimens used to determine bond stress and bond slip information have been of the following form:

- pullout
- tension
- structural element.

The pullout specimen was the first to be used and is shown schematically in Figure 3-4. One end of the rebar is embedded in a block of concrete and the tensile load that is applied to the rebar free end is equilibrated by a fixed steel restraining plate. Pullout specimens are either 'concentric' or 'eccentric' depending on whether the rebar passes through the center of gravity of the concrete cross section. Concentric specimens have a circular, rectangular or square cross section, (Edwards and Yannopoulos,⁽⁸⁴⁾ ⁽⁷⁵⁾, Mathey and Watstein,⁽⁸⁸⁾ Tepfers⁽⁹²⁾ and Untrauer and

Henry⁽⁹¹⁾). Eccentric specimens can have any cross section (Ferguson et al.,⁽⁹⁴⁾ Mains,⁽⁸⁷⁾ Perry and Jundi,⁽⁹⁶⁾ Perry and Thompson⁽⁹⁷⁾) and have been used to more closely replicate conditions found on the tension side of a reinforced concrete beam.

The principal shortcoming of the pullout test (Ferguson et al.,⁽⁹⁴⁾) is that close to the restraining plate the concrete is in an unknown state of compression and lateral constraint, which has an indeterminate effect on bond strength. For this reason more recent investigators (Bresler and Bertero,⁽⁸²⁾ Dorr,⁽⁸³⁾ Goto,⁽⁸⁹⁾ Ismail and Jirsa,⁽⁹⁸⁾ Mirza and Houde⁽⁹⁰⁾) used the tension specimen shown diagrammatically in Figure 3-5. Here both ends of the rebar are in tension and the only concrete stresses are fabrication-induced shrinkage stresses, stresses transferred from the rebar by the bond and stresses arising from known lateral loads (Dorr,⁽⁸³⁾ Untrauer and Henry⁽⁹¹⁾).

The least commonly used specimens for bond stress study are structural elements such as the beam-like specimen employed by Kemp and Wilhelm⁽⁹³⁾ and the column-like specimen of Bertero et al.,⁽⁹⁹⁾. Structural elements are of special interest only, since the stress state around the rebar is extremely complex. Typically, the experimental objective with such a specimen was to understand structural element response rather than gain fundamental insight into steel-concrete bond response.

Originally the only variables that could be measured in pullout, tension and structural element tests were the imposed rebar load and the end slips, which are the displacement differentials between the rebar and concrete at the ends of the concrete cover. Consequently, nothing could be concluded about bond stress and bond slip distributions along the rebar and how these varied with bar end load, although it was known that experimental results were inconsistent with an assumption that bond stress and slip were uniform along the bar embedment length. Starting with Mains⁽⁸⁷⁾ this situation was partially remedied through internally strain-gaged rebars constructed by sectioning a rebar lengthwise, milling out an

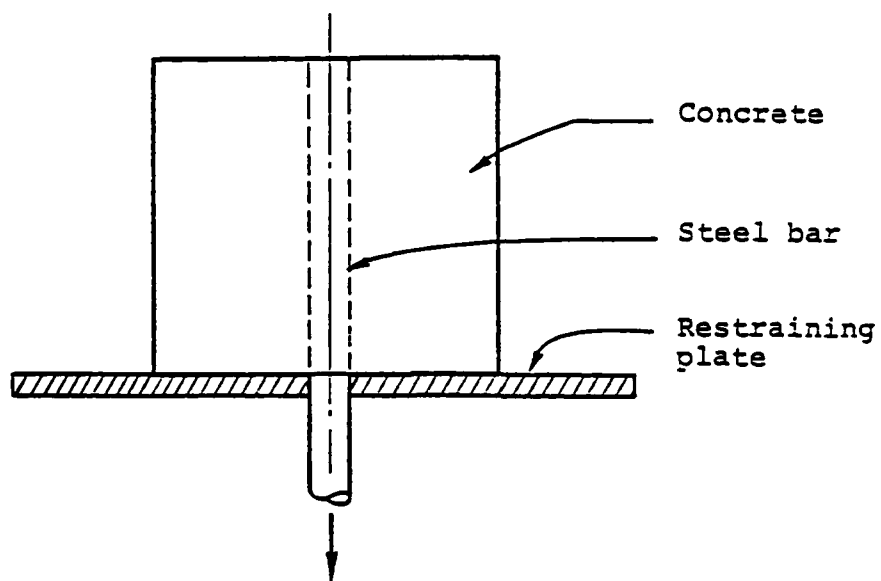


Figure 3-4. Pull out test specimen.

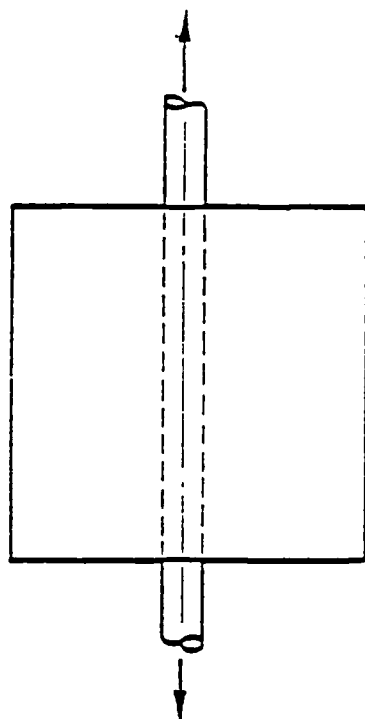


Figure 3-5. Tension test specimen.

internal channel, placing strain gages in the channel, and welding the bar halves together again. With an internally strain-gaged rebar the strain distribution in the rebar was measured and the bond stress distribution compatible with it computed as follows. From Figure 3-6 if $\epsilon(x)$ is the local bar tensile strain then by equilibrium

$$\sigma = E\epsilon \quad , \quad \tau_b = - \frac{A}{p} \frac{d\sigma}{dx} = - \frac{AE}{p} \frac{d\epsilon}{dx} \quad (3-1)$$

where σ and τ_b are the stresses in the bar and bond, E is the bar Young's modulus, and A and p are the average bar cross section area and perimeter respectively. However, currently there does not exist any method of monitoring the slip between steel and concrete away from the ends of the concrete cover.

3.2.4 Parameters Influencing Bond Slip and Attainable Bond Stress

Some of the principal reasons why so little progress has been made in developing constitutive models for the interaction between a rebar and surrounding concrete are the number of independent variables involved, the different measures used to report experimental results and the great scatter that exists in data from ostensibly identical experiments. Experimental variables at the disposal of a researcher include at least those shown in Table 3-1. Additionally, there are non-quantifiable variables such as:

- casting orientation
- bar position
- curing history.

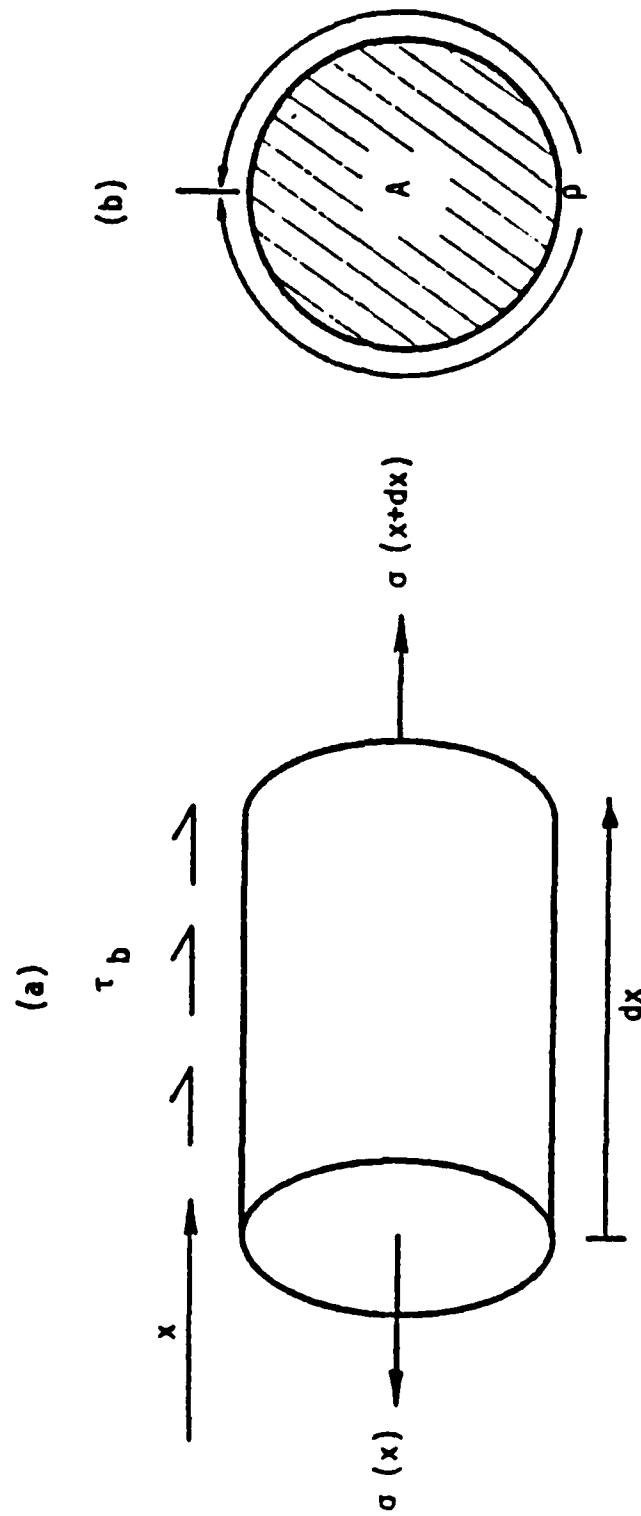


Figure 3-6. (a) Differential bar element, showing uniaxial bar stress σ equilibrated by bond shear stress τ_b . (b) Definition of A and p as bar cross-section area and perimeter.

Table 3-1

Variables in the design of steel-concrete interaction experiment

- Load History
 - Stress Level
 - Monotonic or Cyclic
 - Static or Dynamic
 - Uniaxial or Multiaxial
- Specimen Design
 - Pullout
 - Tension
 - Structural Element
- Rebar Geometry
 - Diameter
 - Surface Finish
 - Embedment Length
- Rebar Material
 - Yield Stress
- Concrete Geometry
 - Cover Dimensions
 - Cross Sectional Shape
 - Aggregate Size
- Concrete Properties
 - f'_c
- Auxiliary Reinforcement
 - Stirrups
 - Wire Cages

Some progress has been made in assessing sensitivity of bond strength and slip to the 15 or so independent variables; the load

parameters will be discussed later and the specimen design has been discussed in the previous section.

Ferguson et al.,⁽⁹⁴⁾ Figure 3-7*, noted that for a constant average bond stress, τ_{av} , end slip increases almost linearly with rebar diameter. Since

$$\tau_{av} = \frac{P}{2\pi dL} \quad (3-2)$$

where P, d, L are bar end load, diameter and embedment length respectively, it is impossible to transform this result into a statement on how τ_{av} varies with d. It is reasonable, however, to expect some sensitivity since rebar diameter influences manufacturing-induced residual shrinkage stresses which in turn control frictional contributions to bond stiffness.

It is demonstrably evident that a bond stress/bond slip constitutive relationship depends on rebar surface conditions. Mains observed that plain bars have half the resistance to bar pullout and/or bond failure as deformed bars while Edwards and Yannopoulos found plain bar bond strength to be 35-50 percent of that of deformed bars. Further Goto,⁽⁸⁹⁾ using three different lug designs, showed that results are also sensitive to lug design.

Embedment length is another parameter with an obvious effect of bond strength. Here, for a pullout test, embedment is defined as the length of rebar covered by concrete and for a tension test it is half the length. Embedment also influences the bond stress distribution and the test specimen failure load, with short embedments resulting in pullout and long embedments producing concrete cracking failures or bar yielding.

*In Figure 3-7 compare solid curves as a group and dashed curves as a group.

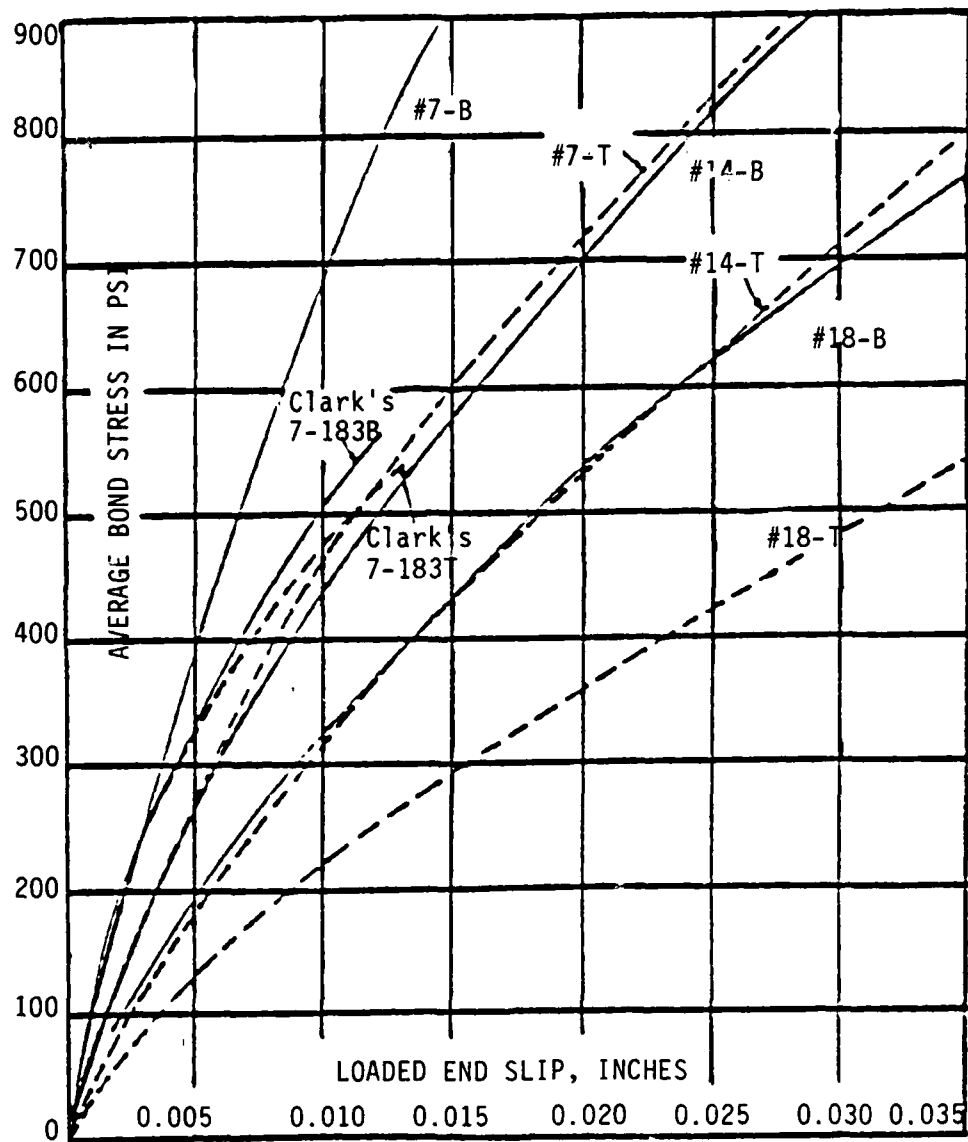


Figure 3-7. Average bond stress versus loaded end slip.

No research has been done on bond strength and bond stress distribution sensitivity to rebar material properties. Rebar Young's modulus and Poisson's ratio vary little from bar to bar, so the only remaining variable is rebar yield stress which can control specimen failure mode in that test specimens with low strength bars might fail in bar yield/fracture, whereas with high strength bars, they might fail by bar pullout.

Concrete cover is a very important parameter in determining test specimen failure mode and load, and is defined to be the minimum distance perpendicular from the rebar to a concrete free surface. Edwards and Yannopoulos⁽⁸⁴⁾ found that by increasing cover from 1.4 to 2.0 bar diameters, specimen pullout strength increased 20 percent. They also noted that increased cover also increased shrinkage stresses on the rebar and the ability of the cover to resist longitudinal and transverse cracking. A similar observation was made by Ferguson et al.⁽⁹⁴⁾ Tepfers⁽⁹²⁾ found that for six different covers the bar load necessary to induce the first surface crack increased monotonically with bar cover.

Using concrete prisms with a square cross section Mirza and Houde⁽⁹⁰⁾ showed that cover controlled the distance between transverse cracks in a specimen, with smaller covers producing shorter inter-crack distances. They also noted that

- bar end slip increases with bar cover (Figure 3-8)
- restraint on the rebar increases with bar cover (Table 3-2)

These statements appear contradictory but are easily reconciled. First, bar end slip was measured at the ends of tension specimens with the same length of concrete cover. Specimens with smaller cover experienced transverse cracking, and slip occurred at these crack locations but was not taken into account. Thus the smaller covers tended to move with the rebars while the larger covers experienced little or no cracking and remained more monolithic. To explain the second statement note that for each cover size, bar slip was computed using rebar lengths equal to the intercrack distance for that cover.

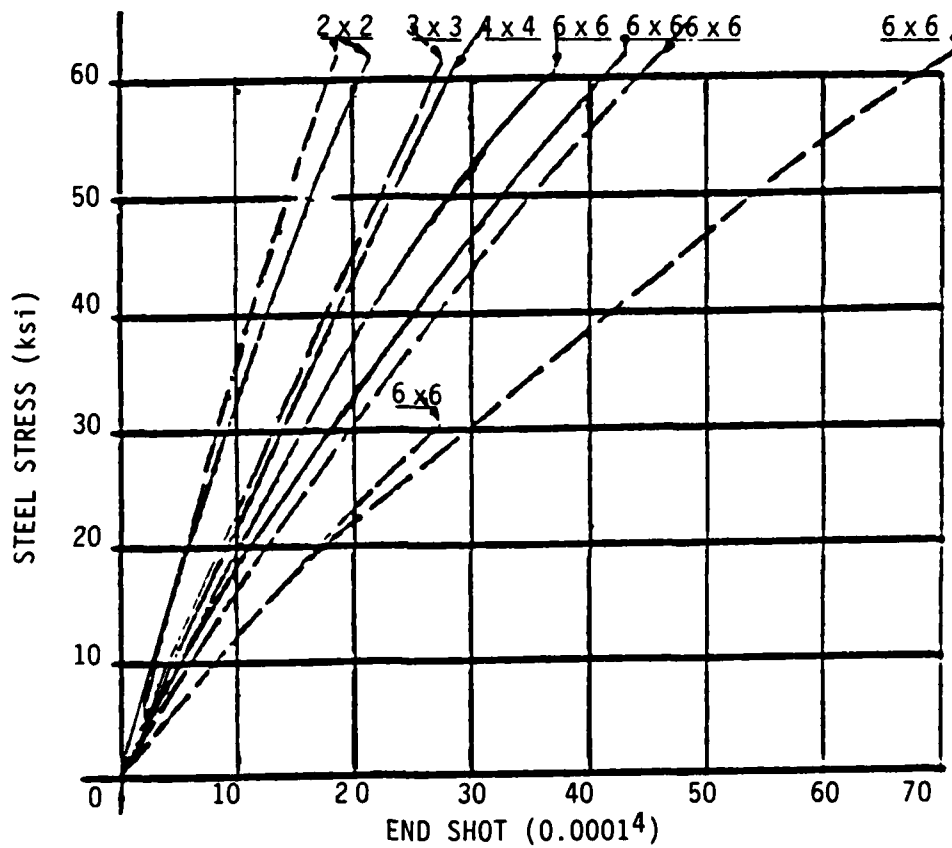


Figure 3-8. Bar end load as a function of end slip for different covers and concrete strengths ---- 3000 psi, _____ 6000 psi.

The effect of aggregate size and shape on bond strength and distribution has never been investigated. Its possible importance would arise from any influence aggregate surface asperities have on the quality of the mechanical interlock between aggregate and rebar lugs.

Table 3-2

Restraint on rebar slip increases with cover

		(a)	(b)	Inter-crack	
Specimen	A_{c2}	Slip	Elongation	Restraint	Distance
Size	(in. ²)	(10 ⁻⁴ in.)	(10 ⁻⁴ in.)	(10 ⁻⁴ in.)	(in.)
2 x 2	4	16.5	17.6	0.9	1.0
4 x 4	16	23.0	44.0	21.0	2.5
6 x 6	36	33.0	70.5	37.5	4.0
8 x 8	64	23.4	70.5	57.1	4.0

(a) Measured at 50 ksi bar end stress

(b) Computed with bar length equal inter-crack distance and with 50 ksi bar stress, $E = 28.4 \times 10^6$ psi.

The most important plain concrete property is its simple compression strength f'_c . Untrauer and Henry⁽⁹¹⁾ in a series of pullout tests found that average bond strength τ_{av} was proportional to f'_c , a result in agreement with the findings of Ferguson et al.⁽⁹⁴⁾ Similar trends were reported by Perry and Jundi.⁽⁹⁶⁾ Perry and Thompson⁽⁹⁷⁾ found that the bond stress distribution was also sensitive to f'_c ; this will be discussed further in the next section. Finally, Mirza and Houde⁽⁹⁰⁾ believed that bond strength is in fact insensitive to concrete strength; however, it is possible that the large scatter in their results precluded observation of a definite trend.

Other variables that influence attainable bond stress levels are less understood. Mains,⁽⁸⁷⁾ Mathey and Watstein,⁽⁸⁸⁾ Bertero et al.,⁽⁹⁹⁾ used stirrups and wire cages in their

specimens to increase resistance to longitudinal splitting. The effect of these added reinforcements was to impose additional radial constraints on the rebar and thus affect both the frictional and mechanical interlock contributions to bond strength. However, no attempt has been made to study this effect in detail.

Finally, the fabrication process itself introduces significant variations in bond strength. In particular, when concrete for eccentric pull specimens is cast with the rebar horizontal, attainable bond strength is sensitive to whether the rebar is towards the top or bottom of the form. Ferguson et al.,^(85,94) noted that because water and entrapped air tend to collect underneath top-cast bars such specimens have up to a 20 percent weaker bond strength than bottom-cast bars. Similarly, when pullout specimens were cast with short covers and with the rebar vertical, Edwards and Yannopoulos⁽⁸⁴⁾ observed that the bond was weaker when the rebar was pulled downwards than when pulled upwards and the difference was attributed to water and pores beneath the rebar lugs.

Not all the variables listed in Table 3-1 would be present in a constitutive theory; load history parameters obviously would be while test specimen type would not be. The theory would relate bond stress to bond slip at each point along a rebar and would be applied to individual rebar-concrete mix combinations. A general theory that has lug design described explicitly through a set of parameters is not anticipated. Instead, specimen tests would have to use the actual rebar type to which the theory would be applied. Rebar embedment length would not be a constitutive parameter; rather its effect would be predicted by the theory. Rebar yield would be a parameter in the theory. Of the concrete geometry listed in Table 3-6, only cover dimensions might be in a constitutive theory, and then, only if the prestressing effect caused by shrinkage during curing could not be accounted for analytically. Concrete compressive strength would be a constitutive variable. Approaches for accommodating stirrups and wire cages into a constitutive theory are not known at present and, of course, the theory would not account for fabrication-induced anomalies in bond strength and stiffness.

3.2.5 Bond Stress Distribution

The measurement of bond stress along an embedded rebar can only be achieved by indirect means through computing the slope of the curve of steel strain versus distance along the rebar. Dörr⁽⁸³⁾ noted that since bond stress is essentially the spatial derivative of a measured quantity, its value is subject to more scatter than bar load, bar end slip and bar strain. Additional scatter is introduced through unevenness in bond arising from curing variations and differences in bar surface conditions. However, general trends are clear. Figure 3-9 is typical of the results obtained and shows how the bond stress distribution varies along a rebar in a pullout test for three different levels of bar end load. For low levels of bar load most of the bond stress is at the loaded end of the bar. As the load increases the maximum bond stress increases and occurs farther along the rebar, also complete debonding occurs at the loaded end. Similar trends can be seen in the work of Mains,⁽⁸⁷⁾ Figure 3-10.

From Figure 3-9 it is clear that maximum local bond stress is a function of both external bar load and, less expectedly, distance from the loaded end of the specimen. This latter observation has been made by several authors; Bertero et al.,⁽⁹⁹⁾ Mains,⁽⁸⁷⁾ Nilson⁽¹⁰⁰⁾ and Perry and Thompson.⁽⁹⁷⁾ There are at least two possible reasons for dependence on distance along the rebar:

- Near the loaded end of the specimen there is not so much constraint from the concrete as would occur deep inside the specimen.
- During curing, water and air pores might have collected around lugs near the specimen ends weakening the concrete.

Edwards and Yannopoulos⁽⁸⁴⁾ contend that maximum bond stress does not vary with distance along the rebar. However, these authors intentionally set out to achieve a uniform bond distribution along their rebar by using a short embedment length. The dependence of maximum bond stress on cover length has an important consequence for

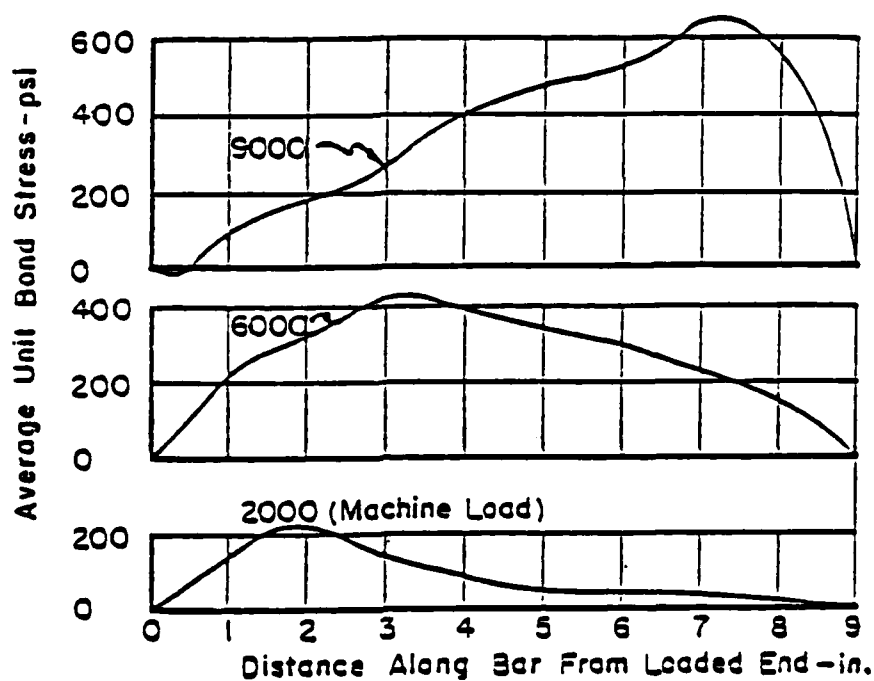


Figure 3-9. Migration of bond stress distribution and increase in maximum bond stress with rebar end load.

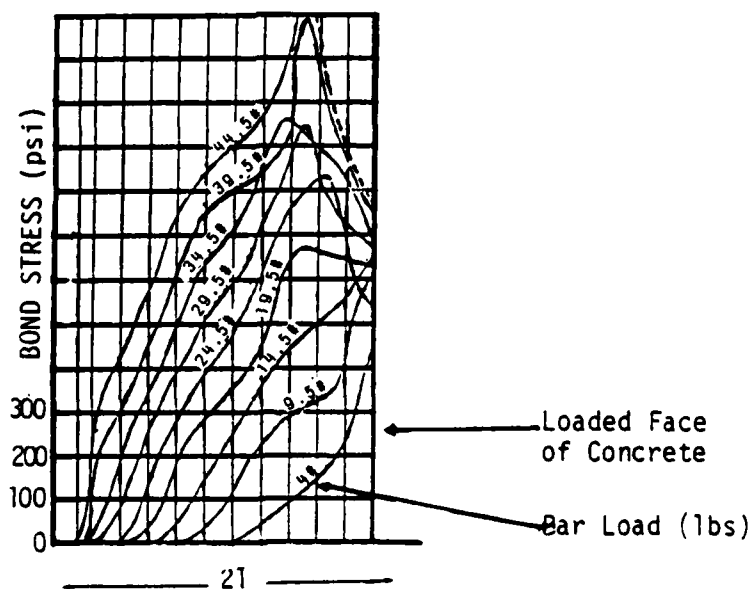


Figure 3-10. Migration of bond stress distribution and increase in maximum bond stress with rebar end load.

specimen design. If a short embedment length is used, a lower maximum bond stress will be measured than would be achieved in an actual structure. Thus to obtain results of practical importance, either a sufficiently long embedment length must be used or additional concrete must be added to the ends of the specimen, as was done by Dörr,⁽⁸³⁾ Figure 3-11, to achieve a high level of constraint about the rebar at the loaded end.

So far the discussion has been limited to rebars under tensile stress. When the rebar is in compression locally high levels of bond stress are achieved where the rebar enters the concrete (Bertero et al.⁽⁹⁹⁾).

3.2.6 Attainable levels of Bond Stress

In this section are gathered together a selection of the values obtained for maximum bond stress under monotonic load. Effects of cyclic loading and lateral constraint will be assessed in the following sections. Because of the large number of experimental variables involved, a wide range of bond strength values has been found that is further complicated by the ways bond strength is defined. Authors that do not use internally instrumented rebars have defined bond stress as bar load divided by embedded bar surface area. Obvious draw-backs to such definition are that computed bond stress decreases as embedment length increases, since the bond stress distribution that reacts the bar load is localized; if only a short embedment length is used, low bond stresses are again obtained because of the lack of concrete constraint. The correct way to define bond stress was shown in Section 3.2.3.

For plain bars, typical values of average maximum bond strength τ_{av} are shown in Table 3-3 where it is seen that average

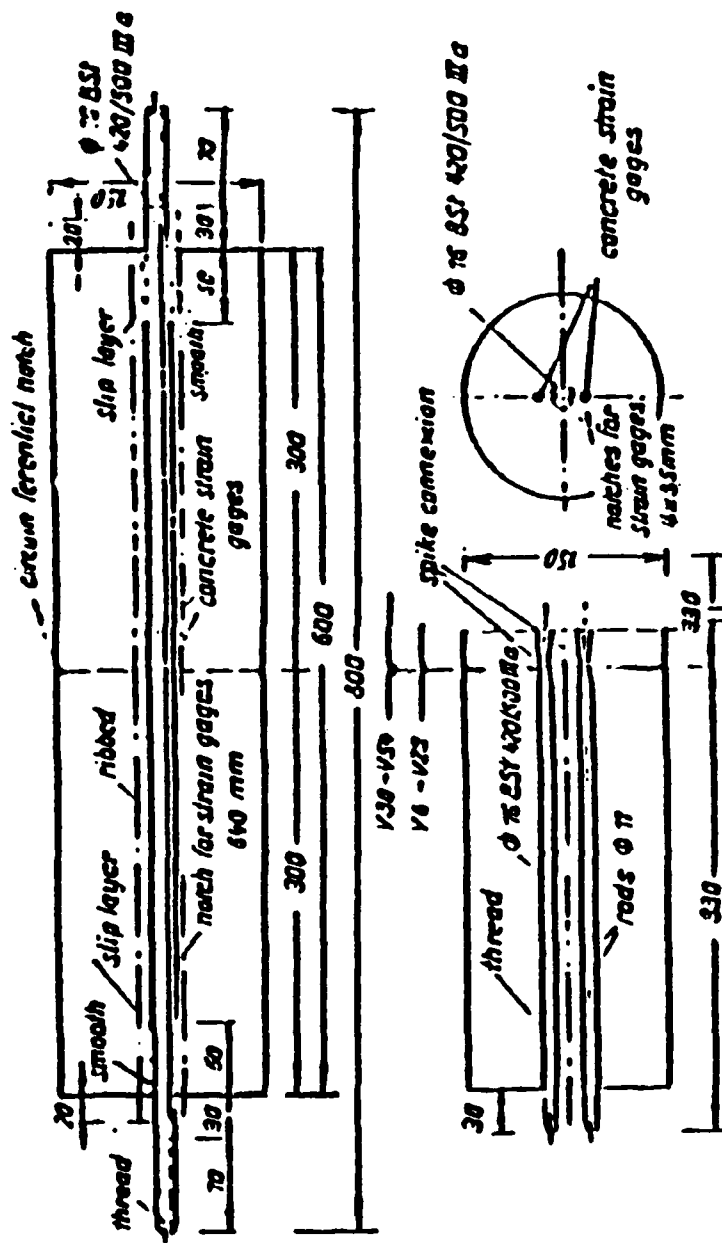


Figure 3-11. Tension specimen showing added concrete at ends of cylinder to increase bar confinement.

Table 3-3
Bond strength for plain bars

Author(s)	Strength (psi)	Cover (in.)	Test Embedment (in.)	Test Type
Edwards and Yannopoulos (84)	522	1.0	1.5	pullout
Edwards and Yannopoulos (84)	638	1.4	1.5	pullout
Mains (87)	460	2.0	21.0	eccentric

bond strength increases with concrete cover and decreases with embedment length. For monotonically loaded deformed bars without any lateral constraint, a sample of measured bond strengths is given in Table 3-4 and it is clear that bond strength is sensitive to experimental details and, therefore, that either development of a theory to predict bond strength or execution of the suite of experiments needed to determine such a theory's constitutive parameters is a non-trivial exercise. It is also clear why no practical theory has been developed to date; the data base for any postulated theory is most certainly inadequate.

3.2.7 Cyclic Loading Effects

In preceding sections bond stress and strength under monotonic loading was examined. In protective structures, concrete can also be expected to experience some cyclic loading under certain circumstances. In this section the effect of cyclic loads on the integrity of the bond between a single rebar and the surrounding concrete is discussed. The presentation is divided into

- rebar loaded in tension only
- rebar loaded in alternating tension and compression.

Bertero et al.,⁽⁹⁹⁾ Bresler and Bertero,⁽⁸²⁾ Edwards and Yannopoulos,⁽⁹⁵⁾ Ismail and Jirsa,⁽⁹⁸⁾ Morita and Kaku,⁽¹⁰¹⁾ and Perry and Jundi⁽⁹⁶⁾ performed experiments to understand how

Table 3-4
Average bond strength for deformed bars

Authors	Bond Strength	Embedded Cover Length	f'_c	Bar Diameter	Test Type
Edwards and Yannopoulos (84)	1116-1363	1.00	1.50	6293	0.63 Pullout
Edwards and Yannopoulos (84)	1407-1682	1.40	1.50	6293	0.63 Pullout
Mirza and Houde (90)	655	5.50	8.00	4800	1.0 Tension
Mirza and Houde (90)	286	2.50	8.00	4120	1.0 Tension
Perry and Jundi (96)	453	0.75	9.00	2200	0.73 Eccentric Pullout
Perry and Jundi (96)	543	0.75	9.00	3360	0.73 Eccentric Pullout
Perry and Jundi (96)	618	0.75	9.00	4030	0.73 Eccentric Pullout
Perry and Jundi (96)	735	0.75	9.00	5060	0.73 Eccentric Pullout
Tepfers (92)	461	0.47	1.97	3567	0.63 Pullout
Tepfers (92)	693	1.22	1.97	3567	0.63 Pullout
Tepfers (92)	734	0.71	3.13	3567	1.00 Pullout
Tepfers (92)	1088	1.89	3.13	3567	1.00 Pullout
Untrauer and Henry (91)	1020-1250	6.00	6.00	4630	1.128 Pullout
Untrauer and Henry (91)	1315-1600	6.00	6.00	4630	0.73 Pullout
Untrauer and Henry (91)	1560	6.00	6.00	6410	1.128 Pullout
Untrauer and Henry (91)	1330	6.00	6.00	6410	0.73 Pullout

cyclic loading in tension degrades the steel-concrete bond. The principal qualitative conclusions were:

- The bond at the loaded end of the rebar slowly degrades and the bond stress distribution migrates inwards away from the loaded end.
- After 10 to 30 cycles at the same maximum, tensile bar stress, maximum bar end slip has not increased significantly.
- The bond stress-bar slip relationship is most sensitive to the previous maximum bar load.
- During the unload portion of a load cycle there is little slip recovery.

These conclusions are illustrated in the following figures. In Figure 3-12, (Perry and Jundi⁽⁹⁶⁾), are shown the bond stress distributions for various load cycles. The test was a pullout and the rebar had a 0.75-inch cover and a 9-inch embedment. In the figure the load was applied at the left and the reason for the high non-zero bond at the right is not understood. However, the slow migration of the bond stress distribution away from the loaded end can be seen.

The non-deleterious effect on bond stress levels of a small number of load repetitions is shown in Figure 3-13 (Ismail and Jirsa⁽⁹⁸⁾) and has also been observed by Bresler and Bertero,⁽⁸²⁾ Dörr⁽⁸²⁾ and by Edwards and Yannopoulos.⁽⁹⁵⁾ In Figure 3-13, steel strain along a tension specimen is plotted for various load cycle numbers. Since the slope of these curves is proportional to local bond stress, it follows that when two curves are close together, little change in bond stress has occurred. The loading history for these curves is given in Table 3-5. In Figure 3-13, it is seen that the bond stress distribution appears primarily controlled by the maximum load experienced over all previous cycles. For example, with specimen T20 the strains for cycles 7 and 22 at a bar end load of 20 ksi are essentially identical (and similarly for cycles 6 and 12 at a bar end load of 40 ksi), while cycles 5 and 7 have markedly different strain distributions because

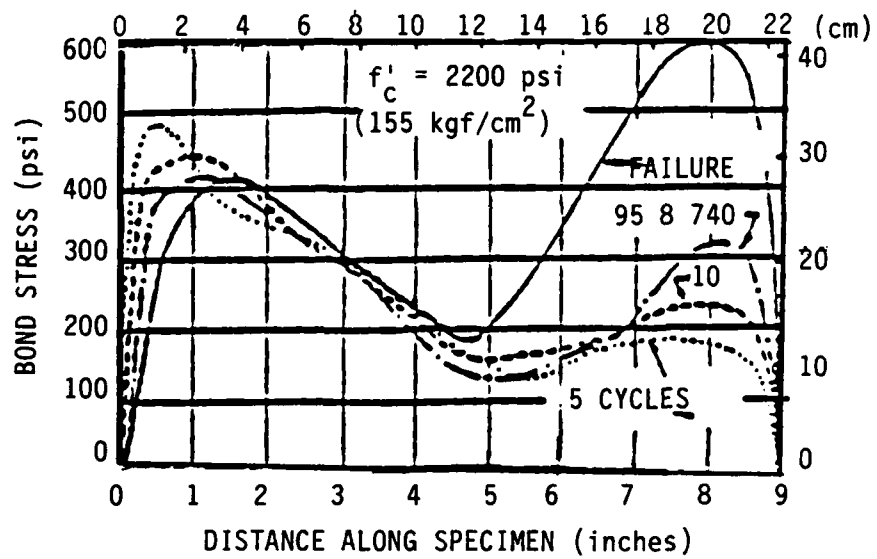


Figure 3-12. Bond stress distribution along rebar for different load cycles.

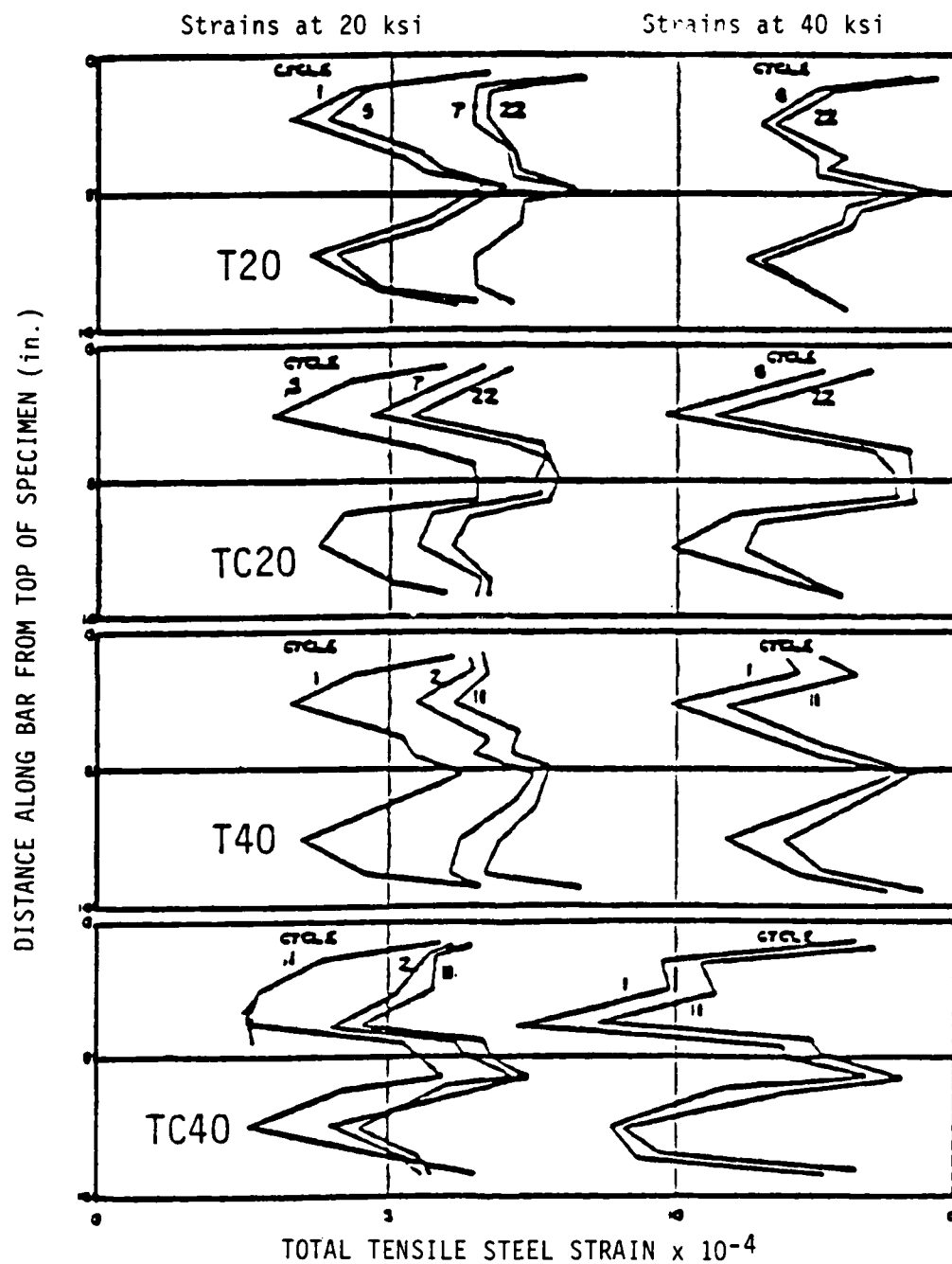


Figure 3-13. Strain distribution along rebar for different cycles and and for the load histories in Table 2-10.

Table 3-5
Load histories corresponding to Figure 3-13

Peak Stresses			
Specimens	Cycle No.	Tension f_s , ksi*	Compression f'_c
T20	1-5	20	0 for T20
TC20	6-7	40	0.4 f'_c for TC20
	8-12	20	
	13-17	30	
	18-19	10	
	20-21	20	
	22	Yield	
T40 and TC40	1-5	40	0 for T40
	6-10	20	0.45 f'_c for TC40
	11	Yield	

*1 ksi = 70.3 kg/cm²

for cycles 6 and 7 (see Table 3-5) the maximum bar stress was raised to 40 ksi. An analogous behavior can be seen when comparing cycles 1 and 11 of specimen T40 at a maximum bar stress of 40 ksi. Sensitivity to maximum bar stress has also been observed by Bresler and Bertero.⁽⁸²⁾

Figure 3-14 (Edwards and Yannopoulos⁽⁹⁵⁾) shows that there is little slip recovery when a test specimen is unloaded. The authors subjected their thin pullout specimens to nine identical load-unload cycles. A large amount of slip accumulated during the first load cycle but subsequently there was minimal recovery. Further, succeeding cycles did little to change the amount of slip, which agrees with remarks made in the preceding paragraph. That it takes increasing bar stress to increase slip can be seen in Figure 3-15 (Morita and Kaku⁽¹⁰¹⁾), who also used a very short embedment length. Again, there is little recovery during unloading.

Morita and Kaku⁽¹⁰¹⁾ also studied cyclic loading involving stress reversals. In Figure 3-16 some of their results are shown schematically. In Figure 3-16a the specimen was cycled between fixed slip limits and after a few cycles the stress-strain curve stabilized and became that shown in Figure 3-17. The horizontal portions of the curve, parts OA and CD, can be thought of as Coulomb friction corresponding to the bar lugs having ground out a small region of the concrete adjacent to the bar. Portions AB and DE correspond to the lugs contacting concrete that has not been severely deformed by the bar lugs. Unloading branches BC and EO are characterized by an almost total lack of strain recovery. This is attributed to the concrete debris locking around the bar lugs inhibiting strain recovery in the bar. It is only after the stress has reversed that strain recovery is possible.

Figure 3-16b shows totally reversed cyclic bond stress versus slip for increasing levels of stress. The presence of Coulomb friction in the strain unloading branches and the small amount of strain recovery in the stress unloading branches can be clearly seen.

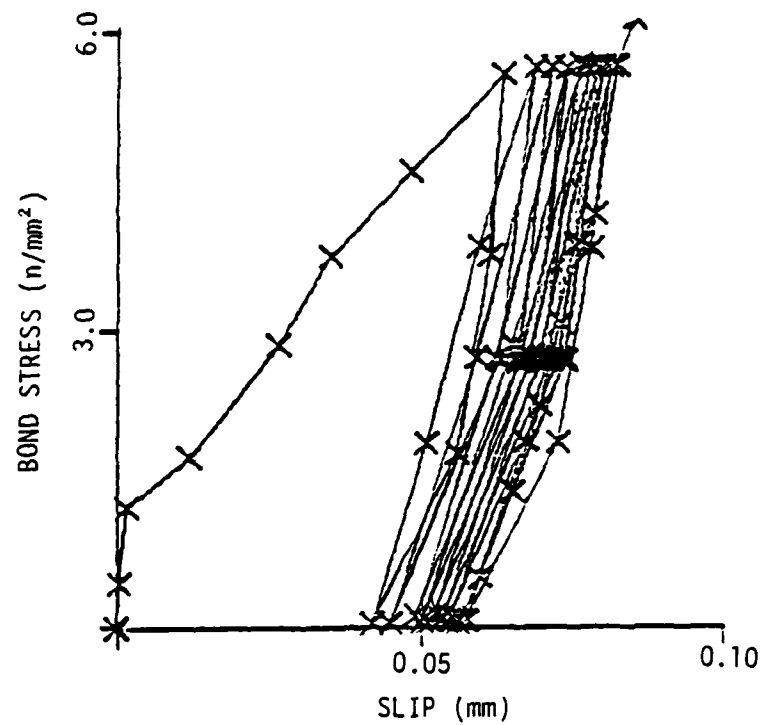


Figure 3-14. Bond stress as function of slip for cyclic history between fixed load limits.

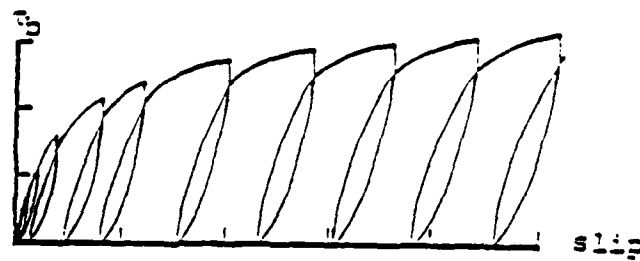


Figure 3-15. Bond stress as function of slip for cyclic history with increasing load amplitude.

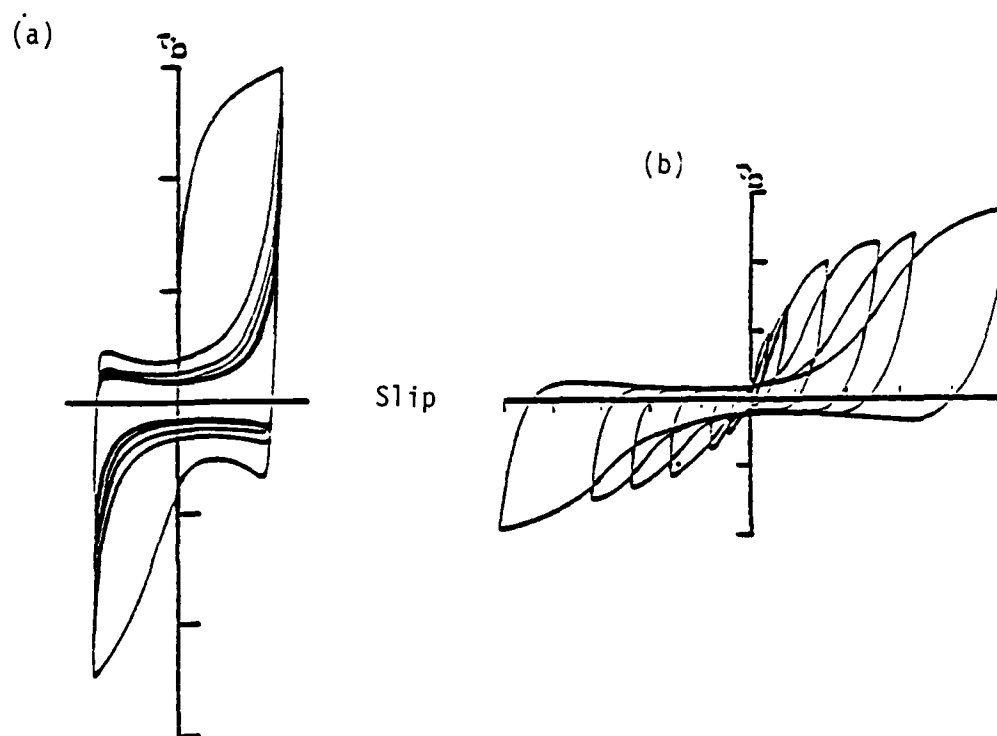


Figure 3-16. Bond stress versus slip for fully reversed cyclic histories (a) fix slip limits, (b) increasing slip limits.

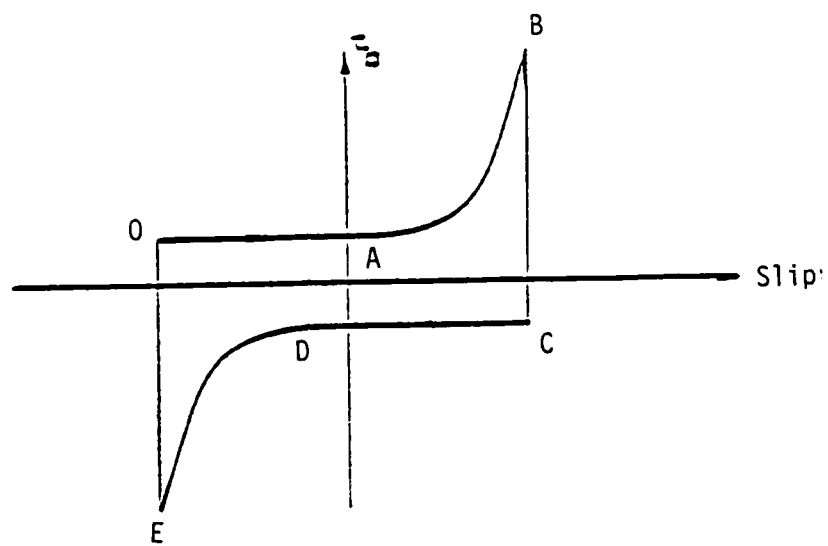


Figure 3-17. Stabilized cyclic bond stress-slip curve for testing between fixed slip limits.

3.2.8 Multiaxial Loading

The least understood aspect of this subject is the effect of multiaxial loading on bond stress. Several researchers (Bertero et al.,⁽⁸⁸⁾ Mains⁽⁸⁷⁾ and Mathey and Watstein⁽⁸⁸⁾) have matter-of-factly used stirrups and wire cages to suppress the longitudinal cracking failure mode. However, since these reinforcements were buried inside specimens and were not strain-gaged, the amount of constraint provided by them is unknown. However, it is clear that if cracking that would otherwise have taken place was prevented then additional pressure was exerted on the rebar and increased bond strength was obtained.

To date, only two studies, Untrauer and Henry⁽⁹¹⁾ and Dörr,⁽⁸³⁾ have sought to systematically determine the effect of external, controlled lateral pressure on bond strength. Dörr used tension specimens with strain-gaged rebars and found that near the ends of his specimens he could double his bond stress and greatly reduce slip by applying a lateral pressure of approximately 2175 psi. In their study Untrauer and Henry used a pullout specimen with square cross section and applied a lateral pressure f_n to only two sides through hydraulic rams. Figure 3-18 shows average bond stress versus end slip curves for zero and 1500 psi lateral pressures and it can be seen that attainable bond stress was doubled in the latter case to over 2 ksi and that controlled slip was also doubled. Figure 3-19 shows bond stress increasing linearly with f_n for various fixed slip levels and two different bar sizes.

3.2.9 Issues

In the preceding sections a detailed discussion of the state of knowledge on the bond between steel and concrete has been given and it can be concluded that:

- Currently there is no universally accepted technique for obtaining experimental data on the steel-concrete bond.
- No technique exists for measuring slip along a rebar embedded in concrete.

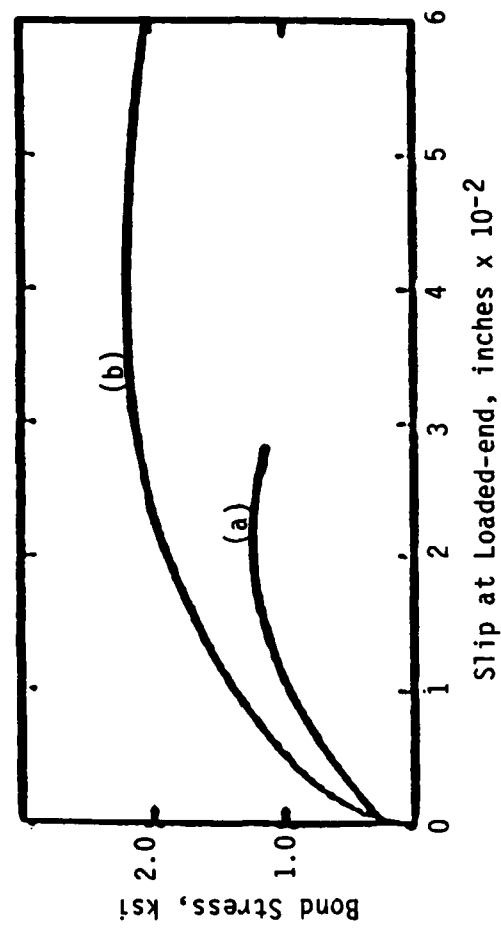


Figure 3-18. Average bond stress as a function of end slip showing effect of external lateral pressure f_n (a) $f_n = 0$, (b) $f_n = 1500$ psi.

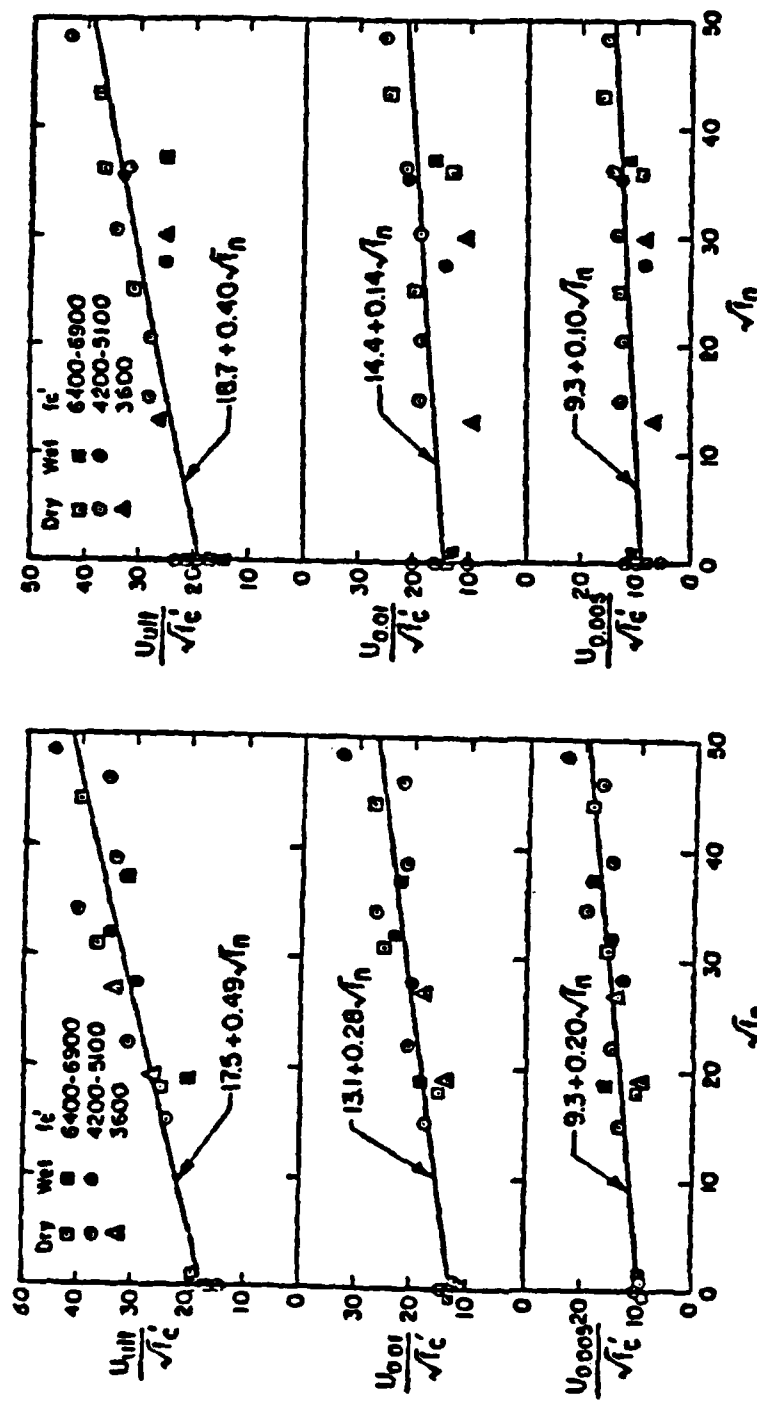


Figure 3-19. Bond stress as a function of external lateral pressure for fixed bond slip and different bar sizes.

- The large number of experimental variables has resulted in a very diverse data base; consequently, a considerable effort is necessary in order to develop a reliable data base from which validation of a constitutive model may be carried out.
- Bond stress and slip depend on
 - bar and concrete constitutive properties
 - bar lug design
 - confining stresses due to applied external pressures of stirrups.

Other steel-concrete interaction items that pertain to containment structures but were not discussed because of a complete lack of experimental data, are:

- Sensitivity of bond stress and slip to strain rate effects.
- Interaction between rebars at right angles to each other.
- Scatter intrinsic to reinforced concrete material properties.

3.3 AGGREGATE INTERLOCK, DOWEL ACTION

As noted previously (see Section I), the dowel and aggregate interlock problems are not treated in the analytical development reported herein. Nevertheless, since the establishment of a sound data base is a necessary prerequisite to further model development, it is deemed appropriate to review such subjects from a test data standpoint. Consequently, in this subsection the pertinent test data concerning aggregate interlock and dowel action is reviewed. The discussion, all of which refers to shear transfer across cracks in reinforced concrete, partially follows the recent review by Leombruni, et al.⁽¹⁰²⁾

3.3.1 Aggregate Interlock

The aggregate interlock problem refers to interface shear transfer (IST) across crack planes, and to joint dilatancy (increase

in crack width) due to relative displacement parallel to the crack. The manner in which IST takes place has a major impact on the effective 'shear modulus' of a reinforced concrete specimen. An understanding of the dilatancy problem, on the other hand, is necessary in order to properly determine the manner in which the reinforcing steel is loaded in the presence of shear deformation.

The tests performed by Fenwick,^(103,104) Figure 3-20, are perhaps typical of the aggregate interlock or IST experiments. Here a predefined crack is subjected to relative slip while the crack opening is maintained essentially constant. The effects of crack width and concrete strength on the load-slip behavior were studied for crack widths ranging from 0.0025 to 0.0150 inches and concrete strengths from 2700 to 8120 psi. Figure 3-21 illustrates typical data for a concrete with $f'_c = 4810$ psi. There appears to be a linear relation between shear stress (average) and interface slip until additional diagonal and flexural cracks appeared in the test blocks. As can be observed, the slopes of the shear stress versus slip curves decrease with increasing crack width. It was also found that increasing concrete strength increased the shear stress versus slip slope for a given crack width, but the effect of strength increase on stiffness was not as pronounced as that of crack width. A decrease in slope occurred with the onset of additional cracking.

Loeber⁽¹⁰⁵⁾ performed similar IST tests, but on specimens with a larger shear area ($A = 33.5 \text{ in}^2$ for Loeber, $A = 12.25 \text{ in}^2$ for Fenwick), Figure 3-22. Reinforcing ties were placed in the specimens to limit additional cracking as shear was applied. The concrete strength used was a nominal 5000 psi and the crack width ranged from 0.005 to 0.020 inches. Representational results from Loeber's tests are shown in Figure 3-23. Loeber's tests show greater slopes and capacity than do those of Fenwick, perhaps because of the added reinforcing ties which limited additional cracking. In both tests, however, the slope of the (average) shear stress versus relative slip is a strong function of the crack width with a decrease observed where the crack width was increased. Based

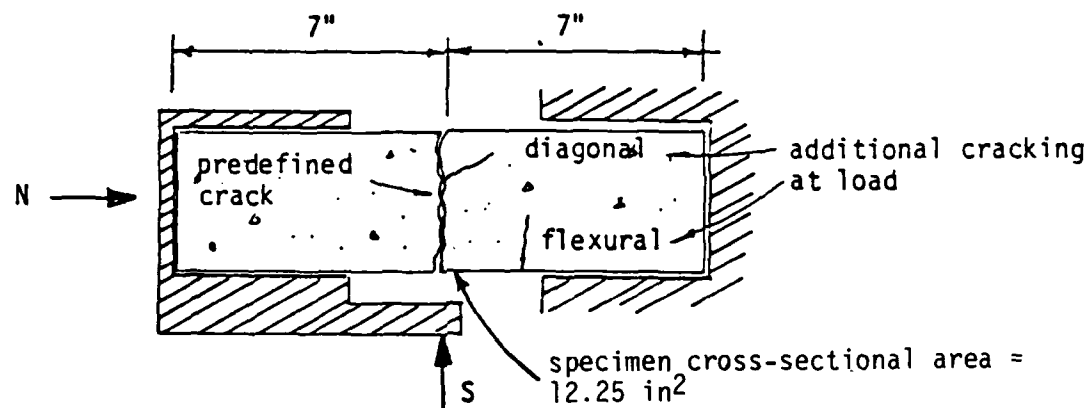


Figure 3-20. Fenwick's aggregate interlock test specimen

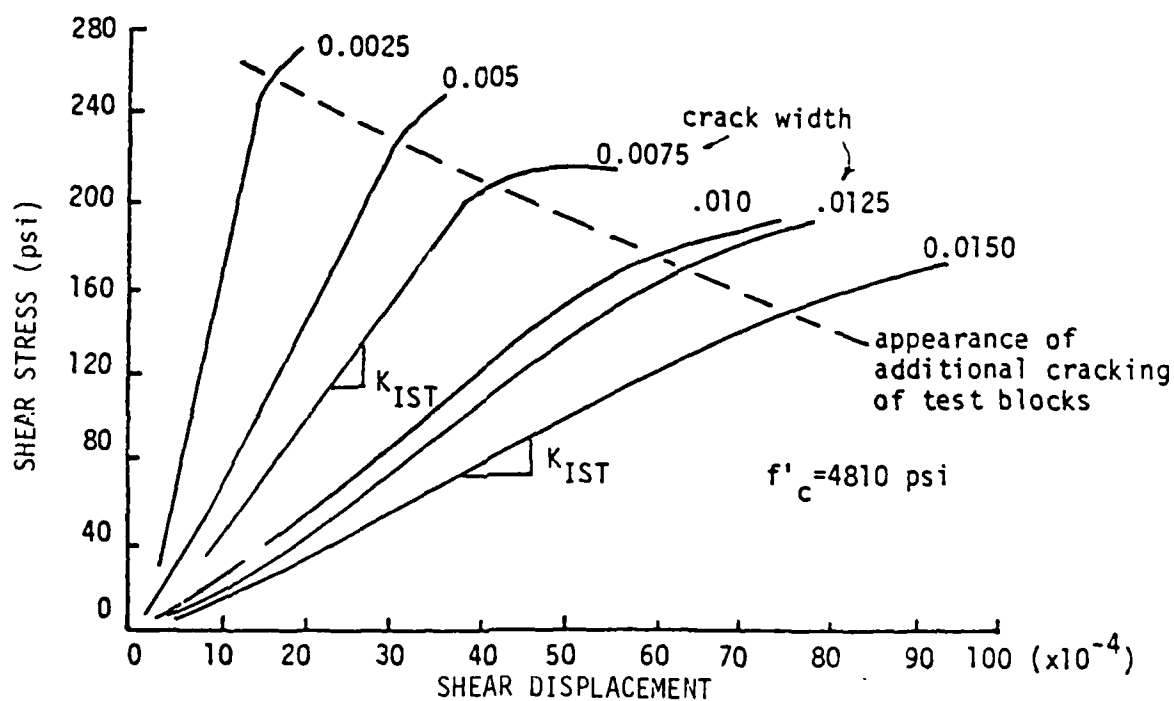


Figure 3-21. Displacement curve for Fenwick's tests.

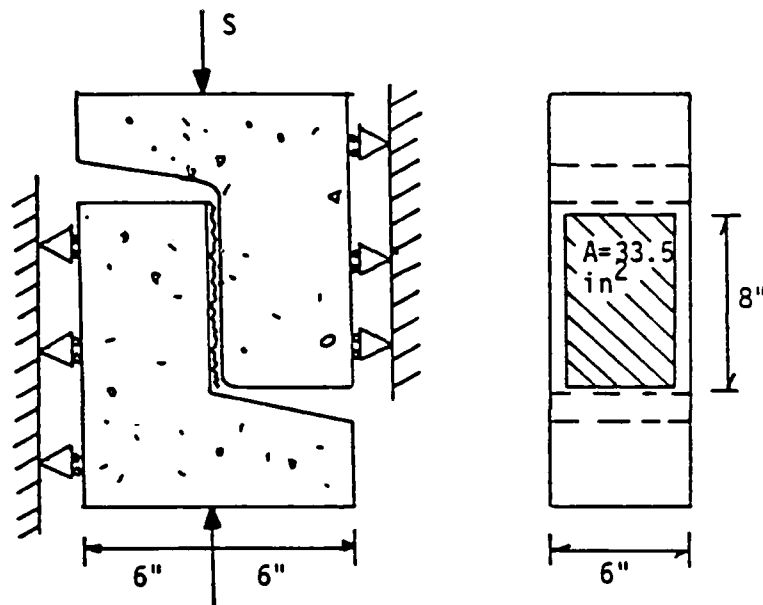


Figure 3-22. Loeber's test specimen.

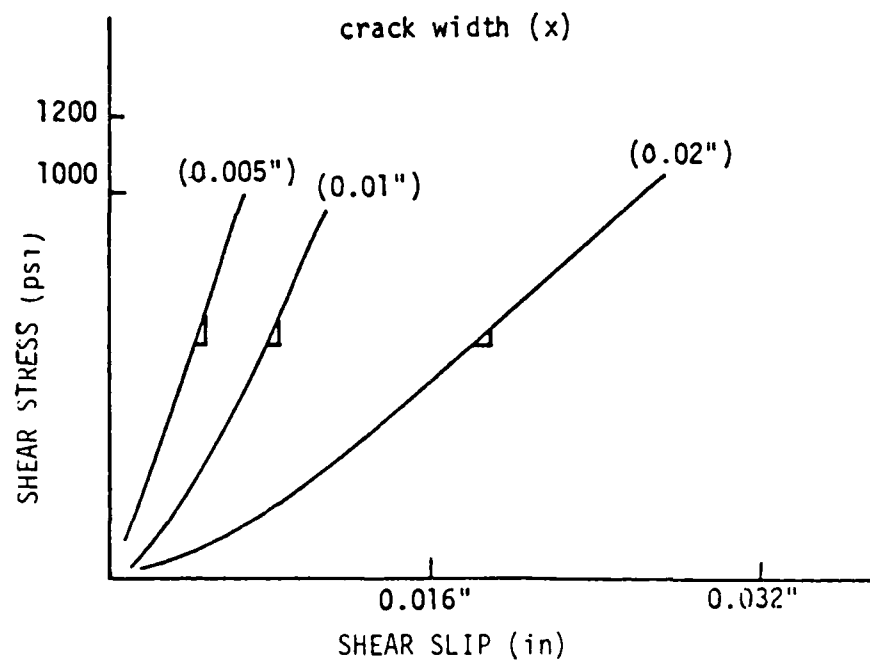


Figure 3-23. Displacement curve for Loeber's tests.

on his tests, Loeber also indicated that the size and type of aggregate do not have a large influence on IST.

Houde and Mirza^(106,107) conducted an experimental program using test specimens similar to Fenwick. The crack width range for these tests was 0.005 to 0.020 inches. Typical results are shown in Figure 3-24. A new feature of this test data is an initial "free slip" observed at the onset of loading for crack widths greater than 0.01 inches. This slip (≈ 0.0015 inches) is attributed to relative free displacement that occurs before asperities on either side of the crack surface come into contact. After the initial free slip, the shear-slip response is linear until additional cracks occur in the test blocks. The main parameters influencing IST were cited as the crack width and the concrete strength.

White and Holly⁽¹⁰⁸⁾ studied IST using two 'rigid' blocks with a preset crack between them, Figure 3-25. The external restraining bars* shown provided a constant 'stiffness' normal to the crack; this is in contrast to the previous tests which were conducted at constant crack widths. The shear loading was applied cyclically in a range of 120 to 160 psi. Typical response for (average) shear stress as a function of shear slip, average crack width, and increase in restraining bar force are shown in Figure 3-26. Within the stress range of 120 psi, relatively small slips are produced during the first cycle of loading, and little increase in slip occurs even after 25 cycles of loading. After 25 cycles, the shear stress is increased monotonically to approximately 400 psi. Appreciable increase in slip, further crack opening and corresponding increase in bar forces were observed for this monotonic increase. It is noted that these specimens exhibited a ductile behavior which was not observed in the specimens tested with constant crack widths.

*These bars were intended to represent the restraining forces provided by embedded bars in actual reinforced concrete. The technique allows one to separate IST and dowel effects.

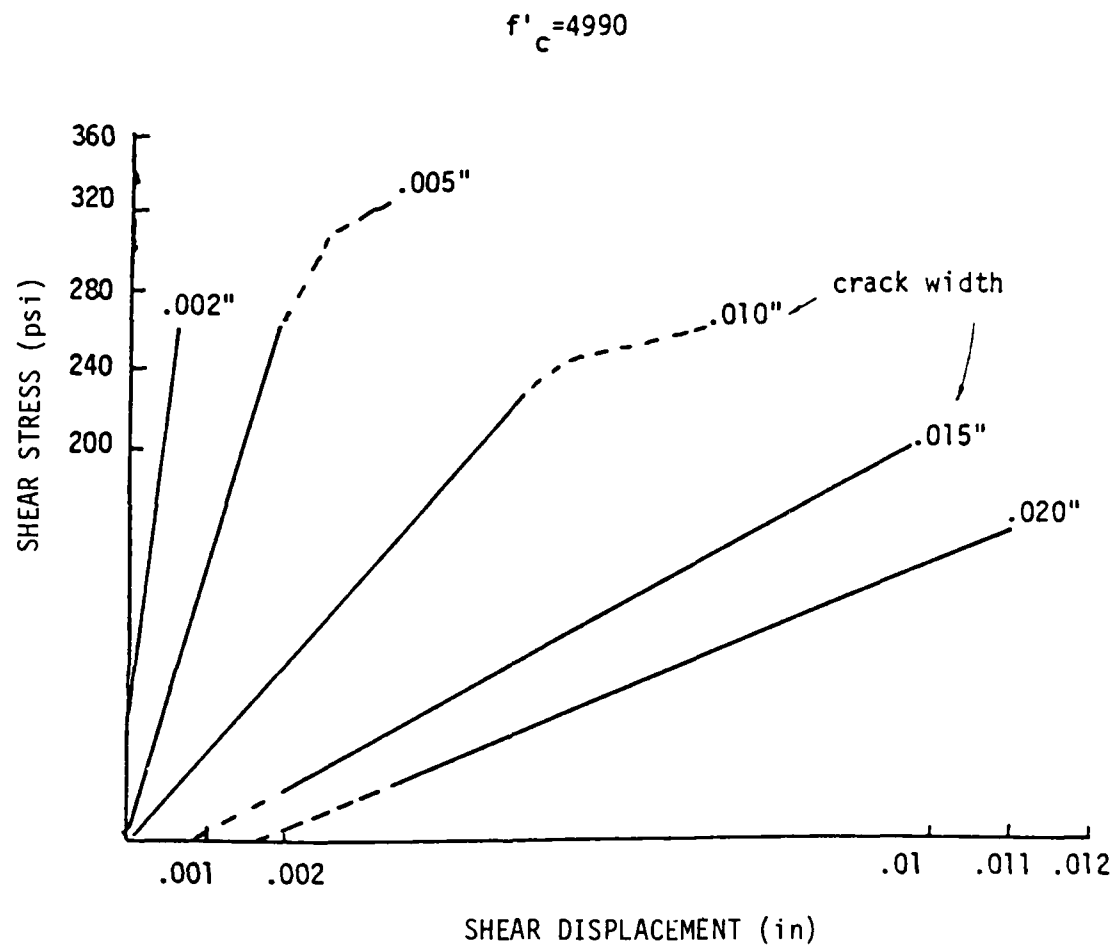


Figure 3-24. Typical displacement curve from Houde.

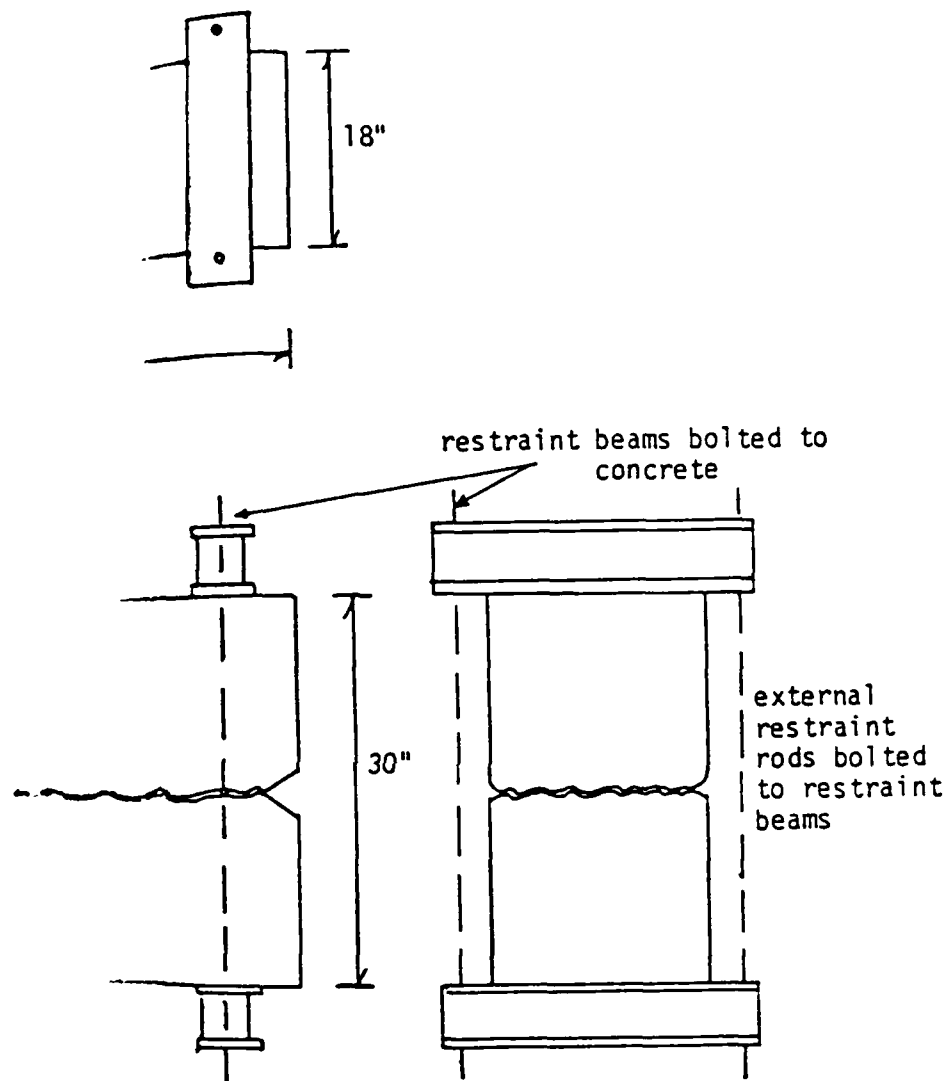


Figure 3-25. Test specimen configuration from work performed by White and Holley.

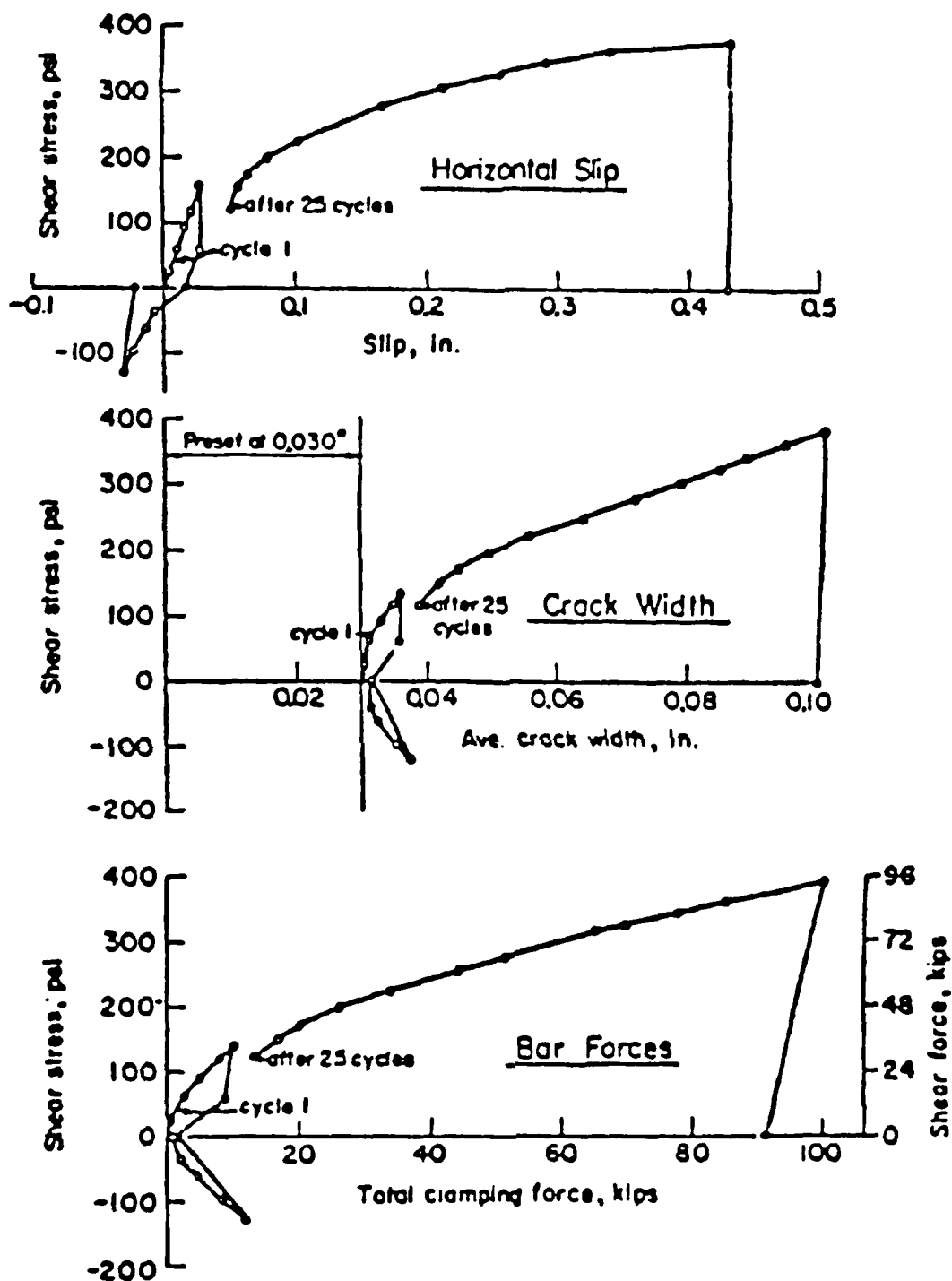


Figure 3-26. Typical response for IST transfer from tests performed by White and Holley.

A study using experimental specimens similar to those used by White and Holly⁽¹⁰⁸⁾ was conducted by Laible.⁽¹⁰⁹⁾ Here thirty direct shear specimens with a shear area of 150 and 300 in² were used in a study of IST. The parameters addressed were specimen geometry, aggregate size and quality, concrete strength, magnitude of cyclic shear stress, effect of initial crack width, effect of degree of reinforcing restraint across the crack (normal stiffness), and the age of concrete. The measured quantities were horizontal slip along the crack, increase in crack width, and increase in restraining steel force. The cyclic shear stress applied ranged from 100 to 270 psi, but the majority of the tests were cycled at a shear stress level of 180 psi. Typical first and 15th cycle load-slip displacement curves are illustrated in Figure 3-27. It can be observed that, although the first level phase is nearly linear, appreciable residual displacement results upon unloading. Subsequent loading cycles exhibit an initial small slope followed by a sudden increase in slope. The unloading stages show higher stiffness than the loading. The initial crack width range in these tests was from 0.01 to 0.03 inches. In general, the increase in crack width as the shear force was applied was small in comparison to the initially prescribed crack width. The authors note that the bar forces induced by asperity overriding from the applied shear stresses were a small percentage of the force required to cause yielding of the bars (This information, however, may be very misleading since the bar stress distribution in an actual reinforced concrete specimen depends strongly on the degree of debonding that has taken place (debonded length)).

3.3.2 DOWEL ACTION, COMBINED IST AND DOWEL ACTION

Jimenez-Perez, et al.^(110,111) conducted an experimental study of IST, with and without dowel action. The test setup used is shown in Figure 3-28. Eight specimens were used for the combined IST and dowel mechanism and five specimens for the dowel action alone. Embedded reinforcing bars were used for the study. Initial tensile stresses were applied to the bars to initiate cracking at a

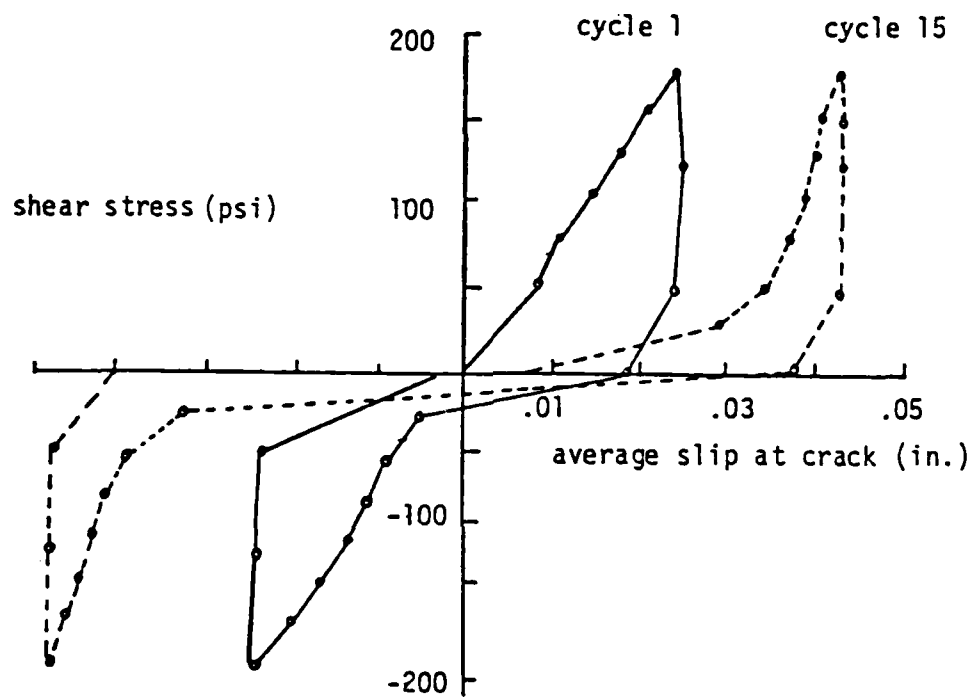


Figure 3-27. Typical shear stress v. shear slip results for IST tests performed by Laible.

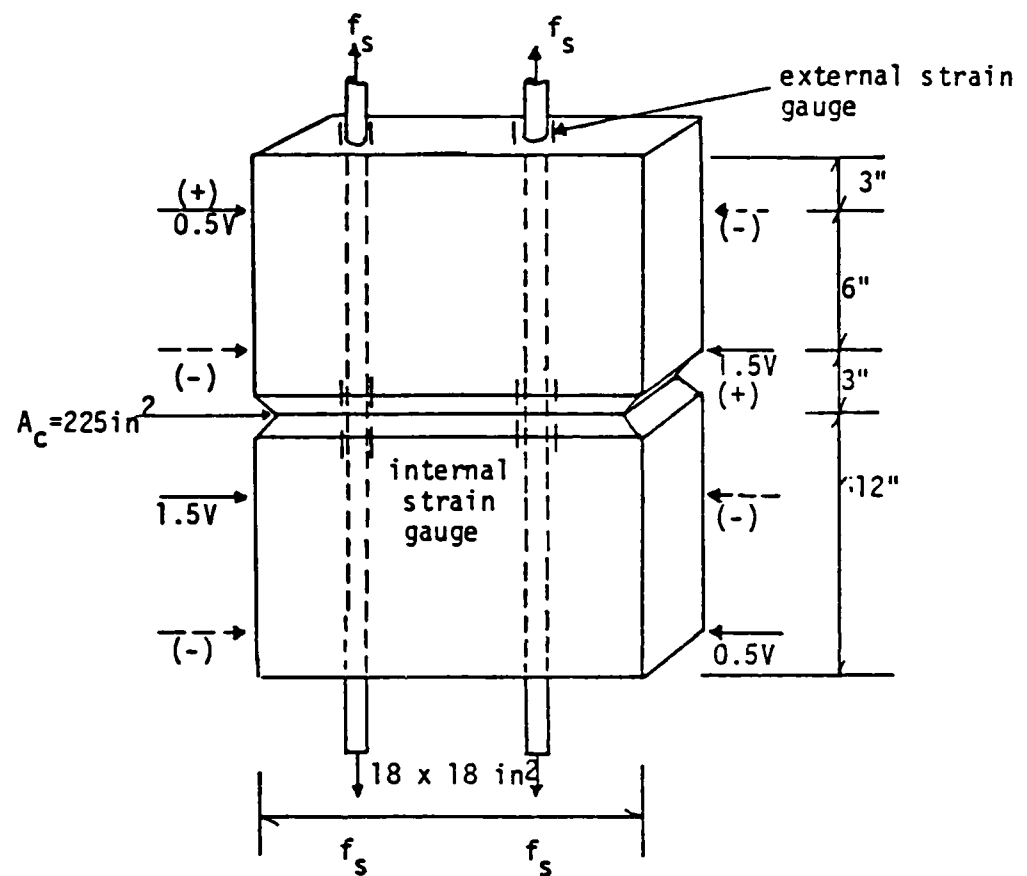


Figure 3-28. Block-type test specimens performed by Jimenez.

predetermined plane (see Figure 3-28). The axial stress was then increased in increments to a maximum of 40 psi (rebar stress). In each stage measurements of the crack width opening and bar stresses were taken. The axial stress was then adjusted to accommodate a desired initial crack width. Shear loading was subsequently applied.

From the combined IST and dowel tests the following behavior was observed: the increase in crack width was insignificant within a range of shear stress up to 200 psi. A noticeable increase occurred only when failure was imminent. The increase in axial stress from the application of shear was normally less than 10 percent of the ultimate axial bar capacity. Figure 3-29 depicts typical load-slip behavior for the combined action tests. Cycle 1 and Cycle 15 shear stress versus shear slip response curves at different stress levels are shown. From the magnitude of the slips observed at these stress levels, it can be inferred that the combined mechanism with large diameter (No. 14) embedded bars shows slips less than half those observed in IST tests performed by Laible.⁽¹⁰⁹⁾ Also, though the load-slip behavior of the combined action specimens is similar to the displacement curves produced by Laible's test, the residual slips were not as pronounced.

Specimens reinforced with No. 9 and No. 14 bars were used to study the dowel action mechanism alone. For this purpose the crack surface is replaced by a smooth lubricated surface. A typical shear stress versus relative displacement response for dowel action is illustrated in Figure 3-30. It is observed that, in comparison to the combined mechanism, much larger shear slips are necessary to develop shear resistance through dowel action. Note that the specimen without initial tensile stress exhibits a stiffer behavior than the specimen stressed initially at 30 ksi. It was concluded that individual bar dowel 'stiffness' increases with bar size, but for larger bars where concrete deterioration may be more significant around the bar, the 'stiffness' was at time lower than the smaller bars. Tensile stress in the bars has a deteriorating effect on the dowel stiffness since it causes more localized bond

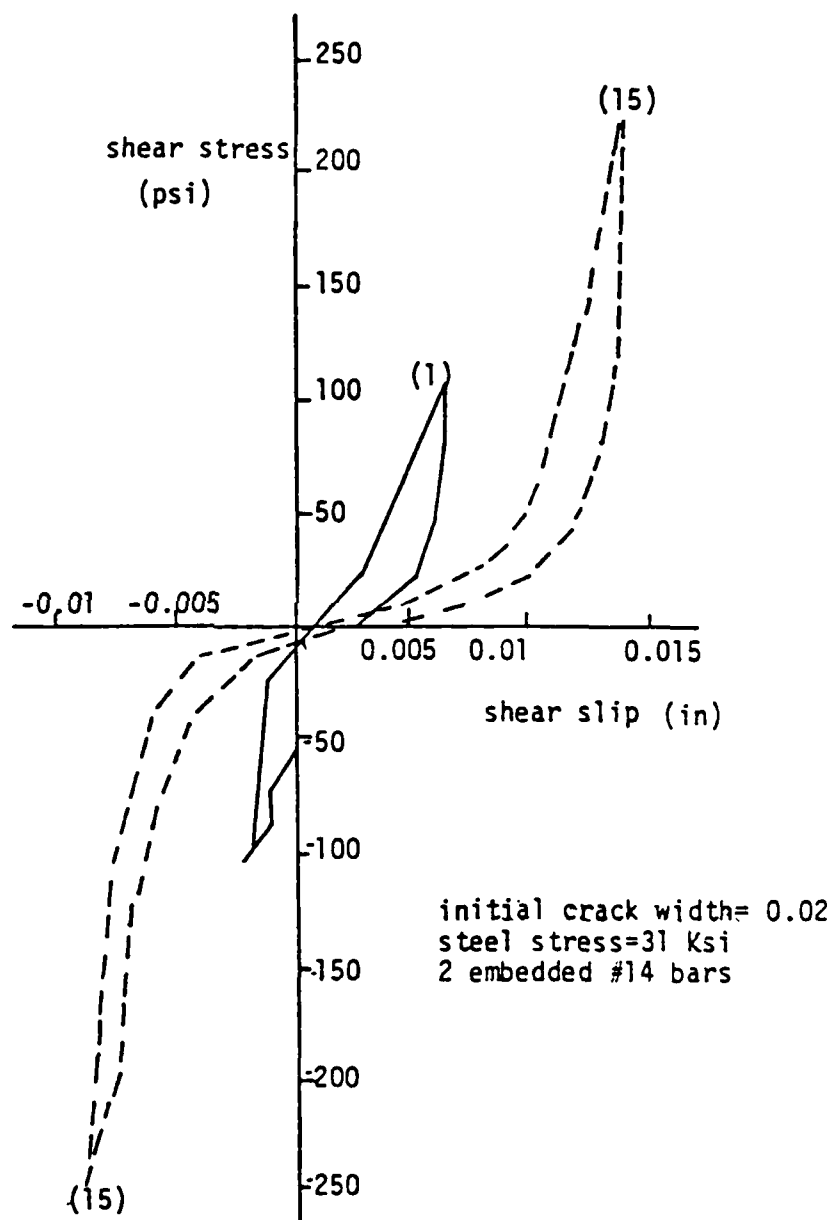


Figure 3-29. Typical load-slip behavior of combined mechanism (IST and dowel).

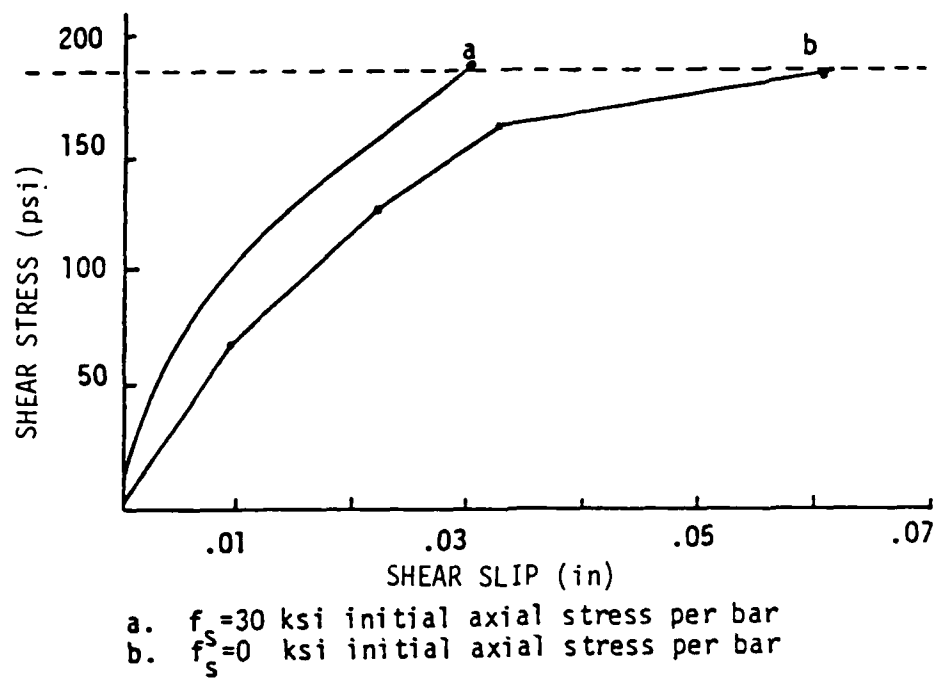


Figure 3-30. First cycle load-displacement curve for dowel action #4-#9 bars.

failure. Most specimens used to assess dowel action failed by concrete splitting.

Based upon the above tests, the authors have attempted to determine the relative amounts of shear taken by each mechanism. Using compatibility arguments and the load slip behavior of the combined mechanisms versus dowel action alone, it was concluded that, for the specimens considered, interface shear transfer assumes 65-75 percent of the total applied shear while the dowel action is responsible for 25-35 percent of the applied shear.

Another test program worthy of mention here is due to Duluscka,⁽¹¹²⁾ who conducted a test program on dowel action with a goal to establish theoretical load-deformation relations for cases where steel is oblique as well as normal to a crack surface. The test setup for these experiments is shown in Figure 3-31. To simulate cracks, two layers of 0.0078-in-thick sheet brass, which was connected in the middle by a skewed steel stirrup, were embedded in the test specimens. During testing, relative slip along the simulated crack and opening of the crack perpendicular to the direction of the load were recorded. Due to the sheet brass, aggregate interlock was not a factor in this study, i.e., dowel action alone was investigated.

Experimental results for the failure load in the bar were found to correlate well with the following relation:

$$T_f = \rho \phi^2 \gamma \sigma_y n \sin \gamma \left[\left(1 + \frac{\sigma_c}{3 \rho \gamma^2 \sigma_y n \sin^2 \gamma} \right)^{1/2} - 1 \right] \quad (3-3)$$

where

- T_f = Failure load of dowel shear
- ϕ = Bar size
- δ = Angle of stirrups in degrees
- σ_y = Yield stress of steel
- σ_c = Cube strength of concrete
- n = Coefficient of local compression of concrete

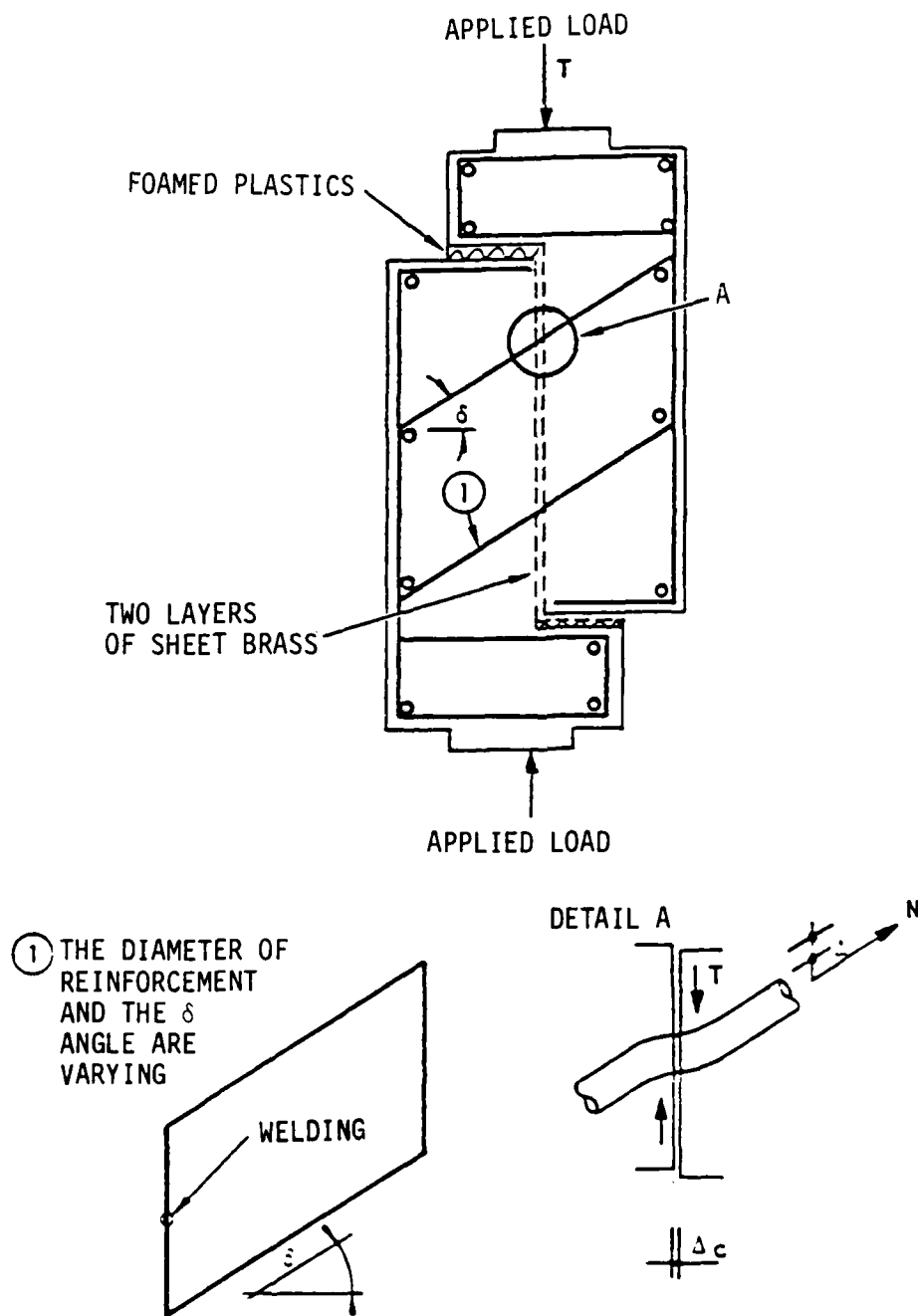


Figure 3-31. Details of test specimen construction.

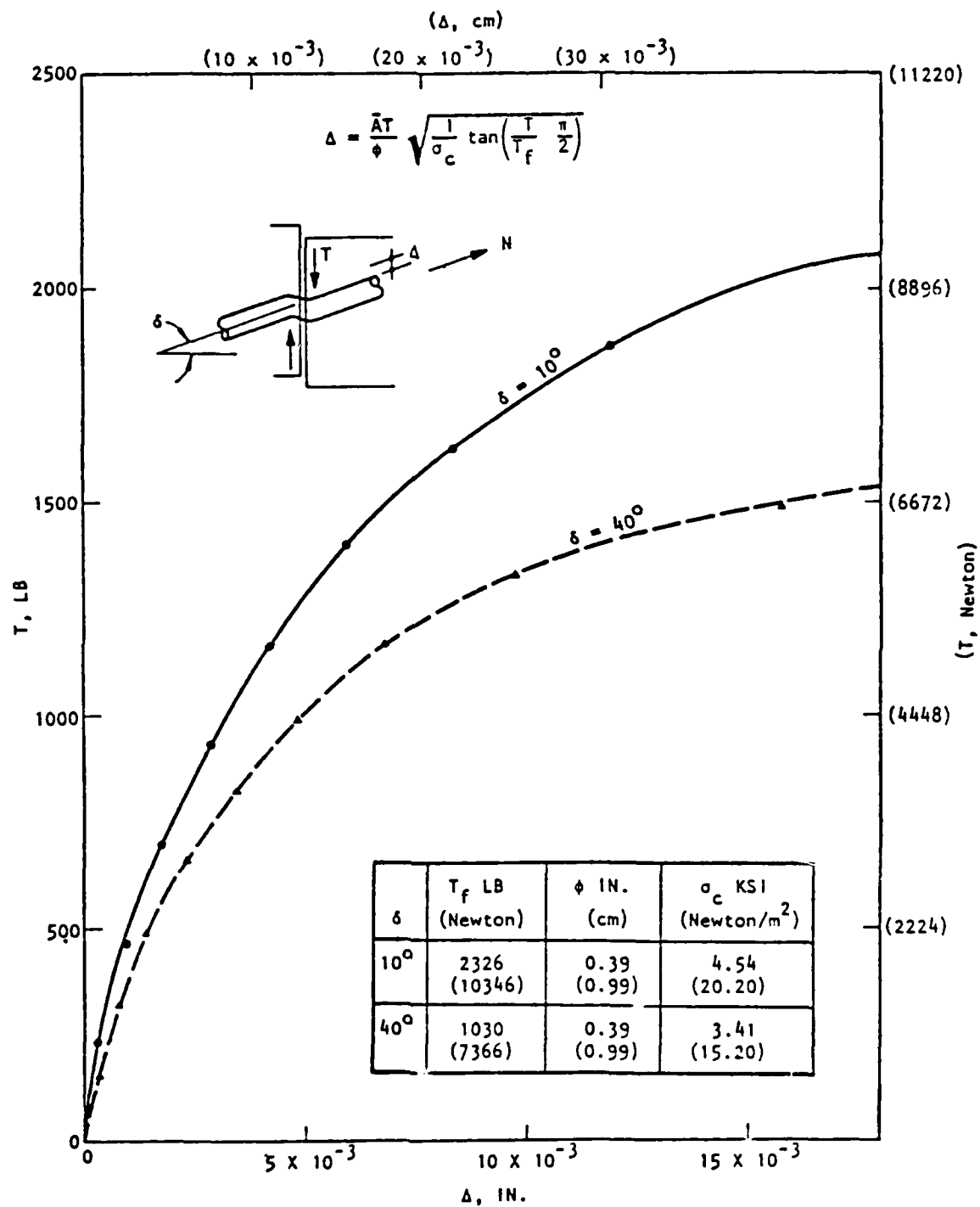


Figure 3-32. Dowel shear force-slip relationship.

- γ = Constant
 ρ = $1 - N^2/N_y^2$
 N = Axial tensile force in bar
 N_y = Axial force inducing yield in pure tension.

Duluscka concluded that, from the test results, a reasonable empirical fit of the slip versus dowel shear load was

$$\Delta = \frac{\bar{A}T}{\phi} \left[\frac{1}{\sigma_c} \tan \left(\frac{T}{T_f} \frac{\pi}{2} \right) \right]^{1/2} \quad (3.4)$$

where

- \bar{A} = Constant
 T = Dowel shear load
 T_f = Failure load of dowel shear computed from Equation (3-1)

Equation (3-2) was plotted as a function of T and Δ for two values of $\delta = 10^\circ$ and 40° respectively, as shown in Figure 3-32. The results indicate that an increase in the angle δ results in a decrease of the dowel shear force T and an increase in the bar's normal force N . Also, an increase in the concrete strength σ_c results in an increase of dowel shear capacity T_f .

3.3.3 Issues

Information on IST, dowel action, and combined IST and dowel action represents a critical link in the constitutive model construction chain. The preceding information constitutes a representative cross-section of the available data on these subjects. An evaluation of this work leads us to the conclusion that additional testing is necessary in order to adequately define the mechanics of the IST, dowel, and combined IST and dowel problems. Such testing should be conducted, in contrast to most previous studies, under displacement control using a closed loop servo-controlled test system.

SECTION 4

PREVIOUS CONSTITUTIVE MODELS: PLAIN CONCRETE

In this section, previous work on constitutive relations for plain concrete is reviewed for background purposes. The discussion is partitioned into (1) uniaxial relations (subsection 4.1), (2) biaxial relations (subsection 4.2) and (3) multiaxial relations (subsection 4.3).

4.1 UNIAXIAL CONSTITUTIVE MODELS

The usual constitutive assumption for concrete in uniaxial tension is linear elasticity, with complete failure occurring when the stress reaches f_t' . For monotonic compressive response many nonlinear stress-strain laws have been postulated. Typically they were designed for use in reinforced concrete beam design and are of the form

$$\sigma = f(\epsilon) \quad (4-1)$$

Eq. 4-1 is not immediately suitable for nonlinear finite element analysis where an incremental stress-strain relation is needed. Further the representations do not admit obvious generalization to multiaxial stress states. The principal usefulness of equations of the form of Eq. 4-1 is as hardening functions for use in multiaxial constitutive models.

Popovics⁽¹¹³⁾ summarized equations of the form Eq. 4-1 and they are given below:

$$\sigma = A \epsilon^n, \quad (4-2)$$

$$\sigma = E \epsilon \left[1 + (3E_0/E - 2) (\epsilon/\epsilon_0) + (1 - 2E_0/E) (\epsilon/\epsilon_0)^2 \right], \quad (4-3)$$

$$\sigma = \frac{E \epsilon}{1 + (E/E_0 - 2) (\epsilon/\epsilon_0) + (\epsilon/\epsilon_0)^2}, \quad (4-4)$$

$$\sigma = E \epsilon (1 - \epsilon/2\epsilon_0) \quad , \quad (4-5)$$

$$\sigma = B \epsilon (1 + C\epsilon^{n-1}) \quad , \quad (4-6)$$

$$\sigma = \frac{E\epsilon}{1 + (\epsilon/\epsilon_0)^2} \quad , \quad (4-7)$$

$$\sigma = \frac{E\epsilon}{D + (\epsilon/\epsilon_0)^n} \quad , \quad (4-8)$$

$$\sigma = E \epsilon \exp (- \epsilon/\epsilon_0) \quad , \quad (4-9)$$

$$\sigma = E \epsilon \exp [- (E\epsilon - 2)^m F] \quad , \quad (4-10)$$

In these equations E_0 and ϵ_0 are the secant modulus and strain at $\sigma = f_c'$ and E is the initial tangent modulus. Parameters A , B , C , D , F , m and n are constants. Eq. 4-2 does not model softening. Equations 4-3 and 4-4 would model softening if cubic terms were added. Equations 4-5 and 4-7 are special cases of Eqs. 4-3 and 4-4 with $E/E_0 = 2$. Equations 4-5, 4-6, 4-7 and 4-9 are less flexible than the others because they predict a fixed value for E/E_0 when in reality the ratio can range anywhere from 1.3 to 4. Equation 4-4 was due to Saenz⁽¹¹⁴⁾ and was used by Darwin and Pecknold in the development of their biaxial theory of cyclic response which is discussed in the next section.

Additional formulae have been postulated by Kriz and Lee⁽¹¹⁵⁾ and by Popovics⁽¹¹⁶⁾.

4.2 BIAXIAL CONSTITUTIVE MODELS

In this section constitutive models developed specifically to describe the biaxial response of plain concrete are discussed. Three-dimensional theories which, of course, are based in part on biaxial data and can describe plain concrete biaxial response are reviewed in Section 4-3. Multiaxial theories of plain concrete response have only appeared in the last ten years and are mainly generalizations of elasticity and plasticity. In the presentation below it is convenient to divide the theories into three categories.

4.2.1 Nonlinear Elasticity Models

The first biaxial constitutive theory developed by Kupfer and Gerstle⁽¹¹⁷⁾ was in matrix form,

$$\underline{\sigma} = [\underline{D}] \underline{\epsilon} \quad , \quad \underline{\sigma}^T = (\sigma_x, \sigma_y, \tau_{xy}) \quad , \quad \underline{\epsilon}^T = (\epsilon_x, \epsilon_y, \epsilon_{xy}) \quad (4-11)$$

where $[\underline{D}]$, a matrix of secant moduli, was itself a function of stress and strain measures. The constitutive model assumed concrete always behaved isotropically thus precluding oriented damage arising from microcracking. More importantly, while the model did replicate monotonic loading results for biaxial compression and compression-tension, it was unable to adequately simulate any cyclic stress-strain response since the theory predicted that unloading occurred along the loading path. Consequently, the theory predicted neither energy dissipation nor residual anelastic strain during unloading. Thus the theory, when specialized to uniaxial cyclic response was totally inadequate. Subsequently, Murray⁽¹¹⁸⁾ corrected the definition of tangent moduli given by Kupfer and Gerstle but did not address any of the theory's shortcomings.

Nilson, Slate and their co-workers^(119,120,121) developed a nonlinear elasticity theory based on a generalization of Saenz's representation for concrete uniaxial response. The authors first considered a single component of stress, σ_x , for biaxial compression and compression-tension and showed that

$$\sigma_x = f(\alpha_x, \epsilon_x) \epsilon_x, \quad \alpha_x = \sigma_y / \sigma_x \quad (4-12)$$

modeled available data well, where f was a judiciously chosen function and ϵ_x was the strain component corresponding to σ_x . Parameter α_x was used to account for biaxiality effects.

Next the authors attempted to introduce stress induced anisotropy by postulating

$$\sigma = [D] \epsilon \quad (4-13)$$

where $[D]$ was a material property matrix with form appropriate to an orthotropic material:

$$[D] = \begin{bmatrix} a & b & 0 \\ b & c & 0 \\ 0 & 0 & d \end{bmatrix} \quad (4-14)$$

and parameters a , b , c , d were functions of ϵ_x , ϵ_y and α_x . Since the constitutive equation expressed total stress in terms of total strain, parameters a , b , c and d had the character of secant moduli. However, in their evaluation the authors expressed them in terms of variables that were tangent modulus-like in nature.

In the present notation a typical tangent modulus was defined to be $df(\alpha_x, \epsilon_x)/d\epsilon_x$. But in reality the value $df(\alpha_x, \epsilon_x)/d\epsilon_x$ was used; α_x was held constant even though it was a function of stress. Parameter d was determined using an ad hoc assumption that resulted in dropping an undesired term. Further, the parameters were defined in terms of strain components in such a way as to be sensitive to coordinate axis orientation.

It is not clear from the authors' presentation what was intended when unloading took place. Anisotropy was introduced to account for stress induced oriented microcracking, but it appears that on unloading to zero stress the physically irreversible microcracking would disappear from the model and on reloading the material would behave as though it were virgin.

Neither of the nonlinear elastic models had criteria for determining when either crushing or cracking failure of concrete had occurred. Also, the models were not used to simulate structural response and so no evidence is available to establish model predictive capabilities. However, because the models are nonlinear elastic and thus fully reversible, while concrete is a microcracking material and thus experiences irreversible phenomena, it is concluded that these models are of limited practical interest and are not suitable for the prediction of the response of concrete structures to general classes of loading.

4.2.2 Plasticity Models

Several authors have developed plasticity theories for simulating concrete biaxial behavior. In small strain, small displacement plasticity total strain is assumed to have the additive decomposition,

$$\underline{\epsilon} = \underline{\epsilon}^e + \underline{\epsilon}^p , \quad (4-15)$$

where $\underline{\epsilon}^e$ and $\underline{\epsilon}^p$ are the elastic and plastic strain contributions respectively. The elastic strains are governed by the usual rules of elasticity. Plastic strains start to occur when the stress state σ at a point in a structure is sufficiently high that it satisfies

$$f(\underline{\sigma}, \underline{a}) = 0 . \quad (4-16)$$

The function f is called the yield function and is assumed to be a material property. The vector \underline{a} is a set of material parameters that characterize the amount of plasticity experienced. As the stresses increase beyond initial yield \underline{a} changes and \underline{a} is constrained to satisfy Eq. 4-16.

When plotted in stress space the yield function defines a yield surface. A material is perfectly plastic if the \underline{a} is constant in which case the yield surface has constant position, shape and size, otherwise the material is work hardening.

In metals plasticity the failure curve for biaxial loading is an ellipse centered at $\sigma_1 = \sigma_2 = 0$ with major and minor axes along $\sigma_1 = \sigma_2$ and $\sigma_1 = -\sigma_2$ respectively. Clearly the failure surface for concrete differs markedly from an ellipse. Therefore the plasticity theories of metals cannot be applied to concrete without some modification. In particular concrete failure, unlike metals failure, (1) depends on the level of hydrostatic pressure and (2) is different in compression and tension. Plasticity theories are nonlinear and the constitutive law for the plastic strain ϵ^p is incremental. A plastic material is said to satisfy normality and have an associated flow rule if an increment in plastic strain is determined by

$$\dot{\epsilon}^p = \dot{\lambda} \frac{\partial f}{\partial \sigma} \quad (4-17)$$

where f is the yield function and $\dot{\lambda}$ a deformation dependent parameter. Geometrically Eq. 4-17 implies that $\dot{\epsilon}^p$ has direction parallel to the normal to the yield surface Eq. 4-16 at the current level of stress. If $\dot{\epsilon}^p$ is not determined by an equation of the form Eq. 4-17 then the incremental curve is a non-associated flow rule.

When plasticity models are employed in finite element analyses, the analyses are performed incrementally. The total load P is divided into a series of steps or increments ΔP^k , $k = 1, 2, \dots$, and the load increments applied successively. At the beginning of an increment existing stresses and strains are known and the objective is to compute increments $\Delta \sigma$, $\Delta \epsilon$, $\Delta \epsilon^p$, Δu in stress, strain, plastic strain and displacement corresponding to load increment ΔP^k . During a load increment the structure is assumed to behave linearly with the plastic strain increment given by $\Delta \epsilon^p = \epsilon^p \Delta t$.

Perfect plasticity models. Perfect plasticity models have been proposed by Hand, Pecknold and Schnobrich⁽¹²²⁾ and by Lin and Scordelis⁽¹²³⁾. These models assumed concrete to be bilinearly

and linearly elastic, respectively, until stresses reached the biaxial failure envelope, i.e., no irreversible damage occurred to the concrete until the failure surface was reached. For compression-tension and tension-tension concrete was assumed to experience tensile cracking failure when the stress reached the failure surface. Cracking failure was simulated by setting to zero the tensile stress and stiffness parallel to the maximum tensile stress.

In the compression-compression quadrant of biaxial stress space, response subsequent to reaching the failure surface was assumed perfectly plastic and finally crushing failure occurred according to a crushing strain criterion. Hand, et al., used the failure surface obtained experimentally by Kupfer, Hilsdorf and Rüschi while Lin and Scordelis employed the von Mises yield surface of classical metals plasticity. The authors incorporated their models into nonlinear finite element codes and for several different monotonic loading analyses of plate and shell structures obtained tolerable accuracy for overall load-deflection results.

The philosophy of the perfect plasticity models was totally different from that used in the nonlinearly elastic models. In the latter, care was taken to replicate the biaxial stress-strain response up to failure while in the present models, attention was focused on response after reaching the failure surface, and from the results of the perfect plasticity models it appears that satisfactory simulation of concrete performance degradation mechanisms is a prerequisite to adequately predicting response under severe loading. Hand et al., and Lin and Scordelis did not use their models to predict structural failure loads, and did not build into their models any ability to simulate strain softening (a further performance degradation mode) and cyclic response. Finally the models could be expected to predict stresses and strains poorly because no attempt was made to incorporate stress-strain data into the models.

Three promising models of plain concrete biaxial response based on work hardening concepts were developed by Buyukozturk,⁽¹²⁴⁾ Chen⁽¹²⁵⁻¹²⁹⁾ and Murray.⁽¹³⁰⁻¹³³⁾

Work Hardening Theory of Buyukozturk. The theory of Buyukozturk was the simplest of the work hardening approaches. In the compression-compression quadrant of biaxial principal stress space the failure surface was represented by the generalized Mohr-Coulomb relationship

$$3J_2 + f'_c I + I_1^2/5 = (f'_t)^2/9 \quad (4-18)$$

where $I_1 = \sigma_x + \sigma_y$, and J_2 was the second invariant of the deviatoric stress tensor s_{ij} :

$$J_2 = \frac{1}{2} s_{ij} s_{ij} \quad , \quad s_{ij} = \sigma_{ij} - \frac{1}{3} \sigma_{kk} \delta_{ij} \quad .$$

In the compression-tension quadrants the failure surface was straight lines drawn between the uniaxial tensile and compression strengths f'_t and f'_c while in the tension-tension quadrant failure occurred when the maximum tensile stress reached f'_t .

Buyukozturk assumed that concrete response was linearly elastic up to failure for stresses in the tension-tension quadrant and applied plasticity only to the remaining quadrants. The initial yield surface, which was taken to be Eq. 4-18 with f'_c replaced by $f'_c/3$, was used in the compression-tension quadrants as well as the compression-compression quadrant. Thus the plasticity part of the Buyukozturk theory replaced Eq. 4-16 with

$$f(g, \bar{\sigma}) = 0 \quad (4-19)$$

where initial yield and ultimate failure corresponded to $\bar{\sigma} = f'_c/3$ and f'_c respectively. An associated flow rule was employed and the variation of $\bar{\sigma}$ with plastic strain was assumed derivable from uniaxial, compressive stress-strain information alone.

Buyukozturk noted that his theory predicted greater strains for a given level of stress than was found experimentally. He attributed this to the inability of his theory to account for sensitivity of the stress-plastic strain response to the ratio of

principal stresses. In his theory only a single principal stress ratio was used to define theory parameters.

It is not clear from the author's discussion how he modeled the response of concrete once the stress state reached the failure surface. Two failure types were identified - tensile cracking and compressive crushing. Tensile failure occurred whenever a tensile principal stress reached the failure surface. Subsequent to a tensile failure, the material was assumed to have zero tensile stiffness in the failed direction. However, it is not stated that the tensile stresses that existed at failure were subsequently set to zero.

Crushing failure was assumed to occur when a compressive principal stress reached the failure surface. Based on existing uniaxial data, concrete behavior after the stress reaches the failure surface should involve progressive load shedding followed by a final complete loss of stiffness and stress. No indication is given of how Buyukozturk simulated crushing.

Only analyses of monotonically loaded structures were performed using the above theory. The global response of the structures were only mildly nonlinear and, where experimental data existed, predicted failure load was seven percent less than the actual failure load.

Work Hardening Theory of Chen and Chen. Chen in a series of papers⁽¹²⁵⁻¹²⁹⁾ developed an alternative work hardening theory where initial yield and final failure surfaces were of the form

$$f(\sigma, \alpha, \beta, \gamma, \tau) = \frac{J_2 - \gamma I_1^2 + \beta I_1/3}{(1 - (\alpha I_1/3))} - \tau^2 = 0 \quad (4-20)$$

where

$$\gamma = \begin{cases} 0 & \text{for compression-compression} \\ -1/6 & \text{otherwise.} \end{cases}$$

Parameters α and β were material constants with one pair of values for compression-compression and another pair for other stress states. Initial yield, subsequent yield and final failure surfaces are shown in Figure 4-1 where it can be seen that the surfaces have discontinuous normals along the simple compression directions.

Parameter τ measured the amount of work-hardening and hence the size of the yield surface for stress states between the initial yield and final failure surfaces. It was assumed that

$$\tau^2 = g(\epsilon^p) , \quad \epsilon^p = \sum_{k=1}^n \Delta \epsilon_{ij}^k \Delta \epsilon_{ij}^k \quad (4-21)$$

where ϵ^p was the equivalent plastic strain and the plastic strain increments $\Delta \epsilon_{ij}^k$ were determined by the associated flow rule Eq. 4-17 for each step k of the incremental analysis. Chen and Chen,⁽¹²⁵⁾ paralleling the later work of Buyukozturk, could not find a unique form for the function g from experimental data and so used an averaging process. They took the biaxial data of Kupfer, Hilsdorf and Rüschi⁽³⁶⁾ and for each stress ratio σ_1/σ_2 computed f from the stress data and ϵ^p from the corresponding strain data, resulting in two families of curves, Figure 4-2. The authors then averaged the two sets of data to define g as two functions, Figure 4-3, one function being used for biaxial compression, the other for compression-tension.

The Chen and Chen theory was only applied to the simulation of plain concrete specimen responses.⁽¹²⁶⁻¹²⁸⁾ In these analyses concrete at a point failed when the stress reached the failure surface. Post failure response was modeled by maintaining the stresses that existed at failure and permitting no stress increase. With this post failure model Chen and Chen⁽¹²⁷⁾ simulated the concrete cylinder splitting test and predicted a tensile failure strength of concrete to be only seven percent greater than that given by the ASTM formula.

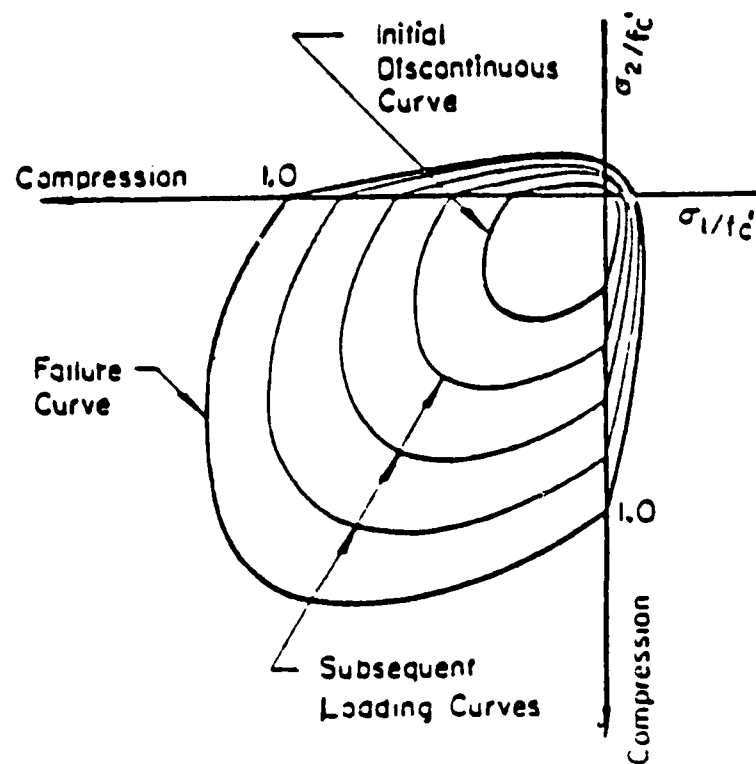


Figure 4-1. Initial and subsequent yield surfaces and failure surface proposed by Chen and Chen.

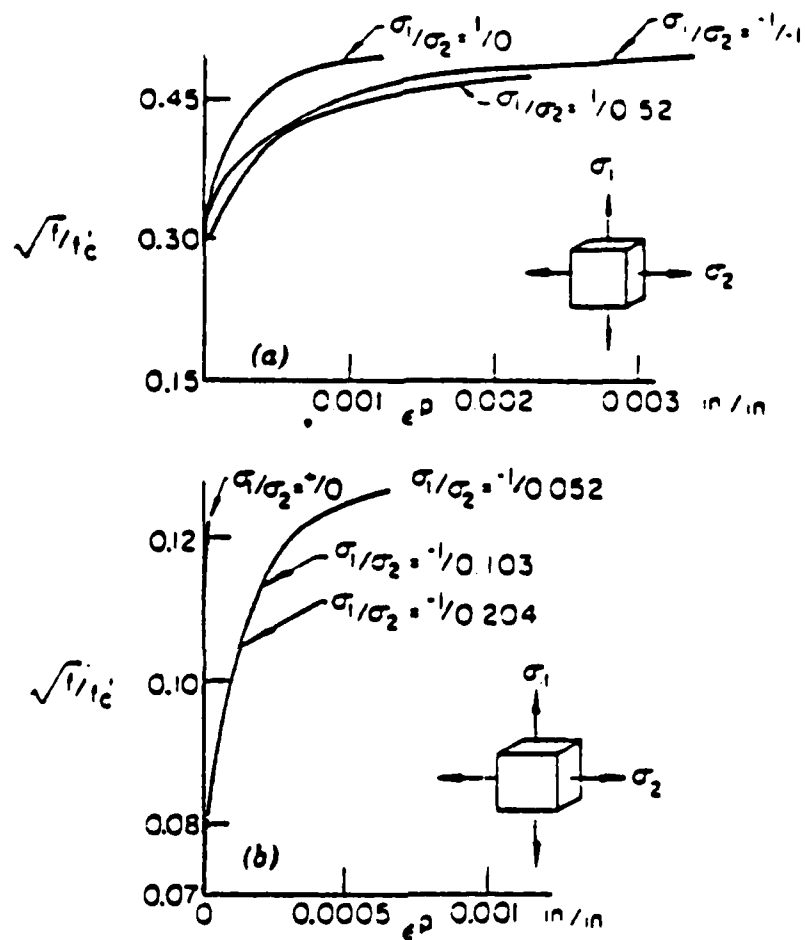


Figure 4-2. Equivalent stress versus equivalent strain curves obtained by Chen and Chen from data of Kupfer, Hilsdorf and Rüschi; (a) biaxial compression, (b) compression-tension.

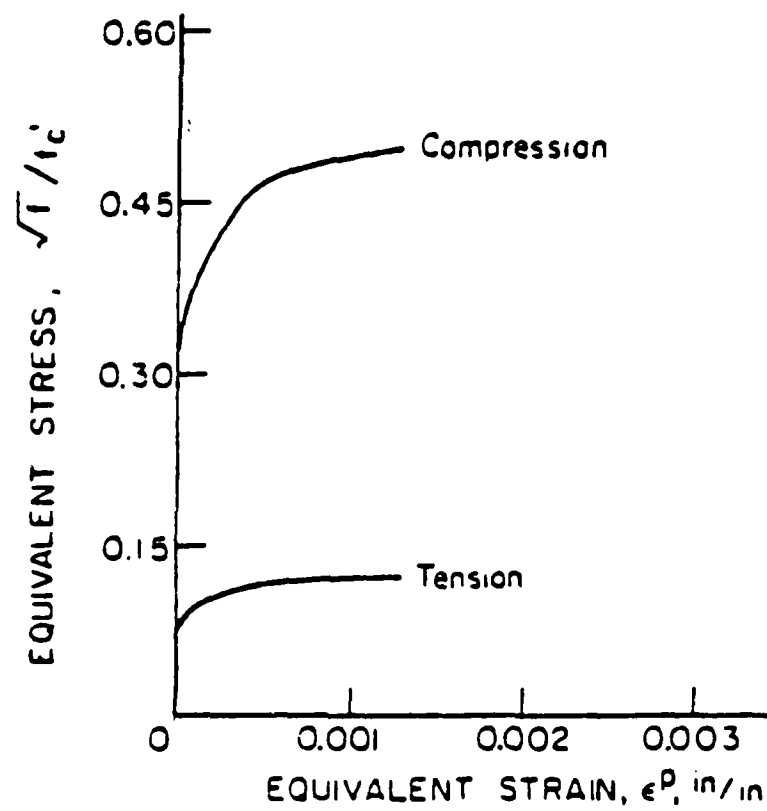


Figure 4-3. Averaged equivalent stress versus equivalent strain curves.

More recently Chen and Suzuki⁽¹²⁹⁾ incorporated a two-part failure criterion into the model. Failure was assumed to occur if either the stress satisfied

$$f(\sigma, \alpha, \beta, \gamma, \tau_u) = 0 \quad (4-22)$$

or the strain reached the strain envelope shown in Figure 4-25. The first criterion implied that the stress lie on the usual biaxial failure surface and it is not clear under what circumstances the strain failure criterion would be satisfied before the stress criterion. Two fracture types -- tensile cracking and compressive crushing -- were defined with crushing occurring only for biaxial compression states. When cracking occurred tensile stiffness and stress parallel to the maximum tensile principal stress were immediately set to zero thus simulating the presence of a crack. Compressive stiffness perpendicular to the crack as well as stiffness and stress parallel to the crack were unaffected. The possibility of subsequent additional cracking was also accounted for. When crushing occurred all stress and stiffness were immediately set to zero simulating complete loss of any load carrying capability.

Using the new failure criterion Chen and Suzuki analyzed the cylinder splitting problem and predicted a dramatic 48 percent decrease in strength relative to the previous result. Although the previous result had been reasonably accurate the authors gave no indication that they thought the new results were in error. However, it is possible that the new failure model was physically and numerically too severe especially for crushing failure. It is reasonable to assume that once peak stresses are achieved at a point, strain softening occurs resulting in a gradual shedding of stresses and reduction of stiffness rather than the immediate total shedding implied by the model. In a nonlinear finite element analysis stresses are accumulated over several loads increments so that the computer code can follow growing areas of material nonlinearity. A sudden shedding of stress cannot be accurately

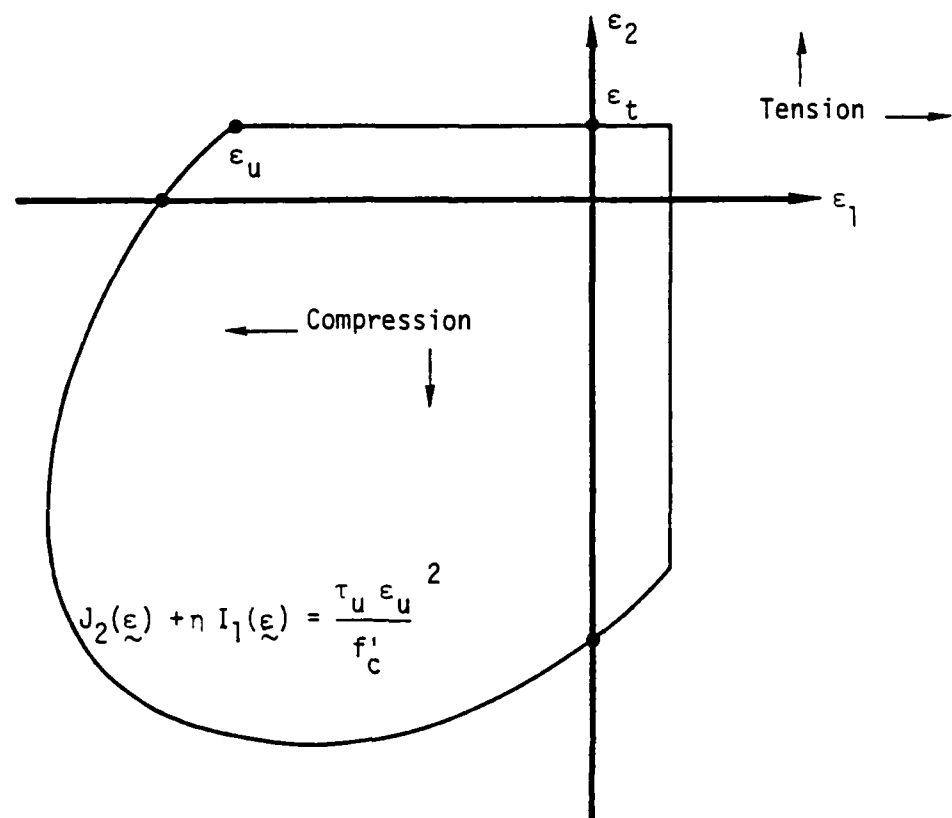


Figure 4-4. Strain based failure criterion.

simulated in one load increment. Thus spurious overloading of neighboring finite elements results and an unrealistically low fracture load predicted. The correct way to simulate concrete crushing failure is to reduce the loads in the failed region over several load increments.

The biaxial constitutive theory developed by Chen and co-workers has not been applied to reinforced concrete structures or to the modeling of cyclic effects. Currently, the post-peak failure model appears to be too severe. Thus usefulness of the theory lies in predicting the stress-strain response of biaxially loaded plain concrete structures for cases where significant material nonlinearities are present but complete failure is not anticipated.

Additionally it is undesirable to have a yield surface with a discontinuous normal along the uniaxial compression directions since it complicates the fitting of an associated flow rule to uniaxial data.

Work Hardening Theory of Murray et al. The novel feature of the theory developed by Murray et al.,⁽¹³⁰⁾ was the definition of three hardening functions. One function, α_c , accounted for hardening in compression while the remaining two, α_{t1} , α_{t2} , allowed tensile hardening to occur independently in the two principal stress directions. The initial yield, subsequent yield and final failure surfaces were given by

$$f(\underline{a}, \underline{a}) = 0 \quad (4-23)$$

where $\underline{a} = (\alpha_1, \alpha_2, \alpha_3) = (\alpha_1, \alpha_{t1}, \alpha_{t2})$ denoted the three hardening functions. In an earlier version of the theory,⁽¹³¹⁾ only one tensile hardening function was used. The failure surface, shown in Figure 4-5, was taken to be that of Kupfer, Hilsdorf and Rüschi, and was modeled piecewise using four or five complicated functions.

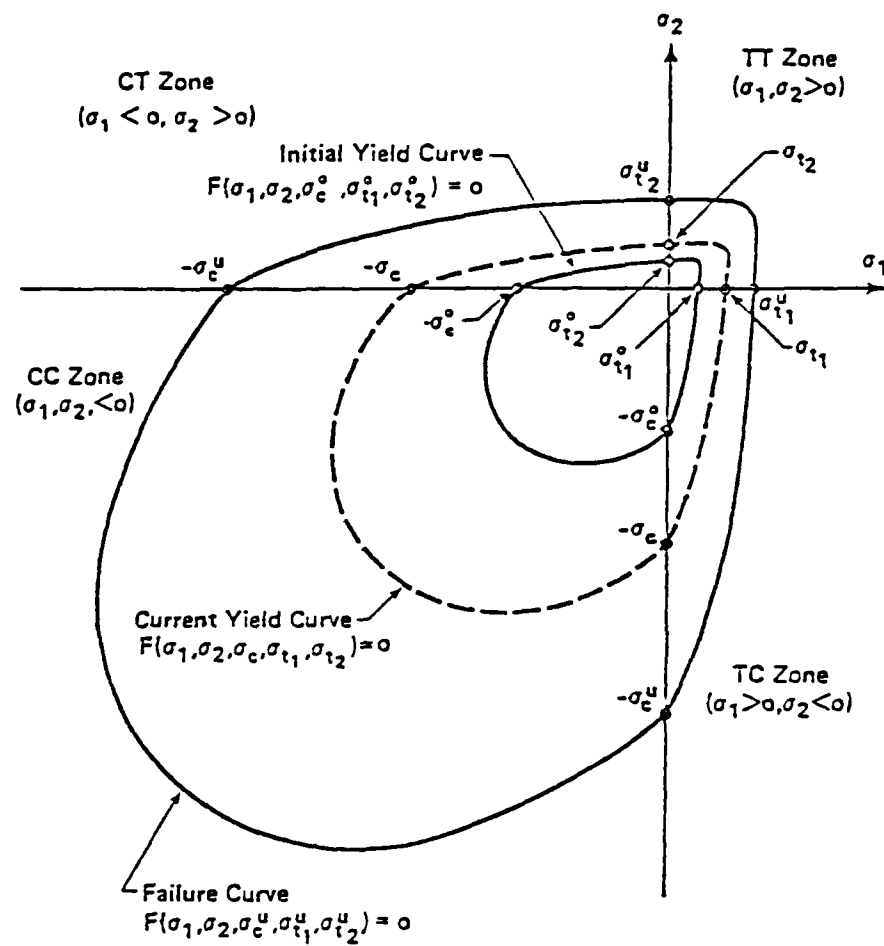


Figure 4-5. Initial yield, subsequent yield and failure curves.

Plastic strain increments were governed by an associated flow rule and the hardening parameters were assumed to vary according to

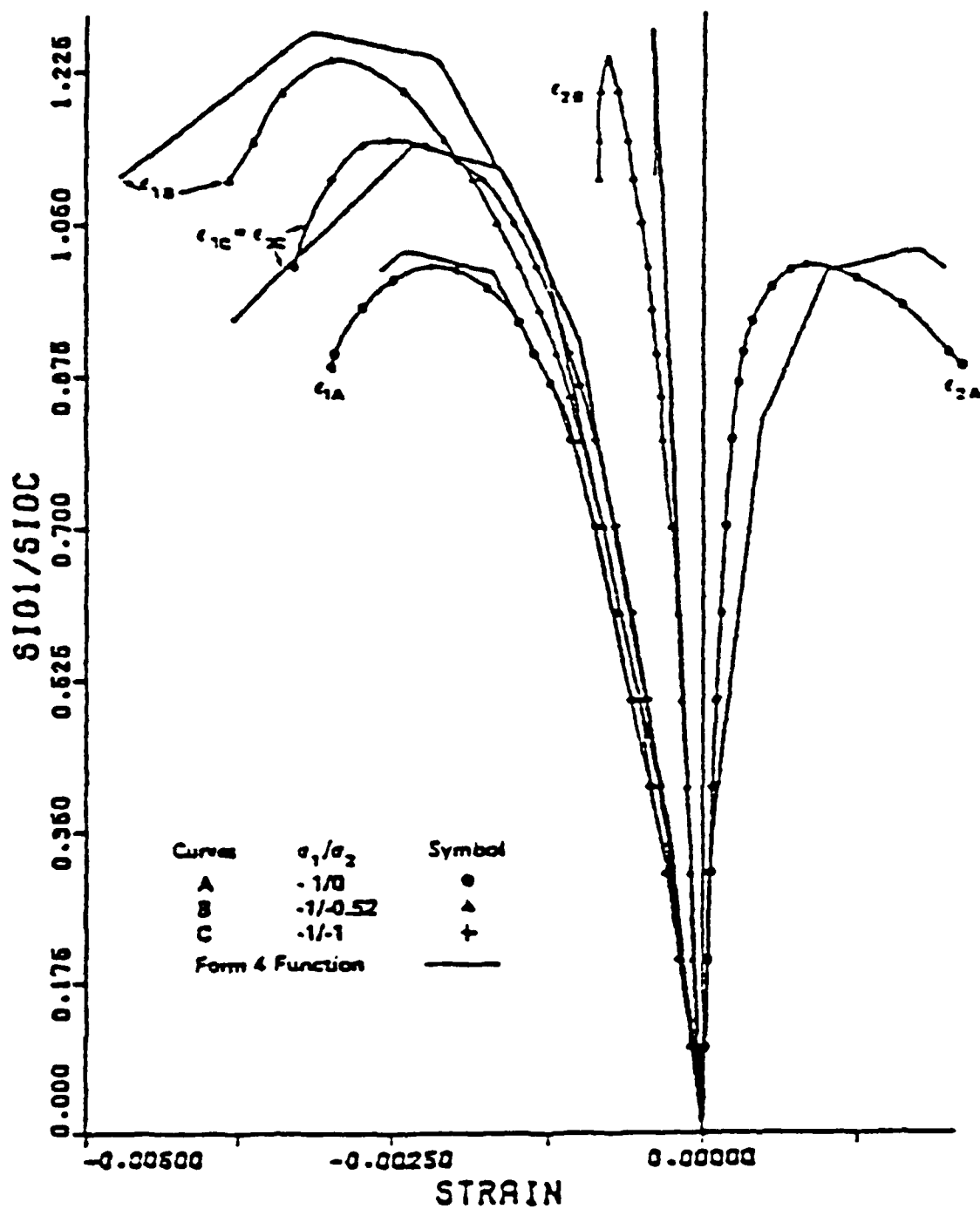
$$\alpha_i = \bar{\alpha}_i + \beta_i(\gamma_i), \quad i = 1, 2, 3$$

$$\gamma_i = \sum_k \delta_i^k \Delta \epsilon^k_p, \quad \Delta \epsilon^k_p = (\Delta \epsilon_{ij}^k \Delta \epsilon_{ij}^k)^{1/2}$$

$$\delta_1^k + \delta_2^k + \delta_3^k = 1 \quad (4-24)$$

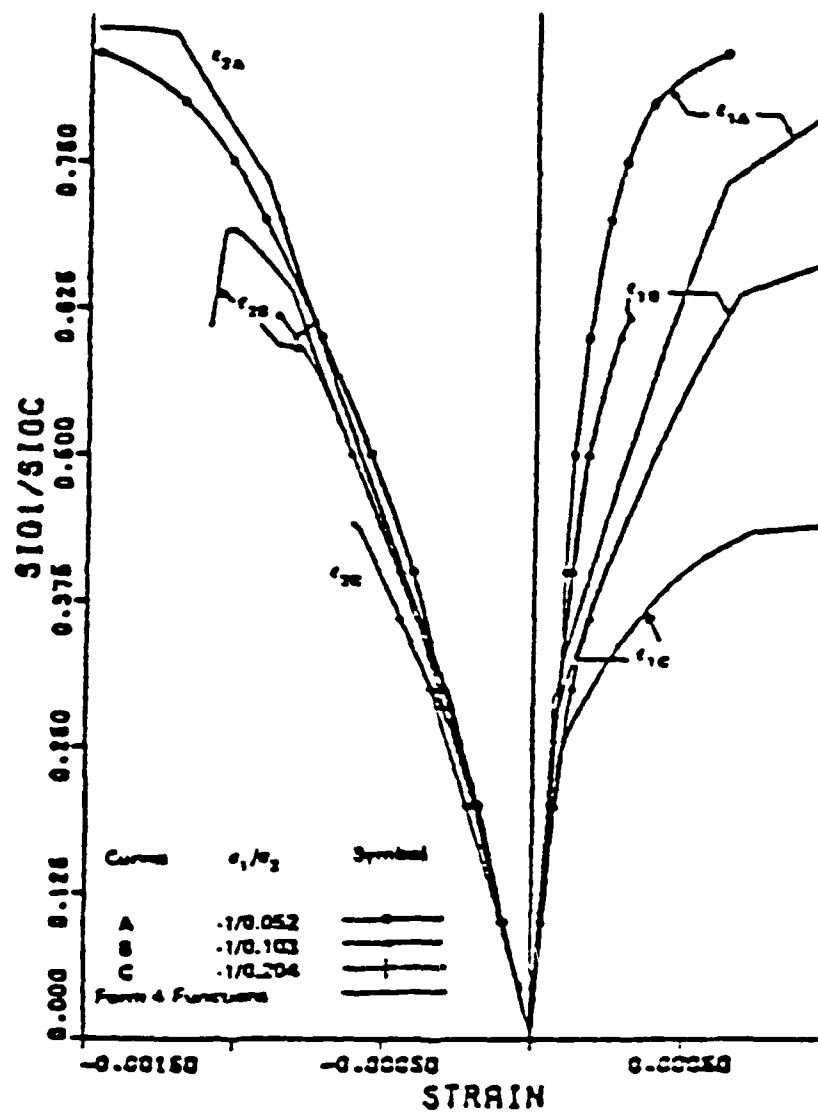
where $\bar{\alpha}_i$ were values of α_i at initial yield, β_i were hardening functions, γ_i were equivalent plastic strain measures, k denoted load increment number, $\Delta \epsilon^k_p$ was the total equivalent plastic strain increment for increment k , and the ' δ 's were increment dependent apportioning constants. Hardening function β_1 , was determined using only uniaxial compression data in the same manner as Chen and Chen. The other hardening functions $\beta_2 \equiv \beta_3$ were obtained from uniaxial tension data. All three functions included a strain softening branch. The ' δ 's were constants with values from zero to one. When the stress state lie in the biaxial compression {tension} quadrant only compressive tensile equivalent plastic strain measure(s) were changing and $\delta_2^k = \delta_3^k = 0$ { $\delta_1^k = 0$ }. In the compression-tension quadrants δ_2^k and either δ_3^k or δ_1^k were non zero and were determined by the ratio of the existing principal stresses.

Murray and co-workers compared the biaxial stress-strain response predicted by the theory with the experimental data of Kupfer, Hilsdorf and Rüschi, Figure 4-6. Since the hardening functions were based on uniaxial data it is not clear why the correlation with uniaxial results is poorer than with biaxial compression results. Also, the theory does not predict the tensile response accurately in compression-tension. In general, results are best for biaxial compression and again it is seen that theoretical predictions for biaxial stress-strain are not uniformly accurate when the hardening functions are derived from only uniaxial data.



(a)

Figure 4-6. Comparison between theory of Murray et al, and data of Kupfer, Hilsdorf and Rüsck: (a) biaxial compression (b) compression-tension.



(b)

Figure 4-6. (Continued) Comparison between theory of Murray et al., and data of Kupfer, Hilsdorf and Rüsch: (a) biaxial compression, (b) compression-tension.

An analysis of a prestressed concrete panel was performed using the constitutive theory; a discussion of the steps necessary to incorporate the theory into a computer code is given in References.^(132,133) In the analysis, results for load versus deflection were found to be sensitive to how the post peak tensile behavior was simulated. Initially, in the tension-tension quadrant, a linearly elastic - perfectly plastic model was used. Thus cracking and concomitant stress reduction were not considered. However, predicted structural response was significantly stiffer than that observed experimentally. When concrete tensile response was subsequently simulated using a strain softening branch, so that tensile stresses were shed after reaching a peak value, predicted results matched experimental quite closely. Thus again, it is seen that to adequately predict gradual softening of a structure's response it is necessary to incorporate into the model mechanisms for progressive performance degradation.

Murray's theory exhibits the same shortcomings as previously discussed theories; an inability to simulate monotonic biaxial stress-strain response with uniform accuracy and a lack of a cyclic response model. Additionally no details are given for handling final crushing or tensile cracking. Finally, compared to the models of Buyukozturk and Chen and Chen, the mathematical descriptions of yield and failure surfaces are overly complicated. Therefore, while the theory does accurately predict monotonic structural response there is nothing to recommend the theory over the previous, simpler theories.

Of the three work hardening, plasticity theories of concrete response none is obviously superior in its predictive capabilities. Thus the Chen and Chen model appears preferable because it simulates concrete stress-strain and failure using a relatively simple mathematical representation.

4.2.3 Biaxial, Cyclic Response Models

None of the preceding theories attempted to simulate the cyclic response of concrete when subjected to biaxial loading.

Darwin and Pecknold^(134,135,136) have been the only authors to develop a concrete biaxial constitutive theory with the principal objective of modeling cyclic response. The theory was not based on plasticity theory concepts but rather was an extension of uniaxial results previously reported by Saenz,⁽¹³⁷⁾ for monotonic loading and by Karsan and Jirsa⁽¹³⁸⁾ for cyclic loading. An incremental stress-strain law was postulated since the model was intended for use in nonlinear finite element codes. For a single increment of externally applied load or displacement the stress and strain increments were assumed linearly related and governed by the orthotropic relation:

$$\begin{bmatrix} d\sigma_1 \\ d\sigma_2 \\ d\tau \end{bmatrix} = \frac{1}{1-\nu^2} \begin{bmatrix} E_1 & \nu \sqrt{E_1 E_2} & 0 \\ \nu \sqrt{E_1 E_2} & E_2 & 0 \\ 0 & 0 & (1-\nu^2)G \end{bmatrix} \begin{bmatrix} d\epsilon_1 \\ d\epsilon_2 \\ d\gamma \end{bmatrix} \quad (4-25)$$

where at each point in the structure the coordinate axes were aligned with principal stress axes at the beginning of the increment. In the equation $d\sigma_1$ and $d\sigma_2$ were increments in stress components referred to the local coordinate system and not increments in principal stress components. Moduli E_1 and E_2 were assumed dependent of the existing state of strain and G was defined in terms of E_1 , E_2 and ν so as to be independent of local coordinate axis orientation.

The strain dependence of E_1 and E_2 was accounted for by first defining 'equivalent strains' ϵ_{1u} , ϵ_{2u} . At the end of the n^{th} load increment these strains were given by

$$\epsilon_{iu} = \sum_{k=1}^n \frac{\sigma_i^k - \sigma_i^{k-1}}{E_i^{k-1}} \quad i = 1, 2 \quad (4-26)$$

Here σ_i and E_e were the principal stress and tangent modulus in the i^{th} direction at the end of the k^{th} load increment. For initial loading up to maximum attainable stress the authors assumed

$$\sigma_i = \frac{\epsilon_{iu} E_0}{1 + \left[\frac{E_0}{E_s} - 2 \right] \frac{\epsilon_{iu}}{\epsilon_{ic}} + \left(\frac{\epsilon_{iu}}{\epsilon_{ic}} \right)^2} \quad (4-27)$$

where E_0 was the concrete initial tangent modulus. Further $E_s = \sigma_{ic}/\epsilon_{ic}$ where σ_{ic} was the stress on the Kupfer, Hilsdorf and Rüsç failure surface for the current principal stress ratio, σ_1/σ_2 and ϵ_{ic} was the corresponding strain. Eq. 4-27 was a generalization of the uniaxial model of Saenz.⁽¹³⁷⁾ E_i was then defined by

$$E_i = d\sigma_i/d\epsilon_{iu} \quad (4-28)$$

To complete the monotonic loading theory mathematical representations were developed for the Kupfer, Hilsdorf and Rüsç failure surface and for the corresponding strain envelope.⁽¹³⁴⁾ Also Poisson's ratio ν was assumed stress dependent for uniaxial compression and biaxial tension-compression and equal to 0.2 otherwise. Because extensive use was made of the Kupfer, Hilsdorf and Rüsç data in the definition of the functional forms of model parameters, the constitutive model replicated that data very well.

The principal objective of Darwin and Pecknold was to simulate cyclic biaxial response in the post-peak stress region. Since no cyclic biaxial data existed, the authors used as their starting point the uniaxial data of Karsan and Jirsa.⁽¹³⁸⁾ Karsan and Jirsa found that the peak stresses for successive cycles of uniaxial, compressive load lay approximately on a single "envelope" curve, Figure 4-7, and that upon unloading to the null stress state, Figure 4-7, the residual plastic strain ϵ_{pi} was related to the strain ϵ_i on the envelope curve at the point of unloading by

$$\frac{\epsilon_{pi}}{\epsilon_{iu}} = 0.145 \frac{\epsilon_i^2}{\epsilon_{cu}} + 0.13 \frac{\epsilon_i}{\epsilon_{iu}} \quad (4-29)$$

where ϵ_{iu} was the uniaxial strain corresponding to the uniaxial compressive strength.

Karsan and Jirsa also defined a 'common point' curve. When unloading occurred from any point on or above the common point curve, such as points 1, 3, 4, 5, 6 in Figure 4-8, the reloading curve always intersected the unload curve where the unload curve intersected the common point line (i.e., points A, B, C, D). When the initial point of unloading was beneath the common point curve (i.e., points 7, 8) the reload curve always passed through the point of initial unload.

Darwin and Pecknold incorporated the residual plastic strain relation and the common point curve into their theory, and in addition introduced a 'turning point' curve which controlled the width of unload-reload loops and hence the amount of energy dissipated during a load cycle. A typical piecewise linear load cycle ABCDEF is shown in Figure 4-9. Segment A B joins the envelope and turning point curves and has the same slope as the concrete initial tangent modulus E_0 . The intersection of A B with the common point curve defines point E. Point D is defined by Eq. 4-29. Unloading from B to the null stress state at C is along a trajectory parallel to D E. Subsequently the strain is reduced to point D before any reloading can occur. Monotonic reloading from D terminates at F after which the response follows the envelope curve. Figure 4-10 shows that by judicious choice of the common and turning point curves, Darwin and Pecknold were able to match the Karsan and Jirsa data reasonably well.

Darwin and Pecknold also included post-crushing and fracture behavior in their model. Crushing failure occurred when the equivalent strain in either principal direction reached $4\epsilon_{cu}$. Tensile

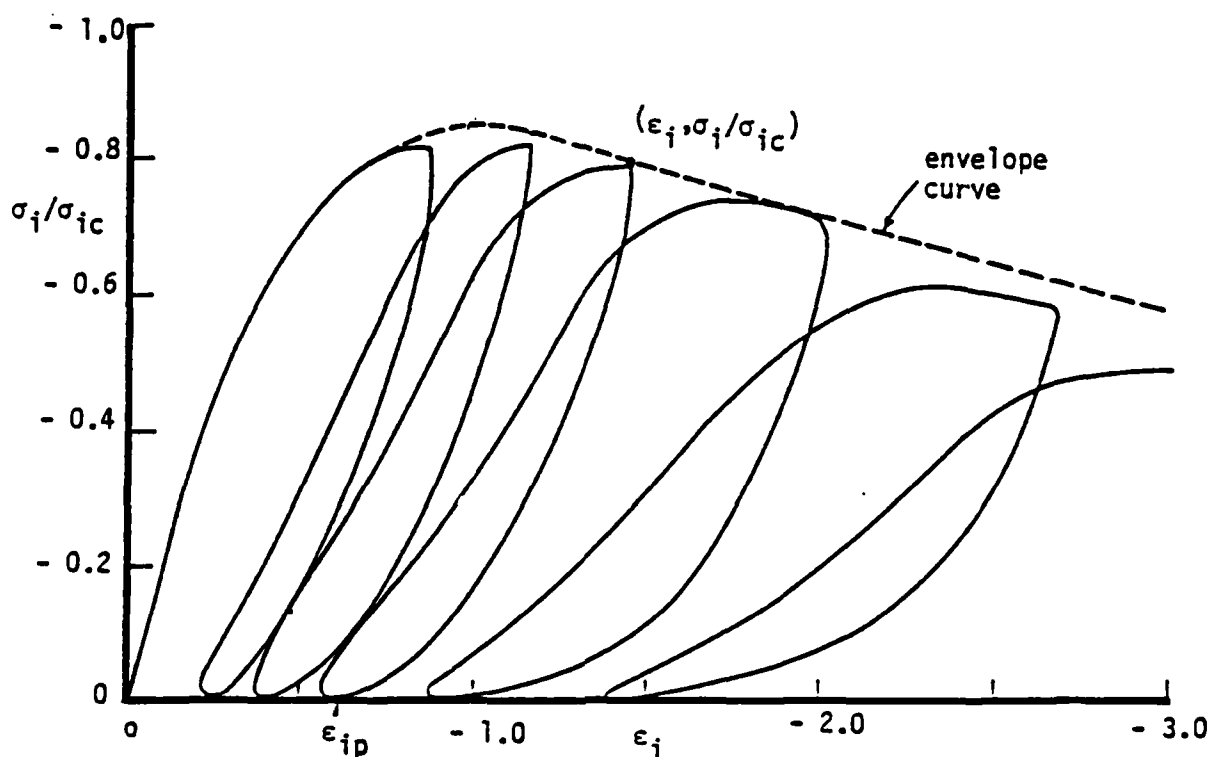


Figure 4-7. Uniaxial, cyclic, compressive stress-strain history showing envelope curve.

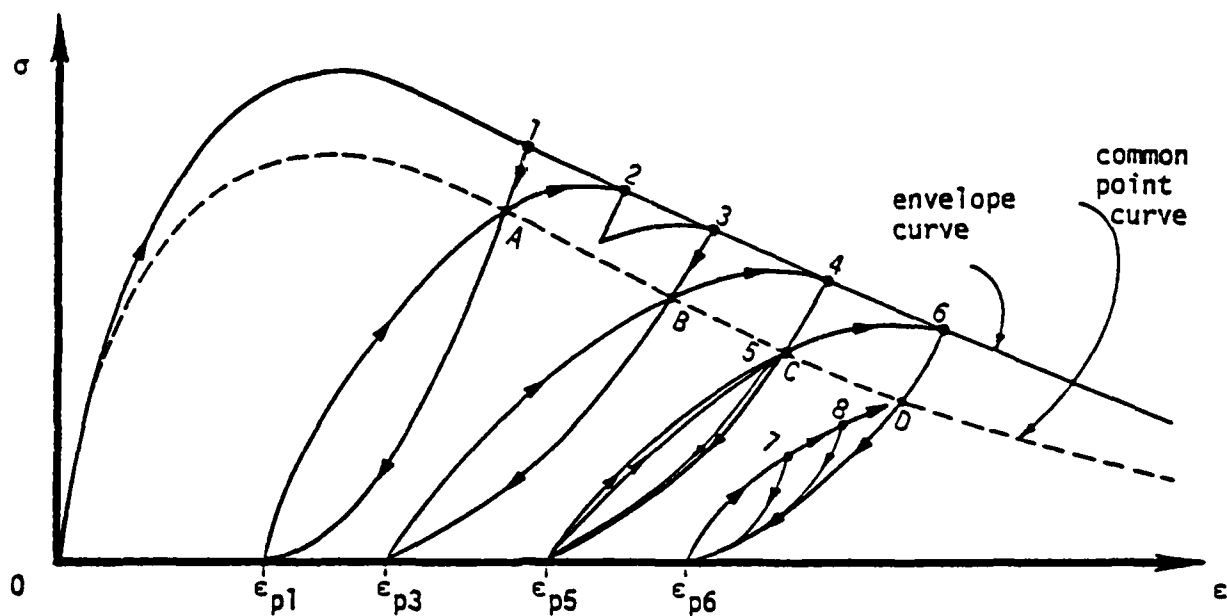


Figure 4-8. Uniaxial, cyclic, compressive stress-strain history showing loop closure on or below common point curve.

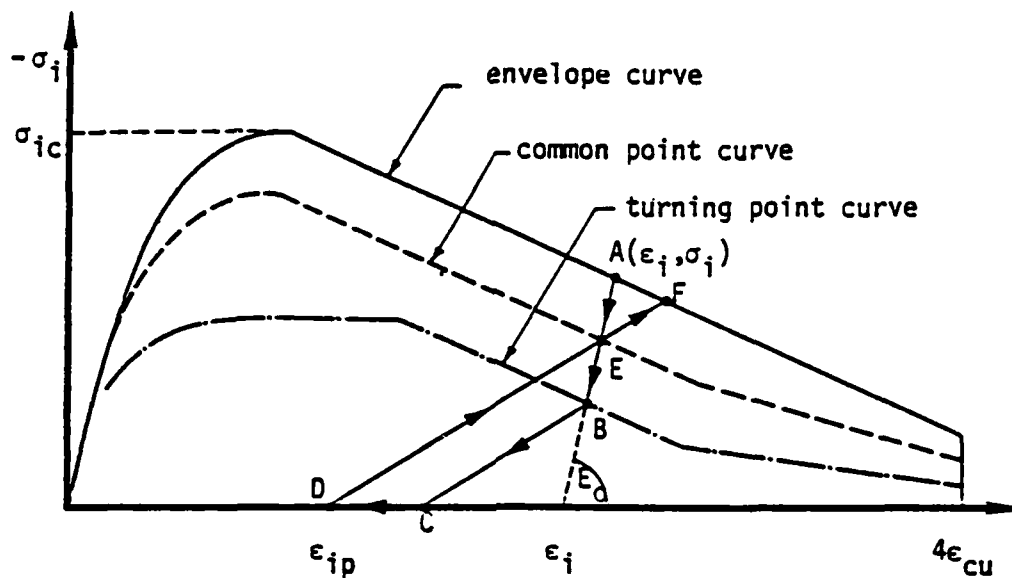


Figure 4-9. Piecewise linear description of stress-strain cycle.

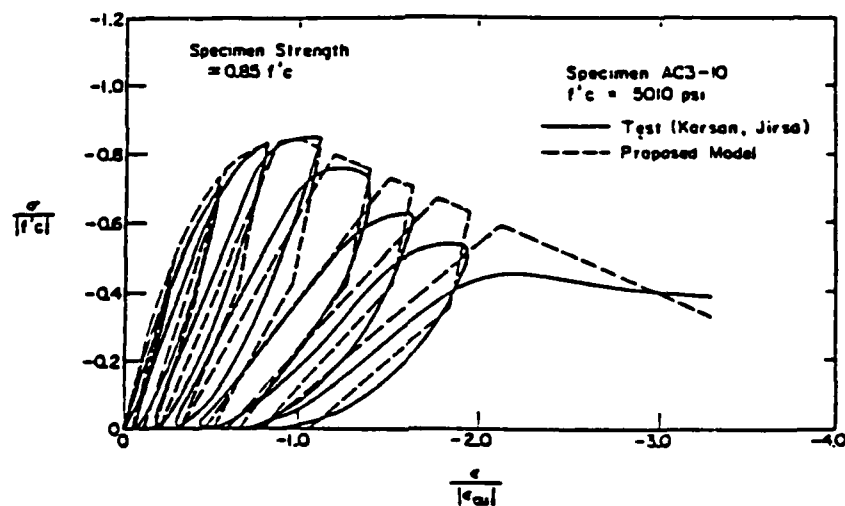


Figure 4-10. Comparison of Darwin and Pecknold proposed model results with experimental data of Karsan and Jirsa.

failure occurred along the two principal stress directions independently. After tensile cracking, tensile stiffness perpendicular to a crack was null, compressive stiffness was unchanged, shear stiffness parallel to the crack was reduced, but not zero, and cracks were allowed to open and close.

Nonlinear finite element analyses were performed and, using the developed theory, cyclic loading of reinforced concrete panels were modeled. In Figure 4-11 is shown a comparison between the experimental load-deflection results of Cervinka and Gerstle,⁽¹³⁹⁾ and the predictions of Darwin and Pecknold.⁽¹³⁵⁾ Results for the first one and a half load cycles are shown and the agreement between theory and experiment was very satisfactory. The authors attributed the quality of the agreement to the inclusion in their theory of, (i) cyclic effects, (ii) independent tensile failure in the two principal stress directions.

4.3 TRIAXIAL CONSTITUTIVE MODELS

Triaxial constitutive models of concrete fall into several categories. The simplest approaches are little more than nonlinear elasticity while the most complicated defy clear non-mathematical discussion. In the following the theories are divided into

- variable modulus
- hypoelasticity
- elastic plastic
- plastic fracturing
- endochronic.

4.3.1 Variable Modulus Models

Theories have been developed by Ahmad and Shah,⁽¹⁴⁰⁾ Decolin, Crutzen and Dei Poli,⁽¹⁴¹⁾ Elwi and Murray⁽¹⁴²⁾ and Kotsovos and Newman.⁽¹⁴³⁾ Typically the models are parameterized curve fits lacking any justification other than they fit selected

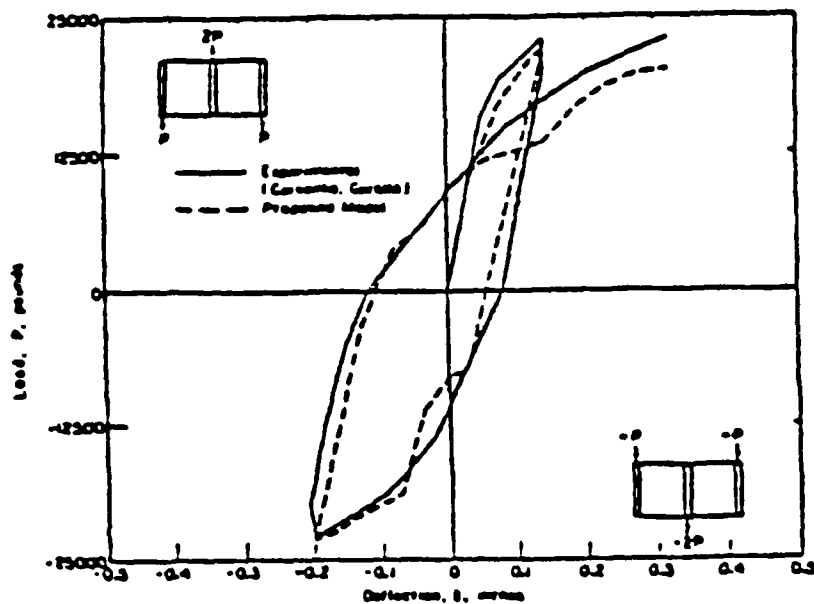


Figure 4-11. Comparison of cyclic panel response predicted by proposed model of Darwin and Pecknold with experimental data of Cervanka and Gerstle.

sets of test data. Ahmad and Shah generalized the uniaxial curve fit of Saenz Eq. 4-4. Elwi and Murray took the same curve fit and defined an incremental stress-strain law for axisymmetric deformations only. The approach paralleled that of Darwin and Pecknold (subsection 4.2.3). Cedolin et al. and Kotsovos and Newman generalized linear elasticity by making the bulk and shear moduli functions of stress invariants I_1 and J_2 . The principal shortcomings of these models are

- They are only designed for monotonic load histories since they unload along a loading path and preclude irreversible effects.
- Most assume strain and stress principal axes always coincide.
- They are unsuitable for insertion into nonlinear finite element codes because they are formulated only in terms of principal stress/strain directions which typically do not coincide with problem coordinate axes. Additionally most models are total stress-total strain relations while finite element codes require nonlinear models be written in terms of incremental stress and strain quantities.
- They have not been used to model the response of even the simplest structures.

4.3.2 Hypoelastic Models

Coon and Evans⁽¹⁴⁴⁾ starting from the general representation of a hypoelastic material developed an incremental stress-strain law of the form

$$d\sigma_{ij} = A_{ijkl} (\sigma_{pq}) d\epsilon_{kl} \quad (4-30)$$

After assuming concrete to be isotropic the authors reduced A_{ijkl} to a linear function of stress depending on seven material constants. A unique feature of Eq. 4-30 was stress induced anisotropy. Concrete failure was not an additional assumption but rather occurred when

$$\det A_{ijkl} = 0 \quad . \quad (4-31)$$

i.e., when additional strain could occur without stress change. The theory was used to replicate the experimental data of Richart, Brandtzaeg and Brown^[72] and of Gardner.^[146] The seven constants in A_{ijkl} were assigned values without discussion and the failure surface was circular on planes of constant pressure. The correlation obtained between stress-strain response predicted by Eq. 4-31 and the experimental data was less satisfactory than that customarily found using other theories. Finally, at any stress state, loading and unloading directions in stress space were parallel. All in all this theory has little to recommend it.

4.3.3 Elastic Plastic Models

The biaxial plasticity models discussed in section 4.2.2 can be extended to triaxial stresses; however their failure surfaces on planes of constant pressure are circles. Two theories that were explicitly developed for triaxial application but still have this weakness are due to Green and Swanson^[76] and Dimaggio and Sandler.^[147]

The first theory assumed that the elastic region of stress space was bounded by two surfaces, F_1 and F_2 , given by

$$\begin{aligned} F_1 &= \sqrt{J_2} + g(I) - K_1 \quad , \quad I = \sigma_{kk} \\ F_2 &= \frac{J_2}{2} + r^2 \frac{I^2}{2} - K_2 \end{aligned} \quad (4-32)$$

$$g(x) = -1000. \left[12.2 - 11e^{(x/40000)} \right] \left[1 - e^{\frac{(x-800)}{700}} \right]$$

Parameter r was a constant while K_1 and K_2 were strain hardening functions that controlled the expansion (i.e., motion) of the surfaces. By using the two functions F_1 and F_2 the authors were

able to predict both specimen contraction (surface F_1) and dilatation (surface F_2) that occurs in uniaxial compression. Failure was governed by assigning a limiting value to K_1 . Strain hardening functions K_1 and K_2 were assumed given by

$$d\epsilon^P = h_1 dK_1, \quad d\epsilon_{VC}^P = h_2 dK_2 \quad (4-33)$$

where $h_1 = h_1(I, T_2)$, $h_2 = (I_1, J_2)$, $d\epsilon^P = \frac{1}{2} d\epsilon_{ij}^P d\epsilon_{ij}^P$.

Thus dK_1 was related to the total plastic strain movement while dK_2 was related only to $d\epsilon_{VC}^P$, the increment in plastic plastic volumetric shrinkage arising from motion of surface F_2 . The authors found it difficult to justify the choice of Eq. 4-33. An associated flow rule was assumed, so

$$\dot{\epsilon}_{ij}^P = \dot{\Lambda}_1 \frac{\partial F_1}{\partial \sigma_{ij}} + \dot{\Lambda}_2 \frac{\partial F_2}{\partial \sigma_{ij}} \quad (4-34)$$

and standard plasticity procedures were used to obtain an incremental stress—strain law. The theory was applied to the simulation of specimen data with mixed success. As a test of the theory a set of thick-walled cylinders subject to axial compression and internal pressure were tested and then modeled. Again some of the tests were simulated well while other correlated poorly and the authors were unable to explain unevenness in the correlation.

The theory of Green and Swanson had some obvious shortcomings

- Failure surface was axisymmetric about pressure axis.
- Unloading and reloading was entirely elastic.
- No strain softening once the strength envelope was reached.
- No hysteresis.

AD-A166 087

ON THE DEVELOPMENT OF CONSTITUTIVE RELATIONS FOR PLAIN
AND REINFORCED CONCRETE(U) S-CUBED LA JOLLA CA
G A HEGEMIER ET AL 09 APR 82 555-R-82-5495

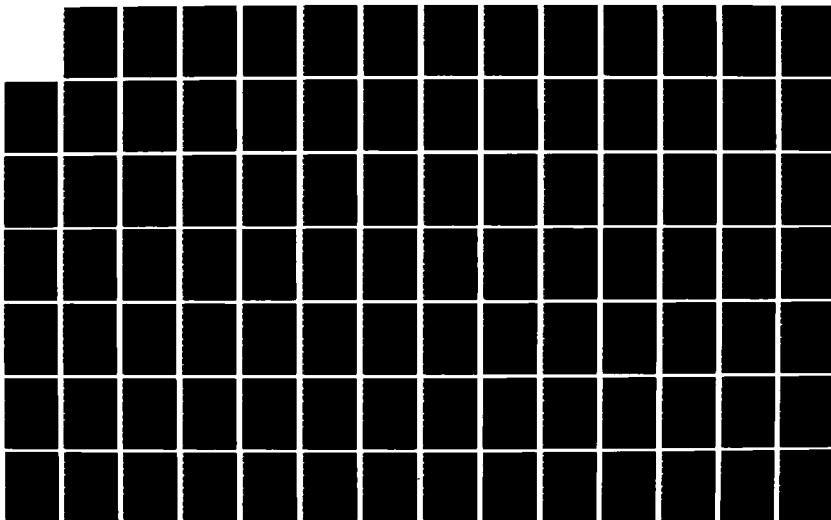
3/4

UNCLASSIFIED

DNA-TR-81-65 DNA001-81-C-0181

F/G 11/2

NL



The theory derived by Dimaggio and Sandler^[147] was originally developed to model soils and was the prototype on which Green and Swanson based their two-surface models. The model derived by Dimaggio and Sandler for concrete became the "Weidlinger Associates" model and was even simpler than that of Green and Swanson in that

- surface F_1 was absent
- surface F_2 was fixed.

Consequently this model could not predict irreversible volume compaction under hydrostatic compression and could not simulate any non-linear response in concrete, prior to failure. Indeed concrete uniaxial response was modeled as elastic-perfectly plastic. In addition the model suffered from all the faults of the Green and Swanson theory. Clearly as a theory to model the complex response of plane concrete the 'Weidlinger Associates' theory was totally inadequate. However, of all concrete models developed this one has seen the most intensive application because the authors assert that uncertainties in structural data obviate the need for more complex models.

4.3.4 Plastic-Fracturing Models

Dougill^[148] developed a theory of elastic-fracturing solids. The model had the following attributes:

- 1) Loss of stiffness due to stable progressive fracturing during loading.
- 2) Linear elastic unload-reload with a tangent stiffness that degrades as internal fracturing progresses - i.e., process dependent elastic moduli.
- 3) No residual strains when stresses are removed, i.e., complete recovery.

Figure 4-13 shows the cyclic uniaxial response predicted by the theory.

Characteristics 1) and 2) are observed in concrete and can be attributed to progressive microcracking or microfracturing. Characteristic 3) is unrealistic for concrete and Dougill noted in his closing paragraph that his fracturing theory "in combination with a hardening or perfectly plastic solid would seem most appropriate."

Bazant and Kim^[149] subsequently combined plasticity with Dougill's elastic-fracturing theory to develop a plastic-fracturing model of plain concrete response. The plasticity portion of the model was a non-associated form of the pressure-dependent Drucker-Prager theory. For monotonic loading Bazant and Kim assumed a loading function of the form

$$\bar{\tau} + g(\sigma) - H = 0 \quad (4-35)$$

where

$$\bar{\tau}^2 = \frac{1}{2} s_{ij} s_{ij} \quad , \quad \sigma = \sigma_{kk}/3 \quad . \quad (4-36)$$

Function H accounted for plastic hardening, though was not explicitly needed. Eq. 4-35 was used only as a loading surface in the sense that it was used to motivate a non-associated flow rule for plastic strains. The flow rule was

$$\dot{\epsilon}_{ij}^p = \dot{\Lambda}^p \left(\frac{s_{ij}}{2\bar{\tau}} + \frac{1}{3} \beta \delta_{ij} \right) \quad (4-37)$$

where

$$\dot{\Lambda}^p = \frac{G s_{ij} \dot{\epsilon}_{ij} + \bar{\tau} K \beta' \dot{\epsilon}_{kk}}{\bar{\tau} (G + K \beta \beta' + h)} \quad (4-38)$$

For an associated flow rule $\beta = \beta' = \partial g / \partial \sigma$. However, the authors independently specified β so that β could account for plastic slip induced dilatancy while β' was identified as an internal friction

coefficient. In the definition of $\dot{\Lambda}^p$, G and K were the elastic shear and bulk moduli, \dot{e}_{ij} was the deviatoric strain increment and h was a plastic tangent modulus associated with H in Eq. 4-35.

To the plasticity theory the authors added an elastic-fracturing theory which accounted for stiffness degradation and strain softening. Dougill's work was taken as the point of departure. Linear elasticity is characterized by $s = 2Ge$, $\sigma = 3K\epsilon$, $\epsilon = \epsilon_{kk}/3$. In the fracturing theory elasticities G and K degraded as strain accumulated because of internal fracturing. The incremental variable modulus constitutive equations were obtained by differentiating the linear elastic laws:

$$\dot{s} = 2G \dot{e} + 2\dot{G} e, \quad \dot{\sigma} = 3K\epsilon + 3\dot{K}\epsilon \quad (4-39)$$

In Eq. 4-39 the fracturing stresses were identified as

$$\dot{s}^f = -2\dot{G}e, \quad \dot{\sigma}^f = -3\dot{K}\epsilon \quad (4-40)$$

To obtain constitutive equations for G and K the existence of a fracturing loading surface was assumed:

$$\phi(\epsilon) = \bar{\gamma} + k(\epsilon) - H_2, \quad \bar{\gamma}^2 = \frac{1}{2} e_{ij}e_{ij} \quad (4-41)$$

Function H_2 characterized the hardening of the surface but did not need to be explicitly identified. Analogous to the plasticity portion of the model the fracturing stress increments were first assumed derived from an associated law:

$$\dot{s}^f \equiv \dot{s}^f + \dot{\sigma}^f \mathbf{1} = \dot{\Lambda} \partial\phi/\partial\mathbf{g} = \frac{\dot{\Lambda} e}{2\bar{\gamma}} + \frac{1}{3} k' \mathbf{1} \quad (4-42)$$

where $k' = dk/d\epsilon$. To improve the theory fit to experimental data, associativity was relaxed and the constitutive assumption

$$\dot{s}^f = \frac{\dot{\lambda} \epsilon}{2\gamma}, \quad \dot{\sigma}^f = \frac{\alpha \dot{\lambda}}{3} \quad (4-43)$$

used. During loading the strain remained on the loading surface Eq. 4-47 and so $\dot{\phi} = 0$. The authors assumed $\dot{H}_2 = \dot{\lambda}\phi$ and thus obtained

$$\dot{\lambda} = \frac{1}{\phi} (\dot{\gamma} + k'\epsilon) \quad (4-44)$$

The plastic-fracturing theory of Bazant and Kim was achieved by combining the two preceding theories as follows:

$$\dot{s} = 2G(\dot{\epsilon} - \dot{\epsilon}^p) - \dot{s}^f \quad (4-45)$$

$$\dot{\sigma} = 3K(\dot{\epsilon} - \dot{\epsilon}^p) - \dot{\sigma}^f$$

Thus stress was influenced by both plastic slip and elastic fracturing. Plastic and cracking effects were additive and interacted through elasticities G and K . The theory embodied in Eqs. 4-35 to 4-45 contained six functions, β' , β , h , α , k , α' , which were obtained analytically through an extensive curve fitting exercise. The functions depended on 22 constants most of which depended on f' . Additionally an initial value of Poisson's Ratio had to be specified.

From Eq. 4-45 it was possible to develop an expression of the form

$$\dot{\sigma}_{ij} = C_{ijkl} \dot{\epsilon}_{ij} \quad (4-46)$$

Thus the theory appeared attractive for finite element applications except that the non-associated laws implied a non-symmetric stiffness matrix. Consequences of this asymmetry for incorporation into a code have not been explored.

In the same paper the concept of jump-kinematic hardening was introduced so that the unload-reload loops seen in concrete uniaxial cyclic compression could be modeled. As the name suggests the centers of the plasticity and fracturing loading surfaces ($\underline{\alpha} = \underline{\alpha}$, $\underline{\epsilon} = \underline{\beta}$) were instantly repositioned when the loading direction was changed. Rules for moving $\underline{\alpha}$ and $\underline{\beta}$ were given and implicit in the presentation was the assumption that during unloading concrete had no finite elastic region.

The authors presented extensive evidence of the ability of their constitutive representation to fit experimental data. This fit resulted from the judicious choice of the 22 constants and six complicated functions. The theory appears straightforward to implement and should be easy to apply since the only free parameter is f'_c . However the theory has not been incorporated into a finite element code and so it is impossible to assess theory predictive capability.

4.3.5 Endochronic Models

Bazant was also responsible for the evolution of a series of endochronic theories of plain concrete response. The principal distinguishing feature of these theories is that they are incrementally non-linear. The first paper, with Bhat^[150] was in 1976. Strain increments $\underline{\dot{\epsilon}}$ had an additive decomposition.

$$\underline{\dot{\epsilon}} = \underline{\dot{\epsilon}}^e + \underline{\dot{\epsilon}}^p \quad (4-47)$$

into elastic and anelastic components. Anelasticity was governed by the set of equations

$$\dot{\epsilon}^p = \dot{\epsilon}^p + \dot{\epsilon}^p \mathbf{1} \quad , \quad \dot{\epsilon}^p = \frac{1}{3} \dot{\epsilon}^p_{kk}$$

$$\dot{\epsilon}^p = \frac{s}{2G} \dot{z} \quad , \quad \dot{z} = f(n, \epsilon) \dot{n} \quad , \quad \dot{n} = g(\epsilon, \epsilon) \dot{\xi} \quad (4-48)$$

$$\dot{\xi}^2 = \frac{1}{2} \dot{\epsilon}_{ij} \dot{\epsilon}_{ij} \quad , \quad \dot{\epsilon}^p \equiv \dot{\lambda} = L(\lambda, \epsilon, \epsilon) \dot{\xi}$$

The theory was similar to viscoelasticity in that anelastic strains accumulated as soon as stress was applied; i.e., no linear elastic region existed. The variable z was called intrinsic time and monotonically increased for all deformation histories. The incremental stress-strain law was

$$\dot{\sigma}_{ij} = C_{ijkl} \dot{\epsilon}_{kl} - s_{ij} \dot{z} - 3K\lambda \dot{\epsilon}_{ij} \quad (4-49)$$

where C_{ijkl} was the usual matrix of elasticities which decreased very slightly with increasing z . The incremental nonlinearity of the theory is evident in Eq. 4-49 where z and λ are functions of ξ .

As with the plastic fracturing theory extensive curve fitting was undertaken to define functions f , g , and L in Eq. 4-48. In all 18 constants and five rather complicated intermediate functions were finally used. The only free parameter was f'_c . Good correlation was obtained between the theory and a diverse suite of experimental data for monotonic loading. Principal theory shortcoming was an inability to adequately predict uniaxial compressive cyclic response in that unload-reload stress-strain paths did not form closed loops.

In a subsequent paper^[151] the authors demonstrated the ability of their theory to replicate the moment-curvature and load-deflection response of reinforced concrete cantilever beams loaded by alternating cyclic end loads. Sorenson^[152,153] and Powell, Villiers and Litton^[154] incorporated the theory into finite element codes. All papers reported good correlation between

their codes and the cyclic response of reinforced concrete beams and shear panels. Sandler^[155] believed the theory was unstable in that small sinusoidal perturbations in strain history would change stress history significantly. Sandler's objection notwithstanding no stability problems were encountered by any author using the theory.

More recently Bazant reformulated the theory with Shieh^[156] and developed entirely new functional forms for f , g , and L . The new functions were as complicated as before but the following features were improved.

- inelastic hydrostatic response
- monotonic strain softening
- cyclic compressive response
- volume changes during strain softening
- differences in radial and non-radial loading
- triaxial failure envelope shape.

The formulation was incorporated into a finite element code and applied to a single, ideal plain concrete problem.

The latest endochronic theory is a hysteretic-fracturing-endochronic model of plain concrete first introduced in^[157] and fully developed in.^[158] The theory combined the endochronic concepts with the fracturing and jump-kinematic ideas contained in^[149] and discussed in Section 4.3.4. As with Bazant's other theories, elaborate curve fits were constructed to accommodate diverse sets of uniaxial, biaxial, triaxial, monotonic and cyclic data. The predictive capability of this theory remains to be demonstrated.

4.3.6 Constitutive Theory Conclusions and Recommendations

Many models for plain concrete triaxial response have been developed. The variable modulus and hypoelastic theories are of no

practical consequence. The conventional elastic-plastic theories are straightforward to implement but have only limited predictive capability because so many observed features of concrete behavior are not replicated. The plastic-fracturing and endochronic theories are first attempts at comprehensive plain concrete response representations and, compared to preceding models are very mathematical with many parameters.

For the analysis of the response of protective structures the most promising theories are those of Bazant since they best simulate post-peak softening and cyclic response. However, these theories are the most recent and so least tested. For accurate protective structure analysis realistic models of plain concrete response are needed; thus the following recommendations are made:

1. The predictive capabilities of the plastic-fracturing and endochronic theories should be further assessed.
2. Plastic-fracturing and endochronic theories should be modified to include strain-rate effects.

SECTION 5

DEVELOPMENT OF IMPROVED CONSTITUTIVE MODEL OF PLAIN CONCRETE

A plastic-fracturing theory was selected for exploration as a candidate for an improved constitutive model of plain concrete. This section documents progress made to-date on the development of this model.

5.1 GENERAL THEORY

The plastic-fracturing theory consists of two main elements: (1) a fracturing element and (2) a plastic element. A judicious combination of these two elements allows simulation of the following fundamental features of plain concrete: (1) strain hardening, (2) strain softening, (3) stiffness degradation, and (4) realistic failure surface geometry.

The fracturing element of this model is due to Dougill⁽¹⁴⁸⁾ and is discussed in subsection 5.1.1 (see also subsection 4.3.4). This portion of the plain concrete model reflects progressive fracture and is the key to the description of progressive stiffness degradation.

The plastic element of the plain concrete model consists of a plasticity theory with strain softening. This portion of the model is intended to simulate inelastic slip which is observed in all test data.

It is noted that the use of a plastic-fracturing theory for plain concrete has been explored previously by Bazant and Kim.⁽¹⁴⁹⁾ A discussion of this work is presented in subsection 4.3.4. The theory presented herein differs from that of Bazant and Kim in that (1) the formulation is more general and (2) the plastic and fracturing elements are combined in a different manner.

5.1.1 The Progressively-Fracturing Solid

Dougill⁽¹⁴⁸⁾ formulated a theory for a pure fracturing elastic material using an analogy with conventional plasticity. This theory, which represents the 'fracturing' part of the plastic-fracturing theory, is the main source of progressive stiffness

degradation and strain softening in plain concrete. Namely, Dougill realized that these phenomena were primarily due to progressive microcracking of the concrete.

Dougill begins his fracturing model by assuming that the material is perfectly elastic. Consequently, upon restricting the discussion to small strain, the stress and strain tensors are related by

$$\sigma_{ij} = C_{ijkl} \epsilon_{kl} \quad (5-1)$$

in which C_{ijkl} represents the current (secant) stiffness tensor of the material; this tensor is in general anisotropic with the exception of the initial (unfractured) state of the material. As fracture progresses, the stiffness tensor changes according to

$$\dot{\sigma}_{ij} = C_{ijkl} \dot{\epsilon}_{kl} + \dot{C}_{ijkl} \epsilon_{kl} \quad (5-2)$$

where the superior dot indicates differentiation with respect to a "bookkeeping" time variable. Dougill associates the first term in (5-2) with the elastic component of the stress rate tensor and the last term with progressive fracture:

$$\dot{\sigma}_{ij}^e \equiv C_{ijkl} \dot{\epsilon}_{kl}, \quad (5-3)$$

$$\dot{\sigma}_{ij}^f \equiv \dot{C}_{ijkl} \epsilon_{kl} \quad (5-4)$$

Dougill next associates σ_{ij} with a 'fracture surface' in strain space. This surface encloses all combinations of strain that can be obtained without changing the stiffness of the material (i.e., without causing further microcracking). The fracture surface is assumed to be regular and of the form

$$F(\epsilon_{ij}, H_n) = 0 \quad (5-5)$$

where the parameters H_n ($n = 1, 2, \dots, N$) describe the history of progressive fracture. These terms are selected such that

$$\frac{\partial F}{\partial H_n} \dot{H}_n < 0 \quad (5-6)$$

during progressive fracture. Consequently, if

$$\dot{F} = \frac{\partial F}{\partial \epsilon_{ij}} \dot{\epsilon}_{ij} + \frac{\partial F}{\partial H_n} \dot{H}_n = 0 \quad (5-7)$$

defines progressive fracture, then the latter occurs only when

$$F = 0 \text{ and } \frac{\partial F}{\partial \epsilon_{ij}} \dot{\epsilon}_{ij} > 0 \quad (5-8)$$

On the other hand, progressive fracture ceases and the material responds elastically without change in the stiffness tensor if

$$F < 0 \text{ , or } F = 0 \text{ and } \frac{\partial F}{\partial \epsilon_{ij}} \dot{\epsilon}_{ij} \leq 0 \quad (5-9)$$

Dougill next notes that, as a consequence of (5-8), it is possible to write the 'fracture stress decrement' σ_{ij} in the form

$$\dot{\sigma}_{ij}^f = g_{ij} \frac{\partial F}{\partial \epsilon_{kl}} \dot{\epsilon}_{kl} \quad (5-10a)$$

Since σ_{ij} is a symmetric tensor, it follows that g_{ij} must be a symmetric tensor. If one now restricts the theory to materials that obey Il'iusin's postulate,⁽¹⁵⁹⁾ i.e., if one requires that the total work done during the application and removal of a small increment of deformation must be positive or zero, and if the tensor g_{ij} is not a function of the strain rate $\dot{\epsilon}_{ij}$, then the fracture stress decrement must be normal to the fracture surface so that

$$\dot{\sigma}_{ij}^f = -K \frac{\partial F}{\partial \epsilon_{ij}} \frac{\partial F}{\partial \epsilon_{kl}} \dot{\epsilon}_{kl}, \quad K > 0. \quad (5-10b)$$

The scalar K may be a function of strain and strain history, but not of the current strain rate.

It is evident at this point that Dougill's model corresponds to conventional plasticity with an interchange of kinematic for static variables. The form (5-10b) corresponds to an 'associated flow rule' within the context of such an interchange. But, as with plasticity it will be necessary to relax the constraint (5-10b) to some degree in order to adequately simulate real material behavior.

The scalar K in (5-10b) can conveniently be expressed in terms of the rate of energy dissipated per unit volume of material, D , and the parameters H_n . The energy per unit volume during progressive fracture (loading) is

$$D = \int_0^t \sigma_{ij} \dot{\epsilon}_{ij} dt - \frac{1}{2} \sigma_{ij} \epsilon_{ij} \quad (5-11a)$$

which, when differentiated, becomes

$$\dot{D} = \frac{1}{2} (\sigma_{ij} \dot{\epsilon}_{ij} - \dot{\sigma}_{ij} \epsilon_{ij}) = -\frac{1}{2} \dot{\sigma}_{ij}^f \epsilon_{ij}. \quad (5-11b)$$

Now, using (5-7) and multiplying both sides of (5-10b) by ϵ_{ij} and using (5-13), one obtains

$$K = \frac{-2\dot{D}}{\frac{\partial F}{\partial \epsilon_{ij}} \frac{\partial F}{\partial H_n} \dot{H}_n}. \quad (5-12)$$

Given the surface F , the rate of change of the stiffness tensor (stiffness degradation) can be computed by rewriting the flow rule (5-10b) in the form

$$\dot{\sigma}_{ij}^f = -K \left(\frac{\frac{\partial F}{\partial \epsilon_{ij}} \frac{\partial F}{\partial \epsilon_k} \frac{\partial F}{\partial \epsilon_{rs}} \dot{\epsilon}_{rs}}{\frac{\partial F}{\partial \epsilon_{pq}} \epsilon_{pq}} \right) \epsilon_{kl} \quad (5-13)$$

Upon combining Eqs. 5-2, 5-3 and 5-13, one obtains the incremental relation

$$\dot{\sigma}_{ij}^f = C_{ijkl}^f \dot{\epsilon}_{kl} \quad (5-14a)$$

where

$$C_{ijkl}^f = C_{ijkl} - \left(\frac{K \frac{\partial F}{\partial \epsilon_{ij}} \frac{\partial F}{\partial \epsilon_{rs}} \frac{\partial F}{\partial \epsilon_{kl}} \epsilon_{rs}}{\frac{\partial F}{\partial \epsilon_{pq}} \epsilon_{pq}} \right) . \quad (5-14b)$$

The form (5-14) is linear in the strain rate and stress rate, i.e., it is incrementally linear.

A comparison of Eq. 5-13 with Eq. 5-4 suggests the following form for the stiffness rate tensor \dot{C}_{ijkl} :

$$\dot{C}_{ijkl} = -K \left(\frac{\frac{\partial F}{\partial \epsilon_{ij}} \frac{\partial F}{\partial \epsilon_{kl}}}{\frac{\partial F}{\partial \epsilon_{pq}} \epsilon_{pq}} \right) \frac{\partial F}{\partial \epsilon_{rs}} \dot{\epsilon}_{rs} + R_{ijkl} \quad (5-15a)$$

where R_{ijkl} is symmetric tensor with the property

$$R_{ijkl} \epsilon_{kl} = 0 . \quad (5-15b)$$

The tensor R_{ijkl} is assumed to be zero in most of Dougill's work.

A useful special case of the above formulation occurs where one assumes F to be a linear function of the strains with a single parameter h :

$$F = \lambda_{ij} \epsilon_{ij} - h \quad (5-16)$$

where λ_{ij} denote constants. This leads to the elementary result

$$\dot{\sigma}_{ij}^f = - \frac{2}{h} \frac{dD}{dh} \lambda_{ij} \lambda_{kl} \dot{\epsilon}_{kl} \quad (5-17)$$

and

$$\dot{c}_{ijkl} = \frac{\dot{\sigma}_{ij}^f \lambda_{kl}}{h} \quad (5-18)$$

The form (5-16) corresponds to isotropic softening and the relations (5-16) - (5-18) will be examined in some detail in Section 6.

The above formulation can easily be extended to include piecewise linear functions F . This subject has been studied by Dougill and Rida. (160)

The above formulation, with an appropriate choice of the dissipation function D , leads to a number of important observed response characteristics of plain concrete. These include degradation of the unload-reload stiffness moduli and strain softening. These effects are depicted in Figure 4-13 for the case of uniaxial compression.

Dougill has explored the behavior of the fracturing element using a precise linear representation for the surface $F = 0$. Typical softening behavior for a uniaxial tensile specimen is shown in Figure 5-1 for an elementary dissipation function $D(h)$. (A similar behavior can be generated in compression.) Typical behavior for a biaxial case is depicted in Figure 5-2. In this example the curve shown represents the peak (this peak is referred to as an 'instability' point.) of stress-strain curves, similar to that shown in Figure 5-1, obtained by radial loading. The similarity of Figure 5-2 to the failure envelop for plain concrete (see Figure 2-30) is evident although it is too early in the exploration phase of this model to make much of this point.

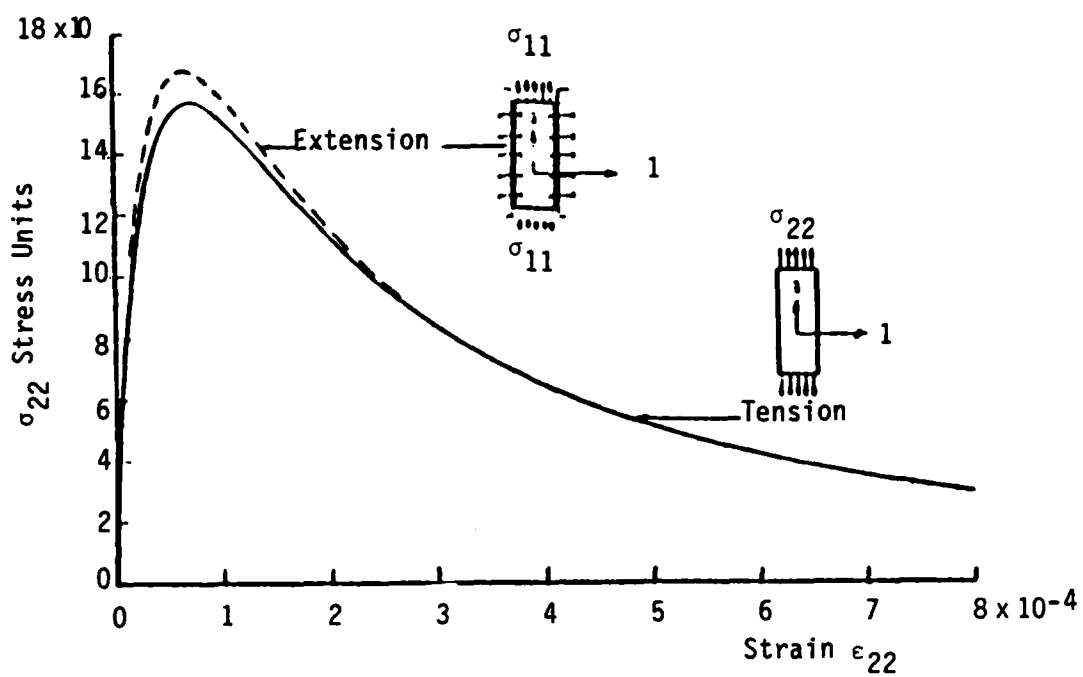


Figure 5-1. Uniaxial tensile behavior.

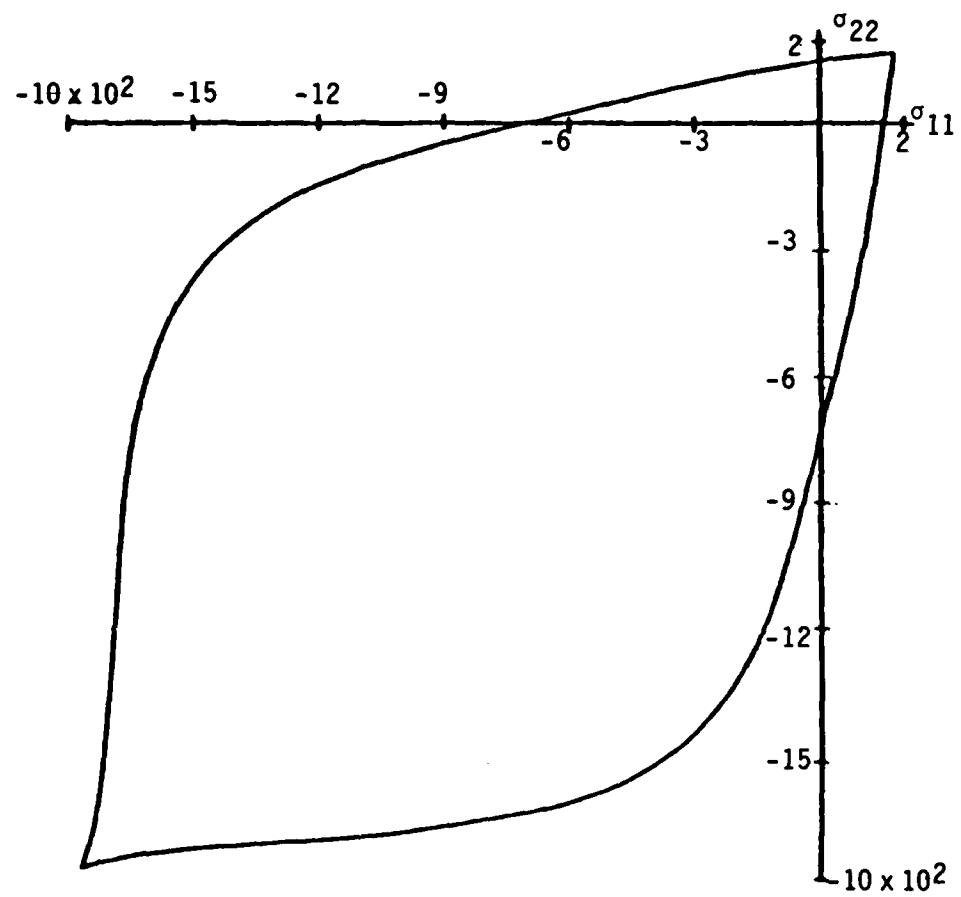


Figure 5-2. Biaxial example of instability surface.

5.1.2 The Plastic Solid

The plastic element is based upon well-known plasticity concepts. Accordingly, for the plastic element one postulates a plastic loading surface (or plastic potential) defined by

$$\phi(\sigma_{ij}, H'_n) = 0 \quad . \quad (5-19)$$

in which H'_n ($n = 1, 2, \dots, N'$) are scalars (hardening parameters). Upon decomposing the strain rate $\dot{\epsilon}_{ij}$ of this element according to:

$$\dot{\epsilon}_{ij} = \dot{\epsilon}_{ij}^e + \dot{\epsilon}_{ij}^p \quad (5-20)$$

with

$$\dot{\epsilon}_{ij}^e \equiv S_{ijkl} \dot{\sigma}_{kl} \quad (5-21)$$

where S_{ijkl} denote constants, and upon associating $\dot{\epsilon}_{ij}^p$ with the potential ϕ , one has

$$\dot{\epsilon}_{ij}^p \equiv \Lambda \frac{\partial \phi}{\partial \sigma_{ij}} \frac{\partial \phi}{\partial \sigma_{kl}} \dot{\sigma}_{kl} \quad (5-22)$$

where Λ denotes a scalar. Plastic flow takes place when $F = 0$ and $\dot{F} = 0$. The element is elastic when $F < 0$, or when $F = 0$ and $\dot{F} < 0$. If one defines the plastic dissipation according to

$$\dot{D} \equiv \frac{1}{2} \sigma_{ij} \dot{\epsilon}_{ij}^p \quad (5-23)$$

then one evaluates the scalar Λ as

$$\Lambda = \frac{2\dot{D}}{\frac{\partial \phi}{\partial \sigma_{ij}} \frac{\partial \phi}{\partial H'_n} \dot{H}'_n} \quad . \quad (5-24)$$

The potential ϕ in the above formulation need not be the yield surface. If the two coincide, then (5-22) constitutes an associated flow rate. In general, it will be necessary to relax the constraint of an associated flow rule in order to properly simulate real material behavior.

5.1.3 The Plastic-Fracturing Solid

The constitutive relations for the plastic and fracturing elements can be placed in the incrementally linear form

$$\dot{\sigma}_{ij}^{(1)} = C_{ijkl}^p \dot{\epsilon}_{kl}^{(1)} \quad , \quad \dot{\epsilon}_{ij}^{(1)} = S_{ijkl}^p \dot{\sigma}_{kl}^{(1)} \quad , \quad (5-25)$$

$$\dot{\sigma}_{ij}^{(2)} = C_{ijkl}^f \dot{\epsilon}_{kl}^{(2)} \quad , \quad \dot{\epsilon}_{ij}^{(2)} = S_{ijkl}^f \dot{\sigma}_{kl}^{(2)} \quad , \quad (5-26)$$

where the superscript (1) denotes the elastic element and the superscript (2) denotes the fracturing element, the tensors C_{ijkl}^p , S_{ijkl}^p , C_{ijkl}^f , S_{ijkl}^f are non-constant and depend upon the current state of stress and strain in each element.

It is emphasized at this point that the stress, strain fields of the two elements are not connected. Specification of relations between the "(1)" fields and the "(2)" fields constitutes a definition of the manner in which the elements are "mixed".

To-date the plastic and fracturing elements have been mixed two ways in the literature. In his plastic-fracturing model, Bazant⁽¹⁴⁹⁾ utilizes a "parallel" mixture of these elements in which

$$\epsilon_{ij}^{(1)} = \epsilon_{ij}^{(2)} \equiv \epsilon_{ij} \quad , \quad \sigma_{ij} \equiv \sigma_{ij}^{(1)} + \sigma_{ij}^{(2)} \quad (5-27)$$

Accordingly, one has for the combined element

$$\dot{\sigma}_{ij} = (C_{ijkl}^p + C_{ijkl}^f) \dot{\epsilon}_{kl} \quad (\text{parallel mixture}) \quad . \quad (5-28)$$

where it is noted that C_{ijkl}^p must be evaluated* at stress state $\sigma_{ij}^{(1)}$.

In his endochronic-fracturing model,⁽¹⁵⁹⁾ Bazant* assumes a 'series' mixture in which

$$\sigma_{ij}^{(1)} = \sigma_{ij}^{(2)} \equiv \sigma_{ij}, \quad \epsilon_{ij} \equiv \epsilon_{ij}^{(1)} + \epsilon_{ij}^{(2)} \quad (5-29)$$

which leads to the combined element:

$$\dot{\epsilon}_{ij} = (S_{ijkl}^p + S_{ijkl}^f) \dot{\sigma}_{kl} \quad (\text{series mixture}) \quad (5-30)$$

where S_{ijkl}^f must be evaluated at strain state $\epsilon_{ij}^{(2)}$.

Other mixture rules may be invoked if appropriate. For example, the stresses in (5-27) can be combined with 'weights' $n^{(1)}$ and $n^{(2)}$ as follows:

$$\epsilon_{ij}^{(1)} = \epsilon_{ij}^{(2)}, \quad \sigma_{ij} \equiv n^{(1)} \sigma_{ij}^{(1)} + n^{(2)} \sigma_{ij}^{(2)} \quad (\text{parallel mixture with weighted stress fields}) \quad (5-31)$$

Under (5-31), the mixture has the constitutive relation

$$\dot{\sigma}_{ij} = (n^{(1)} C_{ijkl}^p + n^{(2)} C_{ijkl}^f) \dot{\epsilon}_{kl} \quad (5-32)$$

The manner in which plastic and fracturing elements are combined is arbitrary at this point. Investigation of both series and parallel mixtures is necessary before one can specify an optimum mixing procedure. Such a study is in progress.

*Bazant⁽¹⁴⁰⁾ does not appear to differentiate between the stress and strain states in the two elements for the purpose of evaluating the coefficient tensors.

5.3 SPECIFICATION OF FAILURE SURFACE FOR PLAIN CONCRETE

The failure surface in stress space represents a very important part of a constitutive relation for plain concrete. In those regions of stress space where brittle fracture does not occur, this surface also marks the beginning of stiffness degradation. The purpose of this section is to present the results of a study⁽¹⁸⁰⁾ designed to construct and validate a failure surface of plain concrete that mirrors actual material behavior.

In view of its importance, a number of previous attempts have been made to formulate a failure criterion for plain concrete. Some of these were aimed at practical design applications; whereas other more complex expressions have been developed for use in advanced computer codes. Examples of both types of formulations are given in References 165, 166, 45, 164, 167, 168, 117, 169, 70, 170, 171, 176, 73. Excellent reviews of previously proposed failure criteria have been presented by Link,⁽¹⁶⁹⁾ Ottosen,⁽¹⁷⁰⁾ and Wastiels.⁽¹⁷²⁾ Most of the failure criteria proposed for three-dimensional stress states involve relatively complex expressions for which more than three material parameters are required.

The aforementioned criteria were developed to model the experimentally determined shape of the failure surfaces as observed in principal stress space. Thus, several studies (165,166,164,168, 70,170,171) have shown that the failure surfaces in the principal stress spaces are shaped as pointed bullets with cross-sections in octahedral planes which are triangular, monotonically curved surfaces with smoothly rounded "corners." Failure surfaces of similar shapes have also been observed for other frictional materials such as sand and clay (see, e.g., (161,162,163)).

In addition to the characteristic cross-sectional shape in the octahedral plane observed in several experimental investigations, the three-dimensional failure surface for concrete has three independent characteristics: (1) the opening angle of the failure

surface, often prescribed by the friction angle, (2) the curvature of the failure surface in planes containing the hydrostatic axis, i.e., curved meridians, and (3) the tensile strength. At least three independent parameters are necessary for description of the failure surface for concrete. The problem is to obtain simulation accuracy without the use of more than three independent parameters. This problem is addressed herein.

5.3.1 Failure Criterion

The proposed failure criterion for plain concrete represents an extension of a three-dimensional failure criterion previously developed for soils with curved failure envelopes.⁽¹⁶¹⁾ This criterion is expressed in terms of the first and the third stress invariants of the stress tensor as follows:

$$(I_1^3/I_3 - 27)(I_1/p_a)^m = \eta_1 \quad (5-33)$$

where

$$I_1 = \sigma_1 + \sigma_2 + \sigma_3 = \sigma_{11} + \sigma_{22} + \sigma_{33} \quad , \quad (5-34)$$

$$\begin{aligned} I_3 &= \sigma_1 \sigma_2 \sigma_3 \\ &= \sigma_{11} \sigma_{22} \sigma_{33} + \sigma_{12} \sigma_{23} \sigma_{31} + \sigma_{21} \sigma_{32} \sigma_{13} \\ &\quad - (\sigma_{11} \sigma_{23} \sigma_{32} + \sigma_{22} \sigma_{31} \sigma_{13} + \sigma_{33} \sigma_{12} \sigma_{21}) \quad . \end{aligned} \quad (5-35)$$

The quantities $\sigma_1, \sigma_2, \sigma_3$ above denote the principal stresses and p_a is a reference pressure (taken as atmospheric). The value of I_1^3/I_3 is 27 at the hydrostatic axis where $\sigma_1 = \sigma_2 = \sigma_3 = \sigma$. The parameters η_1 and m in Eq. (5-33) can be determined by plotting $(I_1^3/I_3 - 27)$ versus (p_a/I_1) at failure in a log-log diagram and locating the best fitting straight line. The intercept of this line with $(p_a/I_1) = 1$ is the value of η_1 , and m is the slope of the line.

In principal stress space the failure surface defined by Eq. (5-33) is shaped like an asymmetric bullet with the pointed apex at the origin of the stress axis as shown in Figure 5-3(a). The apex angle increases with the value of η_1 . The failure surface is always concave towards the hydrostatic axis, and its curvature increases with the value of m . For $m = 0$ the failure surface is straight. Figure 5-3(b) shows typical cross-sections in the octahedral plane ($I_1 = \text{const.}$) for $m = 0$ and $\eta_1 = 1, 10, 10^2$, and 10^3 . As the value of η_1 increases, the cross-sectional shape changes from circular to triangular with smoothly rounded edges in a fashion that conforms to experimental evidence. The shape of these cross-sections do not change with the value of I_1 when $m = 0$. For $m > 0$ the cross-sectional shape of the failure surface changes from triangular to that approximating circular with increasing value of I_1 . Similar changes in cross-sectional shape are observed from experimental studies on soil and concrete. The cross-sections in Figure 5-3(b) also correspond to $m = 1$ and $\eta_1 = 10^2, 10^3, 10^4$ and 10^5 . This criterion has been shown to model the experimentally determined three-dimensional strengths of sand and normally consolidated clay with good accuracy in the range of stresses where the failure envelopes are concave towards the hydrostatic axis. (161,162,163)

Since concrete is a frictional material with many characteristics similar to those of soils, it may be expected that its strength can be expressed by a criterion similar to that in Eq. 5-33. In order to include the cohesion and the tension which can be sustained by concrete, a translation of the principal stress space along the hydrostatic axis is performed as illustrated in Figure 5-4. Thus, a constant stress $a \cdot p_1$ is added to the normal stresses before substitution in Eq. 5-33:

$$\bar{\sigma}_1 = \sigma_1 + a \cdot p_a \quad (5-36a)$$

$$\bar{\sigma}_2 = \sigma_2 + a \cdot p_a \quad (5-36b)$$

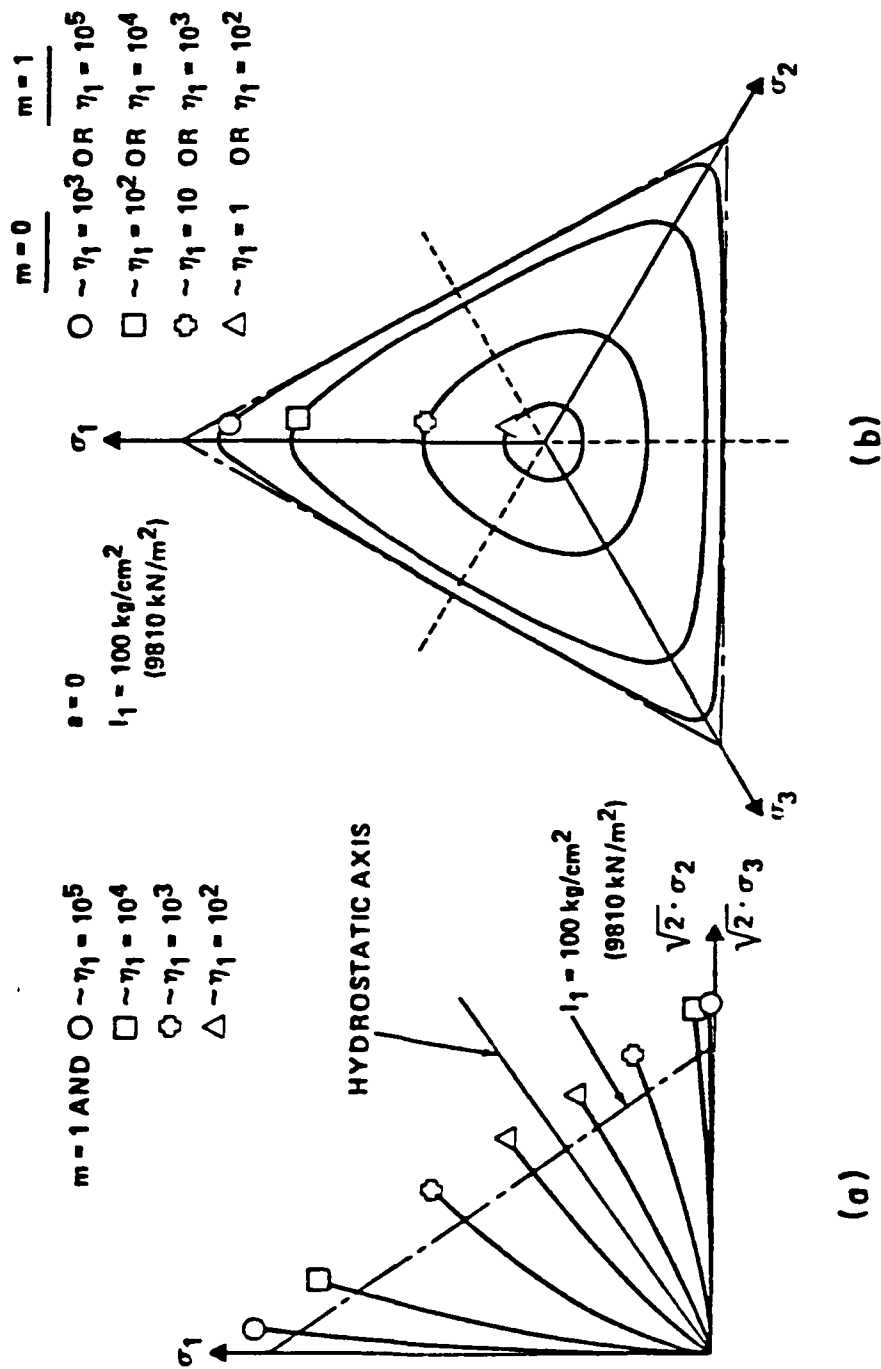


Figure 5-3. Characteristics of proposed failure surfaces shown in principal stress space. Traces of failure surfaces shown in (a) triaxial plane, and in (b) octahedral plane.

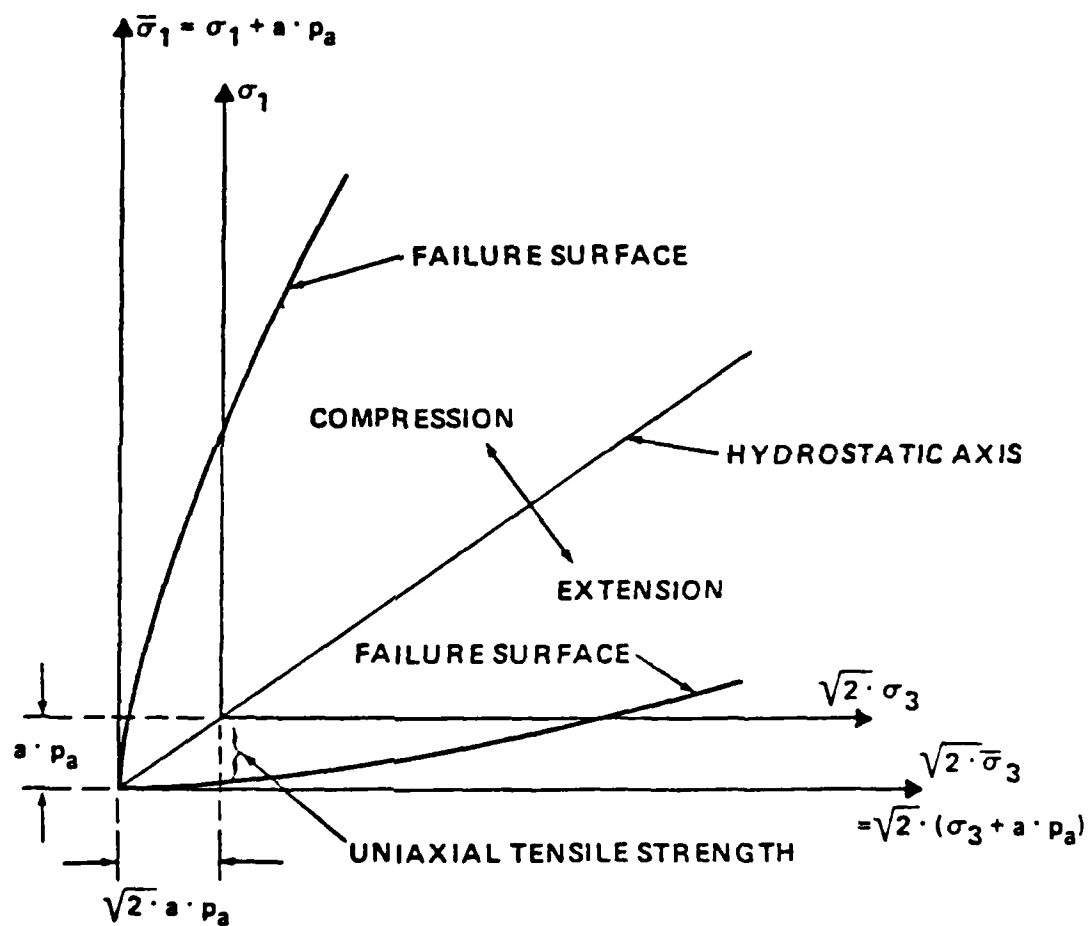


Figure 5-4. Translation of principal stress space along hydrostatic axis to include effect of tensile strength in failure criterion.

$$\bar{\sigma}_3 = \sigma_3 + a \cdot p_a \quad (5-36c)$$

where a is a dimensionless parameter. The value of $a \cdot p_a$ reflects the effect of the tensile strength of the concrete. Although the three material parameters describe separate characteristics of the failure surface, they do interact in calculation of, e.g., the unconfined compressive strength of the concrete. Thus, an infinite number of combinations of n , m , and " a " could result in the same value of the unconfined compressive strength.

5.3.2 Determination of Material Parameters

In order to determine the values of the three material parameters for a given set of experimental data, the value of " a " is estimated and $a \cdot p_a$ is added to the normal stresses before substitution in Eq. 5-33. The procedure for finding n_1 and m as described above is then followed. To facilitate the estimate of " a ", advantage may be taken of the fact that $a \cdot p_a$ must be slightly greater than the uniaxial tensile strength of the concrete as indicated on Figure 5-4. If tensile tests are not part of a regular testing program, a sufficiently accurate value of the uniaxial tensile strength may be obtained from the approximate formula prescribed below.

Uniaxial tensile strength - According to data presented in the literature⁽¹⁶⁴⁾ the uniaxial tensile strength σ_t varies between 5 percent and 13 percent of the unconfined compressive strength σ_c . The values of σ_t and σ_c may be related through a power law of the type:

$$\sigma_t = T p_a \left(\frac{\sigma_c}{p_a} \right)^t \quad (5-37)$$

where T and t are dimensionless parameters. The value of $T = -0.61$ and $t = 2/3$ is appropriate for concrete.

Regression Analyses - Since the failure criterion is expressed in terms of stress invariants, any type of test in which all stresses are measured may be used for determination of the three material parameters. However, it is advantageous to require only the simplest possible types of tests such as, e.g., unconfined compression and triaxial compression or biaxial tests for this determination, and then check whether these simple tests are sufficient for adequate characterization of the failure condition for the particular concrete under investigation. This may be done using various sets of data available in the literature which include both simple and more complex three-dimensional tests.

In order to obtain the overall best fitting parameters, regression analyses may be performed to determine the highest possible value of the coefficient of determination r^2 . Figure 5-5 shows an example of the effect of varying the parameter "a" on the values of r^2 , n_1 , and m for the tests on Mix A concrete performed by Mills and Zimmerman.⁽⁷⁰⁾ Only the results of the unconfined compression and the triaxial compression tests in addition to the estimated value of the uniaxial tensile strength (from Eq. 5-37) were used to determine the three material parameters. The uniaxial tensile strength was estimated to be -23.1 kg/cm^2 (-2266 kn/m^2) for Mix A concrete and the best fit value of "a" = 23.2 resulted in $n_1 = 119,339$ and $m = 1.127$.

Except for the three points corresponding to the uniaxial tensile strength of Figure 5-5, the points corresponding to the other tests do not move enough on the diagram to show their movements. The points corresponding to the uniaxial tensile strength tend to influence the location of the fit straight line. However, each of the three lines would describe the failure surface in the region of compressive stresses with reasonable accuracy. Thus, it is an advantage to incorporate the uniaxial tensile strength, even though it may be an estimate, in determination of the material parameters in order to stabilize the failure criterion in the region close to the origin and to describe the tensile strength for the concrete with reasonable accuracy.

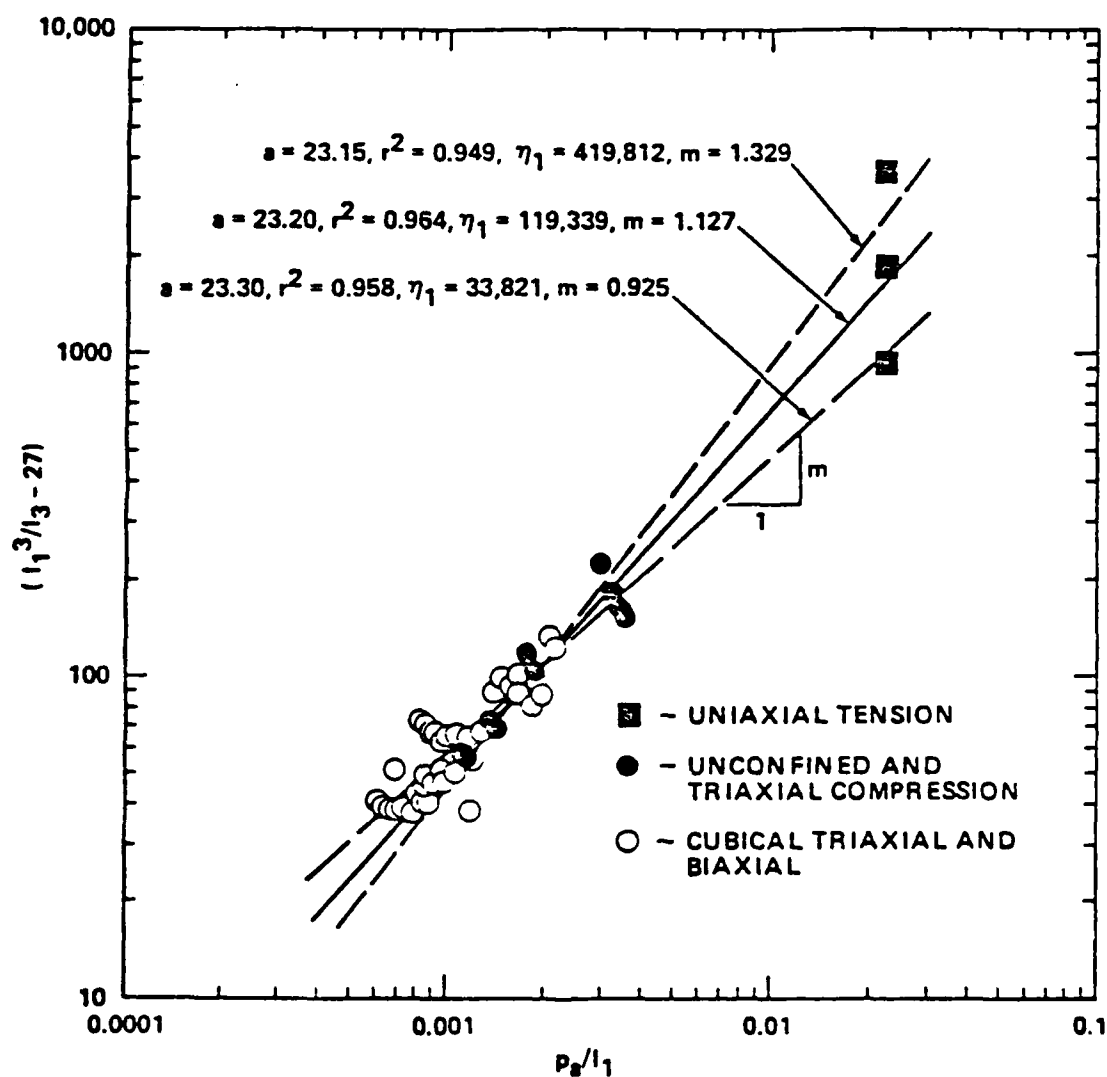


Figure 5-5. Determination of material parameters involved in failure criterion for Mix A concrete tested by Mills and Zimmerman.

The results of the cubical triaxial tests on Mix A concrete are shown on Figure 5-5 for comparison. It may be seen that some scatter of the data around the solid line does exist, but the material parameters selected on the basis of the simple tests appear to represent the data quite well.

5.3.3 Material Parameter Values

Twenty-one sets of data, considered to be of good quality, were employed in a study of the applicability of the proposed failure criterion to plain concrete and mortar. The material parameters obtained in this study are given in Table 5-1 together with the types of tests used for their determination. Where tests of simple and more complex types were present in the investigations, only the simple tests were employed for determination of the material parameters. Thus, the results of unconfined compression tests were always employed. The uniaxial tensile strength was also most often employed in the parameter determination, whether measured or estimated from Eq. 5-37. As indicated on Figure 5-5, the value of the uniaxial tensile strength has a substantial influence on the best fitting material parameters. It was often found that the estimated value from Eq. 5-37 would result in better overall fit than the value determined from experiments, although the two values were not substantially different. This is because the value of $(I_1^3/I_3 - 27)$ is very sensitive to small changes in stress near the origin, but this sensitivity is not reflected severely in the actual fit between the experimental data and the mathematical model for the failure surface.

Table 5-1 indicates that the results of triaxial compression tests or biaxial tests (compression-compression, and sometimes compression-tension) were also employed in most cases for determination of material parameters. Data from these tests were included to provide better overall fit between data and failure criterion. However, the material parameters for the torsion shear tests performed by Bresler and Pister⁽⁴⁶⁾ were determined from the unconfined compressive strengths and the estimated values of the

Table 5-1
Strength parameters for concrete and mortar

Type of Material	Data From Ref. No.	Type of Tests	(σ_c/p_a)	Mat. Param. Based on	a	η_1	m	r_{\max}^2	(I_1^3/I_3-27) at $I_1/p_a=1000$
Plain Concrete	10, 23	UC, UT, C-C	2_{300}	UC, $^3_{UT}$ C-C	27.3	278,267	1.217	0.997	62.3
	4	UC, TS	206.9	UC, $^3_{UT}$	19.8	97,560	1.122	1.0	42.0
	4	UC, TS	300.4	UC, $^3_{UT}$	25.6	157,752	1.105	1.0	76.3
	4	UC, TS	386.5	UC, $^3_{UT}$	31.0	255,398	1.124	1.0	108.5
	10	UC, UT, C-C, C-T, T-T	190	UC, UT C-C, C-T	20.1	147,040	1.220	0.944	32.2
	10	UC, UT C-C, C-T, T-T	315	UC, UT C-C, C-T	28.5	159,795	1.133	0.918	73.1
	10	UC, UT C-C, C-T, T-T	590	UC, UT C-C, C-T	50.9	12,313	0.686	0.371	107.7
	16	UC, TC C-C, CT	234.8	UC, $^3_{UT}$ TC	23.2	119,339	1.127	0.964	54.9
	16	UC, TC C-C, CT	274.6	UC, $^3_{UT}$ TC	25.8	55,173	0.956	0.923	74.9
	16	UC, TC C-C, CT	368.1	UC, $^3_{UT}$ TC	31.3	265,067	1.132	0.902	106.0
	15	UC, C-C	2_{300}	UC, $^3_{UT}$ C-C	27.3	158,222	1.143	0.897	59.0
	5 ⁴ (CU)	UC, TC C-C, CT	301.6	UC, $^3_{UT}$ TC	27.4	681,650	1.412	0.985	39.6
	5 ⁴ (NMSU)	UC, TC C-C, CT	307	UC, $^3_{UT}$ TC	27.8	746,100	1.396	0.979	48.4
	5 ⁴ (ENEL)	UC, TC C-C, CT	273	UC, $^3_{UT}$ TC	25.8	39,750	0.931	0.990	64.0
	5 ⁴ (TUM)	UC, TC C-C, CT	325	UC, TC	28.0	162,347	1.105	0.996	78.0
	5,18 ⁴ (BAM)	UC, TC C-C, CT	312.1	UC, $^3_{UT}$ TC	28.1	367,195	1.263	0.999	59.8
	19	UC, UT C-C, C-T, T-T	339.3	UC, $^3_{UT}$ C-C, C-T	29.7	17,368	0.790	0.896	74.0
Mortar	5 ⁴ (CU)	UC, C-C	2_{300}	UC, $^3_{UT}$ C-C	27.3	300,106	1.241	0.987	56.8
	5 ⁴ (TUM)	UC, C-C	2_{300}	UC, $^3_{UT}$ C-C	27.6	8,671	0.695	0.990	71.0
	5,18 ⁴ (BAM)	UC, C-C	310	UC, $^3_{UT}$ C-C	28.0	54,436	0.969	0.992	67.4
	1	UC, C-C	413.1	UC, $^3_{UT}$ C-C	33.8	314,784	1.172	0.884	96.2

uniaxial tensile strengths. These latter values were estimated from the torsion shear tests involving pure shear. These stress conditions are those closest to the uniaxial tensile stress conditions in this series of tests. However, the uniaxial tensile strengths might also have been estimated with good accuracy from Eq. 5-37 on the basis of the unconfined compressive strengths. Thus, it is clear that the result of one simple test is sufficient for estimation of material parameters. However, inclusion of additional test results is generally advisable in order that the particular characteristics of the concrete under investigation be captured in the modeling of the failure criterion.

The values of "a" listed in Table 5-1 are determined by the regression analyses to within 0.1. These values of 'a' (> 0) are 0.3 percent to 1.4 percent higher than $|\sigma_t/p_a|$, and they vary between 19.8 and 33.8 with a single value as high as 50.9 for the concrete and mortar included in this study, i.e.:

$$a = |\sigma_t/p_a| \cdot (1.003 \text{ to } 1.014) \quad (5-38)$$

with the higher values of the coefficients to $|\sigma_t/p_a|$ associated with the lower values of η_1 and m .

Typical values of m for concrete and mortar vary between 0.9 and 1.2 with extreme values of 0.69 and 1.41. In comparison, values of m determined for cohesionless soil⁽¹⁶²⁾ typically vary between 0.0 and 0.84. Thus, the curvatures of the failure envelopes for concrete and mortar are substantially more pronounced than those for cohesionless soil.

The values of η_1 listed in Table 5-1 vary over a large range. This is because these values are determined at $p_a/I_1 = 1$, which is a value that is very close to the origin of the translated coordinate system as compared to the corresponding values of p_a/I_1 for most tests on concrete. Figure 5-5 indicates that even small variations in m result in large variations in η_1 , because log-log scales are used in this diagram. However, the

values of m and η_1 combine in Eq. 5-33 to produce values of $(I/I_3 - 27)$ of comparable magnitudes at higher values of I_1 where most tests are performed. The values of $(I_1^3/I_3 - 27)$ at $I_1/p_a = 1000$ are listed in Table 5-1. These values are all in the range from 40 to 108. Thus, the actual range of strengths is not as large as may immediately appear from the range of η_1 . Values of η_1 for cohesionless soils⁽¹⁶²⁾ typically vary from 20 to 280, and even smaller values may be obtained for normally consolidated clays, whose effective stress friction angles may be much smaller than those for sand. Thus, the opening angles for concrete and mortar are much larger than those obtained for soils.

5.3.4 Evaluation of Failure Criterion

In order to validate the proposed failure criterion, comparisons have been made between experimental data and failure surfaces calculated from Eq.s 5-33 and 5-36. All data were plotted on the biaxial plane, and data points were projected on the octahedral plane for all data sets except those produced by Bresler and Pister.⁽⁴⁵⁾ Those data sets containing results of triaxial compression and extension tests were also shown on the triaxial plane. The results of torsion shear tests (by Bresler and Pister⁽⁴⁵⁾) were plotted on the τ - σ diagram and on the biaxial plane. The values of 'a', η_1 , and m given in Table 5-1 were used for determination of the theoretical failure surfaces. Examples of these comparisons are given below.

Biaxial Plane - The lowest value of the coefficient of determination, r_{\max}^2 , for all data sets was found for the tests performed on concrete with $\sigma_c = 590 \text{ kg/cm}^2$ (57,880 kN/m^2) by Kupfer et al.⁽³⁶⁾ The comparison of test data (points) and failure surface (solid line) is shown on the normalized biaxial plane in Figure 5-6(a). All data, except those corresponding to tension-tension, were used to determine the material parameters. This set of data resulted in the lowest value of m and the highest value of 'a' encountered in this study. Despite the low value of r_{\max} , the failure criterion is seen to represent the test data

with reasonable accuracy. The data in the compression-tension area exhibit sufficient scatter to cause the low value of r_{\max}^2 . This is because one of the stresses in the translated coordinate system (σ_2) is very small, thus causing the value of I_3 to be small, resulting in a large value of $(I_1^3/I_3 - 27)$. Any small deviation of the data points in this sensitive region from the best fitting failure surface greatly affects the value of r_{\max}^2 . However, the actual fit between data and failure surface in this region is not greatly affected. In order to study the failure surface relative to the data in the tension-tension area, the data are shown on the enlarged diagram in Figure 5-6(b). It may be seen that the failure surface is smoothly rounded at the corner and that it corresponds exceptionally well to the data in this region.

A major investigation was performed by Mills and Zimmerman.⁽⁷⁰⁾ The results of their tests on Mix A concrete, which contained tests in biaxial, triaxial, and octahedral planes, provided a good, coherent set of data for this study. The material parameters for this concrete were determined on the basis of unconfined compression, triaxial compression, and an estimated value of the uniaxial tensile strength. The data obtained in the compression-compression region of the biaxial plane are shown in Figure 5-7(a). Although there is some scatter in the test results, the proposed failure criterion is seen to represent the data quite well. Note that the "pointed corner" in the tension-tension area is actually smoothly rounded as shown in Figure 5-6(a).

The data obtained by Tasuji et al.⁽¹²¹⁾ are compared with the failure surface in the biaxial plane in Figure 5-7(b). Tests in compression-compression, compression-tension, and tension-tension were performed in this study. Again, the overall representation of the data by the proposed failure criterion is reasonably good.

Triaxial Plane - Examples of comparisons between test data and the proposed failure criterion are shown in triaxial planes in Figure 5-8. Note that in both diagrams in this figure, the material parameters were determined on the basis of the unconfined

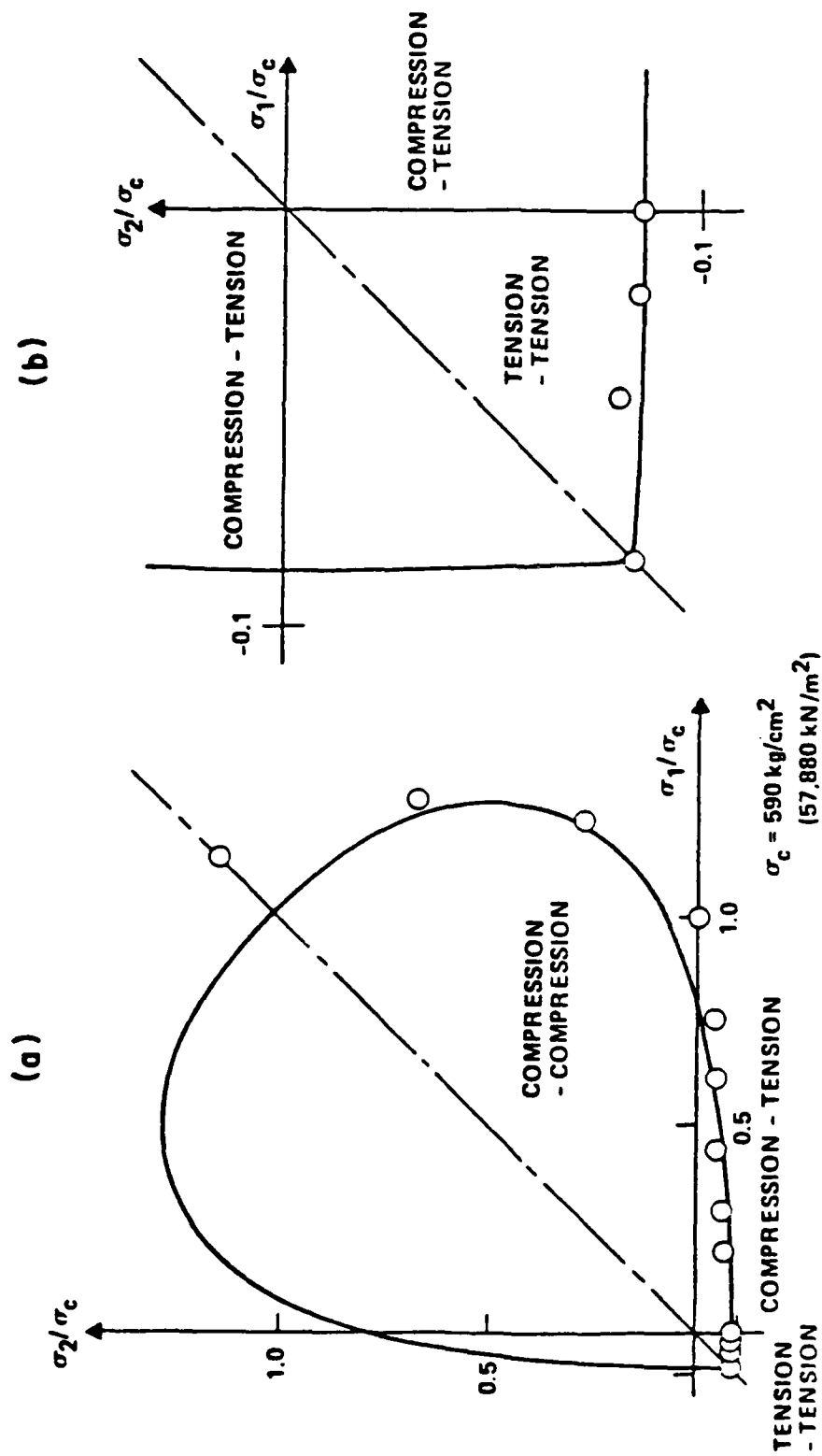


Figure 5-6. Comparison of proposed failure criterion in biaxial planes with results of biaxial tests performed by Kupfer, Hilsdorf, and Rüsche in (a) biaxial plane, and (b) enlarged tension-tension region.

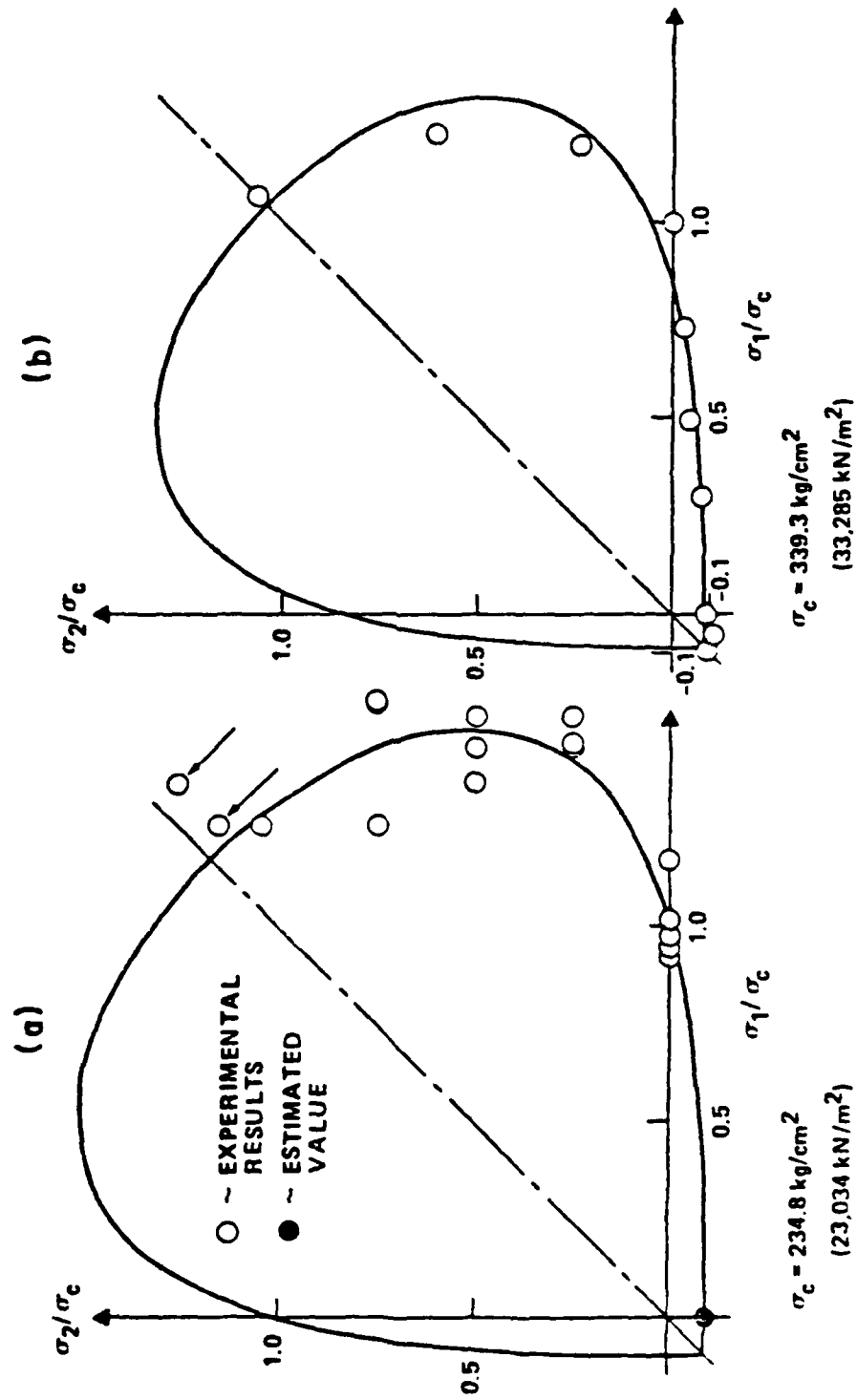


Figure 5-7. Comparison of proposed failure criterion in biaxial planes with results of biaxial tests performed by (a) Mills and Zimmerman on Mix A concrete, and by (b) Tasuji, Slate, and Nilson.

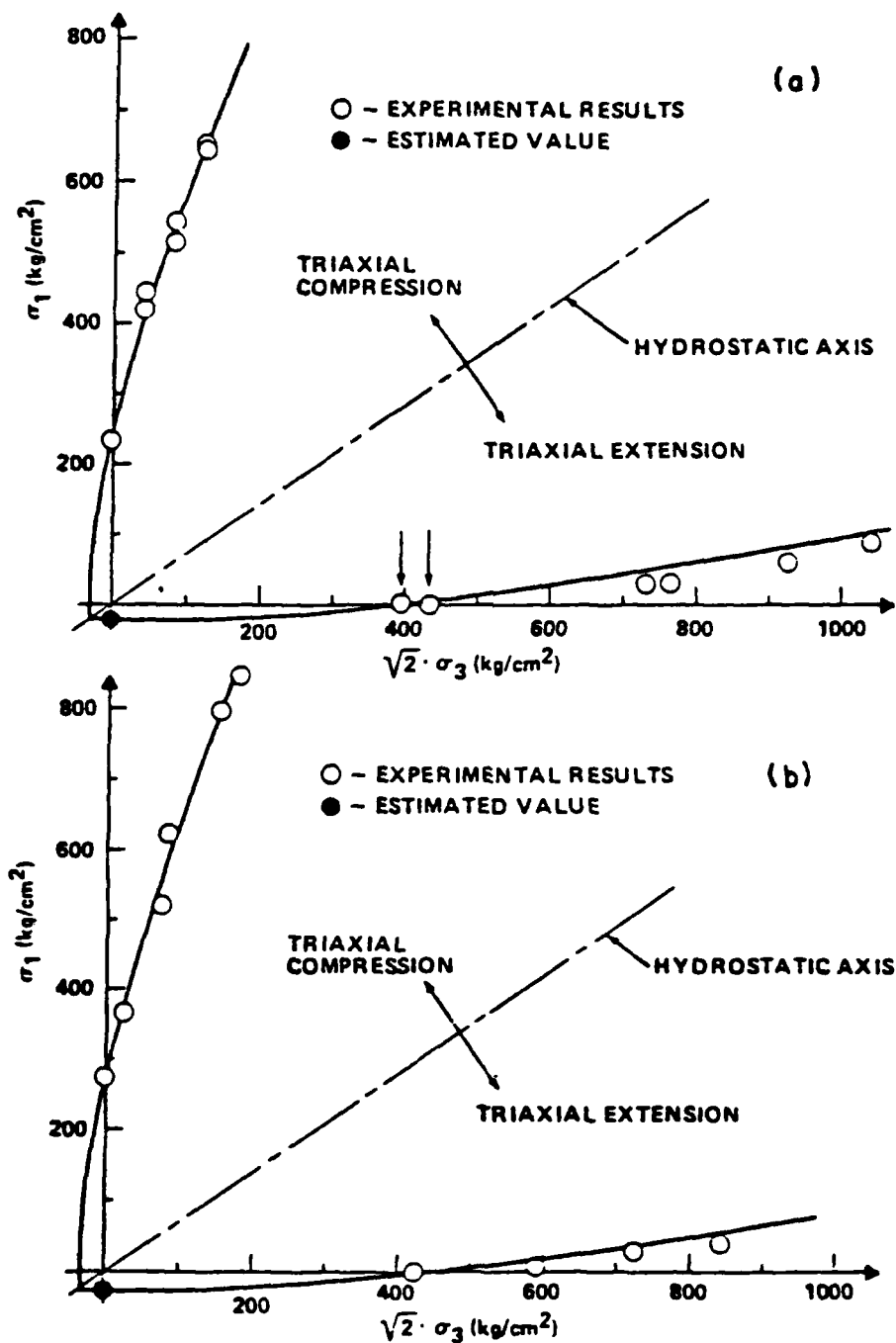


Figure 5-8. Comparison of proposed failure criterion in triaxial planes with results of triaxial compression and extension tests performed by (a) Mills and Zimmerman on Mix A concrete, and by (b) Bertacchi and Rossi. (1kg/cm² = 98.1kN/m²).

compression, the triaxial compression, and on estimated value of the uniaxial tensile strength. Thus, the good agreement between the results of the triaxial compression tests and the proposed failure criterion could be expected. However, the strengths obtained in triaxial extension are also well represented by the failure criterion.

Figure 5-8 also shows that the failure surface in extension cuts across the $\sigma_1 = 0$ plane at a very shallow angle. Therefore, any small deviation between test data and failure surface at this intersection in the triaxial plane will appear as a large deviation in the biaxial plane. Comparison of the data points for Mix A concrete indicated by arrows in Figures 5-7(a) and 5-8(a) shows that these appear to deviate somewhat from the failure surface in the biaxial plane (Figure 5-7(a)), whereas the same points in the triaxial plane are very close to the proposed failure surface. Any little amount of restraint in the testing apparatus would result in too large strength in biaxial extension, and this would show up very clearly in the biaxial plane. However, an evaluation in the triaxial plane would likely show that the test data are not that far from the actual failure surface. The natural scatter in test data could easily account for deviations of the magnitude indicated in Figure 5-7(a)).

Octahedral Plane - The data from cubical triaxial tests on Mix A concrete obtained by Mills and Zimmerman⁽⁷⁰⁾ are projected on the octahedral plane corresponding to $I_1 = 150 \text{ kg/cm}^2$ (14,715 kn/m^2) in Figure 5-9(a). Values of the minor principal stress, σ_3 , of 0, 29.5 kg/cm^2 (2894 kn/m^2), 59.1 kg/cm^2 (5798 kn/m^2), and 88.6 kg/cm^2 (8692 kn/m^2) were used in these tests. The points in Figure 5-9(a) corresponding to these values of σ_3 are shown separately on the octahedral plane for comparison with the proposed failure surface. The projected data points were transferred to the common octahedral plane along the curved meridians using a technique involving the diagram in Figure 5-5.

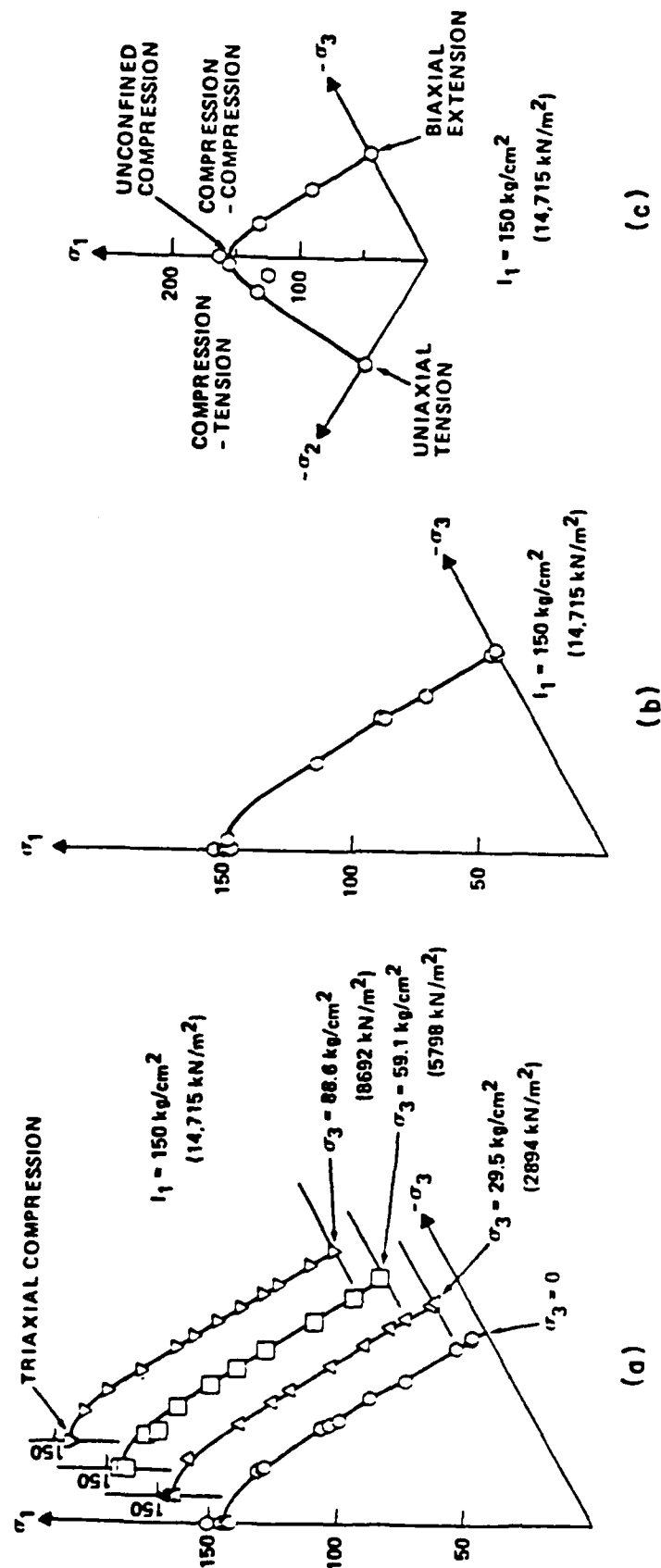


Figure 5-9. Comparison of proposed failure criterion in octahedral planes with results of tests on concrete performed by (a) Mills and Zimmerman on Mix A concrete, (b) Bertacchi and Rossi, and (c) Tasuji, Slate, and Milson.

Note again that only data from unconfined compression, triaxial compression, and uniaxial tension were used for determination of material parameters. The data from these tests are at the top of the diagrams in Figure 5-9(a). Only one sixth of the octahedral plane is shown in Figures 5-9(a) and 5-9(b), and all data points shown in these two diagrams correspond to compressive (or zero) stresses in the cubical triaxial tests. The data shown in Figure 5-9(c) are those produced in the biaxial plane and previously shown on Figure 5-7(b). These data are therefore projected along the respective curved meridians up on the octahedral plane corresponding to $I_1 = 150 \text{ kg/cm}^2$ ($14,715 \text{ kn/m}^2$). Any small amount of scatter in the biaxial plane, especially in the region of compression-tension and tension-tension would be magnified by projection on the octahedral plane. Especially one point on Figure 5-9(c) appears to have moved inside the failure surface in the region of compression-tension. This is the point in Figure 5-7(b) corresponding to $\sigma_1/\sigma_c = 0.5$. The point in Figure 5-7(b) does not appear to be substantially removed from the failure surface, but the magnification of the dislocation of this point relative to the failure surface is evident in Figure 5-9(c). The points corresponding to tension-tension in Figure 5-7(b) are only slightly outside the failure surface. However, these points cannot even be projected on the octahedral plane in Figure 5-9(c), because in the translated stress space they are located in a region of the space which corresponds to one of the principal stresses being negative.

Note that the experimental points on the octahedral planes in all cases describe failure surfaces which are triangular with monotonically curved surfaces and smoothly rounded edges, as does the proposed failure criterion. The overall fit between the data points and the failure surfaces in Figure 5-9 is considered to be accurate and within the natural scatter of data.

$\tau - \sigma$ Plane - The data obtained from torsion shear tests on large hollow cylindrical specimens by Bresler and Pister⁽⁴⁵⁾ are shown on normalized diagrams in Figure 5-10. The $\tau - \sigma$ diagrams in

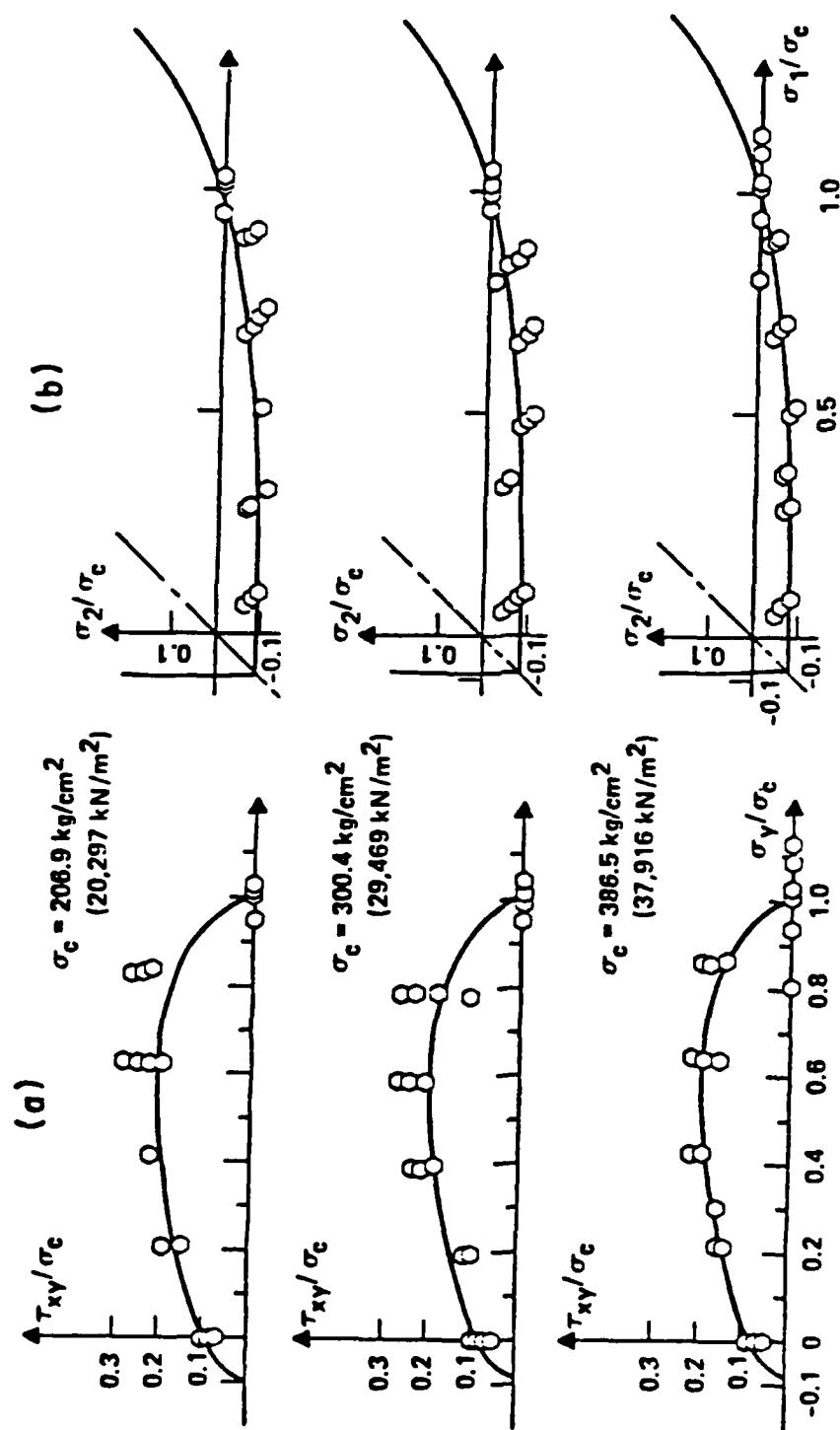


Figure 5-10. Comparison of proposed failure criterion with results of torsion shear tests performed by Bresler and Pister in (a) τ - σ diagrams, and (b) biaxial planes.

Figure 5-10(a) corresponds directly to the applied stresses in these tests, whereas the same test data have been transferred to the biaxial planes in Figure 5-10(b). The results of the tests are located in the compression-tension region of the biaxial plane. The scatter in these data is a little larger than experienced in some of the other investigations reviewed for this study. Only the (average) unconfined compressive strengths and the estimated uniaxial tensile strengths were used for determination of the material parameters for the three batches of concrete used in this study. However, the variation in strength is reasonably well captured by the proposed failure criterion.

5.3.5 Conclusions

In this section a general, three-dimensional failure criterion for plain concrete and mortar was formulated in terms of the first and the third stress invariants of the stress tensor, and it involves only three independent material parameters. Although these parameters interact with one another, each parameter corresponds to each of three failure characteristics of concrete behavior. These material parameters may be determined from simple tests such as unconfined compression and triaxial compression or biaxial tests. For the purpose of including reasonable values of tensile strengths in the failure entering it is advisable to include the uniaxial tensile strength in the parameter determination. A simple expression for evaluation of the uniaxial tensile strength on the basis of the unconfined compressive strength is given. Twenty-one sets of good quality data for concrete and mortar have been included in this study, and comparisons between the proposed failure criterion and the experimental data are made in biaxial, triaxial, octahedral, and $\tau - \sigma$ planes. The ability of this criterion to capture the characteristic of failure in concrete and mortar appears to be excellent with accuracies generally within the natural scatter of the test data.

Finally, the above effort represents an important first step in the direction of constructing an accurate constitutive description of plain concrete.

SECTION 6

DEVELOPMENT OF IMPROVED CONSTITUTIVE MODEL OF REINFORCED CONCRETE

6.1 APPROACH AND SCOPE

The problem of describing the interaction between reinforcing steel and plain concrete constitutes the most important problem associated with constructing an accurate model of reinforced concrete. In most cases, it is this interaction that dominates the global behavior of reinforced concrete.

In this section we present the results of a study to explore the use of mixture theory concepts to mathematically describe the interaction of steel and concrete and the global behavior of reinforced concrete, when viewed as a composite material, in the highly nonlinear range of deformations. The particular mixture theory under study falls into the "mixture-theory-with-microstructure category,"^(174,175) which has been successfully utilized to model other classes of composite materials.

According to the mixture-theory-with-microstructure approach, the constituents of reinforced concrete, i.e., steel and concrete, are modeled at each instant of time as superposed continua in space in a manner similar to a finite element overlay. In contrast to a standard overlay, however, each continuum is allowed to undergo individual deformations. The microstructure of the composite material is then simulated by specifying the interactions between the continua.

Within the context of mixture theories, previous 'smearing' of steel and concrete using a volume weighted mixture rule to determine stiffness and strength may be viewed as a mixture theory in which each component (steel, concrete) is constrained to have the same deformation gradient at the same spatial point. Relaxation of this constraint through an improved mixture framework obtained by micro-mechanical considerations regarding the interactions of the components leads to a marked improvement in the simulation capability of real material behavior.

As was noted in Section 1, two mixture models are currently under study. In one, called the Two-Phase Model, steel and concrete remain distinct materials. In the other, called The Single-Phase Model, steel and concrete are completely "homogenized" into a new continuum. Here the identity of the individual constituents is lost.

The advantage of the Two-Phase Model is accuracy and simulation capability. That of the Single-Phase Model is analytical simplicity. In both models, however, the global properties of reinforced concrete are synthesized from the properties of the steel and concrete, the steel-concrete interface physics, and the steel geometry. The concepts of Single- and Two-Phase Models are depicted in Figure 6-1.

The key to the development of mixture models for reinforced concrete is an asymptotic procedure called "multivariable asymptotic expansions." This mathematical technique may, if properly executed, be applied to both "dense" and "sparse" steel layouts. In what follows the procedure is outlined for a uniaxial dense steel mesh which may be locally approximated as initially periodic. "Dense" here may be anything from 1/2 to 5 percent or more steel. Locally such a mesh typically appears as hexagonal, Figure 6-2, or rectangular, Figure 6-3. The procedure may, it is emphasized, also be applied to locally non-periodic geometries such as the beam cross-section depicted in Figure 6-4. Whether periodic or non-periodic, the development can always be reduced to the analysis of one or several typical "cells," Figures 6-2 to 6-4.

In Section I, it was noted that the problem of mathematically describing reinforced concrete can be divided into several sub-problems. These include (1) the steel-concrete bond problem, (2) the steel-concrete dowel problem, (3) the aggregate interlock problem, and (4) the steel buckling-concrete spallation problem. Only the steel-concrete bond problem will be treated herein. This problem type includes a wide range of practical applications concerning the nonlinear bending and stretching of reinforced concrete beams, plates and shells.

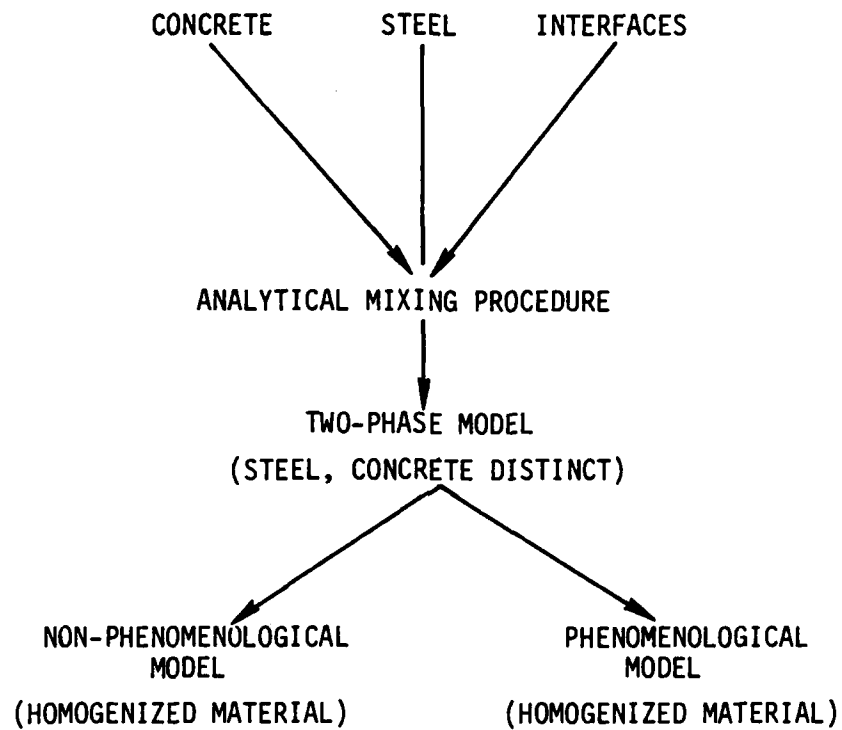


Figure 6-1. Single- and Two-Phase Model concepts.

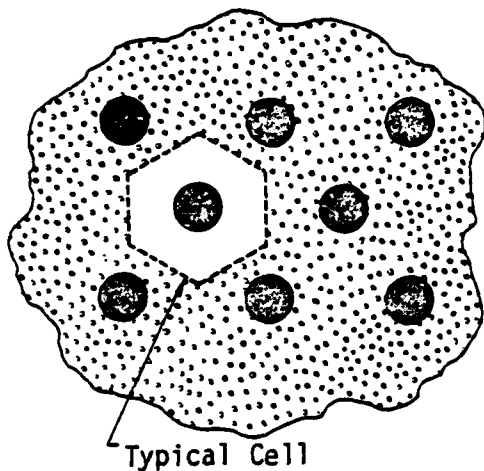


Figure 6-2. Dense mesh, hexagonal layout.

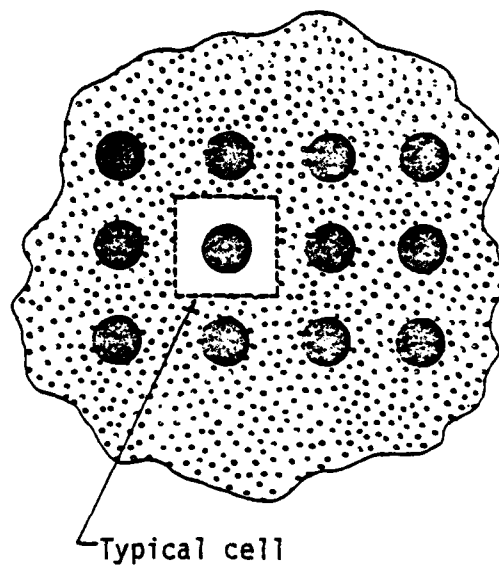


Figure 6-3. Dense mesh, rectangular layout.

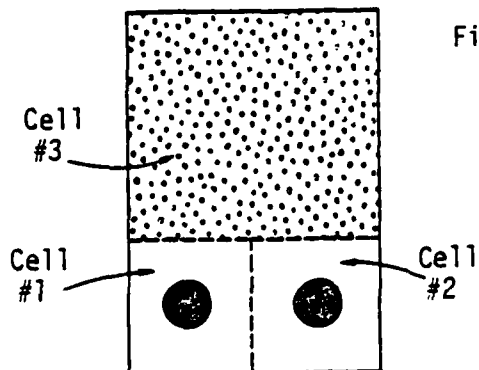


Figure 6-4. Sparse mesh, non-periodic (Beam cross-section).

6.2 DEVELOPMENT OF TWO-PHASE MIXTURE RELATIONS

The purpose of this subsection is to review the development of the basic mathematical mixture description of reinforced concrete. Since the discussion will focus upon the steel-concrete bond problem, the steel layout may be selected as uniaxial with a local periodic array. For simplicity the discussion is restricted to static problems.

6.2.1 Equilibrium Relations - With reference to a typical cell, Figure 6-5, and a spatial or Eulerian description, the condition of equilibrium is

$$\partial \sigma_{ij}^{(\alpha)} / \partial x_j = 0 \text{ on } V^{(\alpha)}; \alpha = 1, 2, \quad i = 1 \text{ to } 3 \quad (6-1)$$

where σ_{ij} denotes the Cauchy stress tensor, superscript $\alpha = 1, 2$ denotes material α ($\alpha = 1$ represents steel, $\alpha = 2$ concrete), which occupies volume $V^{(\alpha)}$. Latin and Greek subscripts, with ranges 1 - 3 and 2 - 3 respectively, denote Cartesian tensors and the usual indicial (summation) notation.

6.2.2 Constitutive Relations - A wide range of elastic-plastic and/or elastic-plastic-brittle fracture material models may be expressed in the form

$$\Delta \sigma_{ij}^{(\alpha)} = C_{ijkl}^{(\alpha)} d_{kl}^{(\alpha)} \quad (6-2a)$$

where Δ denotes the Jaumann stress rate; C_{ijkl} is the tangent stiffness tensor, and $2d_{kl} = (\partial v_k / \partial x_l + \partial v_l / \partial x_k)$ is the rate of deformation tensor, where v_i is the velocity vector. Under the constraint of small deformations, which should suffice for most reinforced concrete problems, Eq. 6-2a may be approximated by

$$\dot{\sigma}_{ij}^{(\alpha)} = C_{ijkl}^{(\alpha)} \dot{e}_{kl}^{(\alpha)} \quad (6-2b)$$

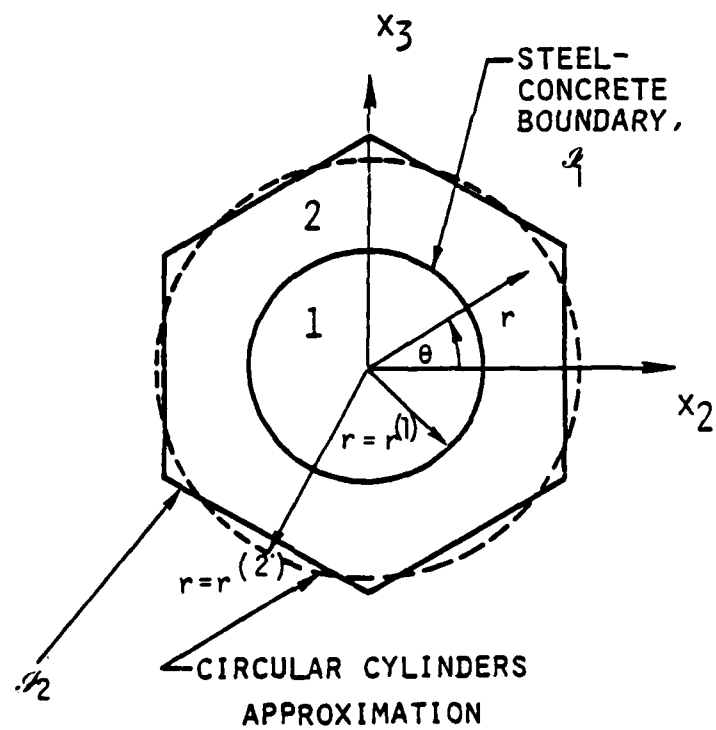
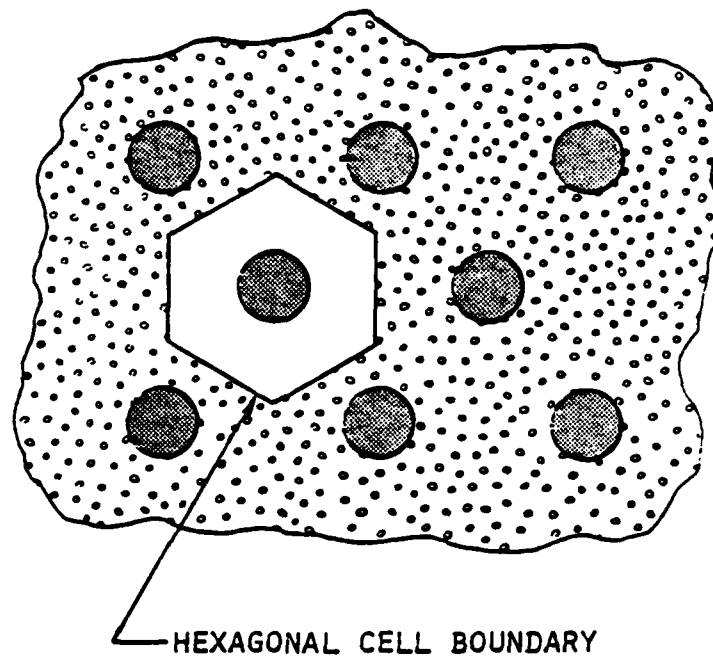


Figure 6-5. Typical cell and coordinate system.

where $(\dot{\cdot})$ denotes the usual time derivative (bookkeeping time for quasi-static problems), and $2e_{k\ell} = (\partial u_k / \partial x_\ell + \partial u_\ell / \partial x_k)$ where $e_{k\ell}$ is the Cauchy strain tensor and u_i the displacement vector. The tensor C_{ijkl} in Eq. 6-2 is assumed to be independent of the stress and strain rates but may depend on the current stress and/or strain states; isotropy of C_{ijkl} may not be assumed in general due to plastic flow and/or prior cracking of the concrete.

6.2.3 Interface Relations - Relations between tractions and displacements for each material across the interface \mathcal{A}_1 , Figure 6-5, must be specified to represent the interaction between steel and concrete. Where slip occurs, an interface stress versus relative slip condition must be defined. For the present discussion, continuity of the normal and tangential displacement components in the x_2, x_3 plane will be assumed; displacements in the x_1 direction may be discontinuous across \mathcal{A}_1 . These conditions can be written as:

$$u_Y^{(1)} v_Y = u_Y^{(2)} v_Y, \quad u_Y^{(1)} s_Y = u_Y^{(2)} s_Y, \quad (6-3a,b)$$

$$\sigma_{Y\delta}^{(1)} v_Y v_\delta = \sigma_{Y\delta}^{(2)} v_Y v_\delta, \quad \sigma_{Y\delta}^{(1)} v_Y s_\delta = \sigma_{Y\delta}^{(2)} v_Y s_\delta \quad (6-3c,d)$$

where $\gamma, \delta = 2,3$ and where v_Y is the unit outer normal vector to the surface \mathcal{A}_1 and s_Y is the unit tangent vector to \mathcal{A}_1 . The relations (6-3a to d) represent, respectively, the continuity of: (1) the displacement component normal to \mathcal{A}_1 , (2) the displacement component tangent to \mathcal{A}_1 (in the x_2, x_3 plane), (3) the normal stress on \mathcal{A}_1 , and (4) the shear stress on \mathcal{A}_1 in the tangential direction. In addition to Eqs. 6-3, a slip condition shall be assumed in the incremental form

$$\dot{\sigma}_{1Y}^{(1)} v_Y = \dot{\sigma}_{1Y}^{(2)} v_Y = C(\dot{u}_1^{(2)} - \dot{u}_1^{(1)}) \equiv C \Delta \dot{u} \text{ on } \mathcal{A}_1, \quad (6-3e)$$

where C is a tangent modulus which depends on the normal stress on \mathcal{A}_1 and the relative deformation history.

6.2.4 Microcoordinates - It is to be expected that stress and deformation fields will vary significantly with respect to two basic length scales: (1) a "global length" typical of the loading condition, body size, or crack pattern, and (2) a "micro length" typical of the cell planar dimensions. Further, these scales will differ by at least one order of magnitude in most cases. This suggests the use of multivariable asymptotic expansions which commences by introducing the "microcoordinates" x_2^* , x_3^* according to

$$(x_2^*, x_3^*) \equiv \frac{1}{\epsilon} (x_2, x_3) \quad (6-4)$$

where $\epsilon \ll 1$ is a parameter that represents the ratio of typical micro-to-macro dimensions of the problem. All functions $f(x_i)$ are next written in the form

$$f(x_i) = F(x_1; x_\gamma^*; \epsilon) \quad ; \quad i = 1 - 3, \quad \gamma = 2, 3 \quad . \quad (6-5a)$$

Spatial derivatives of a function $f(x_i)$ then take the form

$$\frac{\partial f}{\partial x_1} = \frac{\partial F}{\partial x_1}, \quad \frac{\partial f}{\partial x_\gamma} = \frac{\partial F}{\partial x_\gamma} + \frac{1}{\epsilon} \frac{\partial F}{\partial x_\gamma^*} \quad ; \quad \gamma = 2, 3 \quad . \quad (6-5b)$$

For notational convenience in the following development, the functions f and F will both be written simply as f .

6.2.5 Basic Relations: Asymptotic Form - The operations, Eq. 6-5, when applied to all fixed variables, furnish the basic relations, Eqns. 6-1 and 6-2b in the new form

$$\frac{\partial \sigma_{ij}^{(\alpha)}}{\partial x_j} + \frac{1}{\epsilon} \frac{\partial \sigma_{ij}^{(\alpha)}}{\partial x_j^*} = 0 \quad , \quad \frac{\partial \sigma_{ij}^{(\alpha)}}{\partial x_1^*} = 0 \quad ; \quad (6-6)$$

$$\dot{\sigma}_{ij}^{(\alpha)} = C_{ijkl}^{(\alpha)} (\dot{e}_{kl}^{(\alpha)} + \frac{1}{\epsilon} \dot{e}_{kl}^{*(\alpha)}) \quad ; \quad (6-7a)$$

where

$$x_1^* = \frac{x_1}{\epsilon},$$

$$e_k^{(\alpha)} = \frac{1}{2} (\partial u_k^{(\alpha)} / \partial x_\ell + \partial u_\ell^{(\alpha)} / \partial x_k), \quad e_{k\ell}^{(\alpha)} = \frac{1}{2} (\partial u_k^{(\alpha)} / \partial x_\ell^* + \partial u_\ell^{(\alpha)} / \partial x_k^*),$$

$$\partial u_k^{(\alpha)} / \partial x_1^* = 0 \quad ; \quad (6-7b)$$

6.2.6 Periodicity Condition - For a dense mesh (typically one to five percent steel), local periodicity in the planar variables x_2^*, x_3^* may be assumed⁽¹⁷⁵⁾ with respect to all field variables. This condition, which allows one to analyze a single typical cell as illustrated in Figures 6-2,3 takes the form:

$$f(x_i; r^*; \theta; \epsilon) = f(x_i; r^*; \theta + \pi; \epsilon) \text{ on } \mathcal{A}_2 \quad (6-8)$$

where $r^* \equiv r/r^{(2)}$ and f represents any of the field variables.

In the event that the steel does not constitute a dense mesh, such as illustrated in Figure 6-4, one must consider several cells with boundary conditions on \mathcal{A}_2 that differ from Eq. 6-8. However, only a limited number of cell geometries and boundary conditions need be considered for steel layouts of practical interest.

6.2.7 Smoothing Operation - According to Eq. 6-4, variations of the field variables over global and local (micro) dimensions are represented by the explicit dependence on x_i and x_i^* , respectively. That is, all field variables vary "slowly" with respect to x_i and rapidly with respect to x_i^* . In the process of synthesizing a continuum model of a composite such as reinforced concrete one would like to "smooth out" the rapid or micro variations. In view of the explicit dependence on x_i^* , this smoothing process can be easily accomplished by performing averages over the microvariables x_2^*, x_3^* as follows:

$$f^{(\alpha a)}(x_i) = \frac{1}{A^{(\alpha)}} \int_{A^{(\alpha)}} f^{(\alpha)}(x_i; x_2^*, x_3^*) dx_2^* dx_3^* . \quad (6-9)$$

The averaged or "global" variables $f^{(\alpha a)}$, where the superscript "a" denotes an average over the microstructure, are functions only of the global coordinates x_i . The functions $f^{(\alpha)}$ in Eq. 6-9 refer to any of the field variables.

6.2.8 Two-Phase Mixture Equations: Equilibrium and Constitutive -
Upon averaging the equilibrium equations 6-6 according to Eq. 6-9, use of Gauss' Theorem, and application of the periodicity condition Eq. 6-8, one obtains

$$\frac{\partial \sigma_{ij}^{(\alpha p)}}{\partial x_j} + (-1)^{1+\alpha} p_i = 0 , \quad (6-10)$$

where

$$\sigma_{ij}^{(\alpha p)} \equiv n^{(\alpha)} \sigma_{ij}^{(\alpha a)} , \quad n^{(\alpha)} \equiv A^{(\alpha)} / A \quad (6-11)$$

represent partial stresses (denoted by the superscript "p") and volume fractions, respectively, and where

$$p_i \equiv \frac{1}{\epsilon A} \oint_{\mathcal{A}_1} \sigma_{i\gamma}^{(\alpha)} v_\gamma ds \quad (i = 1-3, \gamma = 2,3) \quad (6-12)$$

represent "stress interaction" terms which result from the transfer of normal and shear stresses across the surface \mathcal{A}_1 with unit outer normal v , Figure 6-5.

Upon averaging Eq. 6-6, use of Gauss' Theorem, and application of the periodicity condition Eq. 6-8, one obtains

$$\dot{\sigma}_{ij}^{(\alpha p)} = n^{(\alpha)} C_{ijkl}^{(\alpha a)} \dot{e}_{kl}^{(\alpha a)} + (-1)^{1+\alpha} C_{ijkl}^{(\alpha a)} \dot{s}_{kl}^* \quad (6-13)$$

where

$$S_{ij}^* \equiv (S_{ij} + S_{ji})/2, \quad S_{ij} \equiv \frac{1}{\epsilon A} \int_{\mathcal{A}_1} u_i^{(\alpha)} v_j ds, \quad (6-14)$$

and where $C_{ijkl}^{(\alpha a)}$ and $C_{ijkl}^{*(\alpha a)}$ are defined by*

$$C_{ijkl}^{*(\alpha a)} \int_{A(\alpha)} e_{kl}^{*(\alpha)} dx_2^* dx_3^* \equiv \int_{A(\alpha)} C_{ijkl}^{(\alpha)} e_{kl}^{*(\alpha)} dx_2^* dx_3^*, \quad (6-15)$$

$$C_{ijkl}^{(\alpha a)} e_{kl}^{(\alpha a)} \equiv \frac{1}{A(\alpha)} \int_{A(\alpha)} C_{ijkl}^{(\alpha)} e_{kl}^{(\alpha)} dx_2^* dx_3^*.$$

The form of Eq. 6-13 is based upon continuity of the component of the displacement vector in the x_2, x_3 plane across \mathcal{A}_1 ($u_v^{(1)} = u_v^{(2)}$ on \mathcal{A}_1 , $v = 2, 3$) but allows longitudinal slip ($u_1^{(1)} \neq u_1^{(2)}$ on \mathcal{A}_1). The functions S_{ij}^* in Eq. 6-13 represent "displacement interaction" terms across the boundary \mathcal{A}_1 . Note that, since $v_1 = 0$, then $S_{i1} = 0$ ($i = 1-3$).

Equations 6-10 and 6-13 are the two-phase mixture forms of the equilibrium and constitutive relations. These forms can be interpreted as an overlay of two continua (steel and concrete) which interact via P_i and S_{ij} . The interaction in Eq. 6-10 appears as an effective body force while that in Eq. 6-13 as a modification of the strain tensor which resembles a thermal effect.

6.2.9 Interaction Terms and Closure - The mixture theory defined by Eqs. 6-10 and 6-13 is closed by providing relations between the interaction terms P_i , S_{ij} and the dependent field (global) variables $u_i^{(\alpha a)}$. In addition, the functional dependence of the tangent moduli C_{ijkl} , C_{ijkl}^* on the partial stresses must be specified. To accomplish this task it is necessary to determine the

*Note that the averages for C_{ijkl} are weighted here and are not defined by (6-9).

functional dependence of the field variables on the microcoordinates x^*_2, x^*_3 . This dependence is also of direct interest. In particular, a main feature of the two-phase mixture theory under development is the simulation of stress and deformation fields throughout the components of the composite, i.e., in the steel and concrete, as well as average or global stresses and deformation.

For the purpose of constructing estimates of the "microfields," an asymptotic procedure is used. This commences by expanding the displacements and stresses in each material in a regular asymptotic series⁽¹⁷⁵⁾ as follows:

$$\begin{aligned} u_i^{(\alpha)}(x_k; x_j^*; \epsilon) &= \sum_{n=0}^{\infty} \epsilon^n u_{i(n)}^{(\alpha)}(x_i; x_j^*) , \\ \sigma_{ij}^{(\alpha)}(x_k; x_j^*; \epsilon) &= \sum_{n=0}^{\infty} \epsilon^n \sigma_{ij(n)}^{(\alpha)}(x_k; x_j^*) . \end{aligned} \quad (6-16)$$

The expansions (6-16) are suggested by the form of (6-6) and (6-7a), and the premise that $\epsilon \ll 1$.

Upon substituting Eq. 6-16 into Eqs. 6-6, 6-7a and equating coefficients of each ϵ -order, one obtains

$$\begin{aligned} \partial \sigma_{ij(0)}^{(\alpha)} / \partial x_j^* &= 0 , \\ \partial \sigma_{ij(n)}^{(\alpha)} / \partial x_j^* &= - \partial \sigma_{ij(n-1)}^{(\alpha)} / \partial x_j \quad (n \geq 1) , \\ \partial \sigma_{ij(n)}^{(\alpha)} / \partial x_1^* &= 0 , \\ c_{ijkl(0)}^{(\alpha)} \dot{e}_{kl(0)}^* &= 0 , \\ \dot{\sigma}_{ij(n)}^{(\alpha)} &= c_{ijkl(0)}^{(\alpha)} [\dot{e}_{kl(n)}^{(\alpha)} + \dot{e}_{kl(n+1)}^*] + c_{ijkl(1)}^{(\alpha)} [\dot{e}_{kl(n-1)}^{(\alpha)} + \dot{e}_{kl(n)}^*] + \end{aligned} \quad (6-17)$$

$$\begin{aligned}
& + C_{ijkl}^{(\alpha)}(2) [\dot{e}_{kl}^{(\alpha)}(n-2) + \dot{e}_{kl}^{*(\alpha)}(n-1)] + C_{ijkl}^{(\alpha)}(3) [\dot{e}_{kl}^{(\alpha)}(n-3) + \dot{e}_{kl}^{*(\alpha)}(n-2) \\
& + \dots + C_{ijkl}^{(\alpha)}(n+1) \dot{e}_{kl}^{*(\alpha)}(0) \quad , \quad (6-18)
\end{aligned}$$

$$\partial \dot{e}_{ij(n)}^{(\alpha)} / \partial x_1^* = 0 \quad ,$$

where $\dot{\sigma}_{ij(n)}$, $\dot{e}_{ij(n)} \equiv 0$ for $n < 0$.

Substitution of Eq. 6-16 into the periodicity condition (6-8) furnishes:

$$u_{i(n)}^{(\alpha)}, \sigma_{ij(n)}^{(\alpha)} \in x^* - \text{periodic on } \mathcal{H}_1 \quad . \quad (6-19)$$

Now, the interface continuity conditions (6-3a to d) give

$$u_{\gamma(n)}^{(1)} v_{\gamma} = u_{\gamma(n)}^{(2)} v_{\gamma} \quad , \quad u_{\gamma(n)}^{(1)} s_{\gamma} = u_{\gamma(n)}^{(2)} s_{\gamma} \quad , \quad (6-20a)$$

$$\sigma_{\gamma\delta(n)}^{(1)} v_{\gamma} v_{\delta} = \sigma_{\gamma\delta(n)}^{(2)} v_{\gamma} v_{\delta} \quad , \quad \sigma_{\gamma\delta(n)}^{(1)} v_{\gamma} s_{\delta} = \sigma_{\gamma\delta(n)}^{(2)} v_{\gamma} s_{\delta} \quad (6-20b)$$

while the slip condition, Eq. 6-3e, furnishes

$$\begin{aligned}
\sigma_{1\gamma(n)}^{(1)} v_{\gamma} &= \sigma_{1\gamma(n)}^{(2)} v_{\gamma} = C_{(n)} \dot{\Delta u}_{(0)} + C_{(n-1)} \dot{\Delta u}_{(1)} + C_{(n-2)} \dot{\Delta u}_{(2)} \\
&+ \dots + C_{(0)} \dot{\Delta u}_{(n)} \quad , \quad n = 0, 1, 2 \dots \quad (6-20c)
\end{aligned}$$

where $C_{(n)} = \Delta u_{(n)} \equiv 0$ for $n < 0$.

In addition to Eq. 6-20, one must specify a normalization condition⁽¹⁷⁵⁾ of the form

$$u_{i(n)}^{(1)}(x_i; 0) = 0 \quad , \quad n \geq 1 \quad . \quad (6-21)$$

Equations 6-17 through 6-21 define a set of so-called micro boundary value problems (MBVPs) on the typical cell. For mixture construction purposes only the first few terms of the expressions (6-16) need be retained and thus the resulting set of problems is relatively small. In general, however, they constitute a difficult analytical problem and a comprehensive treatment of this subject is beyond the scope of this report. For discussion purposes it will suffice to note that the solutions to the MBVPs can usually be cast in the form

$$u_{i(n)}^{(\alpha)}(x_j; x_\gamma^*) = u_k^{(\alpha a)}(x_j) f_{ik(n)}^{(\alpha)}(x_\gamma^*) \quad (i, j, k = 1-3, \quad \gamma = 2, 3) \quad (6-22)$$

Substitution of Eq. 6-22, and a similar form for the stresses $\sigma_{ij(n)}^{(\alpha)}$, into Eqs. 6-12 and 6-14 then provides closure of the mixture model in the form

$$\dot{p}_i = G_i(\dot{u}_k^{(\alpha a)}, \dot{\sigma}_{k\ell}^{(\alpha p)}) \quad , \quad \dot{s}_{ij}^* = H_{ij}(\dot{u}_k^{(\alpha a)}, \dot{\sigma}_{k\ell}^{(\alpha p)}) \quad (6-23)$$

where the expressions (6-23) are linear in the rates.

6.3 VALIDATION OF TWO-PHASE MIXTURE RELATIONS FOR STEEL-CONCRETE BOND PROBLEM

At this point the mixture problem will be confined to a consideration of the steel-concrete bond problem. And for this purpose it will suffice to consider the uniaxial tension-compression case. In particular, in what follows, an attempt is made to simulate material response from displacement-controlled tension-compression tests of reinforced concrete. Of interest is (1) typical behavior as predicted by the model (simulation capability) and (2) simulation accuracy.

The uniaxial tension-compression test is an excellent vehicle to demonstrate both the simulation capability and the simulation accuracy of the mixture model. In this respect it should be recalled that the behavior of reinforced concrete under direct

tension is extremely complex. In monotonic extension one observes strain softening and subsequent strain hardening. In cyclic loading one observes stiffness degradation and considerable hysteresis which is the basis for (composite) material damping. These effects are the result of progressive cracking of the concrete, degradation of the steel-concrete bond and subsequent relative slip, and yielding of the steel rebar. Figures 6-6 and 6-7 illustrate these phenomena for a reinforced concrete (masonry) specimen with approximately 0.1 percent steel.

6.3.1 Basic Mixture Relations

For illustration purposes, let the rebar layout be uniaxial and periodic as shown in Figure 6-5. Let a specimen of initial length 2ℓ be subjected to a uniform boundary displacement in the x_1 -direction. Then, periodicity of the microstructure (steel layout) allows us to examine a typical cell as shown in Figure 6-5. Previous experience with fibrous composite materials leads us to conclude that a concentric cylinder approximation of this cell will suffice. The cell may also be envisioned as a classical tension test with the geometry defined by the steel spacing and volume.

For the problem under consideration, it is appropriate to model the plain concrete (material 2) as elastic-brittle fracture (Figure 6-8a), and the steel as elastic-plastic, Figure 6-8b. For monotonic extension the concrete-steel bond will be modeled as perfect below a critical interfacial shear stress, and purely frictional when the critical value is reached and slip occurs (Figures 6-8c,d). For hysteretic loading involving tensile load-unload-reload cycles or tension-compression load-unload-reload cycles, a more complex bond behavior will be adopted based on recent experimental data.

Now, for simplicity let Poisson's ratio of each material be zero. Then, solution of the micro boundary value problem appropriate to the case under consideration furnishes the following mixture relations:

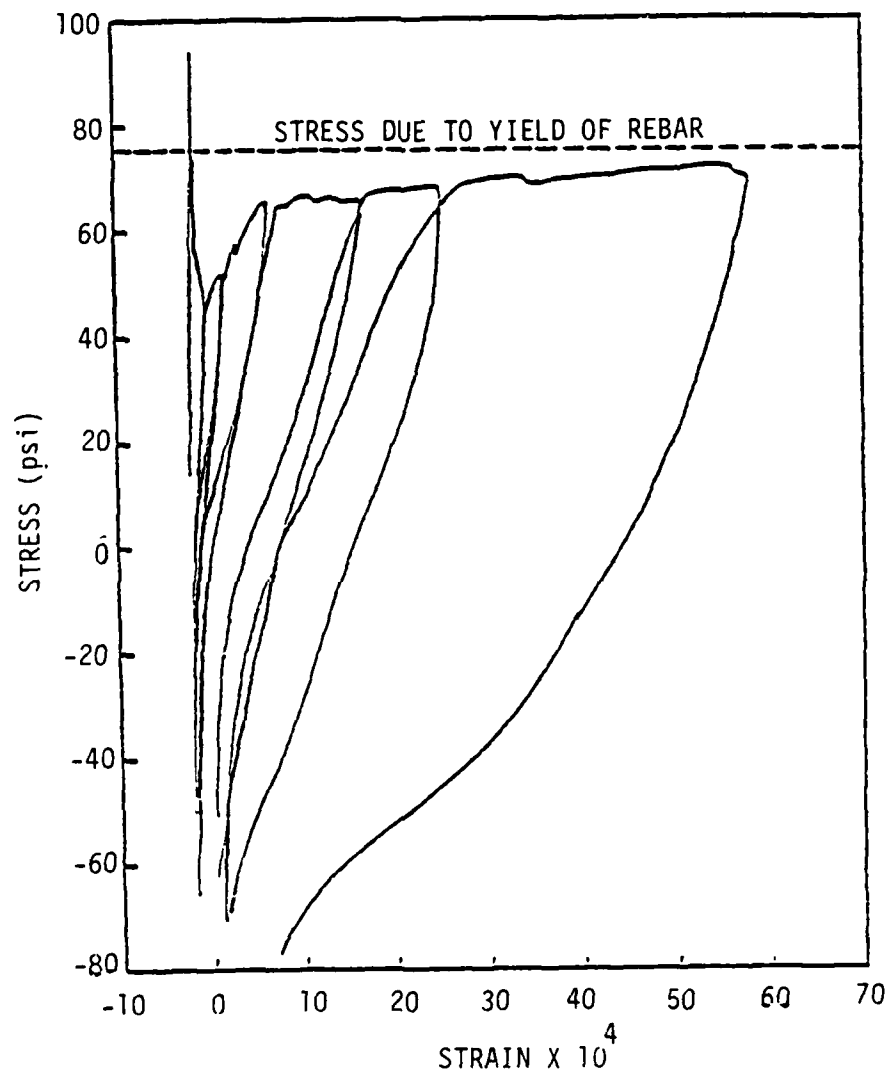


Figure 6-6. Reinforced concrete (masonry) under cyclic tensile loading.

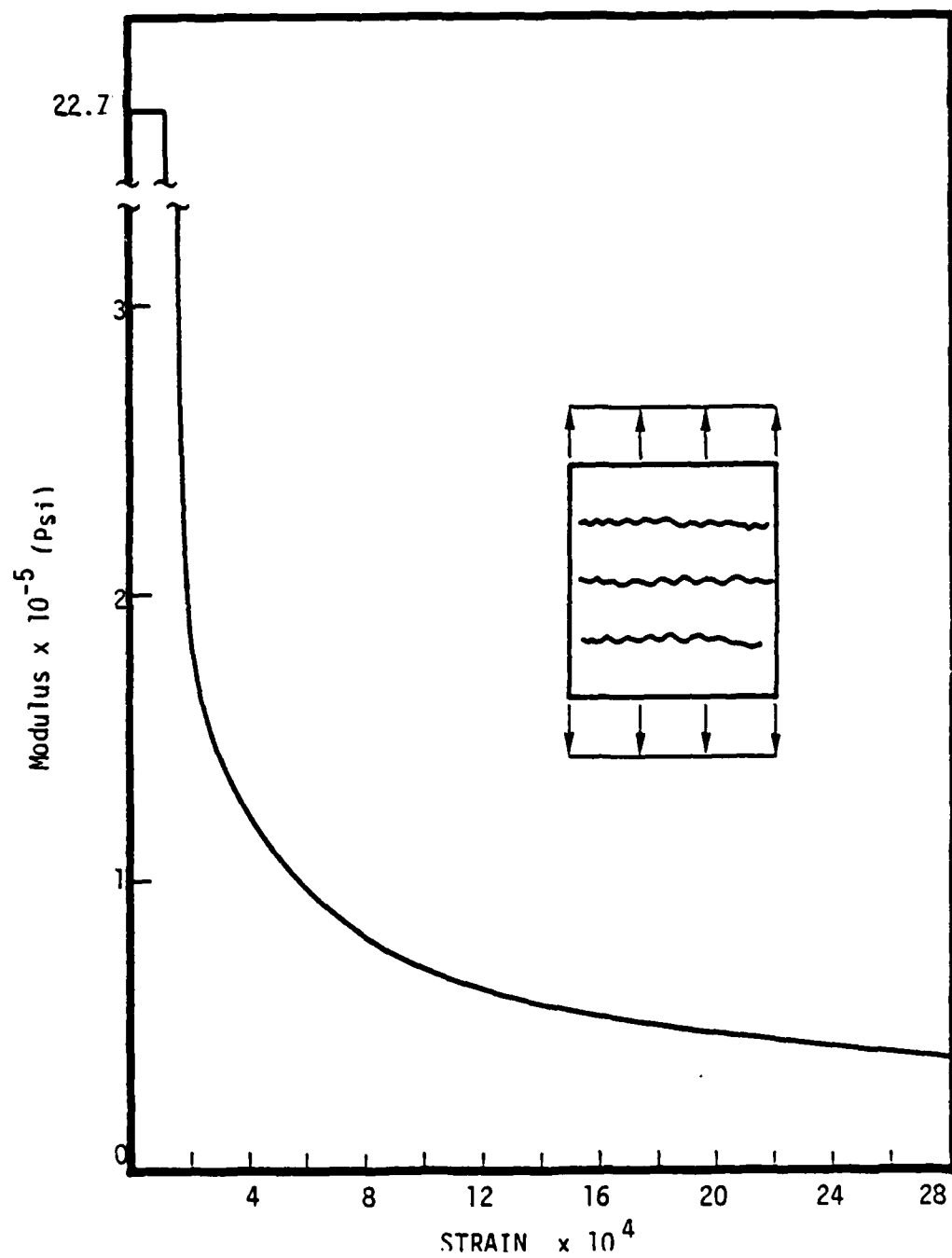


Figure 6-7. Stiffness degradation in a reinforced concrete (masonry) specimen.

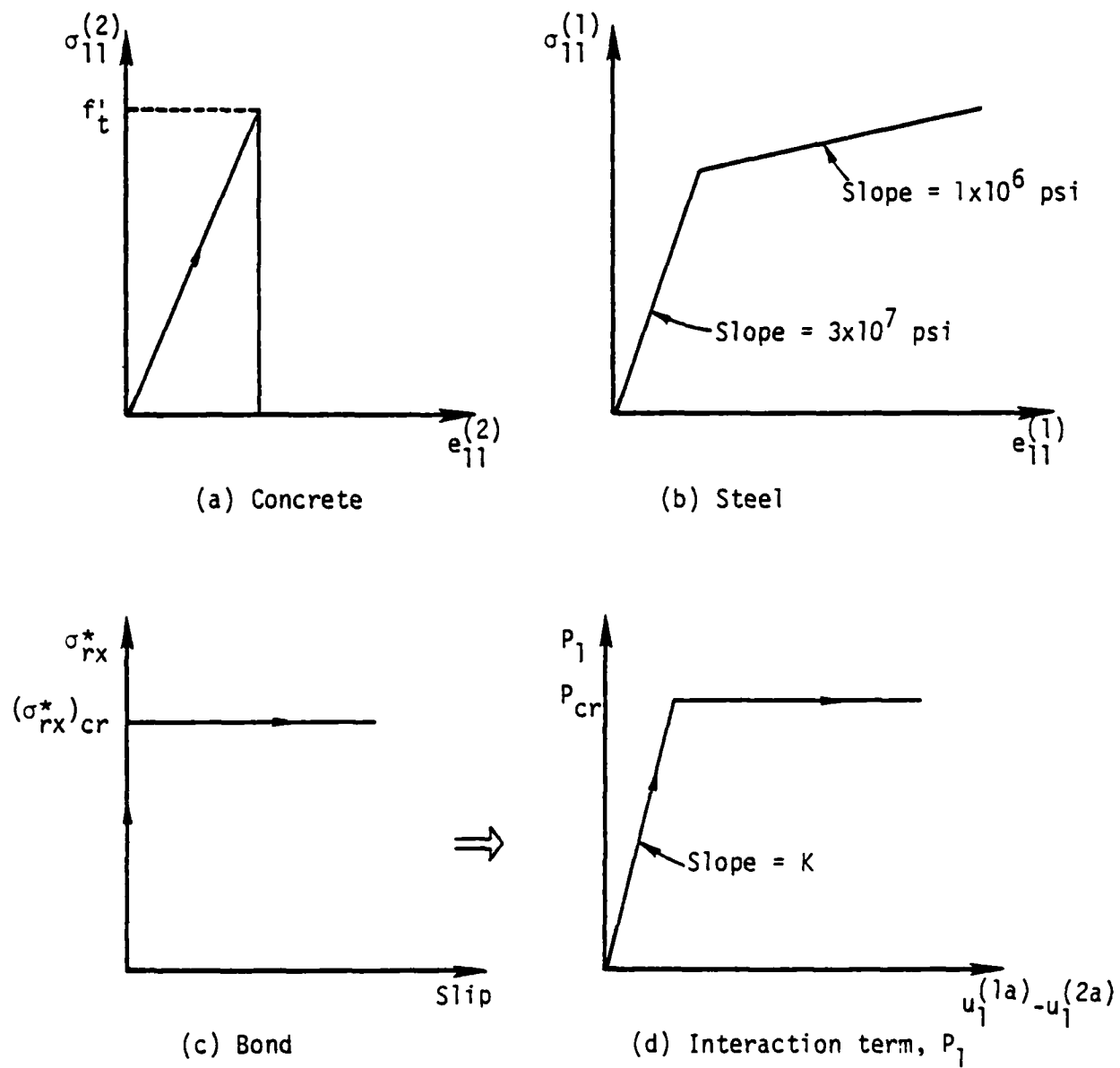


Figure 6-8. Behavior of constituents and steel-concrete interface for monotonic extension example.

(a) Equilibrium

$$\partial \sigma_{11}^{(1p)} / \partial x_1 = -p_1, \quad \partial \sigma_{11}^{(2p)} / \partial x_1 = p_1. \quad (6-24)$$

(b) Constitutive

$$\dot{\sigma}_{11}^{(1p)} = n^{(1)} E^{(1)} \dot{u}_1^{(1a)} / \partial x_1, \quad \dot{\sigma}_{11}^{(2p)} = n^{(2)} E^{(2)} \dot{u}_1^{(2a)} / \partial x_1. \quad (6-25)$$

(c) Interaction term

$$\dot{p}_1 = K(\dot{u}_1^{(1a)} - \dot{u}_1^{(2a)}) \text{ if } p_1 < p_{cr}, \quad (6-26a)$$

(monotonic)

$$p_1 = p_{cr} \operatorname{sgn}(\dot{u}_1^{(1a)} - \dot{u}_1^{(2a)}) \text{ if } p_1 = p_{cr} \quad (6-26b)$$

or

$$\dot{p}_1 = K^*(\dot{u}_1^{(1a)} - \dot{u}_1^{(2a)}) \quad (\text{cyclic}) \quad (6-27)$$

In the above, recall that "1" and "2" denote steel and concrete, respectively; averaged quantities (denoted by the superscript "a") are defined by Eq. 6-9, or in terms of the cylindrical cell geometry by (Figure 6-5)

$$(\quad)^{(1a)} \equiv \frac{1}{\pi r^{(1)2}} \int_0^{r^{(1)}} 2\pi r (\quad)^{(1)} dr, \quad (6-28)$$

$$(\quad)^{(2a)} \equiv \frac{1}{\pi(r^{(2)2} - r^{(1)2})} \int_{r^{(1)}}^{r^{(2)}} 2\pi r (\quad)^{(2)} dr.$$

the quantities

$$\sigma_{11}^{(1p)} \equiv n^{(1)} \sigma_{11}^{(1a)} \quad , \quad \sigma_{11}^{(2p)} \equiv n^{(2)} \sigma_{11}^{(2a)} \quad (6-29)$$

are partial stresses and $n^{(1)}$, $n^{(2)}$ denote volume fractions of steel and concrete, respectively:

$$n^{(1)} = r^{(1)2} / r^{(2)2} \quad ; \quad n^{(2)} = 1 - n^{(1)} \quad . \quad (6-30)$$

The quantities $E^{(1)}$, $E^{(2)}$, K^* are tangent moduli and K is a constant defined by

$$-K = \frac{8}{(r^{(2)})^2} \left(\frac{1}{\mu^{(1)}} + \frac{Q^*}{\mu^{(2)}} \right)^{-1} \quad (6-31a)$$

where $\mu^{(1)}$, $\mu^{(2)}$ are initial shear moduli, $(\mu^{(\alpha)} = E^{(\alpha)}/2$ if $\nu^{(\alpha)} = 0$), and where

$$Q^* = - \left(1 + \frac{2}{n^{(2)}} + \frac{2 \ln n^{(1)}}{n^{(2)2}} \right) . \quad (6-31b)$$

The critical value P_{cr} is related to the critical interface shear stress $(\sigma_{rx}^*)_{cr}$ by (see Figure 6-8d)

$$|P_{cr}| = \frac{2n^{(1)}}{r^{(1)}} \quad |(\sigma_{rx_1}^*)_{cr}| : \quad (6-31c)$$

(d) Boundary Conditions

In addition to Eqs 6-24 to 6-27, boundary conditions must be specified. A complete solution to the tension or tension-compression problem will necessitate consideration of two sub-problems involving the following boundary conditions:

Problem No. 1

$$u_1^{(1a)} = u_1^{(2a)} = -u_0 \text{ at } x_1 = 0 \quad ,$$

$$u_1^{(1a)} = u_1^{(2a)} = 0 \text{ at } x_1 = \ell$$

(6.32a)

Problem No. 2

$$u_1^{(1a)} = -u_0, \quad \sigma_{11}^{(2a)} = 0 \quad \text{at } x_1 = 0$$

(6-32b)

$$u_1^{(1a)} = u_1^{(2a)} = 0 \quad \text{at } x_1 = \ell.$$

6.3.2 Monotonic Extension

Averaged Fields in Each Constituent - Consider now the case of monotonic (displacement controlled) extension. The solution sequence begins by solution of Eqs. 6-24, 6-25 and 6-26a together with the boundary conditions 6.32a. This corresponds to an initial specimen in which the concrete is linear and uncracked, the steel is linear, the steel-concrete bond is perfect, and the boundaries at $x = 0, 2\ell$ suffer uniform extension. This is illustrated as state (1) of Figure 6-9. The solution to this elementary problem furnishes the global (effective) stress-strain relation

$$\sigma_{(e)} = \bar{E} e_{(e)} \quad (6-33)$$

where

$$e_{(e)} \equiv -u_0/\ell, \quad (6-33a)$$

$$\sigma_{(e)} \equiv n^{(1)} \sigma_{11}^{(1a)} + n^{(2)} \sigma_{11}^{(2a)}, \quad (6-33b)$$

$$\bar{E} \equiv n^{(1)} E^{(1)} + n^{(2)} E^{(2)}. \quad (6-33c)$$

The average or global stresses in the steel and concrete are

$$\sigma_{11}^{(1a)} = \frac{E^{(1)} \sigma_{(e)}}{\bar{E}} = E^{(1)} e_{(e)}, \quad \sigma_{11}^{(2a)} = \frac{E^{(2)} \sigma_{(e)}}{\bar{E}} = E^{(2)} e_{(e)} \quad (6-34)$$

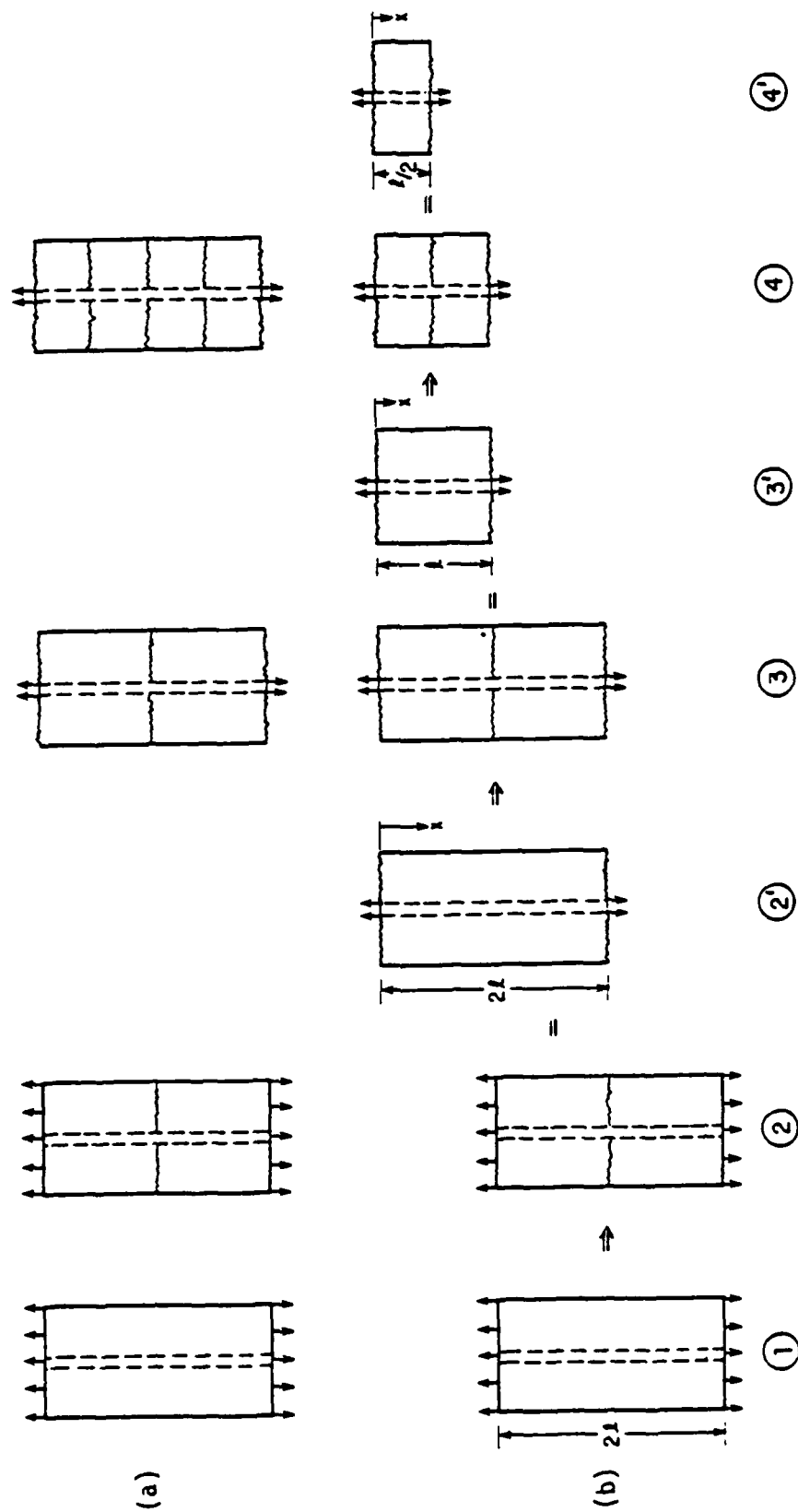


Figure 6-9. Typical cell cracking sequence: (a) physical, (b) mathematical.

First cracking of the concrete occurs when the average* concrete stress $\sigma_{11}^{(2a)} = f'_t$, i.e., when the tensile strength of the concrete is reached. The corresponding global stress $\sigma_{(e)}$ at this point is given by

$$(\sigma_{(e)})_{cr} = E f'_t / E^{(2)} . \quad (6-35)$$

The actual location of the first crack is flaw-dominated. In what follows it will be assumed that a single initial crack occurs at the cell center, $x = \ell$. This is illustrated as state (2) of Figure 6-9.

Subsequent to the first crack one must recompute the field variables for the state (2) of Figure 6-9. However, state (2) is mathematically equivalent to state (2'). Consequently, one must consider a steel-loaded specimen of length 2ℓ , and the boundary conditions 6-33b with

$$-u_0/\ell = f'_t / E^{(2)} . \quad (6-36)$$

An analytical solution of this problem, which includes bond slip, can be obtained in the form:

Slip Zone ($0 \leq x_1 \leq x_{(p)}$)

$$\sigma_{11}^{(1a)}(x_1) = \sigma_{(e)} - \frac{P_{cr} x_1}{n^{(1)}} , \quad \sigma_{11}^{(2a)}(x_1) = \frac{P_{cr} x_1}{n^{(2)}} ; \quad (6-37a,b)$$

$$\sigma_{rx_1}^*(x_1) = r^{(1)} P_{cr} / 2n^{(1)} ; \quad (6-37c)$$

*Specification of failure in terms of local stresses has been investigated and was found to not alter the results significantly for this problem.

$$u_1^{(1a)}(x_1) = \frac{P_{cr}}{2n^{(1)}E^{(1)}} (x_{(p)}^2 - x_1^2) - \frac{\sigma(e)}{n^{(1)}E^{(1)}} (x_{(p)} - x_1) + \frac{\sigma(e)}{E} \left[(x_{(p)} - \ell) - \frac{n^{(2)}E^{(2)}}{\beta n^{(1)}E^{(1)}} \left(1 - \frac{P_{cr} x_{(p)} E}{n^{(2)}E^{(2)}\sigma(e)} \right) \tanh \beta(\ell - x_{(p)}) \right], \quad (6-38a)$$

$$u_1^{(2a)}(x_1) = -\frac{P_{cr}}{2n^{(2)}E^{(2)}} (x_{(p)}^2 - x_1^2) + \frac{\sigma(e)}{E} \left[(x_{(p)} - \ell) + \frac{1}{\beta} \left(1 - \frac{P_{cr} x_{(p)} E}{n^{(2)}E^{(2)}\sigma(e)} \right) \tanh \beta(\ell - x_{(p)}) \right] ; \quad (6-38b)$$

Perfect Bond Zone ($x_{(p)} \leq x \leq \ell$)

$$\sigma_{11}^{(1a)}(x_1) = \frac{\sigma(e)E^{(1)}}{E} \left[1 + \frac{n^{(2)}E^{(2)}}{n^{(1)}E^{(1)}} \left(1 - \frac{P_{cr} x_{(p)} E}{n^{(2)}E^{(2)}\sigma(e)} \right) \frac{\cosh \beta(\ell - x_1)}{\cosh \beta(\ell - x_{(p)})} \right], \quad (6-39a)$$

$$\sigma_{11}^{(2a)}(x_1) = \frac{\sigma(e)E^{(2)}}{E} \left[1 - \frac{\cosh \beta(\ell - x_1)}{\cosh \beta(\ell - x_{(p)})} \left(1 - \frac{P_{cr} x_{(p)} E}{\sigma(e)n^{(2)}E^{(2)}} \right) \right], \quad (6-39b)$$

$$\sigma_{rx_1}^*(x_1) = r^{(1)}K(u_1^{(1a)} - u_1^{(2a)})/2n^{(1)}, \quad (6-39c)$$

$$u_1^{(1a)}(x_1) = \frac{\sigma(e)}{E} \left[(x_1 - \ell) - \frac{n^{(2)}E^{(2)}}{\beta n^{(1)}E^{(1)}} \left(1 - \frac{P_{cr} x_{(p)} E}{n^{(2)}E^{(2)}\sigma(e)} \right) \frac{\sinh \beta(\ell - x_1)}{\cosh \beta(\ell - x_{(p)})} \right], \quad (6-40a)$$

$$u_1^{(2a)}(x_1) = \frac{\sigma(e)}{E} \left[(x_1 - \ell) + \frac{1}{\beta} \left(1 - \frac{P_{cr} x_{(p)} E}{n^{(2)}E^{(2)}\sigma(e)} \right) \frac{\sinh \beta(\ell - x_1)}{\cosh \beta(\ell - x_{(p)})} \right], \quad (6-40b)$$

where

$$\beta^2 \equiv K \left(\frac{1}{n^{(1)} E^{(1)}} + \frac{1}{n^{(2)} E^{(2)}} \right) , \quad (6-41)$$

All functions in the interval $\ell \leq x \leq 2\ell$ can be obtained from Eqs. 6-37 to 6-40 and symmetry.

The foregoing stresses and displacements are illustrated in Figure 6-10 for typical material properties. The interval $0 \leq x \leq x_{(p)}$ represents a zone of interfacial slip while the interval $x_{(p)} < x \leq \ell$ represents an interval of perfect steel-concrete bond. The transition point $x_{(p)}$ is obtained by setting

$$u^{(1a)}_{(0)} = -\ell f'_t E^{(2)} \quad (6-42)$$

in Eq. 6-38a and solving (numerically) the resulting transcendental relation for $x_{(p)}$; this is the steel displacement corresponding to the first crack in the concrete.

Consider now Figure 6-9 again. Examination of Eq. 6-37b and 6-39b, which define the concrete (average) stress distributions, reveals that $\max. \sigma^{(2a)}_{11}$ occurs at $x = \ell$ of problem (2') which corresponds to the boundary of problem (1). Consequently, if the concrete at the cell boundary is allowed to crack, then a new crack will initiate at $x = \ell$ of problem (2') when $\sigma^{(2a)}_{11}(\ell)$ of Eq. 6-39b reaches the value f'_t , and the crack pattern of the entire cell corresponds to that shown in Figure 6-9. The value of $\sigma(e)$ corresponding to fracture is obtained from Eq. 6-39b by setting $\sigma^{(2a)}_{11}(\ell) = f'_t$; the steel has extended at this point by the amount of $2u^{(1a)}_1(0)$ where the latter is obtained by substituting the value of $\sigma(e)$ above into Eq. 6-40a; this corresponds to $e(e) = u^{(1a)}_{(0)}/\ell = u_0/\ell$.

Subsequent to the initiation of the above crack pattern, one must recompute the field variables in each material. This is shown as problem (3) of Figure 6-9 which is mathematically equivalent to problem (3'). However, it is evident that (3') is obtained from

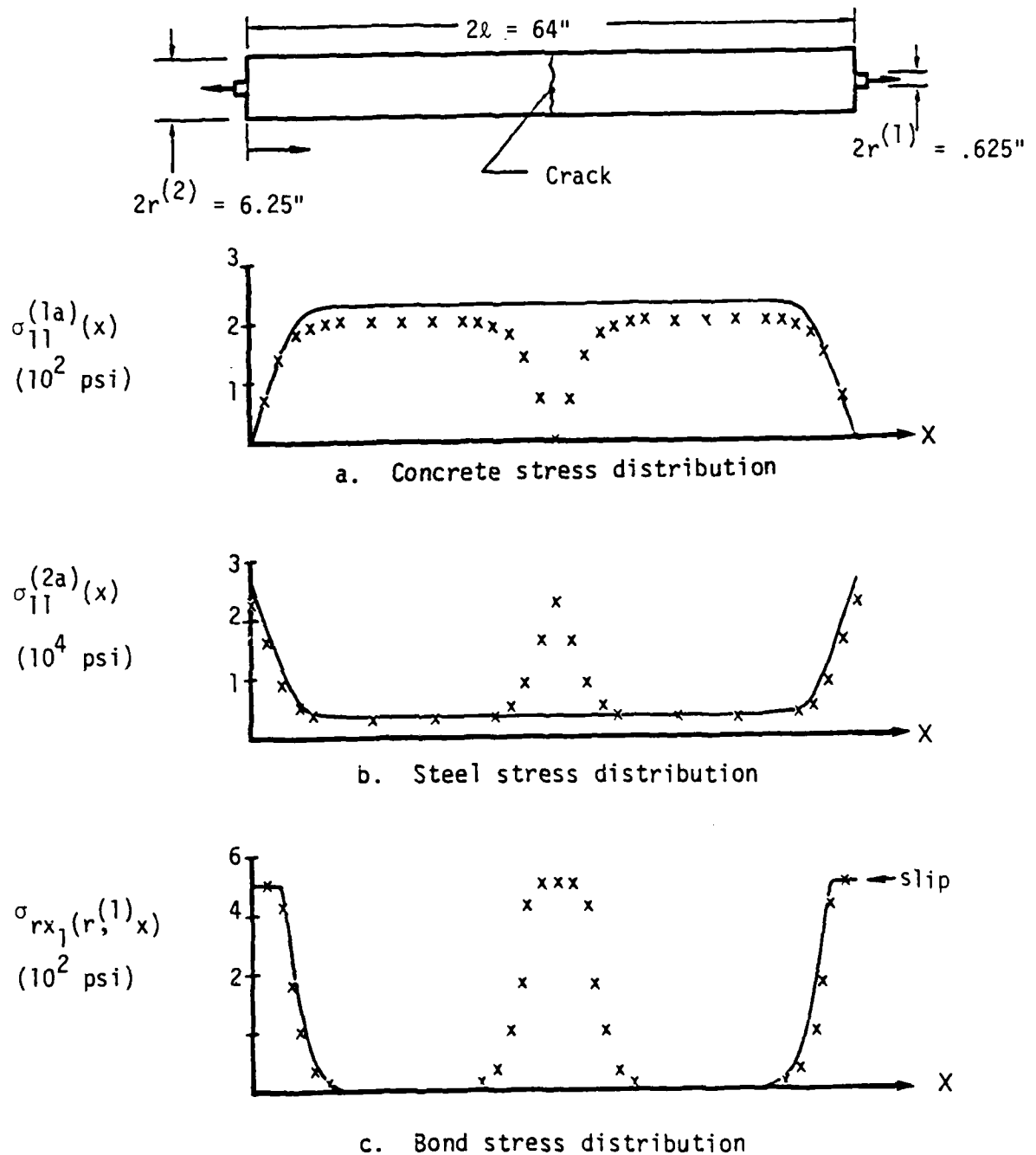


Figure 6-10. Typical stress distributions prior to (solid lines) and after (x's) concrete cracking at $x = \ell$ for bond strength = 700 psi and concrete tensile strength = 230 psi.

(2') by replacing 2ℓ by ℓ . Thus, the field variables may be obtained from Eqs. 6-37 - 6-40 by simply replacing ℓ by $\ell/2$. This suggests the following solution sequence:

1. Consider a uniformly extended, uncracked specimen of length 2ℓ . ((1) of Figure 6-9.) Let u_0 denote this extension.
2. After the first crack, consider a steel-loaded specimen of length 2 . ((2) of Figure 6-9.) Find the equilibrium state corresponding to $e_{(e)} = -u_0/\ell = f'_t/E^{(2)}$.
3. Continue loading (extending) until $\sigma_{11}^{(2a)}(\ell)$, given by the perfect bond solution, reaches f'_t . Let $e^*_{(i)}$ be the effective strain at failure.
4. Reduce the length of the steel-loaded specimen by $1/2$ (corresponding to (3') of Figure 6-9) and find an equilibrium state for the new length corresponding to $e_{(e)} = e^*_{(i)}$.
5. $i = i + 1$: Repeat steps 3 and 4.

The above sequence is illustrated schematically in Figure 6-9.

Composite Global Fields - Equations 6-37 through 6-40 furnish the average stresses and displacements in each constituent. One may also completely homogenize the steel and concrete at this point by defining $\sigma_{(e)}$, $e_{(e)}$ as the "effective" stress, strain for the specimen, respectively. Thus:

$$\sigma_{(e)} \equiv n^{(1)}\sigma_{11}^{(1a)} + n^{(2)}\sigma_{11}^{(2a)} = \frac{-P_{cr}E}{n^{(2)}E^{(2)}} \left[x_{(p)} + (\beta \tanh \beta(\ell - x_{(p)}))^{-1} \right], \quad (2-43a)$$

$$\begin{aligned}
e_{(e)} \equiv - \frac{u^{(1a)}(o)}{\ell} = & - \frac{\sigma_{(e)}}{\bar{E}} \left[\left(\frac{x_{(p)}}{\ell} - 1 \right) - \frac{n^{(2)}E^{(2)}}{n^{(1)}E^{(1)}} \left(\frac{1}{\beta \ell} \right) \right. \\
& \cdot \left. \left(1 - \frac{P_{cr} x_{(p)} \bar{E}}{n^{(2)}E^{(2)} \sigma_{(e)}} \right) \tanh \beta(\ell - x_{(p)}) \right] \\
& + \frac{\sigma_{(e)} x_{(p)}}{n^{(1)}E^{(1)} \ell} - \frac{P_{cr} x_{(p)}^2}{2n^{(1)}E^{(1)} \ell} .
\end{aligned} \tag{6-43b}$$

Given Eqs. 6-43a,b, an effective secant modulus can be defined by:

$$\begin{aligned}
E_{(e)} \quad \frac{\sigma_{(e)}}{e_{(e)}} = & - \bar{E} \left[\left(\frac{x_{(p)}}{\ell} - 1 \right) - \frac{n^{(2)}E^{(2)}}{\beta n^{(1)}E^{(1)}} \left(1 - \frac{P_{cr} x_{(p)} \bar{E}}{n^{(2)}E^{(2)} \sigma_{(e)}} \right) \tanh \beta(\ell - x_{(p)}) \right. \\
& \left. + \frac{\sigma_{(e)} x_{(p)}}{n^{(1)}E^{(1)} \ell} - \frac{P_{cr} x_{(p)}^2}{2n^{(1)}E^{(1)} \ell} \right]^{-1} .
\end{aligned} \tag{6-44}$$

A tangent modulus can be similarly defined by utilizing increments of the effective stress and strain.

C. Typical Behavior. Let us now examine the typical simulation character of the mixture model for monotonic extension when both bond slip and concrete cracking are present. For this purpose consider a hypothetical laboratory test. In the laboratory one would measure the total tensile force applied to a specimen and the overall change in length. If one divides the former by the total specimen cross-sectional area and the latter by the original specimen length, then one obtains the effective stress $\sigma_{(e)}$ and the effective strain $e_{(e)}$, respectively. It is appropriate, therefore, to employ these quantities as response measures.

Figures 6-11a,b illustrate typical graphs of effective stress versus effective strain for a steel volume fraction of one percent, a steel-concrete bond strength of three times the concrete tensile strength, and an initial crack length of $\ell = 10r^{(2)}$ ($\epsilon = 0.10$)

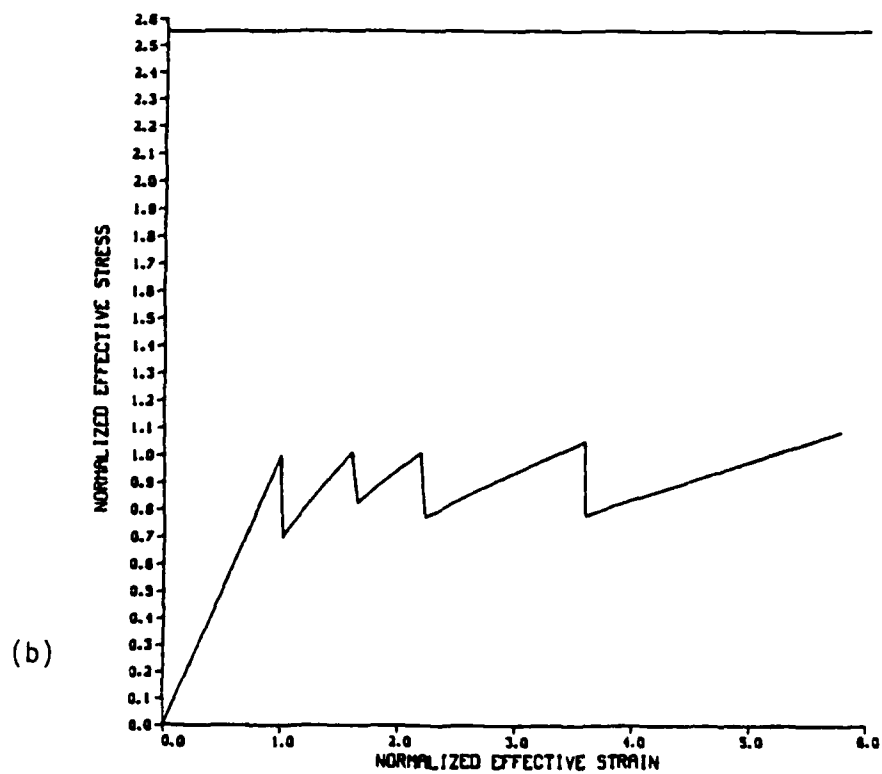
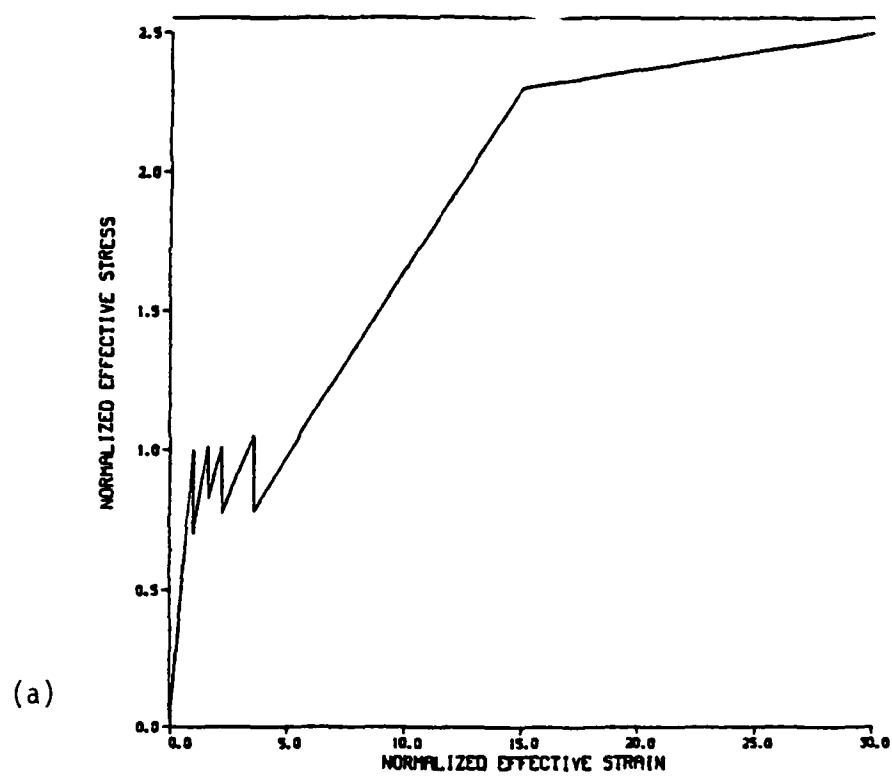


Figure 6-11a,b. Effective stress versus effective strain for monotonic extension and $\epsilon = 0.1$, $n^{(1)} = 0.01$, $(\sigma_{rx}^*)_{cr} = 3f_t'$.

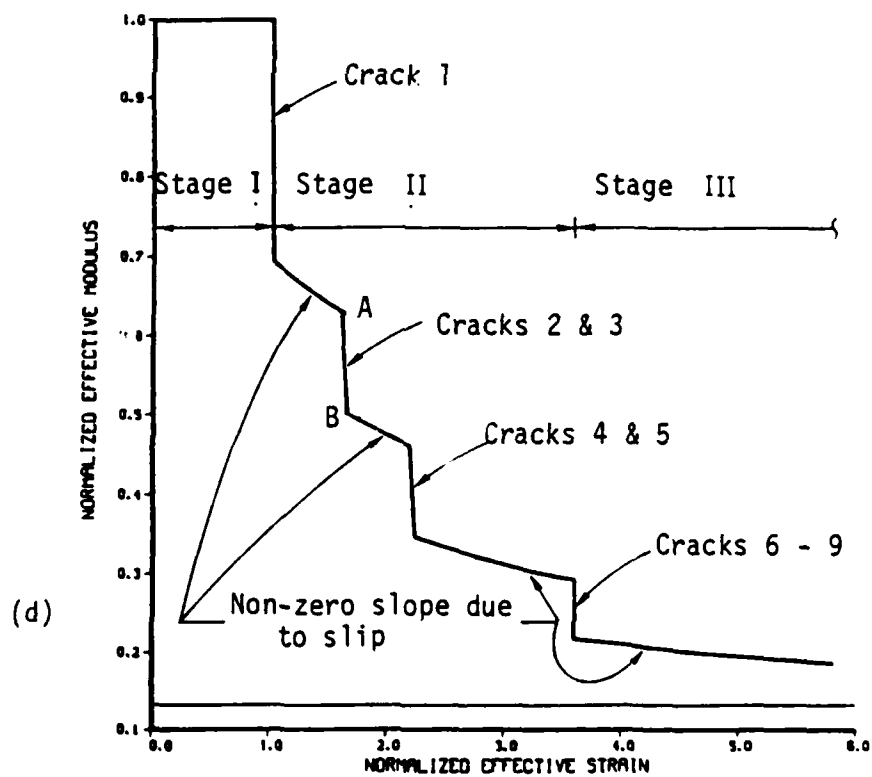
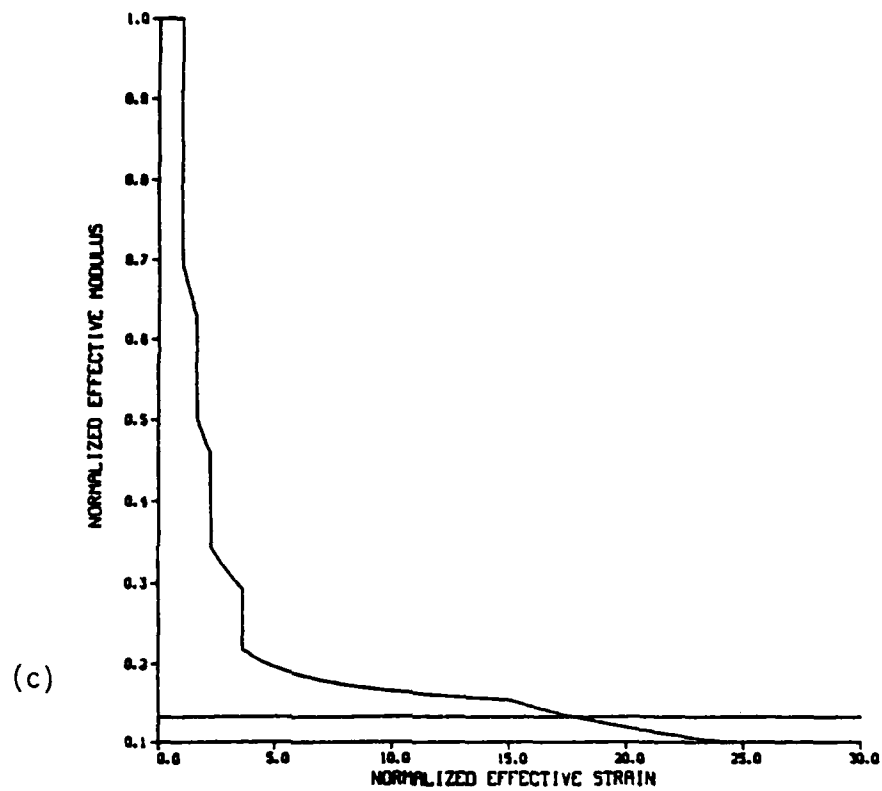


Figure 6-11c,d. Stiffness degradation for $\epsilon = 0.1$, $n^{(1)} = 0.01$,
 $(\sigma_{rx}^*)_{cr} = 3 f'_t$.

where $2r^{(2)}$ is the "cell" diameter. The stress drops represent the formation of new cracks in the concrete. One would expect such cracks to lead to stiffness degradation. This is illustrated in Figures 6-11c,d where the normalized effective modulus $E_{(e)}/E$ is graphed versus the normalized effective strain $e_{(e)} f_t/E^{(2)}$ for the aforementioned parameter values. As can be observed, the degradation in specimen stiffness, as measured here by the secant modulus, $E_{(e)}$, is severe.

The behavior depicted by Figures 6-11a-d can be partitioned into three stages as shown in Figure 6-11d. In Stage I, the concrete is uncracked, the steel-concrete bond is perfect, and the response is elastic. The beginning of Stage II corresponds to the first concrete crack; during this stage the number of cracks increases as the effective strain increases and the major decrease in the effective specimen stiffness occurs; cracking is manifested by drops in the effective stress; the effective stress versus effective strain curve is discontinuous but the mean effective stress remains relatively constant (Figure 6-11b). Cracking of the concrete ceases at the end of Stage II and Stage III corresponds to bond slip without further cracking; yielding of the rebar generally occurs in this stage. Both Stages II and III represent highly nonlinear behavior.

Consider next an actual laboratory test. Figure 6-12a shows the results of two such tests on the wire reinforced mortar specimen illustrated in Figure 6-13. The specimen was subjected to monotonic extension via a displacement-controlled test system. The authors of this data describe three basic stages of material behavior; they correspond exactly to the stages defined above for the simulation of material response using the mixture model. The stress drops in Figure 6-12 correspond, as with the simulation, to the formation of new cracks in the concrete. Vertical stress drops are not observed in the test results as a consequence of inadequate system stiffness. Vertical drops require an extremely stiff test system and precision displacement control; as the test system stiffness decreases the drops become smeared as indicated in Figure 6-12.

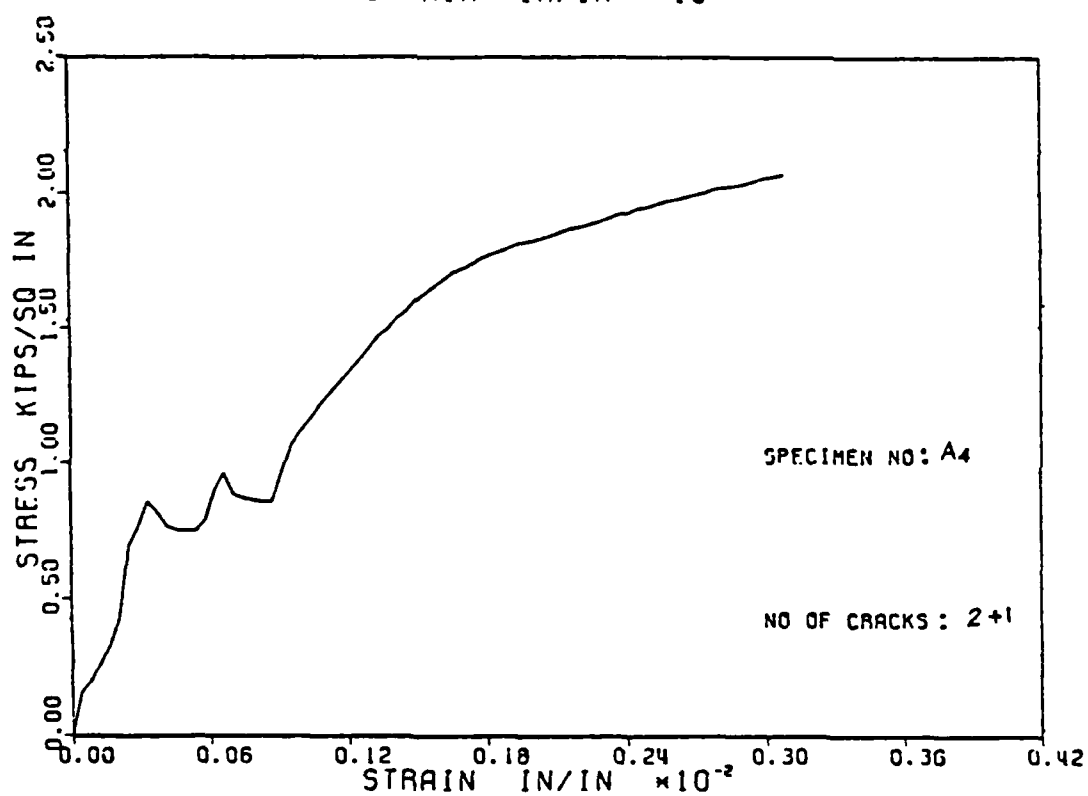
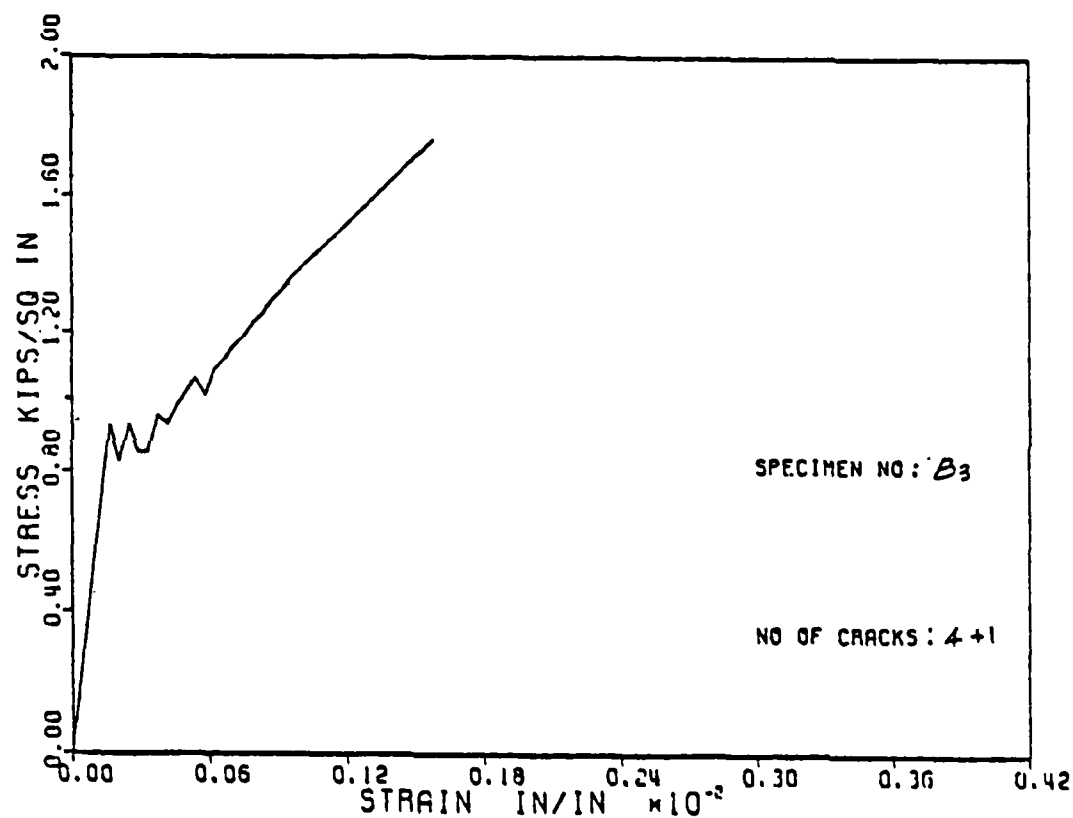


Figure 6-12a,b. Response of wire-reinforced test specimen under monotonic extension.

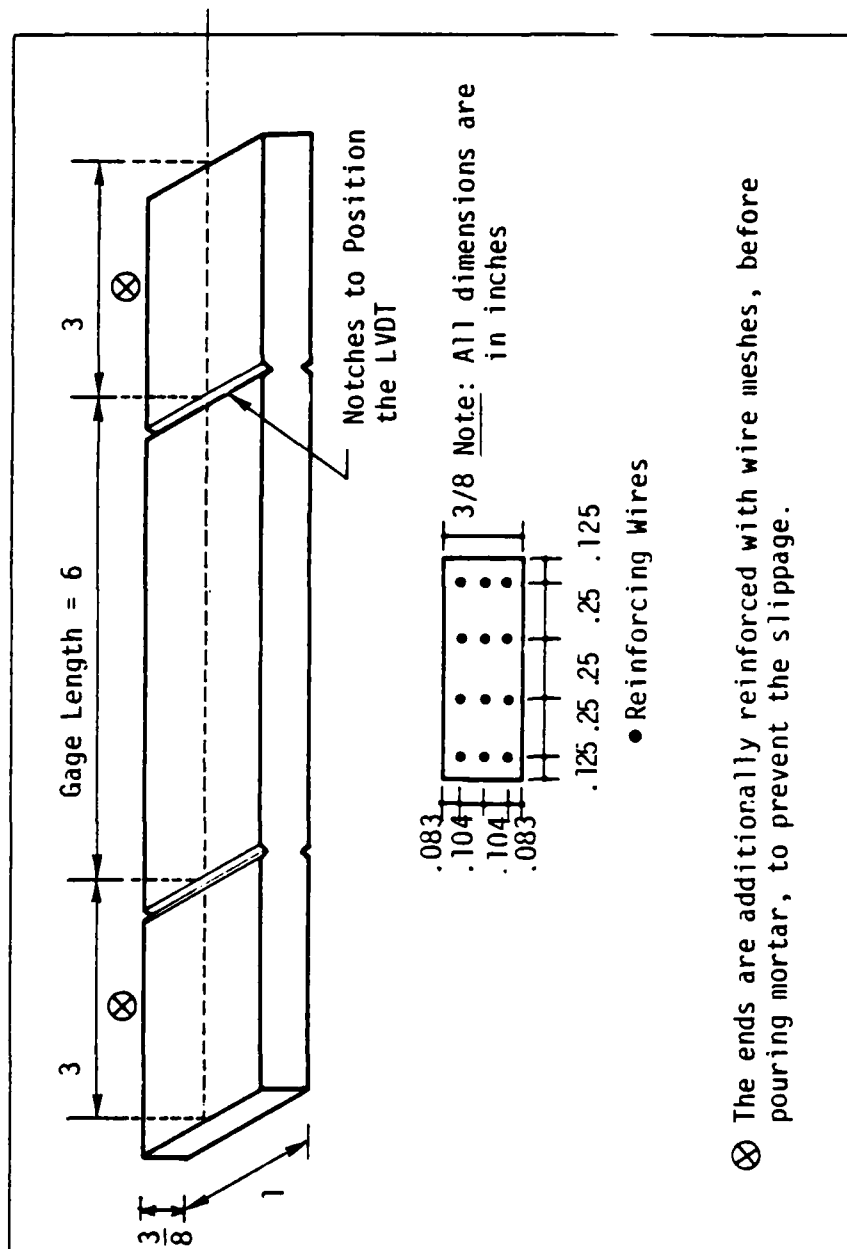


Figure 6-13. Specimen details.

In view of the above, one concludes that the global response predicted by the mixture model embodies all of the basic features of actual material response for monotonic extension. Consequently, it can be stated that the mixture model is capable of realistic response simulation for monotonic extension.

Typical Accuracy. Theory versus Experiment

In order to validate the mixture model, a set of accurate and complete test data is necessary. Unfortunately, appropriate test data on full-scale reinforced concrete is currently not available for monotonic extension. However, data on scaled reinforced concrete is available in the form of a test series by Somayaji and Shah^(176,177) on wire-reinforced mortar. In an effort to explore the simulation accuracy of the mixture model, several specimens in this test series were investigated. Figure 6-14 shows the results of one such simulation for monotonic extension. The specimen geometry is illustrated in Figure 6-13. The component and interface properties were deduced from component and pullout test data.

The agreement between synthesized and measured effective stress, effective strain, and total number of cracks (over the specimen gage length between the notches in Figure 6-13) is seen to be good over most of the strain interval shown. The disagreement in final slopes is believed to be due to pullout of the wires from the specimen end sections at the original groove locations (see Figure 6-13).

In view of the above, it is concluded that the mixture model is capable of accurate simulations of real material behavior for monotonic extension.

6.3.3 Hysteretic Extension

Typical Behavior. Let us now turn to hysteretic extension involving load-unload-reload cycles. For such deformation an analytical solution of Eqs. 2-24, 2-25, 2-27 and 2-33b is not feasible. Consequently, the mixture relations were discretized and a numerical

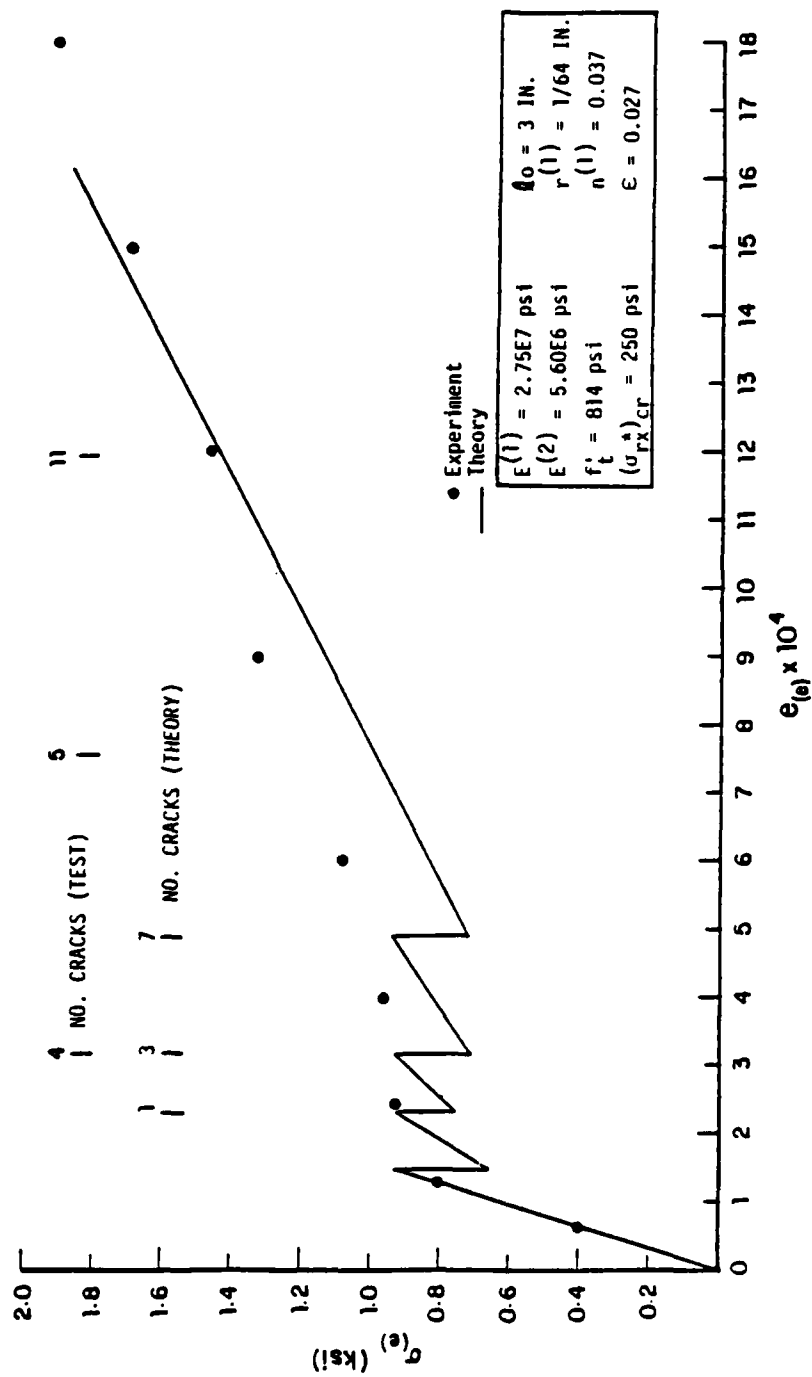


Figure 6-14. Theory versus experiment for monotonic extension.

solution was carried out. The details of the numerics will not be presented herein. It is noted that the resulting numerical program was validated by comparing numerical and analytical results for the case of monotonic extension.

For hysteretic deformation it is necessary to extend the description of the steel-concrete interface bond, i.e., to provide a definition of the tangent stiffness K^* in Eq. 2.27 for arbitrary interface slip histories. Figure 6-15a illustrates the slip law adopted for unloading to zero effective stress while Figure 6-15b depicts the slip law used for tension-compression load-unload-reload cycles. Both bond slip descriptions reflect recent data⁽¹⁷⁸⁾ on steel-concrete bond slip behavior.

Typical hysteretic response of the mixture model for unloading to zero effective stress is illustrated in Figure 6-16. The similarity of this response with the test data shown in Figure 6-6 is evident. Although the strain histories differ,** it can be observed that the mixture model exhibits all of the basic features of real material behavior. These include stress drops due to progressive cracking, stiffness degradation due to cracking and bond slip, strain hardening due to load transfer to the steel, and hysteresis due to bond slip.

A single cycle of response for tension-compression cyclic loading is shown in Figure 6-17 for the mixture model and Figure

*The vast majority of pullout and tension test data in the literature are not of sufficient quality or completeness to be useful for model validation purposes. Most such tests have been conducted without any material model in mind. Consequently the objectives of the test are not clear. Additional experiments devoted specifically to mixture model validation are needed.

**The test specimen was subjected to reversed (compressive) loading resulting in a return to zero effective strain while the model was subjected to unload-reload cycles to zero effective stress. In addition, the peak (first crack) test specimen stress is not shown in Figure 6-16.

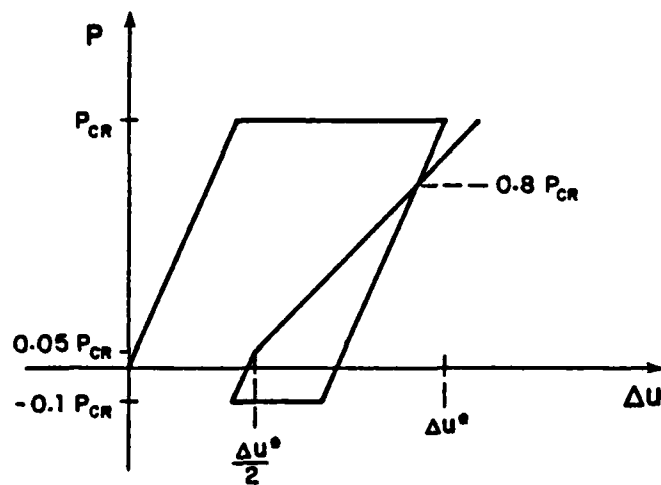


Figure 6-15a. Bond Slip Law for Unloading to Zero Effective Stress.

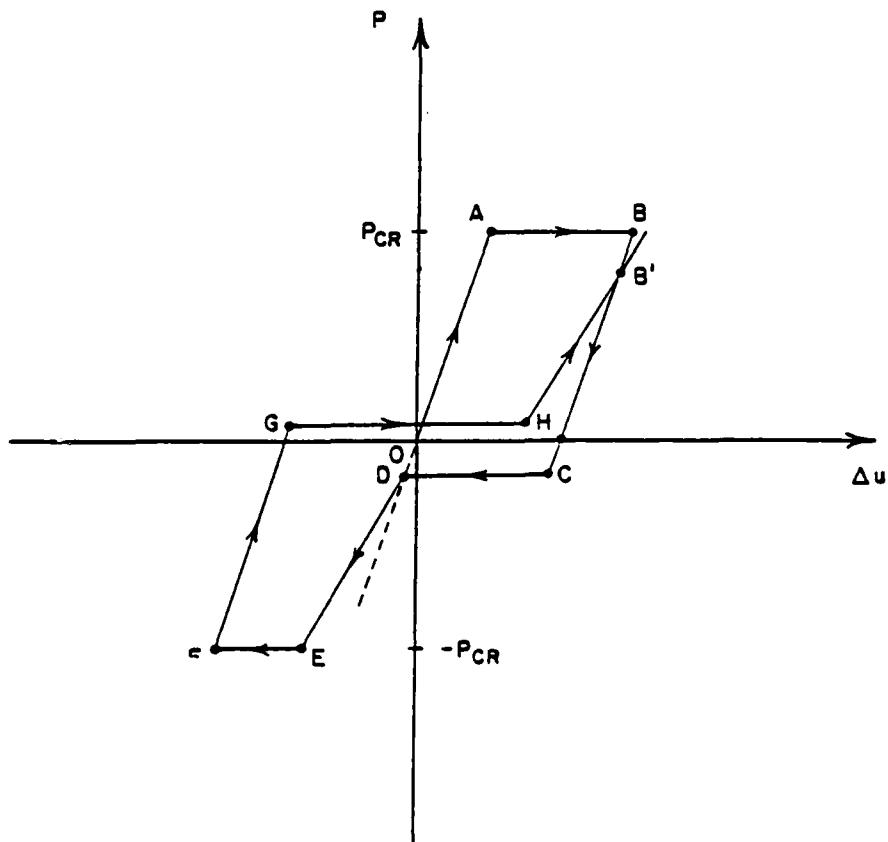


Figure 6-15b. Bond Slip Law for Cyclic Deformation.

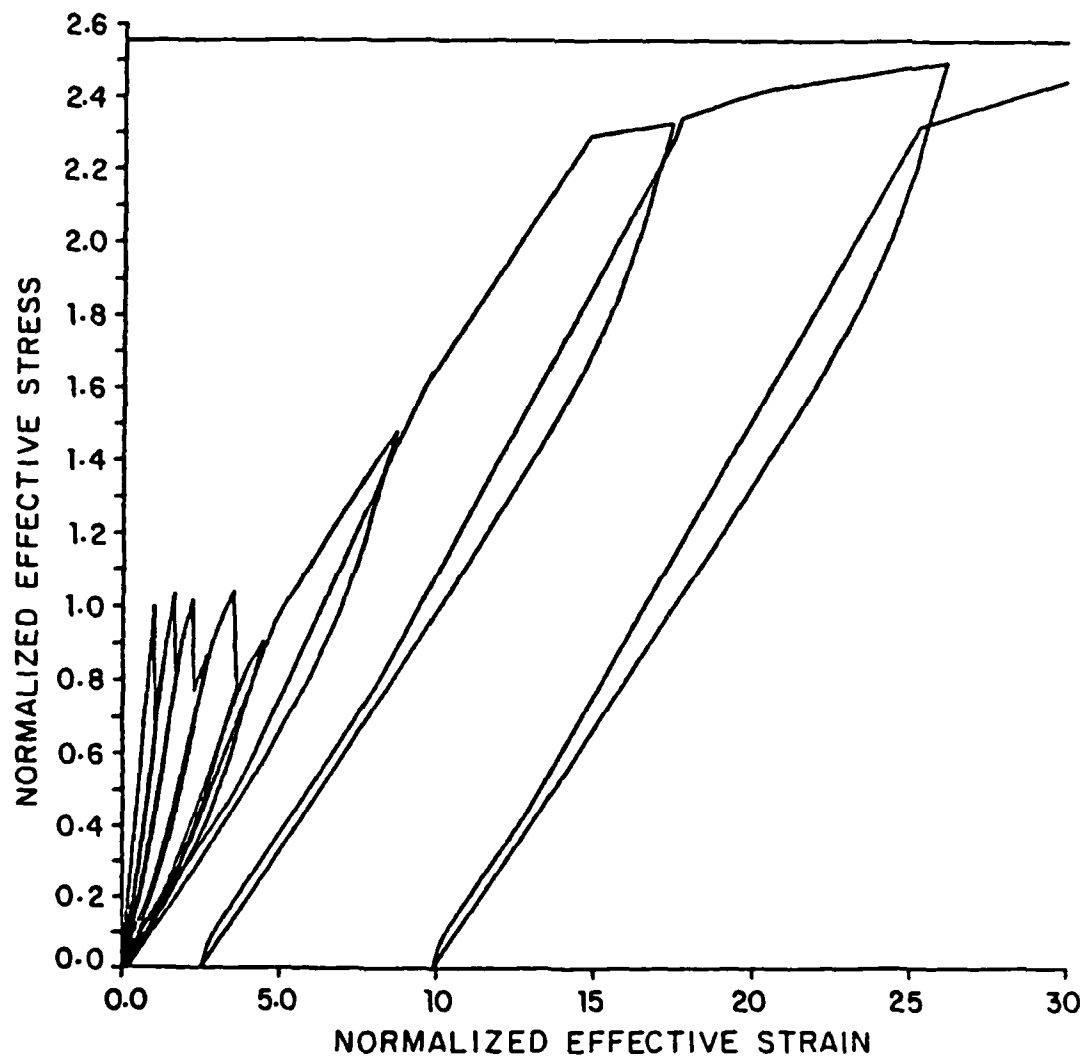


Figure 6-16. Mixture model response under cyclic loading.

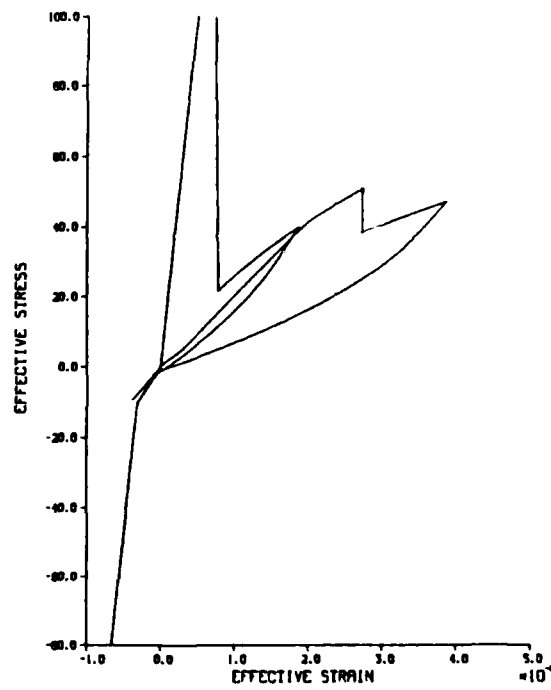


Figure 6-17. Single cycle of deformation for mixture model.

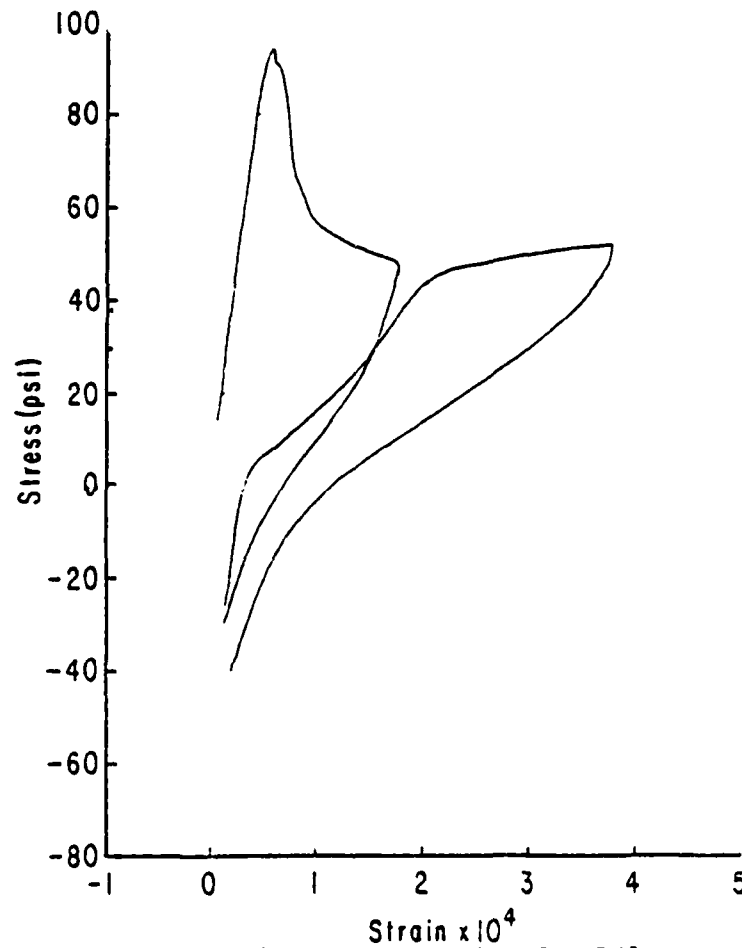


Figure 6-18. Single cycle of deformation for R/C test specimen.

6-18 for an actual test specimen. In this case the simulation includes both opening and closing of cracks and reversed bond slip. Once again one observes a realistic simulation of hysteretic material response.

In view of the above it may be concluded that the mixture model is capable of realistic material simulations for hysteretic deformations.

Typical Accuracy: Theory versus Experiment. For the purpose of validating the mixture model for hysteretic deformations, the test data of Hegemier et al⁽¹⁷⁹⁾ is selected. This is apparently the only data available on full-scale materials. The material, it should be noted, is reinforced concrete masonry. However, the concrete (grout) cells constitute the primary structural components subsequent to first cracking. Consequently the data is applicable to the present validation problem.

A theory versus experiment comparison of the effective stress versus effective strain envelope is shown in Figure 6-19. This envelope exhibits reasonably good agreement. The number of theoretical cracks agree with the observed test specimen cracks.

Figure 6-20 compares theoretical and experimental stiffness degradation. Here the agreement is seen to be excellent.

In view of the above, it is concluded that the mixture model is capable of accurate nonlinear simulations of real material response.

6.3.4 Influence of Basic Parameters.

In subsection 6.3.2 and 6.3.3 it was demonstrated that the mixture model is capable of accurate simulations of material response. One is therefore in a position to utilize this simulation tool to investigate the influence of the basic input parameters. It is instructive to do so at this point.

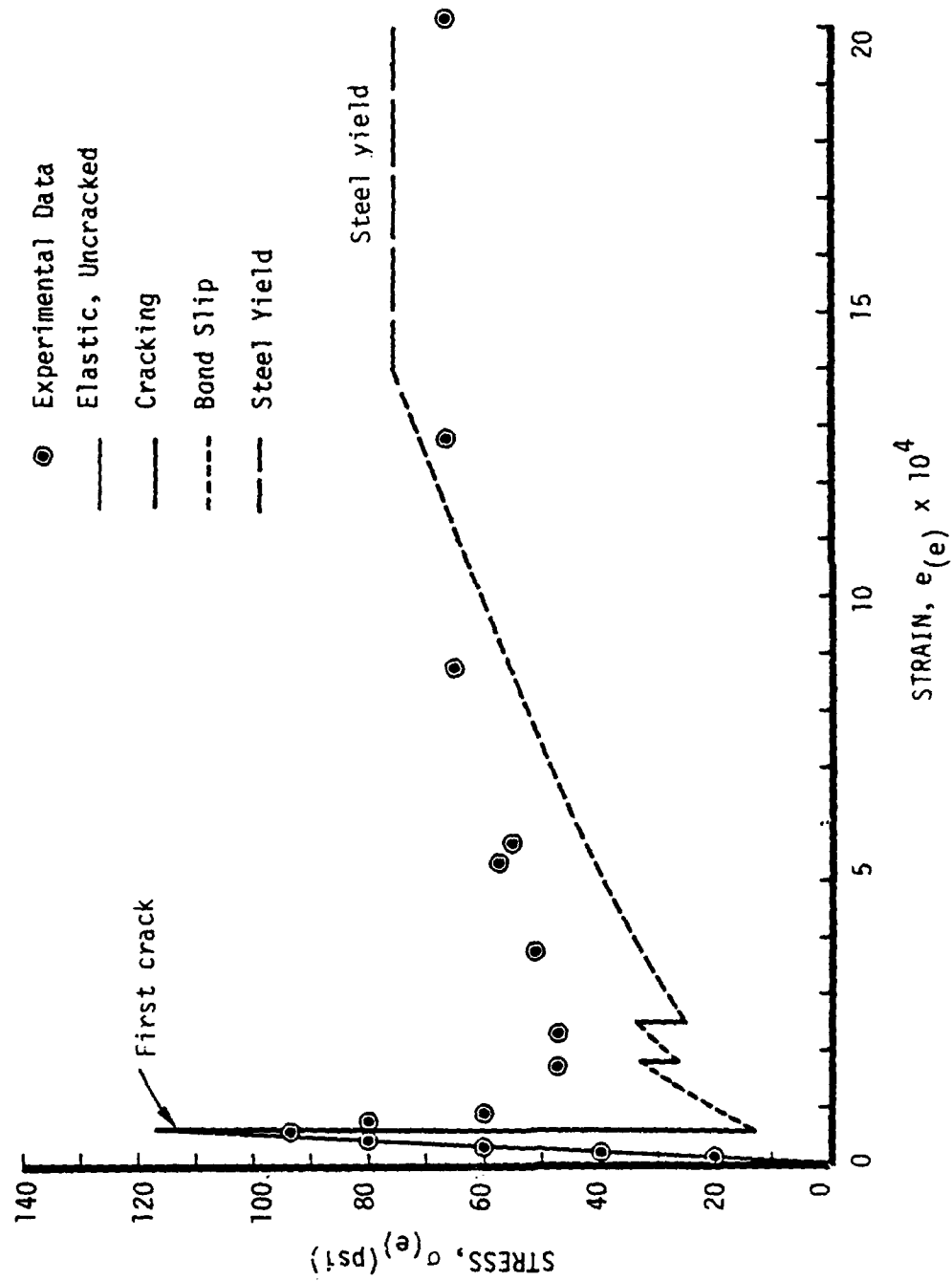


Figure 6-19. Comparison of theory and experiment for cyclic deformation (envelopes shown).

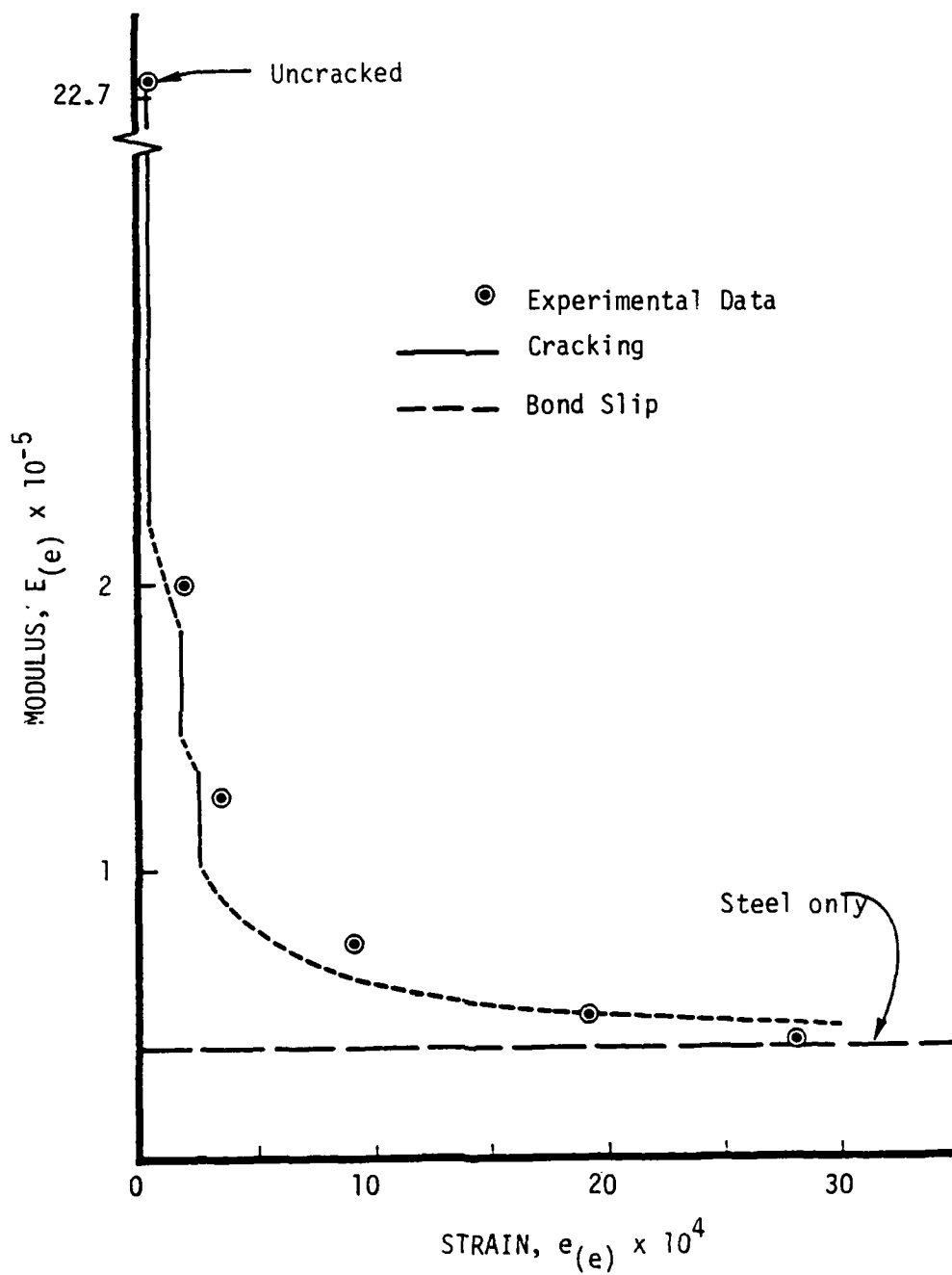


Figure 6-20. Comparison of theoretical and experimental stiffness degradation for cyclic deformation.

Initial Crack Spacing. The quantity $2l$ defines the initial crack spacing (see Figure 6-9). It is expected that a practical range for this parameter is (in nondimensional form) represented by $0.04 \leq \epsilon \leq 0.25$. Figure 6-21 shows the typical effect of the initial crack spacing in this range on the effective stiffness. The latter is observed to depend weakly on ϵ . This is fortunate from two viewpoints: (1) in most problems the location of the first crack is flaw dominated and is not known from a deterministic standpoint; (2) in the process of complete homogenization (single phase mixture) one seeks a continuum model without explicit dependence on initial crack location. With respect to item (2), such a model can be constructed by averaging out the ϵ -dependence over the ϵ -interval of interest. The dashed curve on Figure 6-22 represents such an average, obtained here by a least squares fit of the data to the curve

$$\frac{E(e)}{E} \doteq \left(\frac{n^{(1)} E^{(1)}}{E} + b \right) + \frac{1}{\left[\frac{1}{1 - \left(\frac{n^{(1)} E^{(1)}}{E} + b \right)} - a \right] e(e) + a e^2(e)} \quad (6-45)$$

with, $b = 0.034$, $a = 0.30 + 58.5 n^{(1)}$.

This elementary expression is observed to be a good representation of stiffness degradation.

Bond Strength. Steel-concrete bond strength can be expected to be in the range $f_t' \leq (\sigma_{rx}^*)_{cr} \leq 3 f_t'$, i.e., from one to three times the concrete tensile strength. Figure 6-23 illustrates the typical effect that this variation has on effective stiffness; Figure 6-24 depicts the typical influence on the effective stress-strain response. The result is surprising: for monotonic extension the model indicates that response is weakly dependent on bond strength. Care must be exercised in the interpretation of this result, however. The foregoing simulations apply to a steel-pull tension test, Figure 6-9. For example, one would expect a strong dependence of bond strength on the response of a pull-out test. Thus, the importance of bond strength may be problem dependent.

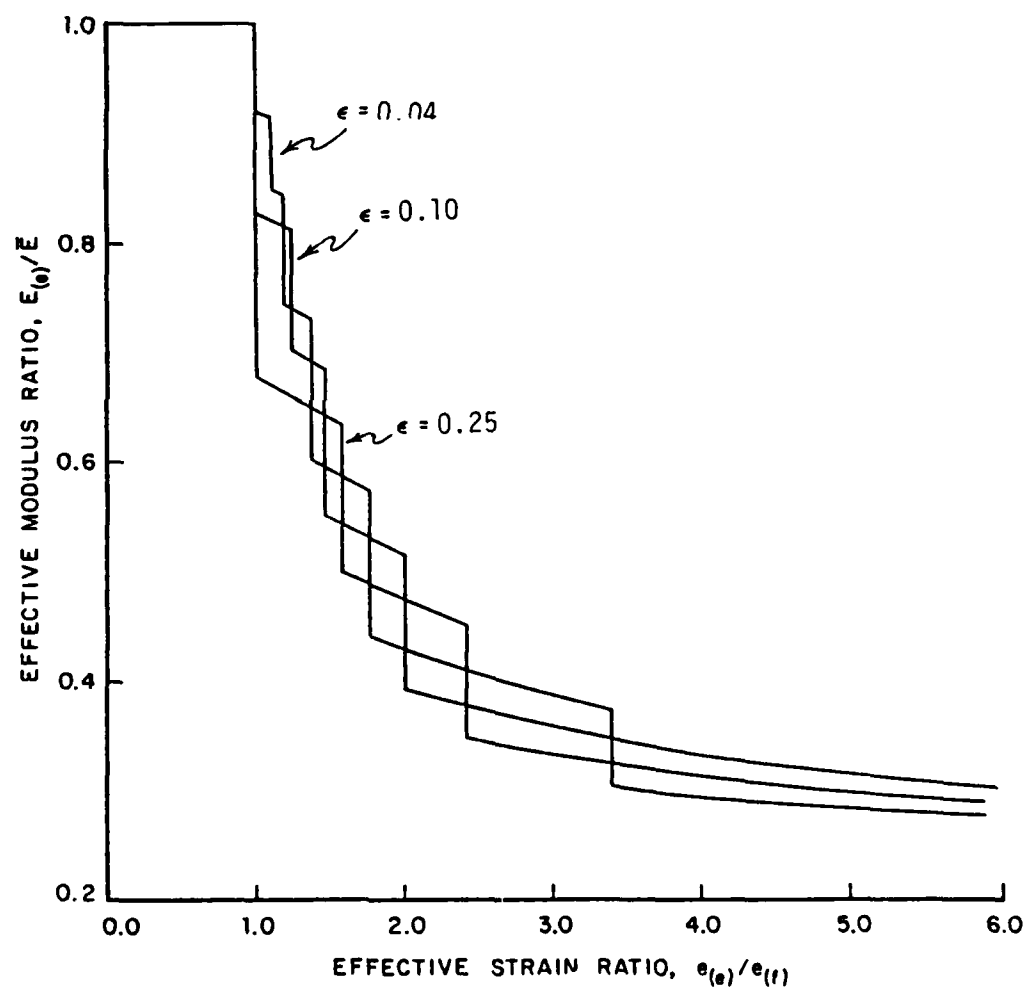


Figure 6-21. Effect of initial crack spacing on stiffness degradation.

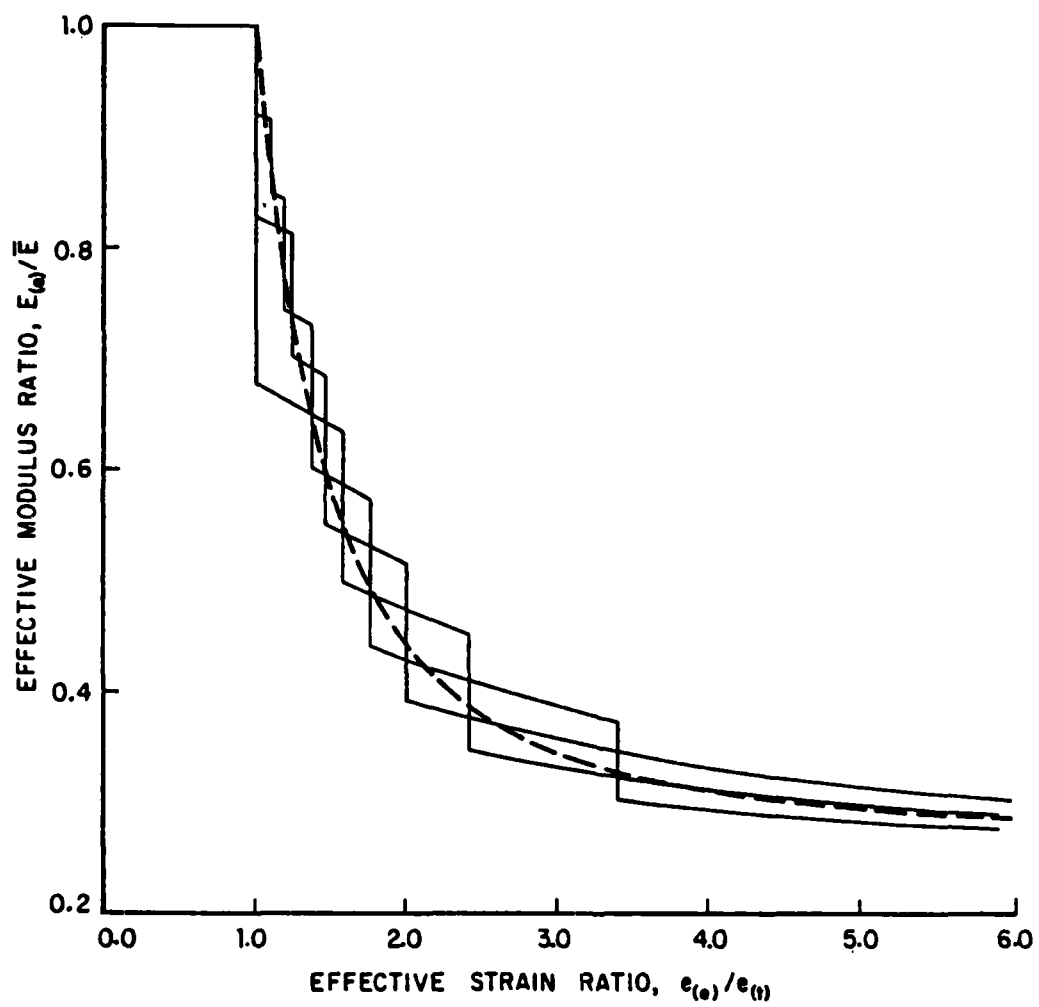


Figure 6-22. Smoothing of the Stiffness Degradation
 $\epsilon =$ Dependence.

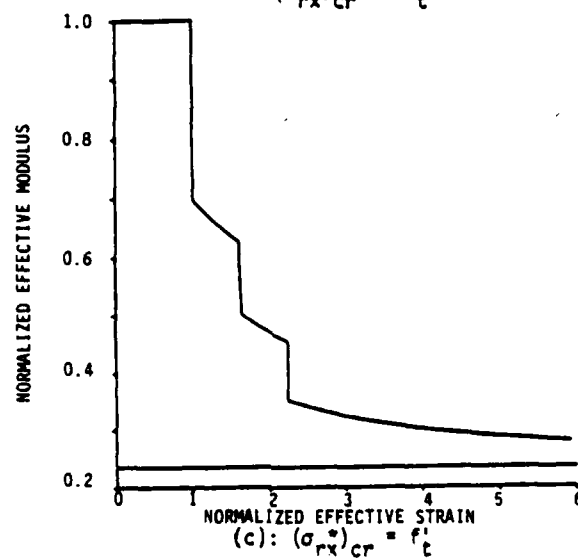
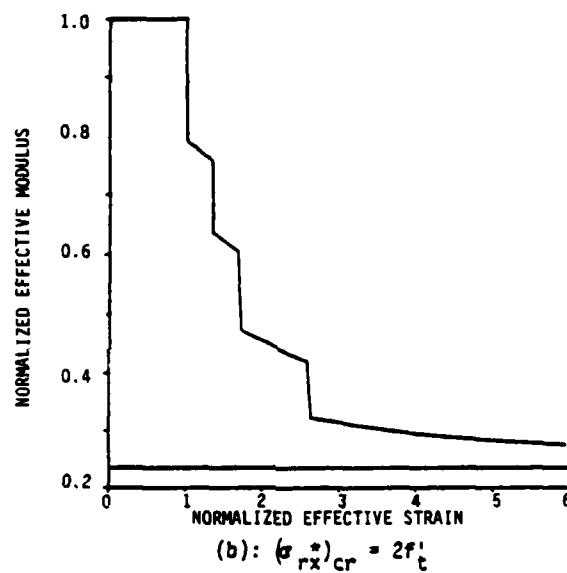
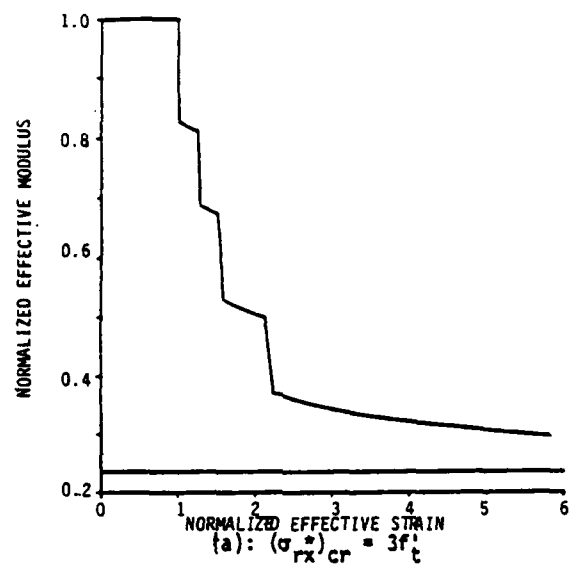


Figure 6-23a,b,c. Influence of Bond Strength on Stiffness Degradation ($n(1) = 0.02$, $\epsilon = 0.10$).

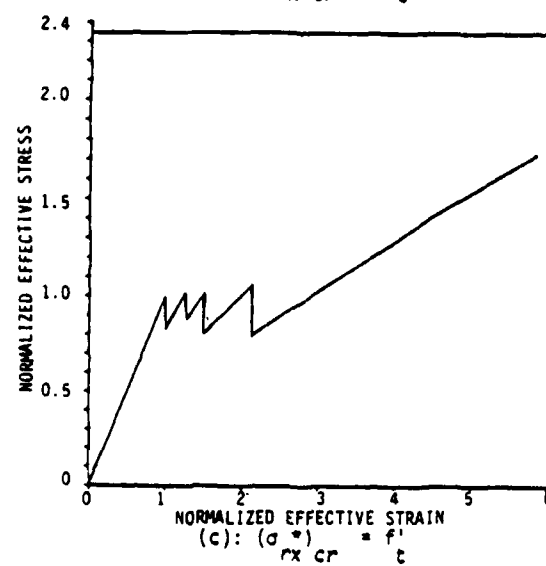
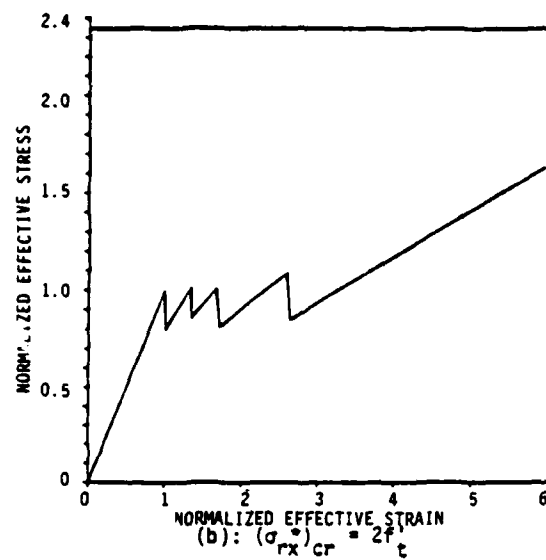
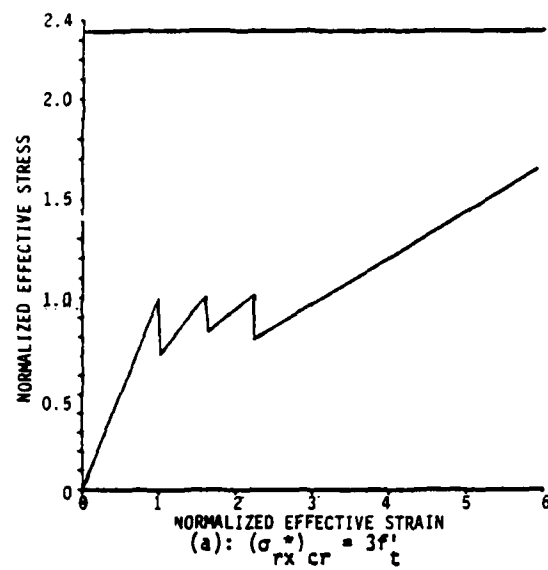


Figure 6-24a,b,c. Variation of Monotonic Response with Bond Strength ($n(1) = 0.02$, $\epsilon = 0.10$).

Steel Volume. Figures 6-25,26 show the dependence of effective stiffness and effective stress-strain response on the steel volume fraction, $n^{(1)}$. As one would expect, the response is a strong function of the steel volume fraction.*

6.3.5 Recovery of Microstructure

In the foregoing discussion only averaged field variables in each constituent were considered. The mixture construction procedure used, however, also allows one to describe the local variations of the field variables to a certain (asymptotic) degree of accuracy. For example, the axial components of displacement can be written as

$$\dot{u}_1^{(1)} \approx \dot{u}_1^{(1a)} + \frac{r^{(2)2} \dot{p}_1}{2n^{(1)} u^{(1)}} \left(\frac{r^{*2}}{2r^{(2)2}} - \frac{n^{(1)}}{4} \right) \quad (6-46a)$$

$$\dot{u}_1^{(2)} \approx \dot{u}_1^{(2a)} - \frac{r^{(2)2} \dot{p}_1}{2n^{(2)} u^{(2)}} \left(\frac{r^{*2}}{2r^{(2)2}} - \ln \left(\frac{r^*}{r^{(2)}} \right) - \frac{3}{4} - \frac{n^{(1)}}{4} - \frac{n^{(1)} \ln n^{(1)}}{2n^{(2)}} \right). \quad (6-46b)$$

Figures 6-27a,b show typical local variations of the field variables at a specific axial location. Such detailed information is of interest if one is concerned with items such as local cone failures which are common to steel-pull tension tests.

6.4 REMARKS

The steel-concrete bond problem examined in the foregoing sections corresponds to the special case where the principal stress directions and steel layout directions coincide, and where concrete cracking, bond slip, and steel-yield dominate natural response. Examination of this case reveals that the mixture approach provides exceptional modeling capability for both monotonic and hysteretic

*The data in Figure 6-25 is based on Equation 6-45 which, in view of the weak dependence on bond strength, does not depend on bond strength.

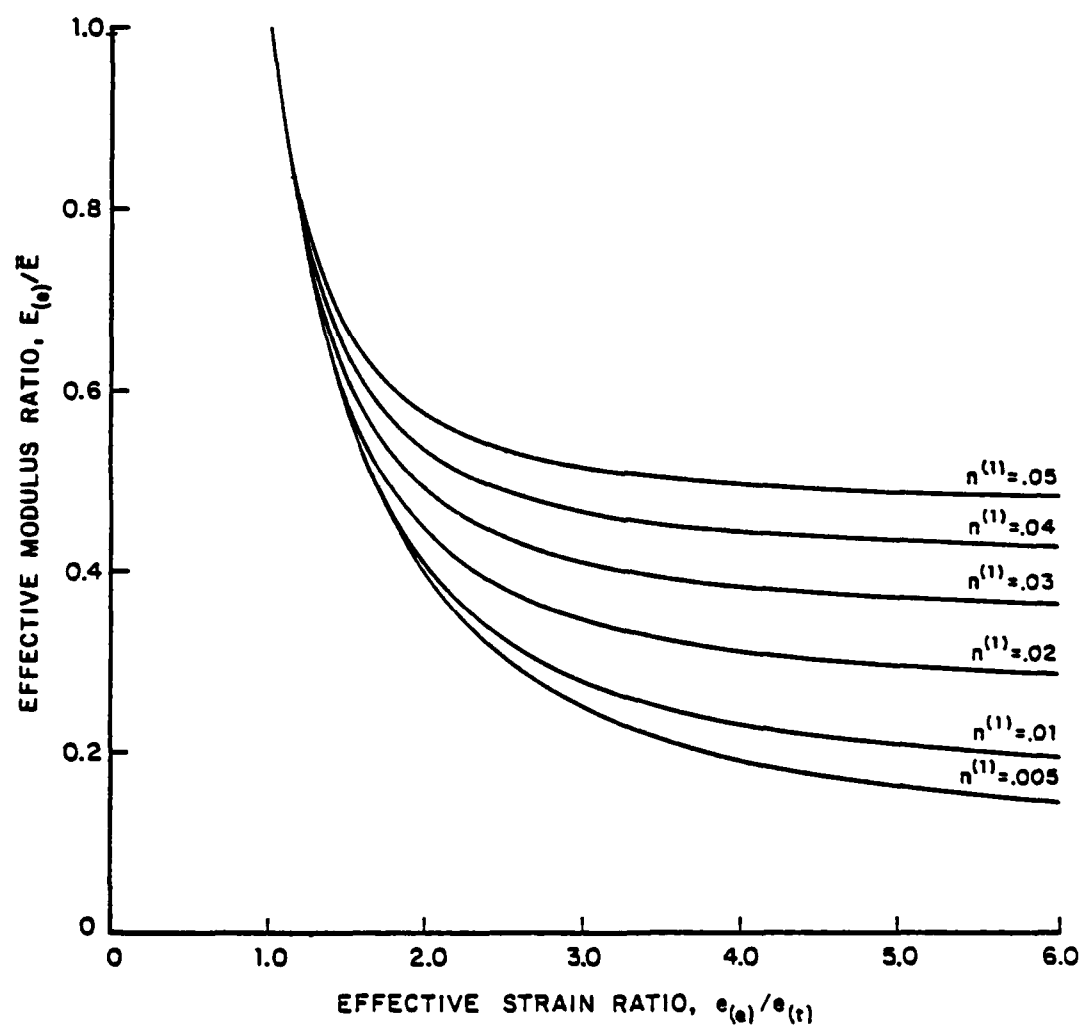


Figure 6-25. Influence of Steel Volume Fraction on Stiffness Degradation.

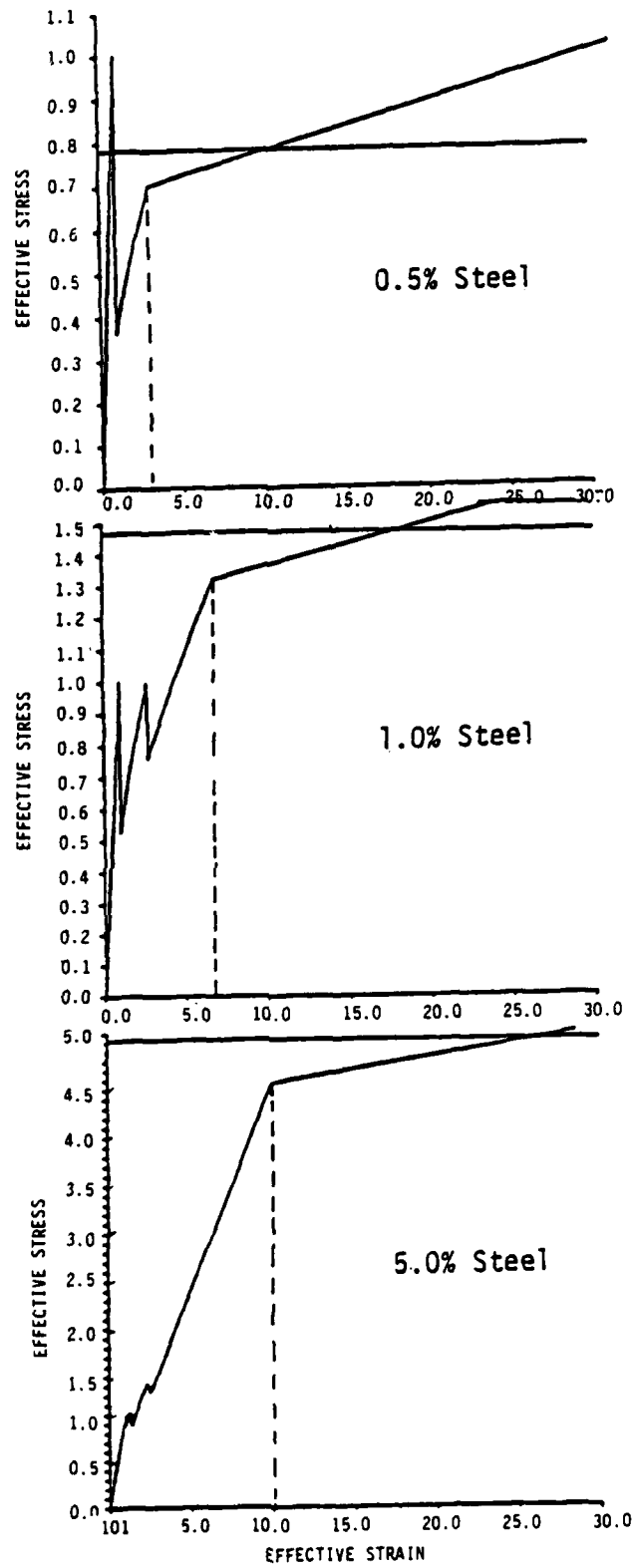


Figure 6-26. Influence of Steel Volume Fraction on Monotonic Response ($\epsilon = 0.10$, $(\sigma_{rx}^*)_{cr} = f'_t$)

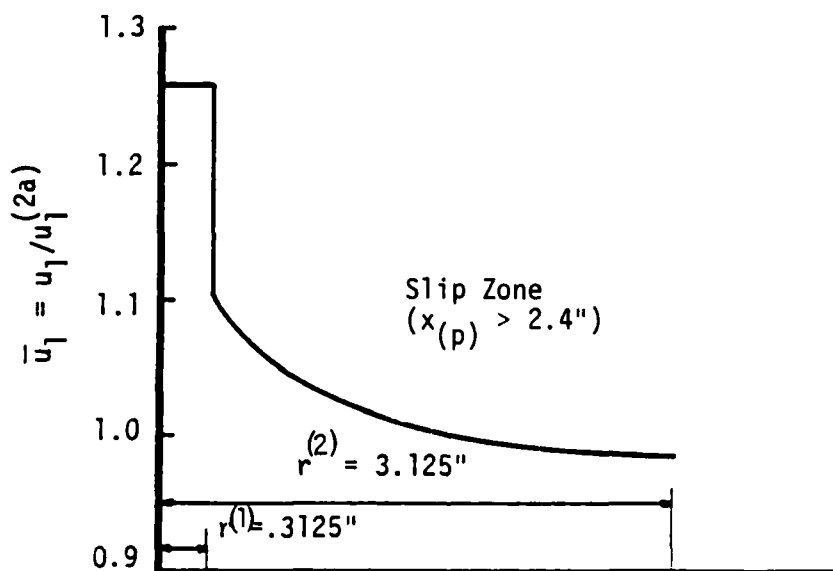
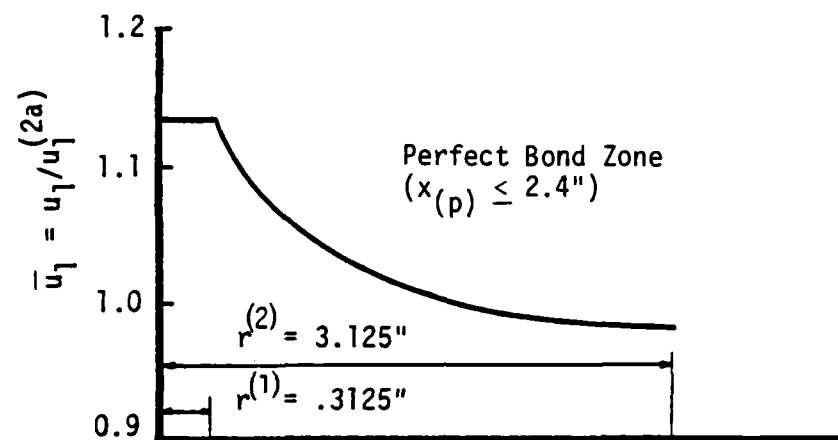


Figure 6-27a. Local axial displacements in steel and concrete a distance 2.4 in from crack face. Axial displacements normalized on cross-sectional average in concrete.

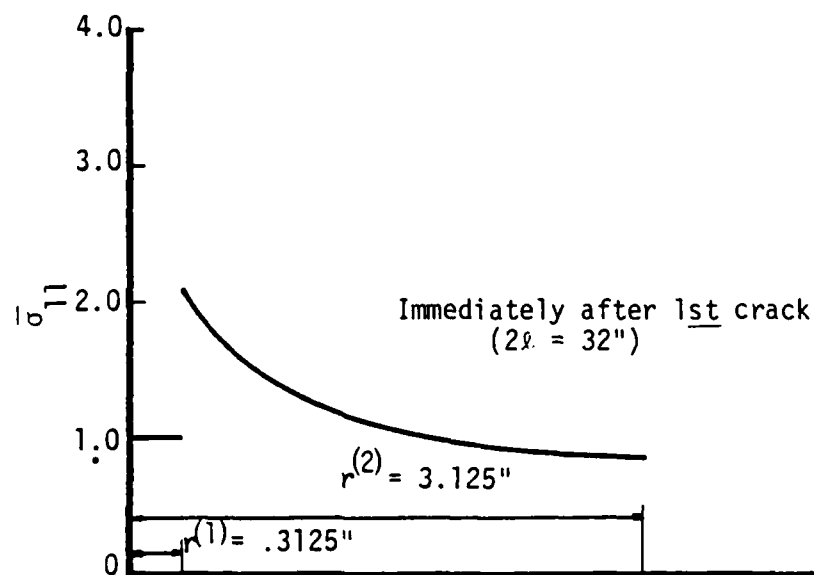
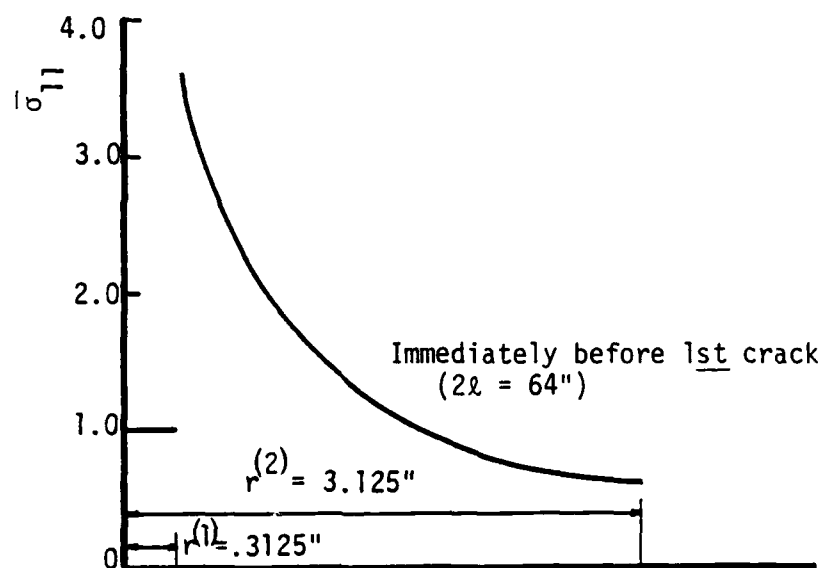


Figure 6-27b. Variation of local axial stress in steel and concrete a distance 2.5 from crack face. Axial stresses normalized on cross-sectional average of each material.

deformations with relatively few model input parameters. In particular, global stress and deformation fields and important global nonlinear response measures concerning stiffness degradation, strain softening, strain hardening, and hysteresis (damping) can be accurately simulated. Most important is the conclusion that the above global features can be synthesized from elementary material property data on the constituents (steel and concrete) and the constituent interfaces (steel-concrete interfaces). Finally, in addition to global quantities, local stress and deformation fields in the steel, the concrete, and at steel-concrete interfaces can be simulated to a certain degree of accuracy.

It was noted previously that a significant number of problems fall into the category above, i.e., where the principal stress directions coincide with the primary steel layout directions. These include beams, plates and shells subject to bending and/or nonlinear membrane action, but with negligible in- and out-of-plane shear stresses. These modes of behavior are relevant to both shell and box (plate)-type protective reinforced concrete structures, for example, in regions sufficiently far from support boundaries or constraints.

6.5 ON SINGLE-PHASE MODELS

In Section I it was noted that single-phase models are of interest because of their mathematical and numerical simplicity. In particular, one expects the mathematical formulation of a single-phase model to be easily implemented into current finite element programs.

There are, in principle, two ways to construct a single phase model of reinforced concrete. One is to perform an appropriate mathematical smoothing operation on the two-phase mixture model. This, however, is a difficult task that, if not performed properly, can lead to considerable loss in simulation capability and accuracy. Mathematical homogenization to furnish a single-phase model has been studied but as yet the appropriate procedure has not been discovered.

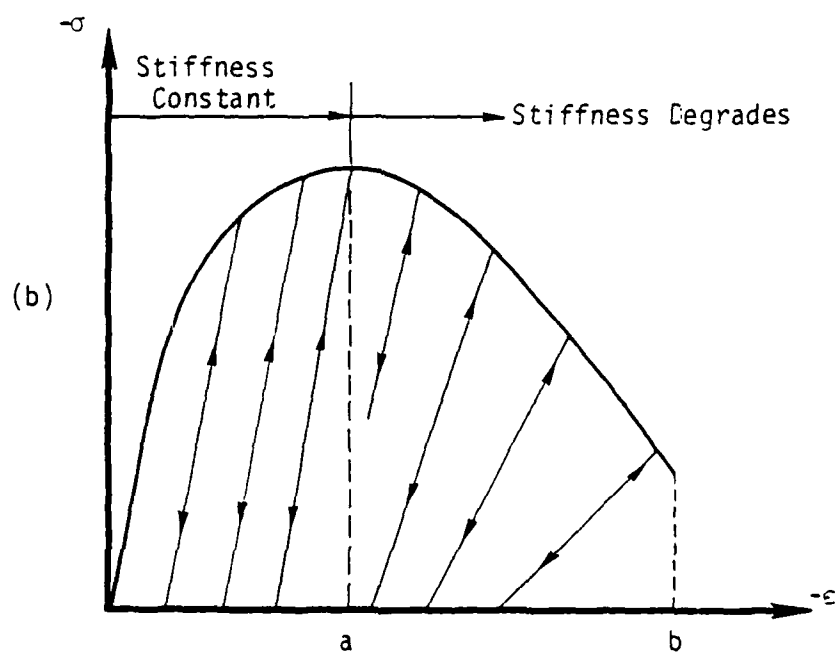
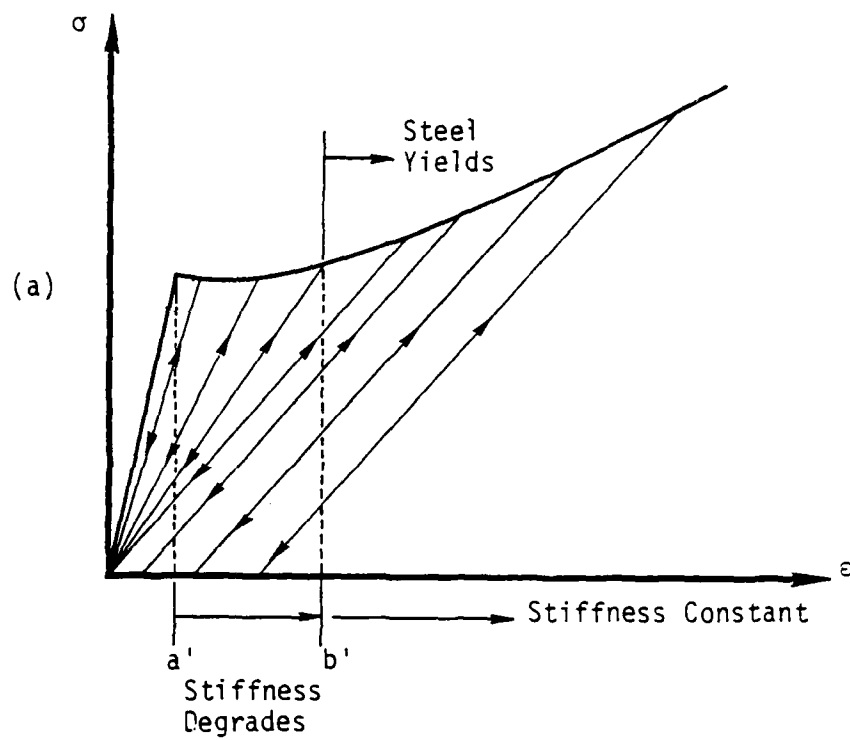


Figure 6-28. R/C stiffness behavior in (a) tension, (b) compression.

Another approach is to postulate a phenomenological single-phase model and then to evaluate the model parameters or functions by using 'data' produced by the Two-Phase Model. This approach is very attractive since: (1) one has much more control over two-phase model simulations than one does over an experiment; (2) two-phase model simulations are much less costly than actual experiments; and (3) the accuracy of the Two-Phase Model has been demonstrated to be excellent (at least as far as it has been developed).

To illustrate the phenomenological approach, let us adopt a plastic-fracture model of reinforced concrete (see Section 5.1). For simplicity, let us focus on biaxial behavior, i.e., let us consider two-dimensional composites.

Within the context of two-dimensional composites, consider Figure 6-28. Experimental data reveals that, if the maximum principal normal stress is positive, then stiffness degradation occurs immediately and continues until the onset of steel yielding after which it essentially ceases. This is demonstrated in Figure 6-28(a) for uniaxial tension. In contrast, if the maximum principal normal stress is negative, then stiffness degradation does not commence until one reaches a strain corresponding to approximately the ultimate stress in monotonic deformation. This is demonstrated in Figure 6-28(b) for uniaxial compression.

Information of the above type indicates that one should associate the initial fracture surface in the Dougill fracture element with the initiation of concrete fracture in quadrants I,

II, and IV of (biaxial) stress space, and with $\max \underline{g}$, along a path corresponding to monotonic deformation in strain space, in quadrant III of (biaxial) stress space. An elementary initial fracture surface in (biaxial) strain space satisfying these conditions is shown in Figure 6-29. The associated surface in stress space, and a comparison of this surface with actual test data, is shown in Figure 6-30. Considering the scatter in test data, and the fact that fracture and ultimate stress surfaces need not coincide exactly (stiffness degradation may commence prior to ultimate stress), the comparison indicates that the assumed initial fracture surface is, although elementary, a reasonable approximation of test data (A Coulomb model is also shown in Figure 6-30 for comparison purposes).

Let us focus now on quadrants I, II and IV of strain space. For strain paths in these regions plastic effects are not significant until the onset of steel-yielding. Consequently, prior to yielding of the rebar, a single Dougill fracture element is appropriate.

Since the fracture surface selected is piecewise linear, the loading function F can be written in the form

$$F = \sum_{n=1}^N \alpha_{(n)} \left[(\lambda_{ij})_{(n)} \epsilon_{ij} - h_{(n)} \right] \quad (6-47)$$

where $\alpha_{(n)}$ are weight functions with the value 1 or 0, and $h_{(n)} = h_{(n)}(D)$, where D is the dissipation function:

$$\dot{D} \equiv -\frac{1}{2} \dot{\sigma}_{ij}^f \epsilon_{ij} \quad (6-48)$$

Here σ_{ij}^f is defined by

$$\begin{aligned} \dot{\sigma}_{ij}^f &= -\frac{2}{h_{(n)}} \frac{dD}{dh_{(n)}} (\lambda_{ij})_{(n)} (\lambda_{kl})_{(n)} \dot{\epsilon}_{kl} \quad \text{if } F = \dot{F} = 0, \\ \dot{\sigma}_{ij}^f &= 0 \quad \text{if } F < 0 \text{ or if } F = 0 \text{ and } \dot{F} < 0. \end{aligned} \quad (6-49)$$

AD-A166 087

ON THE DEVELOPMENT OF CONSTITUTIVE RELATIONS FOR PLAIN
AND REINFORCED CONCRETE(U) S-CUBED LA JOLLA CA
G A HEGEMIER ET AL 09 APR 82 SSS-R-82-5495

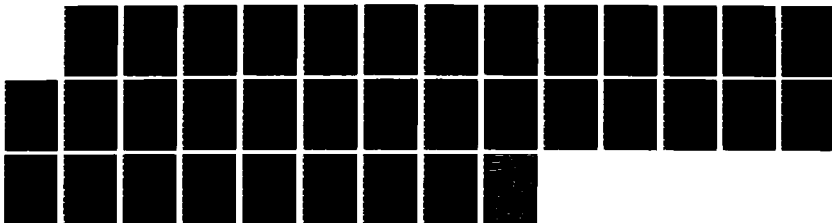
4/4

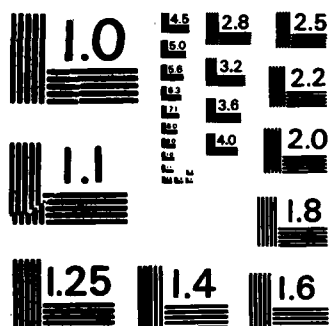
UNCLASSIFIED

DNA-TR-81-65 DNA001-81-C-0181

F/G 11/2

NL





MICROCOPY RESOLUTION TEST CHART
NATIONAL BUREAU OF STANDARDS - 1963 - A

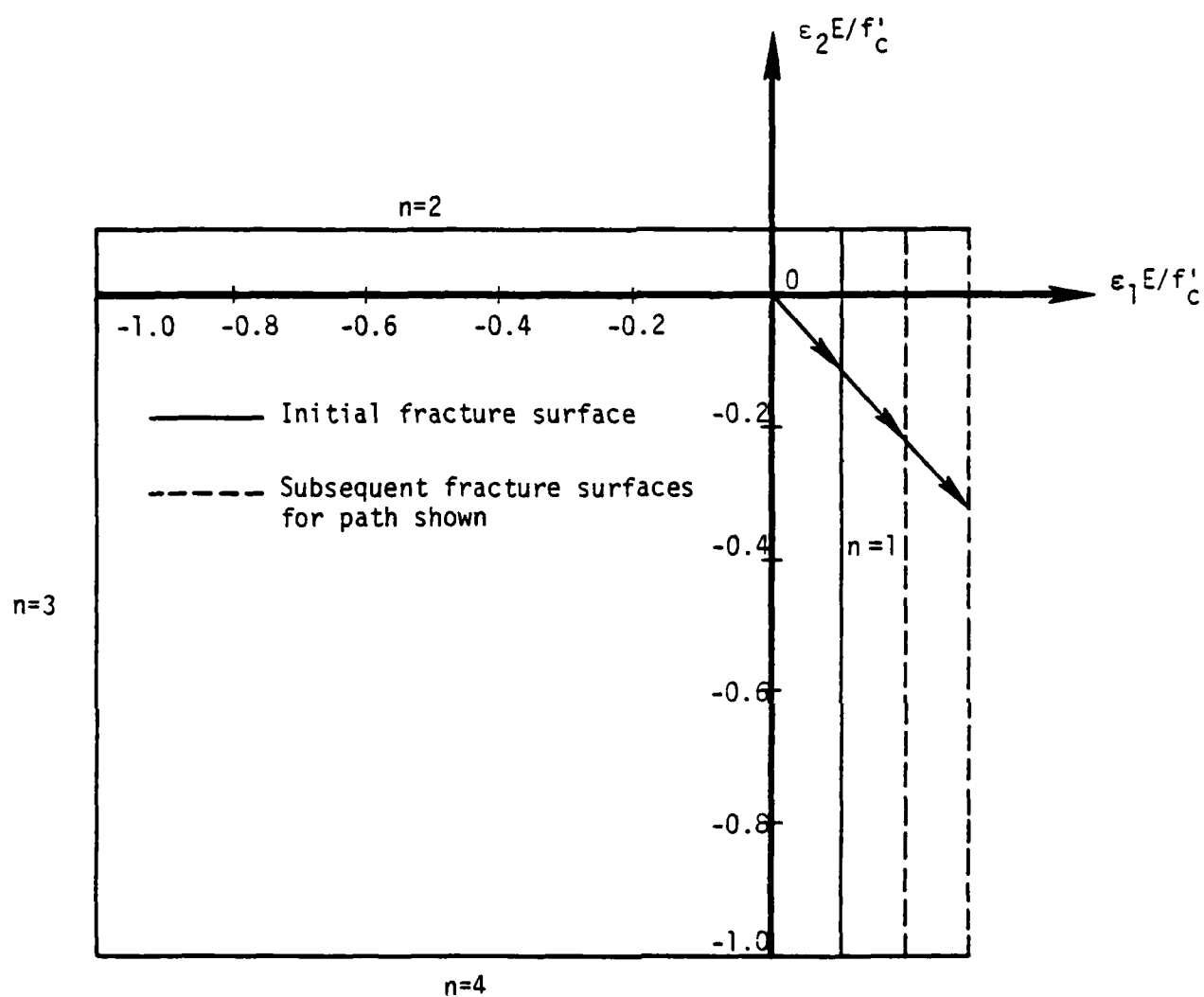


Figure 6-29. Initial and subsequent biaxial fracture surfaces in strain space. ϵ_2, ϵ_1 denote principal strains.

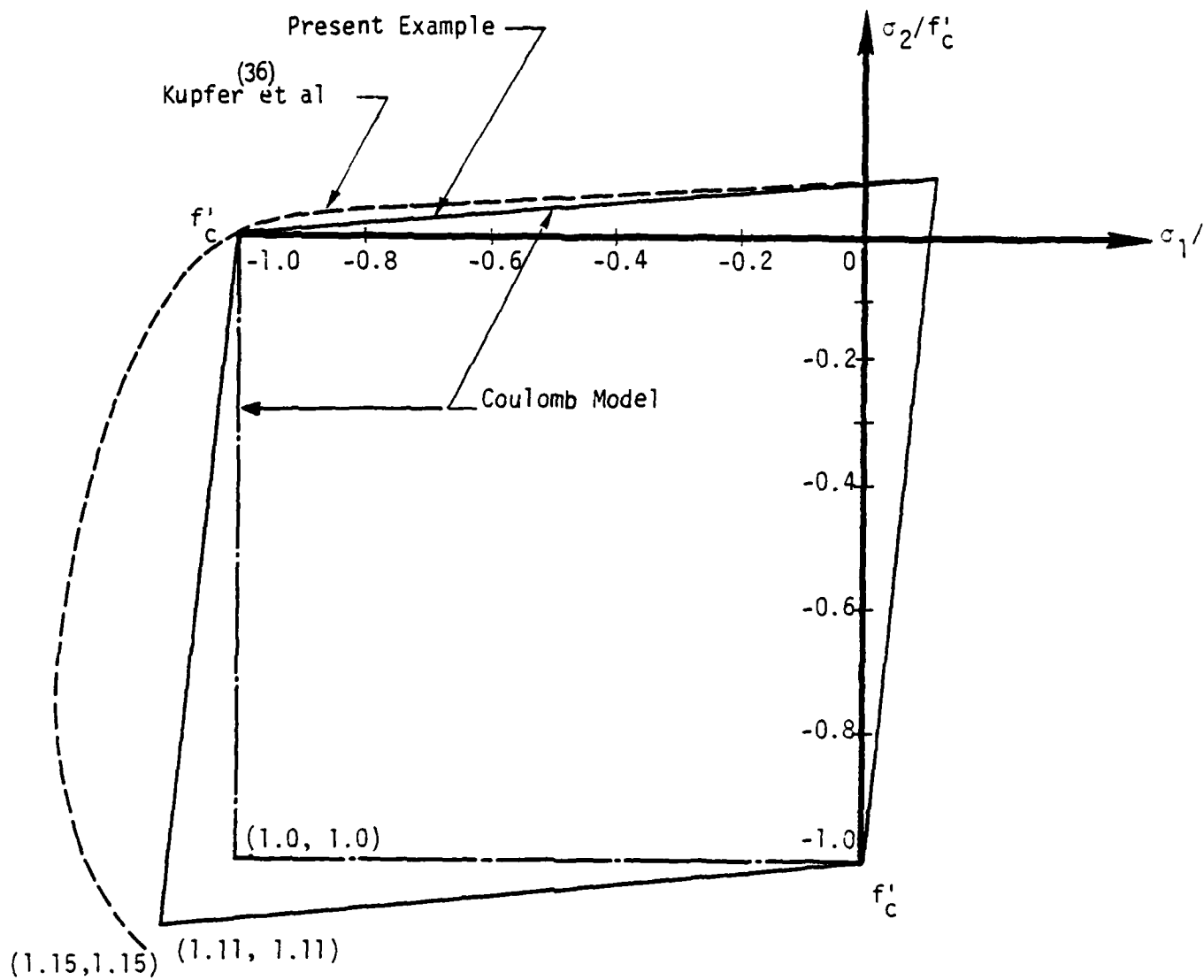


Figure 6-30. Initial biaxial fracture surface in stress space.
 σ_2, σ_1 denote principal stresses.

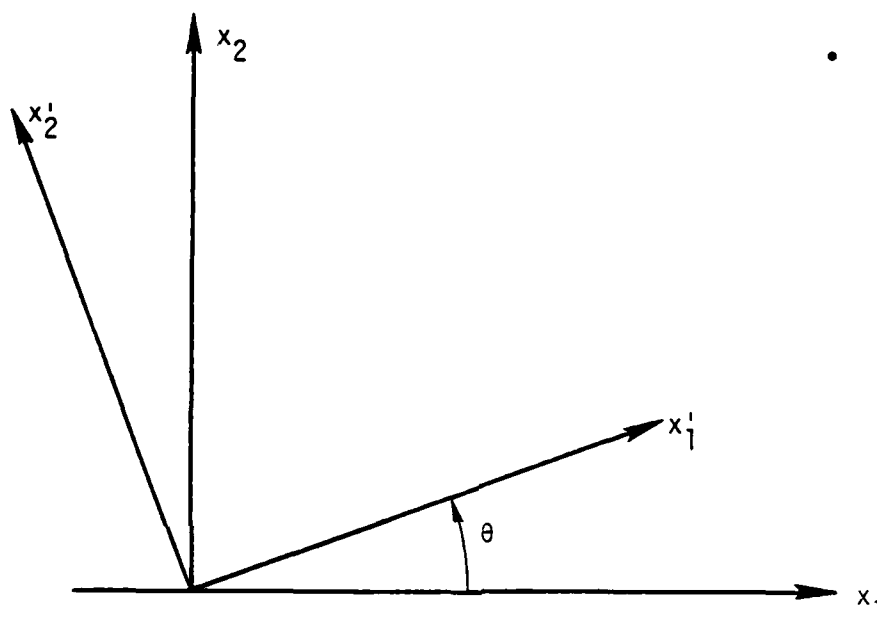


Figure 6-31. Principal coordinates (x_1, x_2) and reference coordinates (x'_1, x'_2) .

The resulting constitutive relation is of the form

$$\dot{\sigma}_{ij} = C_{ijkl} \dot{\epsilon}_{kl} + \dot{\sigma}_{ij}^f \quad (6-50)$$

The initial moduli $C_{ijkl}(0)$ must be specified (i.e., uncracked elastic properties). Subsequent stiffness moduli are computed from:

$$\dot{C}_{ijkl} = \dot{\sigma}_{ij}^f(\lambda_{kl})_{(n)} / h_{(n)} \quad (6-51)$$

Given the above phenomenological model, the problem is now to define suitable functional forms for $h_{(n)}(D)$, and to prescribe the variables λ_{ij} . Let us consider the latter, i.e., the prescription of λ_{ij} . One possibility is depicted in Figure 6-29 for the path shown. Here the λ_{ij} are constants and each linear surface segment undergoes isotropic expansion. In this case properties in the 2-direction are not influenced by extension in the 1-direction. In terms of an arbitrary reference coordinate system x'_i (Figure 6-31), the loading function in this case has the form

$$F = \lambda'_{ij} \epsilon'_{ij} - h(D) \quad (i, j = 1, 2) \quad (6-52)$$

where (6-52) corresponds to $n = 1$ (the subscript 'n' is dropped in what follows) and where

$$\lambda'_{11} = \frac{1+\cos 2\theta}{2}, \quad \lambda'_{22} = \frac{1-\cos 2\theta}{2}, \quad 2\lambda'_{12} = \sin 2\theta \quad (6-53)$$

The angle θ in (6-53) denotes the angle between the principal and reference 1-axis, Figure 6-31. The stresses in the reference coordinate system are given by

$$\dot{\sigma}'_{ij} = C'_{ijkl} \dot{\epsilon}'_{kl} + \dot{\sigma}'_{ij}^f \quad (i, j, k, l = 1, 2) \quad (6-54)$$

where

$$\dot{\sigma}_{ij}' = - \frac{2}{h} \frac{dD}{dh} \lambda_{ij}' \lambda_{kl}' \dot{\epsilon}_{kl}' \quad \text{if } F = F = 0 \quad (i, j, k, l = 1, 2) \quad (6-55)$$

Examination of the relations (6-52) - (6-55) reveals realistic simulation of material stiffness degradation with an appropriate choice of the dissipation function D . For example, the effective shear modulus of a specimen degrades with increasing shear strain ϵ'_{12} and further, this degradation is a function the extension of the specimen. Figure 6-32 depicts an example situation where a specimen is first extended ($\epsilon'_{11} \neq 0$ only), then subjected to shear deformation (ϵ'_{12}) with $\epsilon'_{11} = \text{constant}$.

Additional coupling can be obtained by allowing the surface to rotate as well as translate in strain space. Figure 6-33 illustrates a candidate model where, for the path shown,

$$\begin{aligned} \lambda_{11}' &= \frac{1+\cos 2\theta}{2} + (h-0.1) \frac{1-\cos 2\theta}{2} , \\ \lambda_{22}' &= \frac{1-\cos 2\theta}{2} + (h-0.1) \frac{1+\cos 2\theta}{2} , \\ 2\lambda_{12}' &= (1.1-h) \sin 2\theta . \end{aligned} \quad (6-56)$$

Let us focus upon the case of $\lambda_{ij} = \text{const.}$, and consider the next problem - that of specifying the form of $h(D)$. For the surface $n=1$, one has

$$\lambda_{11} = 1 , \quad \lambda_{22} = \lambda_{12} = 0 . \quad (6-57)$$

Thus, during loading, one has, in the principal strain coordinates,

$$\dot{\sigma}_{11}' = - \frac{2}{h} \frac{dD}{dh} \dot{\epsilon}_{11}' , \quad (6-58)$$

$$h = \epsilon_{11} , \quad (6-59)$$

$$\dot{E} \equiv \dot{C}_{1111} = - \frac{2}{h} \frac{dD}{dh} \dot{\epsilon}_{11}' . \quad (6-60)$$

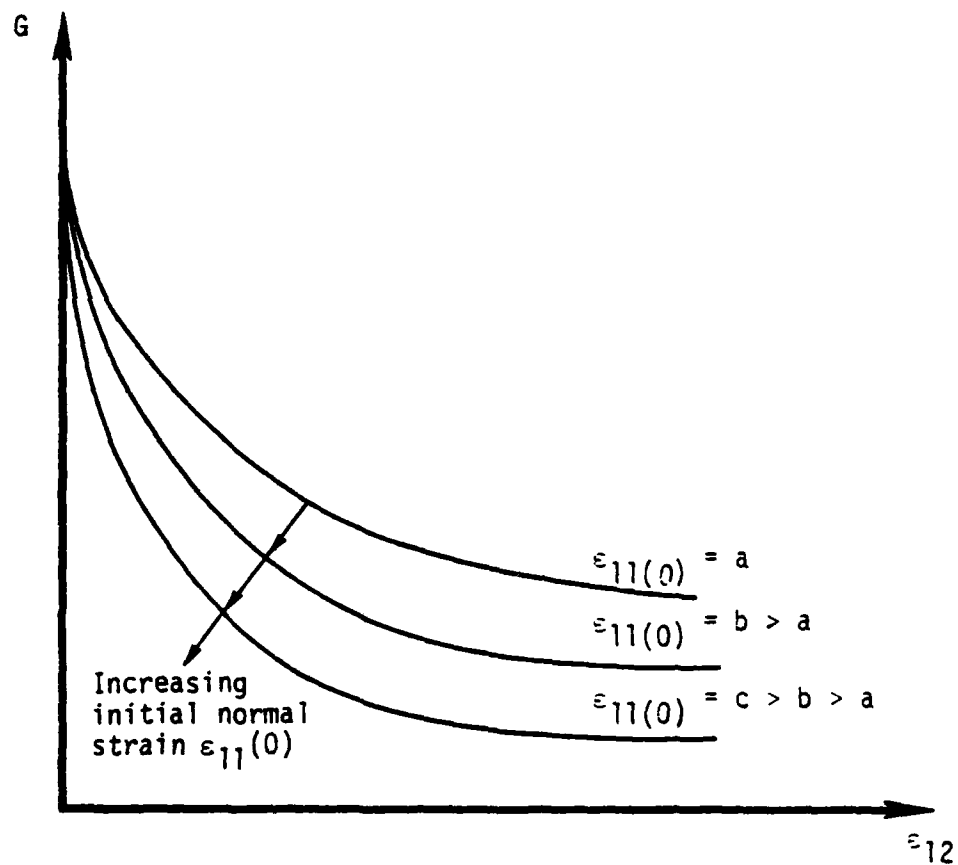


Figure 6-32. Influence of initial normal strain on shear modulus.

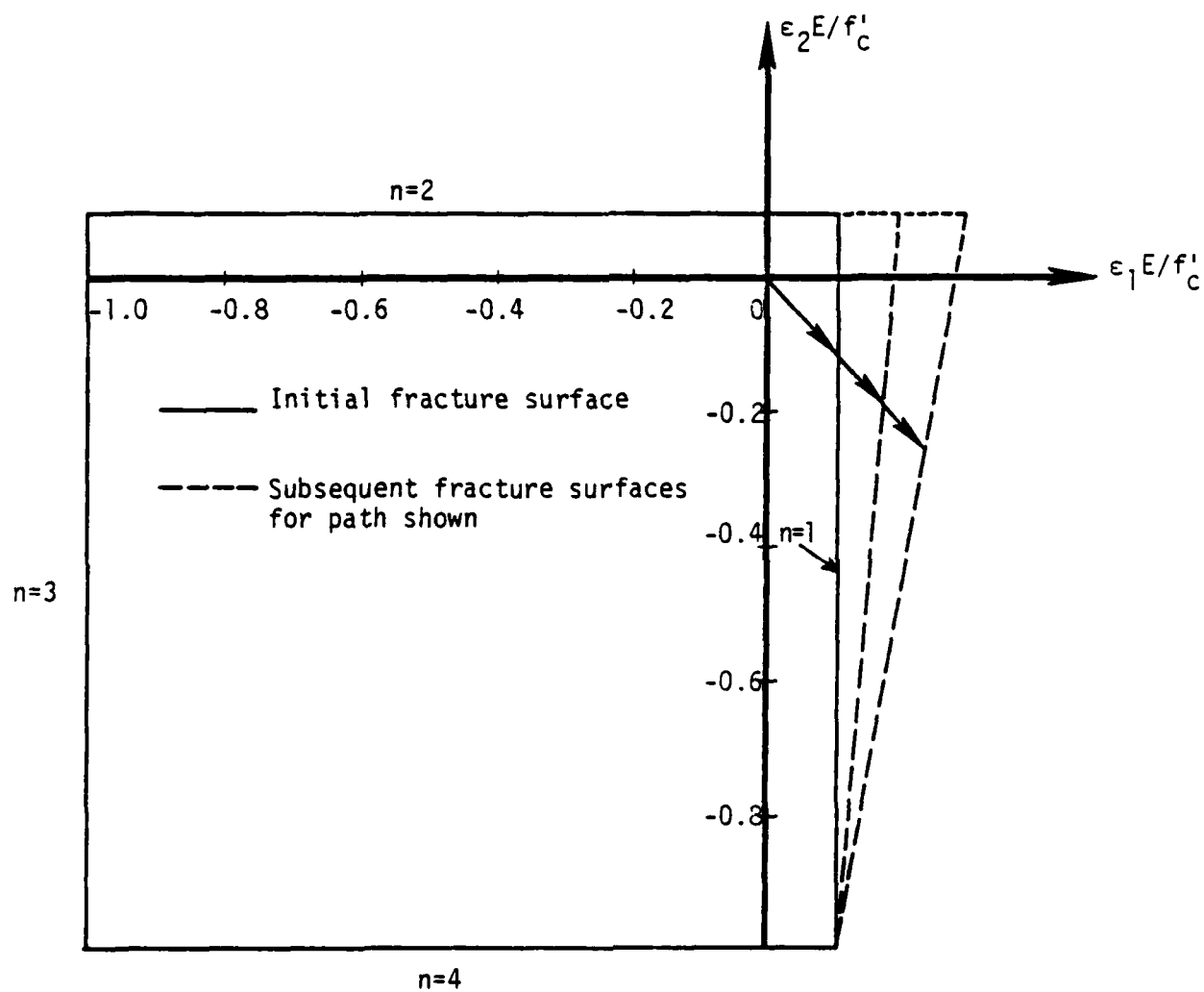


Figure 6-33. Initial and subsequent biaxial fracture surfaces in strain space. ϵ_1, ϵ_2 denote principal strains.

Equations (6-59) and (6-60) furnish

$$\frac{dE}{d\epsilon_{11}} d\epsilon_{11} = - \frac{2}{\epsilon_{11}} \frac{dD}{d\epsilon_{11}} d\epsilon_{11} . \quad (6-61)$$

Thus,

$$D = - \frac{1}{2} \int \epsilon_{11}^2 \frac{dE}{d\epsilon_{11}} d\epsilon_{11} + D_0 . \quad (6-62)$$

Now, from the two-phase simulation (Section 6.3), the following form was found to accurately represent E versus ϵ_{11} :

$$E = a_1 + \left[\left(\frac{1}{1-a_1} - a_2 \right) \epsilon_{11} + a_2 \epsilon_{11}^2 \right]^{-1} \quad (6-63)$$

where a_1, a_2 are constants. Hence

$$\frac{dE}{d\epsilon_{11}} = - \frac{(b_1 + 2b_2 \epsilon_{11})}{\epsilon_{11}^2 (b_1 + b_2 \epsilon_{11})^2} \quad (6-64)$$

where

$$b_1 = \frac{1}{1-a_1} - a_2 , \quad b_2 \equiv a_2 . \quad (6-65)$$

The dissipation function corresponding to the stiffness degradation function (6-63) can be found by substituting (6-64) into (6-62):

$$D = \frac{1}{2} \int \frac{(b_1 + 2b_2 \epsilon_{11})}{(b_1 + b_2 \epsilon_{11})^2} d\epsilon_{11} + D_0 . \quad (6-66)$$

Performing the integration gives

$$D = \frac{b_1}{b_2} \left[\frac{1}{2(b_1 + b_2 \epsilon_{11})} + \frac{\ln(b_1 + b_2 \epsilon_{11})}{b_1} \right] + D_0 \quad (6-67)$$

The constant of integration can be evaluated from the condition $D[(\epsilon_{11})_{cr}] = 0$, where $(\epsilon_{11})_{cr}$ corresponds to the strain at first fracture:

$$D_0 = -\frac{b_1}{b_2} \left[\frac{1}{2(b_1 + b_2(\epsilon_{11})_{cr})} + \frac{\ln(b_1 + b_2(\epsilon_{11})_{cr})}{b_1} \right] \quad (6-68)$$

Using (6-68), D can be written as

$$D = b_3 \left[\frac{(\epsilon_{11})_{cr} - \epsilon_{11}}{2b_2(b_3 + \epsilon_{11})(b_3 + (\epsilon_{11})_{cr})} + \frac{1}{b_1} \ln \left(\frac{b_3 + \epsilon_{11}}{b_3 + (\epsilon_{11})_{cr}} \right) \right] \quad (6-69)$$

where

$$b_3 \equiv \frac{b_1}{b_2} = \frac{1}{a_2(1-a_1)} - 1 \quad (6-70)$$

The form (6-69) indicates that the appropriate dissipation function for any strain path activating the $n = 1$ surface is

$$D = b_3 \left[\frac{h_{cr} - h}{2b_2(b_3 + h)(b_3 + h_{cr})} + \frac{1}{b_1} \ln \left(\frac{b_3 + h}{b_3 + h_{cr}} \right) \right] \quad (6-71)$$

The quantity $h_{cr} = (0.1)f'_c/E_c$ in the above example, where E_c denotes the (uncracked) Young's modulus for concrete. Typical uniaxial stress-strain response versus volume fraction is depicted in Figure 6-34 while Figure 6-35 shows the associated stiffness (normalized) degradation. The corresponding (normalized) dissipation function is graphed in Figure 6-36.

The above curves represent the "macro" monotonic response of reinforced concrete to uniaxial tension in the direction of the reinforcement. The Two-Phase Model parameter study noted previously indicated that the residual strain due to bond slip where the specimen was unloaded to zero stress was negligible. Only when the steel began to yield did the residual strains become significant. Further, in all cases, the stiffness modulus was essentially constant immediately before yielding began. This suggests, for incorporation of yielding, a simple superposition of fracturing and

INFLUENCE OF STEEL VOLUME FRACTION

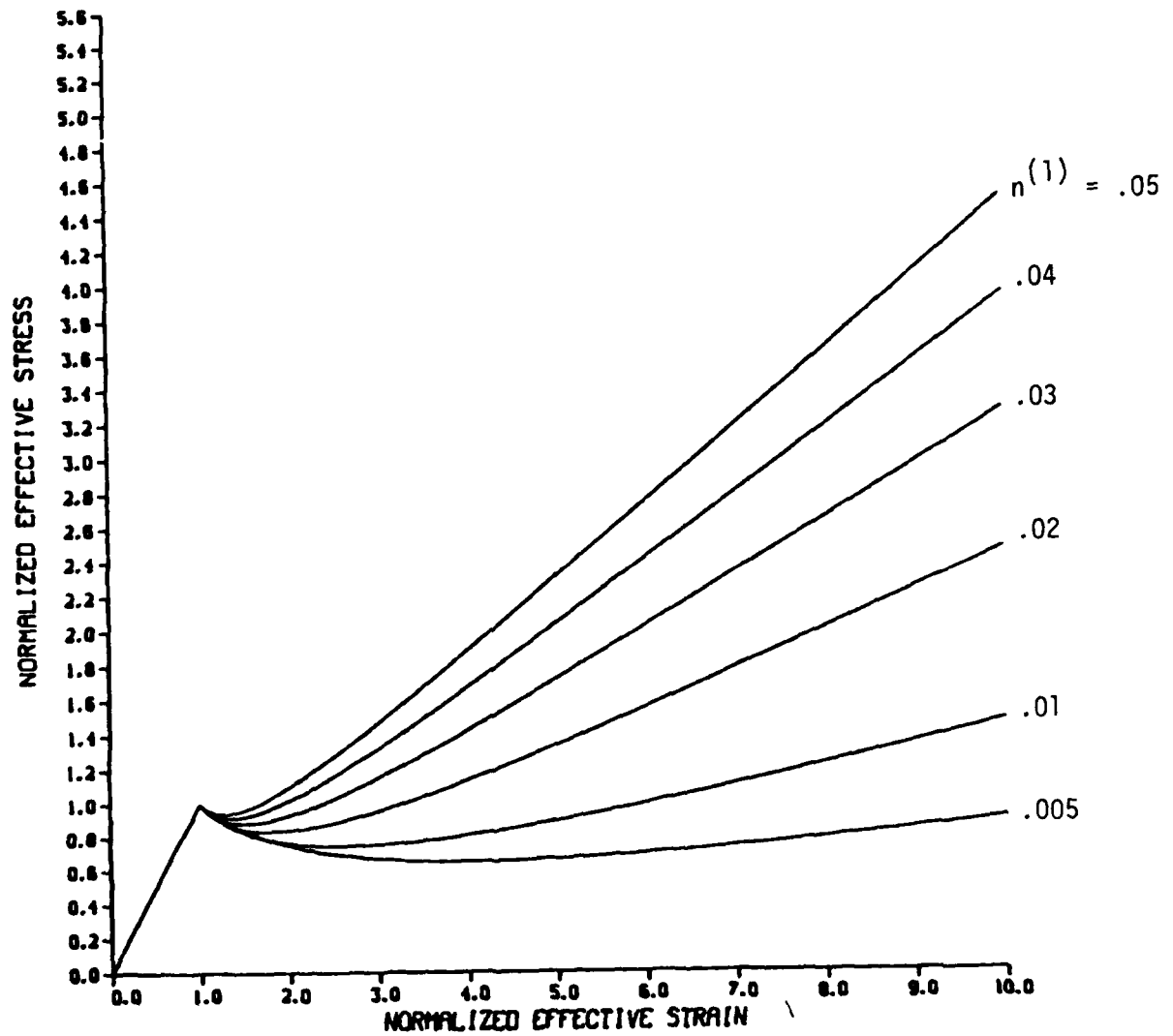


Figure 6-34. Single-phase model simulation of stress versus strain.

INFLUENCE OF STEEL VOLUME FRACTION

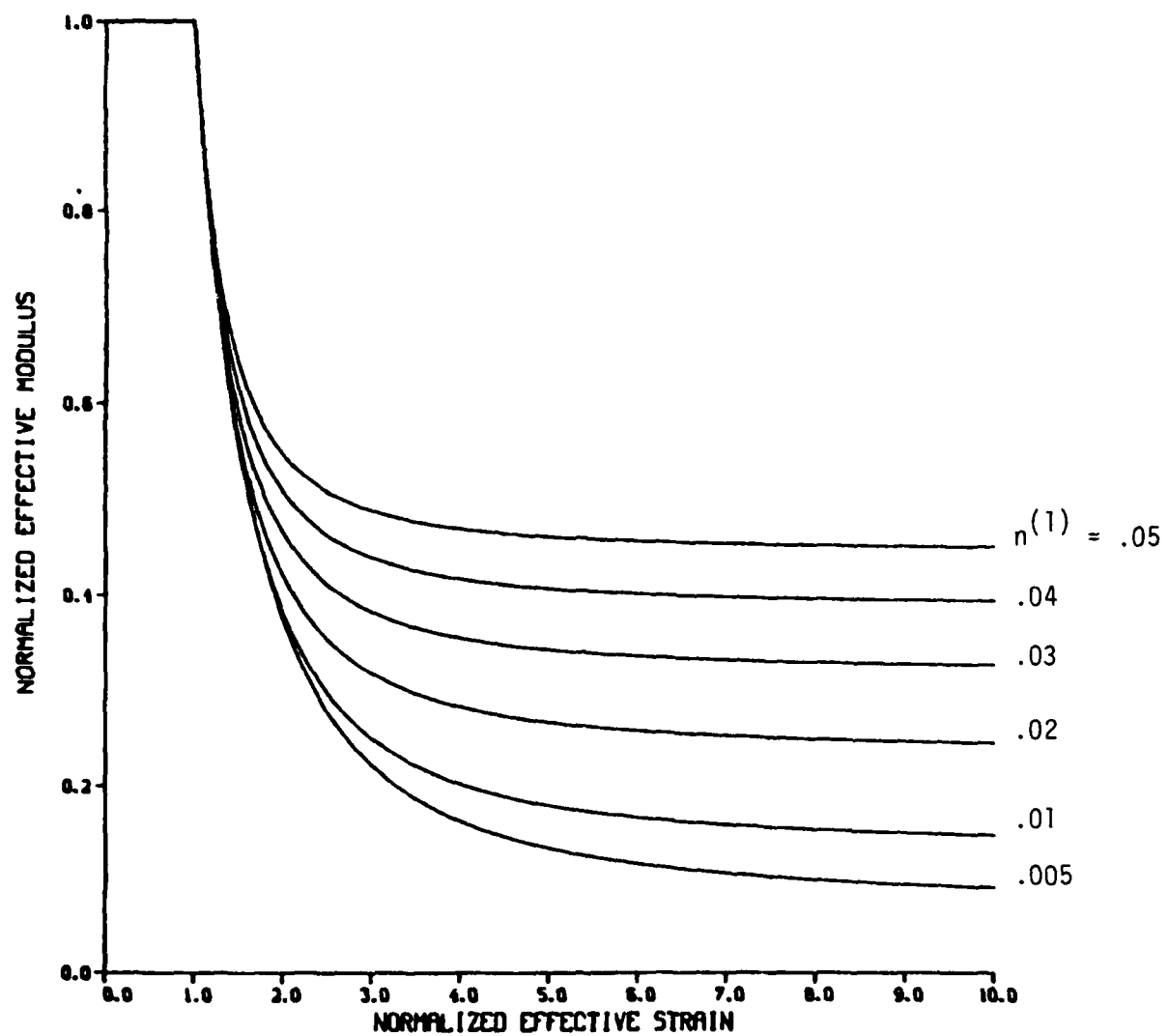


Figure 6-35. Single-phase model simulation of stiffness degradation.

INFLUENCE OF STEEL VOLUME FRACTION

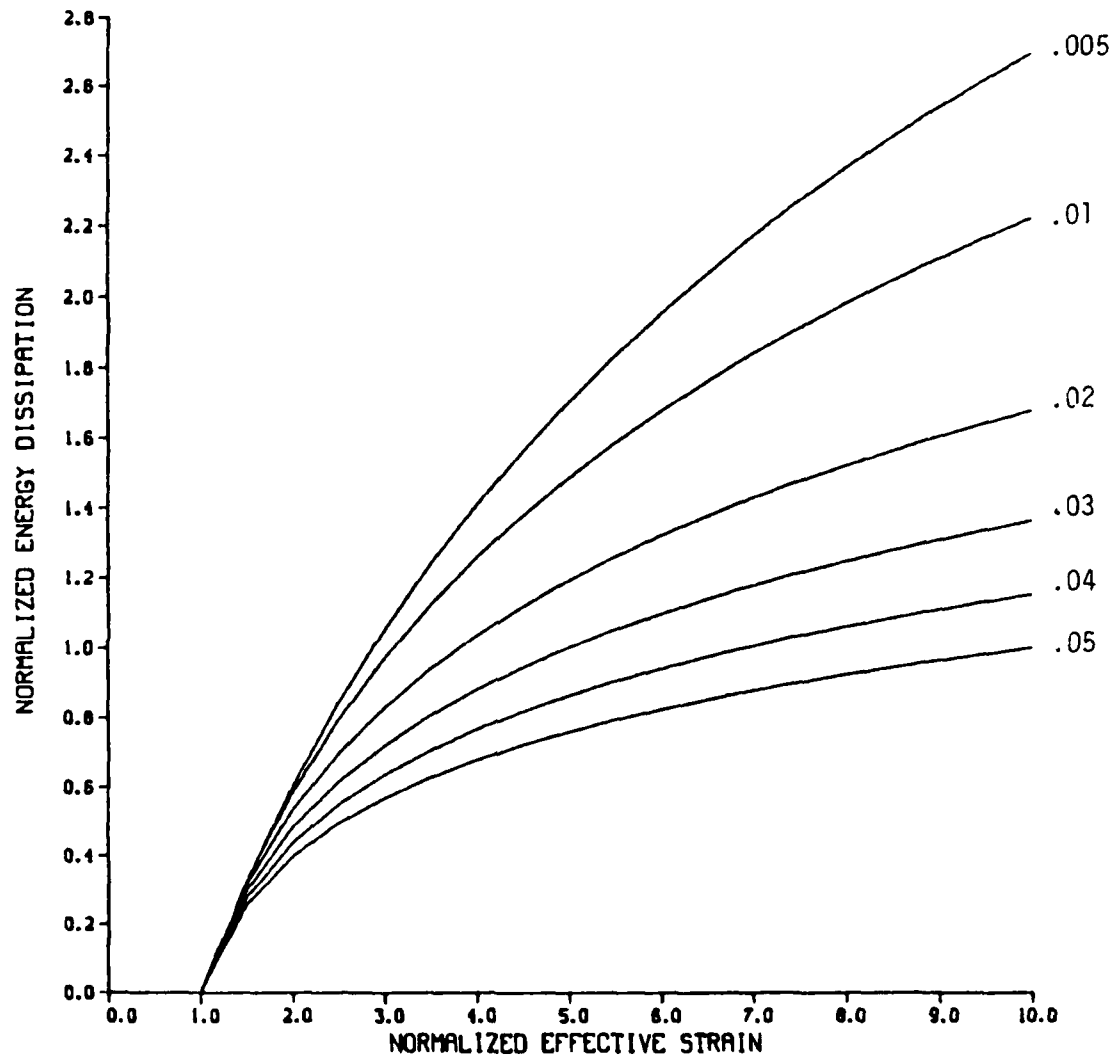


Figure 6-36. Normalized dissipation function.

plasticity models and a division of response into three connective stages of response for extension:

- I. Linear Elastic
- II. Progressive fracturing with stiffness degradation
- III. Yielding with strain hardening and constant elastic moduli.

SECTION 7

CONCLUDING REMARKS

The following were presented in this report: (1) a state-of-the-art review of plain and reinforced concrete data and models, (2) progress made to-date concerning the development of an improved nonlinear plain concrete model and (3) progress made to-date on the construction of a nonlinear model for reinforced concrete.

Discussion in the first area included a very comprehensive review and evaluation of the experimental and theoretical literature on plain concrete, and steel-concrete interaction. In the area of plain concrete it was noted that improvement is needed in the mathematical description of yield and failure surface geometry, strain softening, stiffness degradation, and strain rate effects. In the area of reinforced concrete it was noted that the manner in which steel and concrete are conventionally mixed analytically is in need of considerable improvement. Problems in this area were classified into four basic groups: (1) the steel-concrete bond problem, (2) the steel-concrete dowel problem, (3) the aggregate interlock problem, and (4) the steel buckling-concrete spallation problem.

Discussion in the second area focused upon the development of an improved failure surface for plain concrete. Such a surface plays an important role in the mathematical description of plain concrete. A three parameter surface was postulated and shown to provide an excellent fit to uniaxial, biaxial, and triaxial experimental data on plain concrete. The failure surface is written in terms of two stress invariants.

Discussion in the third area focused upon the development of a mixture theory with microstructure to model reinforced concrete. Attention here was confined to the steel-concrete bond problem. A general theoretical framework was presented and the resulting theory was 'closed' for a class of problems. Comparisons of experimental data and theoretical simulations were made for monotonic and cyclic

uniaxial extension. These comparisons revealed excellent simulation capability and accuracy. In particular, strain hardening, strain softening, stiffness degradation, and hysteresis were properly simulated. Consequently, the mixture theory approach appears to offer considerable improvement in simulation capability.

It is recommended that priority for future developments in this area be given to (1) an appropriate combination of plastic and fracturing elements for plain concrete, (2) the steel-concrete dowel problem for reinforced concrete and (3) the strain rate problem for plain concrete.

With respect to item (1) it is noted that procedures for combining plastic and fracturing elements have remained arbitrary up to this point. A comprehensive study of series, parallel, and various weighted techniques is necessary in order to fully understand the implications of each model.

Item (2) above constitutes the next basic step in the mixture theory construction process. This is a difficult task which will require a combined theoretical and experimental effort.

Item (3) has not been seriously approached in the literature as yet. In particular, virtually all current models of plain and reinforced concrete are strain rate independent. This is in contrast to the vast majority of the defense community-related problems which involve high strain rates. Consequently, an effort should be made to incorporate strain rate effects into a constitutive model of plain and reinforced concrete. Two avenues are open in this subject area. One is the use of a viscoplastic model in place of the current rate independent plastic element. The other is the use of the endochronic theory with time included in the definition of the intrinsic time variable.

LIST OF REFERENCES

1. Whitney, C. S. "Discussion on a Paper by M. P. Jensen." American Concrete Institute J., Vol. 39, 1943, pp. 582-586.
2. Hudson, J. A., S. L. Crouch and C. Fairhurst. "Soft Stiff and Servo-Controlled Testing Machines: A Review with Reference to Rock Failure." Engineering Geology, Vol. 6, 1972, pp. 155-189.
3. Ahmad, S. H. and S. P. Shah. "Complete Stress-Strain Curve of Concrete and Nonlinear Design." In Nonlinear Design of Concrete Structures. CSCE-ASCE-ACI-CEB International Symposium, University of Waterloo, Ontario, Canada. August 7-9, 1979, pp. 61-81.
4. Sigvaldason, O. T. "The Influence of Testing Machine Characteristics Upon the Cube and Cylinder Strength of Concrete." Magazine of Concrete Research, Vol. 18, 1966, pp. 197-206.
5. Hsu, T. T. C., F. O. Slate, G. M. Sturman and G. Winter. "Microcracking of Plain Concrete and the Shape of the Stress-Strain Curve," American Concrete Institute J., Vol. 60, 1963, pp. 209-223.
6. Hughes, B. P. and G. P. Chapman. "The Complete Stress-Strain Curve for Concrete in Direct Tension." RILEM Bulletin, No. 30, March, 1966, pp 95-97.
7. Rusch, H. Letter to the Editor, American Concrete Institute J., May, 1954, pp. 803-804.
8. Jones, R. "A Method of Studying the Formulation of Cracks in a Material Subjected to Stress." British Journal of Applied Physics, Vol. 3, 1952, pp. 229-232.
9. Hughes, B. P. and B. Bahramian. "Cube Tests and the Uniaxial Compressive Strength of Concrete." Magazine of Concrete Research, Vol. 17, 1963, pp. 177-182.
10. Newman, K. and O. T. Sigvaldason. "Testing Machine and Specimen Characteristics and Their Effect on the Mode of Deformation, Failure, and Strength of Materials." Proc. Institution of Mechanical Engineers, Vol. 180 Part 3A, 1965-6, pp. 399-410.
11. Cole, D. G. "Some Mechanical Aspects of Compression Testing Machines." Magazine of Concrete Research, Vol. 19, 1967, pp. 247-251.
12. Sabnis, G. M. and S. Aroni. "Size Effects in Material Systems -- The State of the Art." in Structure, Solid Mechanics and Engineering, edited by M. Te'Eni. J. Wiley and Sons, 1971, pp. 131-142.

13. Newman, K. "The Structure and Properties of Concrete -- An Introductory Review." in The Structure of Concrete edited by A. E. Brooks and K. Newman. Cement and Concrete Association, England, 1968, pp. xiii-xxxii.
14. Newman, K. and L. Lachance. "The Testing of Brittle Materials under Uniform Uniaxial Compressive Stress." Proc. American Society for Testing and Materials, Vol., 1964, pp. 1044-1067.
15. Mirza, S. A., M. Hatzinikolas and J. G. MacGregor. "Statistical Descriptions of Strength of Concrete." ASCE J. Structural Div., Vol. 105, 1979, pp. 1021-1036.
16. Jones, P. G. and F. E. Richart. "The Effect of Testing Speed on Strength and Elastic Properties of Concrete." Proc. ASTM., Vol. 36, Part II, 1936, pp. 380-391.
17. Kaplan, S. A. "Factors Affecting the Relationship Between Rate of Loading and Measured Compressive Strength of Concrete." Magazine of Concrete Research, Vol. 32, 1980, pp. 79-88.
18. Ferrito, J. M. "Dynamic Tests of Model Concrete." Naval Civil Engineering Laboratory, Port Hueneme, California, Report No. R650, DASAC318, 1969.
19. Watstein, D. "Effect of Straining Rate on the Compressive Strength and Elastic Properties of Concrete." American Concrete Institute J., Vol. 49, 1954, pp. 729-744.
20. Atchley, W. L. and H. L. Furr. "Strength and Energy Absorption Capabilities of Plain Concrete under Dynamic and Static Loadings." American Concrete Institute J., Vol. 64, 1967, pp. 745-756.
21. Hughes, B. P. and A. J. Watson. "Compressive Strength and Ultimate Strain of Concrete under Impact Loading." Magazine of Concrete Research, Vol. 30, 1978, pp. 189-199.
22. Nelissen, L. J. M. "Biaxial Testing of Normal Concrete." Heron, Vol. 18, No. 1, 1972, pp. 1-90.
23. Rüsç, H. "Researches Toward a General Flexural Theory for Structural Concrete." American Concrete Institute J., Vol. 57, 1960, pp. 1-28.
24. Wang, P. I., S. P. Shah and A. E. Naaman. "Stress-Strain Curves of Normal and Lightweight Concrete in Compression" American Concrete Institute J., Vol. 75, 1978, pp. 603-611.

25. Hognestad, E., N. W. Hanson and D. McHenry. "Concrete Stress Distribution in Ultimate Strength Design." American Concrete Institute J., Vol. 52, 1955, pp. 455-479.
26. Desayi, P. and C. S. Viswanatha. "True Ultimate Strength of Plain Concrete." RILEM Bulletin, No. 36, 1967, pp. 163-173.
27. Shah, S. P. and S. Chandra. "Fracture of Concrete Subjected to Cyclic and Sustained Loading." American Concrete Institute J., Vol. 67, 1970, pp. 816-825.
28. Sinha, B. P., K. H. Gerstle and L. G. Tulin. "Stress-Strain Relations for Concrete Under Cyclic Loading." American Concrete Institute J., Vol. 61, 1964, pp. 195-211.
29. Karsan, I. D. and J. O. Jirsa. "Behavior of Concrete under Compressive Loadings." ASCE. J. Structural Division, Vol. 95, 1969, pp. 2543-2563.
30. Cook, D. J. and P. Chindaprasirt. "Influence of Loading History upon the Compressive Properties of Concrete." Magazine of Concrete Research, Vol. 32, 1980, pp. 89-100.
31. Al-Kubaisy, M. A. and A. G. Young. "Failure of Concrete under Sustained Tension." Magazine of Concrete Research, Vol. 27, 1975, pp. 171-178.
32. Domone, P. L. "Uniaxial Tensile Creep and Failure of Concrete." Magazine of Concrete Research. Vol. 26, 1974, pp. 144-152.
33. Buyukozturk, O., A. H. Nilson, and F. O. Slate. "Stress-Strain Response and Fracture of a Concrete Model in Biaxial Loading," ACI. J., Vol. 68, 1971, pp. 590-99.
34. Carino, N. J., and F. O. Slate. "Limiting Tensile Strain Criterion for Failure of Concrete." ACI. J., Vol. 73, 1976, pp. 160-65.
35. Liu, T. C. Y., A. H. Nilson, and F. O. Slate. "Stress-Strain Response and Fracture of Concrete in Uniaxial and Biaxial Compression." ACI. J., Vol. 69, 1966, pp. 291-95.
36. Kupfer, H., H. K. Hilsdorf, and H. Rüschi. "Behavior of Concrete under Biaxial Stresses." ACI. J., Vol. 66, 1969, pp. 656-66.
37. Atan, Y., and F. O. Slate. "Structural Lightweight Concrete Under Biaxial Compression." ACI. J., Vol. 70, 1973, pp. 182-86.

38. Gerstle, K. H., et al. "Concrete under Multiaxial Stress States." Douglas McHenry International Symposium on Concrete and Concrete Structures. ACI. SP-55, 1978, pp. 103-31.
39. Robinson, G. S. "Behavior of Concrete in Biaxial Compression." ASCE. J. Struct'l. Div., Vol. 93, 1967, pp. 71-86.
40. Vile, G. W. D. "The Strength of Concrete under Short-Term Static Biaxial Stress." In the Structure of Concrete edited by A. E. Brooks and K. Newman, London: Cement and Concrete Assoc., 1968, pp. 275-88.
41. Weigler, H., and G. Becker. "Ueber das Bruch- und Verformungsverhalten von Beton bei Mehrachsiger Beanspruchung." Der Bauingenieur, 1961.
42. Weigler, H., and G. Becker. "Untersuchungen ueber das Bruch- und Verformungsverhalten von Beton bei Zweiachsiger Beanspruchung." DAfS., H 157.
43. Andenaes, E., K. Gerstle, and H-Y Ko. "Response of Mortar and Concrete to Biaxial Compression." ASCE. J. EM Div., Vol. 104, 1977, pp. 515-26.
44. Iyengar, K. T. S. R., K. Chandrashekara, and K. T. Krishnaswamy. "Strength of Concrete under Biaxial Compression." ACI. J., Vol. 62, 1965, pp. 239-49.
45. Bresler, B., and K. S. Pister. "Failure of Plain Concrete under Combined Stresses." Paper 2897, ASCE. Transactions, 1955, pp. 1049-68.
46. Bresler, B., and K. S. Pister. "Strength of Concrete under Combined Stresses." ACI. J., Vol. 55, 1958, pp. 321-45.
47. Goode, C. D., and M. A. Helmy. "The Strength of Concrete under Combined Shear and Direct Stress." Magazine of Concrete Research, Vol. 19, 1967, pp. 105-12.
48. Isenberg, J. "Properties of Concrete Change when Micro-cracking Occurs." Causes, Mechanism and Control of Cracking in Concrete, ACI. SP-20, 1968, pp. 29-41.
49. Rosenthal, I., and J. Glucklich. "Strength of Plain Concrete under Biaxial Stress." ACI. J., Vol. 67, 1970, pp. 903-14.
50. Fumagalli, E., et al. "Discussion of 'Strength of Concrete under Biaxial Compression' by K. T. S. R. Iyengar, K. Chandrashekara and K. T. Krishnaswamy." ACI. J., Vol. 68, Feb. 1965, pp. 239-49.
51. Nelissen, L. J. M. "Biaxial Testing of Normal Concrete." Heron, Vol. 18, No. 1, 1972.

52. Kijellmann, W. "Om Unders dening av Jordartes Deformations Egenskaper (Research on the Strain Characteristics of Soils)." Teknisk Tids Krift, Stockholm, 1936.
53. Hilsdorf, H. "Die Bestimmung der zweiachsiger Festigkeit des Betons Zusammenfassung and Kritik fruherer Versuche und Vorschlag für eine neue Prüfmethode." DAfS., H.173, 1965.
54. Ko, H-Y., and S. Sture. "Three-Dimensional Mechanical Characterization of Anisotropic Composites." J. Composite Materials, Vol. 8, 1974, p. 178.
55. Kupfer, H. "Das Verhalten des Betons unter mehrachsiger Kurzzeit belastung unter besonderer Berücksichtigung der Zweiachsigen Beanspruchung." DAfS., H.229, 1973.
56. Kupfer, H. "Das Verhalten des Betons unter Zweiachsiger Beanspruchung." Wissensch. Zeitschrift. der T.U. Dresden, Bd. 17, H.6, 1968.
57. Kupfer, H. "Das Verhalten des Betons unter Zweiachsiger Beanspruchung." Lehrstuhl für Massivbau, T. H. Munchen., Bericht No. 78, 1969.
58. Kupfer, H. "Das Nicht-lineare Verhalten des Betons bei Zweiachsiger Beanspruchung." Beton und Stahlbeton-bau, 1973.
59. Kupfer, H., and K. H. Gerstle. "The Nonlinear Behavior of Concrete under Biaxial Stress States." ASCE National Structural Engineering Meeting, Cleveland, OH, 1972.
60. Dei Poli, S. "Microfessurazione, Leggi Costitutive e Condizioni di Rottura del Calcestruzzo in Stati de Tensione Mono e Pluriassiali." Costruzione in Cemento Armato, Studi e Rendiconti, Vol. 15, Milan Polytechnic, 1978.
61. Johnson, R. P., and P. G. Lowe. "Behavior of Concrete under Biaxial and Triaxial Stress." In Structure, Solid Mechanics and Engineering Design, edited by M. Te'Eni, London: J. Wiley, 1971, pp. 1039-51.
62. Taylor, M. A., and B. K. Patel. "The Influence of Path Dependency and Moisture Conditions on the Biaxial Compression Envelope for Normal Weight Concrete." ACI. J., Vol. 71, 1974, pp. 627-33.
63. Krishnaswamy, K. T. "Strength and Microcracking of Plain Concrete Under Triaxial Compression." ACI. J., Vol. 65, 1968, pp. 856-62.
64. Palaniswamy, R. and S. P. Shah. "Fracture and Stress-Strain Relationship of Concrete under Triaxial Compression." ASCE. J. Struct'l Div., Vol. 100, 1974, pp. 901-916.

65. Chinn, J. and R. M. Zimmerman. "Behavior of Plain Concrete under Various High Triaxial Compression Loading Conditions." Air Force Weapon Laboratory Report WLTR-64-163, August, 1965.
66. Gardner, N. J. "Triaxial Behavior of Concrete." ACI. J., Vol. 66, 1969, pp. 136-146.
67. Gerstle, K. H. et al. "Strength of Concrete Under Multiaxial Stress States." In Douglas McHenry International Symposium on Concrete and Concrete Structures, ACI. SP-55, 1978, pp. 103-31.
68. Johnson, R. P. and P. G. Lowe. "Behavior of Concrete Under Biaxial and Triaxial Stress." In Structure, Solid Mechanics and Engineering Design, edited by M. Te'eni, J. Wiley and Sons, London, 1971, pp. 1039-1051.
69. Launay, P. and H. Gachon. "Strain and Ultimate Strength of Concrete under Triaxial Stress." In Concrete for Nuclear Reactors, ACI. SP-34, 1972, pp. 269-282.
70. Mills, L. L. and R. M. Zimmerman. "Compressive Strength of Plain Concrete Under Multiaxial Loading Conditions." ACI. J. Vol. 67, 1970, pp. 802-807.
71. Newman, J. B. "Apparatus for Testing Concrete Under Multiaxial States of Stress." Magazine of Concrete Research, Vol. 26, 1974, pp. 229-238.
72. Richart, F. E., A. Brandtzaeg and R. L. Brown. "A Study of the Failure of Concrete under Combined Compressive Stresses." University of Illinois Engineering Experiment Station, Bulletin 185, November, 1928.
73. Bertacchi, P. "Behavior of Concrete Under Combined Loads. A Comparison of the Concrete Shearing Strength Values Obtained from Direct Tests with the Values obtained from Triaxial Tests." Ente Nazionale per L'Energia Ellectrica, Studi e Recherche, No. 8, 1976.
74. Dei Poli, S. "Microfessurazione, leggi, costitutive e condizioni di rottura del calcestruzzo in stati di tensione mono e pluriassiali." Costruzione in Cemento Armato, Studi e Rendiconti, 15, 1979.
75. Kotsovos, M. D. "Effect of Stress Path on the Behavior of Concrete Under Triaxial Stress States." ACI. J., Vol. 76, 1979, pp. 213-223.
76. Green, S. J. and S. R. Swanson. "Static Constitutive Relations for Concrete." Air Force Weapons Laboratory Report AFWL-TR-72-24, April, 1973.

77. Schickert, G. and H. Winkler. "Results of Test Concerning Strength and Strain of Concrete Subjected to Multiaxial Compressive Stresses." Deutscher Ausschuss für Stahlbeton, Vol. 277, 1977.
78. Bertacchi, P. and R. Belloti. "Experimental Research on Deformation and Failure of Concrete under Triaxial Loads, ENEL, Studi e Ricerche, No. 8, 1976.
79. Bremer, F. "On a Triaxial Strength Criterion for Concrete." In Concrete for Nuclear Reactors, ACI SP-34, Vol. I, 1972, pp. 283-94.
80. Ahmad, S. and S. P. Shah. "Complete Triaxial Stress-Strain Curves for Concrete." University of Illinois at Chicago, Materials Engineering Report. March 1981.
81. Cedolin L., Y. R. J. Crutzen and S. Dei Poli. "Triaxial Stress-Strain Relationship for Concrete." ASCE. J. EM. Div., Vol. 103, 1977, pp. 423-439.
82. Bresler, G., and V. Bertero. "Behavior of Reinforced Concrete Under Repeated Load." ASCE. J. Struct'l Div., Vol. 94, 1968, pp. 1567-1590.
83. Dorr, K. "Bond-Behavior of Ribbed Reinforcement Under Transversal Pressure." in Nonlinear Behavior of Reinforced Concrete Spatial Structures, G. Mehlhorn et al., Editors. Proc. IASS Symposium, Dusseldorf, 1978, pp. 13-24.
84. Edwards, A. D., and P. J. Yannopoulos. "Local Bond Stress to Slip Relationships for Hot Rolled Deformed Bars and Mild Steel Plain Bars." ACI. J., Vol. 76, 1979, pp. 405-420.
85. Ferguson, P. M., et al. "Bond Stress - The State of the Art." ACI. J., Vol. 63, 1966, pp. 1161-1189.
86. Lutz, L. A., and P. Gergely. "Mechanics of Bond and Slip of Deformed Bars in Concrete." ACI. J., Vol. 64, 1967, pp. 711-721.
87. Mains, R. M. "Measurement of the Distribution of Tensile and Bond Stresses Along Reinforcing Bars." ACI. J., Vol. 48, 1951, pp. 225-252.
88. Mathey, R. G., and D. Watstein. "Investigation of Bond in Beam and Pull-out Specimens with High Yield-Strength Deformed Bars." ACI. J., Vol. 57, 1961, pp. 1071-1090.
89. Goto, Y. "Cracks Formed in Concrete Around Deformed Tension Bars." ACI. J., Vol. 68, 1971, pp. 244-251.

90. Mirza, S. M., and J. Houde. "Study of Bond Stress - Slip Relationships in Reinforced Concrete." ACI. J., Vol. 76, 1979, pp. 19-46.
91. Untrauer, R. E., and R. L. Henry. "Influence of Normal Pressure on Bond Strength." ACI. J., Vol. 62, 1965, pp. 577-585.
92. Tepfers, R. "Cracking of Concrete Cover Along Anchored Deformed Reinforcing Bars." Magazine of Concrete Research, Vol. 31, 1979, pp. 3-12.
93. Kemp, E. L., and W. J. Wilhelm. "Investigation of the Parameters Influencing Bond Cracking." ACI. J., Vol. 76, 1979, pp. 47-71.
94. Ferguson, P. M., J. E. Breen, and J. Neils Thompson. "Pullout Tests on High Strength Reinforcing Bars." ACI. J., Vol. 62, 1965, pp. 993-949.
95. Edwards, A. D., and P. J. Yannopoulos. "Local Bond Stress-Slip Relationship Under Repeated Loading." Magazine of Concrete Research, Vol. 30, 1978, pp. 62-72.
96. Perry, E. S., and N. Jundi. "Pullout Bond Stress Distribution Under Static and Dynamic Repeated Loadings." ACI. J., Vol. 66, 1969, pp. 377-380.
97. Perry, E. S., and J. Neils Thompson. "Bond Stress Distribution on Reinforcing Steel in Beams and Pullout Specimens." ACI. J., Vol. 63, 1966, pp. 865-875.
98. Ismail, M. A. F., and J. O. Jirsa. "Bond Deterioration in Reinforced Concrete Subject to Low Cycle Loads." ACI. J., Vol. 69, 1972, pp. 334-343.
99. Bertero, V. V., E. P. Popov, and S. Viwathanatepa. "Bond of Reinforcing Steel: Experiments and a Mechanical Model." In Nonlinear Behavior of Reinforced Concrete Spatial Structures. G. Mehlhorn et al., Editors, Proc. IASS Symposium, Dusseldorf, 1978, pp. 3-17.
100. Nilson, A. H. "Internal Measurement of Bond Slip." ACI. J., Vol. 69, 1971, pp. 439-441.
101. Morita, S., and T. Kaku. "Local Bond Stress-Slip Relationship Under Repeated Loading." In Symposium on the Resistance and Ultimate Deformability of Structures. IABSE, Lisbon, 1973, pp. 221-227.

102. Leombruni, P., O. Buyukozturk, and J. J. Connor. "Analysis of Shear Transfer in Reinforced Concrete with Application to Containment Wall Specimens," U.S. Nuclear Regulatory Commission Report NRC FIN. NO. B6618, October, 1979.
103. Fenwick, R. C. "The Shear Strength of Reinforced Concrete Beams," Thesis, University of Canterbury, Christ Church, New Zealand, 1966.
104. Fenwick, R. C., and T. O. Pauley. "Mechanism of Shear Resistance in Concrete Beams," Journal of the Structural Division, ASCE, Vol. 94, No. ST 10, October, 1968.
105. Loeber, P. J. "Shear Transfer by Aggregate Interlock," Thesis, University of Canterbury, Christ Church, New Zealand, 1970.
106. Houde, J. "Study of Force-Displacement Relationship for the Finite Element Analysis of Reinforced Concrete," Structural Concrete Series, No. 73-2, McGill University, Montreal, December, 1973.
107. Houde, J. and M. S. Mirza. "Investigation of Shear Transfer Across Cracks by Aggregate Interlock," Research Report No. 72-06, Ecole Polytechnique de Montreal, Dept. of Gene Civil, Division de Structures, 1972.
108. White, R. N., and M. J. Holley. "Experimental Studies of Membrane Shear Transfer," Journal of the Structural Division, American Society of Civil Engineers, No. ST3, August, 1972.
109. Laible, J. P. "An Experimental Investigation of Interface Shear Transfer and Application in the Dynamic Analysis of Nuclear Containment Vessels," Thesis, Cornell University, August, 1973.
110. Jimenez, R., P. Gergely, and R. N. White. "Shear Transfer Across Cracks in Reinforced Concrete," Report No. 78-4, Department of Structural Engineering, Cornell University, Ithaca, New York, August, 1979.
111. Jimenez, R., P. Perdikaris, P. Gergely, and R. N. White. "Interface Shear Transfer and Dowel Action in Cracked Reinforced Concrete Subject to Cyclic Shear," Proceedings of ASCE Specialty Conference on Structural Analysis, Macison, Wisconsin, August, 1976.
112. Dulucska, H. "Dowel Action of Reinforcement Crossing Cracks in Concrete," Journal of the American Concrete Institute, December, 1972.

113. Popovics, S. "A Review of Stress-Strain Relationships for Concrete." American Concrete Institute J., Vol. 67, 1970, pp. 243-248.
114. Saenz, L. P. "Discussion of Paper by Desayi and Krishnan." American Concrete Institute J., Vol. 61, 1964, pp. 1229-1235.
115. Kriz, L. B. and S. L. Lee. "Ultimate Strength of Over Reinforced Beams." ASCE J. Engineering Mechanics Division, Vol. 86, 1960, pp. 95-105.
116. Popovics, S. "A Numerical Approach to the Complete Stress-Strain Curve of Concrete." Cement and Concrete Research, Vol. 3, 1973, pp. 583-599.
117. Aoyama, H. and H. Noguchi. "Mechanical Properties of Concrete Under Load Cycles Idealizing Seismic Actions." In AICAP-CEB Symposium on Structural Concrete Under Seismic Actions, Rome, 1979, Theme 1b.
118. Murray, D.W. "Octahedral Based Incremental Stress-Strain Matrices." ASCE. J. EM. Div., Vol. 105, 1979, pp. 501-13.
119. Liu, T. C. Y., A. H. Nilson, and F. O. Slate. "Biaxial Stress-Strain Relations for Concrete." ASCE. J. Struct. Div., Vol. 98, 1972, pp. 1025-34.
120. Tasuji, M. E., F. O. Slate, and A. H. Nilson. "Stress-Strain Response and Fracture of Concrete in Biaxial Loading." ACI. J., Vol. 75, 1978, pp. 306-12.
121. Tasjui, M. E., F. O. Slate and A. H. Nilson. "Biaxial Stress-Strain Relationships for Concrete." Magazine of Concrete Research, Vol. 31, 1979, pp. 217-24.
122. Hand, F. R., D. A. Pecknold, and W. C. Schnobrich. "Nonlinear Layered Analysis of RC Plates and Shells." ASCE. J. Struct'l. Div., Vol. 99, 1973, pp. 1491-1505.
123. Lin, C-S., and A. C. Scordelis. "Nonlinear Analysis of RC Shells of General Form." ASCE. J. Struct'l. Div., Vol. 101, 1975, pp. 523-38.
124. Buyukozturk, O. "Nonlinear Analysis of Reinforced Concrete Structures." Computers and Structures, Vol. 7, 1977, pp. 149-56.
125. Chen, A. C. T., and W. F. Chen. "Constitutive Relations for Concrete." ASCE. J. EM. Div., Vol. 101, 1975, pp. 465-81.

126. Chen, A. C., and W. F. Chen. "Constitutive Equations and Punch Identification of Concrete." ASCE. J. EM. Div., Vol. 101, 1975, pp. 889-906.
127. Chen, A. C., and W. F. Chen. "Nonlinear Analysis of Concrete Splitting Tests." Computers and Structures, Vol. 6, 1976, pp. 451-57.
128. Chen, W. F., and T. Y. P. Chang. "Plasticity Solutions for Concrete Splitting Tests." ASCE. J. EM. Div., Vol. 104, 1978, pp. 691-704.
130. Chen, W. F., and H. Suzuki. "Constitutive Models for Concrete." Computers and Structures, Vol. 12, 1980, pp. 23-32.
131. Epstein, M. "A Biaxial Constitutive Law for Concrete Incorporated BOSOR5." Computers and Structures, Vol. 9, 1978, pp. 57-63.
132. Murray, D. W., L. Chitnuyanondh, and C. Wong. "Implementation of an Elastic-Plastic Concrete Relationship." Computer Methods in Applied Mechanics and Engineering., Vol. 23, 1980, pp. 35-57.
133. Murray, D. W., L. Chitnuyanondh, and C. Wong. "Computer Implementation of an Elastic-Plastic Concrete Relationship." Paper M2/4, SMIRT 5, Berlin, 1979.
134. Darwin, D., and D. A. W. Pecknold. "Inelastic Model for Cyclic Biaxial Loading of Reinforced Concrete." University of Illinois at Urbana-Champaign, July 1974. UIU-ENG-74-2018.
135. Darwin, D., and D. A. W. Pecknold. "Analysis of RC Shear Panels under Cyclic Loading." ASCE. J. Struct'l. Div., Vol. 102, 1976, pp. 355-69.
136. Darwin, D., and D. A. W. Pecknold. "Analysis of Cyclic Loading of Plane R/C Structures." Computers and Structures, Vol. 7, 1977, pp. 137-46.
137. Saenz, L. P. "Discussion of the Paper by Desayi and Krishnan." ACI., J., Vol. 61, 1964, p. 1229.
138. Karsan, I. D., and J. O. Jirsa. "Behavior of Concrete under Compressive Loadings." ASCE. J. Struct'l Div., Vol. 95, 1969, pp. 2543-63.
139. Cervenka, V., and K. H. Gerstle. "Inelastic Analysis of Reinforced Concrete Panels. Part II: Experimental Verification and Analyses." IABSE Publications, Vol. 32-II, 1972, pp. 25-39.

140. Ahmad, S. and S. P. Shah. "Complete Triaxial Stress-Strain Curves for Concrete." University of Illinois at Chicago, Materials Engineering Report. March 1981.
141. Cedolin, L., Y. R. J. Crutzen and S. Dei Poli. "Triaxial Stress-Strain Relationship for Concrete." ASCE. J. EM. Div., Vol. 103, 1977, pp. 423-439.
142. Elwi, A. A., and D. W. Murray. "A 3-D Hypoelastic Concrete Constitutive Relationship." ASCE. J. EM. Div., Vol. 105, 1979, pp. 623-41.
143. Kotsovos, M. D. and J. B. Newman. "Generalized Stress-Strain Relations for Concrete." ASCE. J. EM. Div., Vol. 104, 1978, pp. 845-856.
144. Coon, M. D. and R. J. Evans. "Incremental Constitutive Laws and Their Associated Failure Criteria with Application to Plain Concrete." Int'l J. Solids and Structures, Vol. 8, 1972, pp. 1169-1183.
145. Truesdell, C. A. and W. Noll. "The Nonlinear Field Theories of Mechanics." in Handbuch der Physik, Vol. III/3, Springer Verlag, 1965.
146. Gardner, N. J., "Triaxial Behavior of Concrete." ACI. J., Vol. 66, 1969, pp. 136-146.
147. De Maggio, F. L. and I. Sandler. "Material Model for Granular Soils." ASCE. J. EM. Div., Vol. 97, 1971.
148. Dougill, J. W. "On Stable Progressively Fracturing Solids." Zeitschrift fur Angewandte Mechanik und Physik, Vol. 27, 1976, pp. 423-437.
149. Bazant, Z. P., and S.-S. Kim. "Plastic-Fracturing Theory for Concrete." ASCE J. EM. Div., Vol. 105, 1979, pp. 407-428.
150. Bazant, Z. P., and P. D. Bhat. "Endochronic Theory of Inelasticity and Failure of Concrete." ASCE. J. EM. Div., Vol. 102, 1976, pp. 701-722.
151. Bazant, Z. P., and P. D. Bhat. "Prediction of Hysteresis of Reinforced Concrete Members," ASCE. J. Struct'l Div., Vol. 103, 1977, pp. 153-167.
152. Sorenson, S. I. "Endochronic Theory in Nonlinear Finite Element Analysis of Reinforced Concrete." Report 78-1, Division of Structural Mechanics, the Norwegian Institute of Technology, March 1978.

153. Sorenson, S. I., A. Arnesen and P. G. Bergan. "Nonlinear Finite Element Analysis of Reinforced Concrete using Endochronic Theory." in Finite Elements in Nonlinear Mechanics, edited by P. G. Bergan et al., Tapir, Norwegian Institute of Technology, Trondheim, Vol. I, 1978, pp. 167-189.
154. Powell, G. H., I. P. de Villiers and R. W. Litton. "Implementation of Endochronic Theory for Concrete with Extension to Include Cracking." in SMIRT 5, 1979, Paper M2/6.
155. Sandler, I. S. "On Uniqueness and Stability of Endochronic Theories of Material Behavior." Report DNA001-76-C-0127, Defense Nuclear Agency, 1976.
156. Bazant, Z. P. and C.-L. Shieh. "Endochronic Model for Nonlinear Triaxial Behavior of Concrete." Nuclear Engineering and Design, Vol. 47, 1978, pp. 305-315.
157. Bazant, Z. P. "Material Problems in Accident Analysis of Prestressed Concrete Reactor Vessels." SMIRT 4, 1977, Paper E6/1*.
158. Bazant, Z. P. and C.-L. Shieh. "Hysteretic Fracturing Endochronic Theory for Concrete." ASCE, J. EM. Div., Vol. 106, 1980, pp. 929-950.
159. Il'iushin, A. A. "On the Postulate of Plasticity," Appl. Math. Mech., Vol. 25, pp. 746-752.
160. Dougill, J. W. and M. A. M. Rida. "Further Consideration of Progressively Fracturing Solids," ASCE Journal, Vol. 106, NOSEM5, October 1980, pp. 1021-1038.
161. Lade, P. V. "Elasto-Plastic Stress-Strain Theory for Cohesionless Soil with Curved Yield Surfaces." International Journal of Solids and Structures, Pergamon Press, Inc., New York, NY, Vol. 13, November 1977, pp. 1019-1035.
162. Lade, P. V. "Prediction of Undrained Behavior of Sand," Journal of the Geotechnical Engineering Division, ASCE, Vol. 104, No. GT6, Proc. Paper 13834, June 1978, pp. 721-735.
163. Lade, P. V., and H. M. Musante. "Three-Dimensional Behavior of Remolded Clay," Journal of the Geotechnical Engineering Division, ASCE, Vol. 104, No. GT2, Proc. Paper 13551, February 1978, pp. 193-209.
164. Hannant, D. J. "Nomograms for the Failure of Plain Concrete Subjected to Short-Term Multiaxial Stresses." The Structural Engineer, Vol. 52, No. 5, May 1974, pp. 151-165.

165. Argyris, J. H., G. Faust, J. Szimmat, E. P. Warnke, and K. J. Willam. "Recent Developments in the Finite Element Analysis of Prestressed Concrete Reactor Vessels." Nuclear Engineering and Design, Vol. 28, North-Holland Publishing Company, 1974, pp. 42-75.
166. Argyris, J. H., G. Faust, and K. J. Willam. "A Unified Stress-Strain Law for Triaxial Concrete Failure, Third Post Conference on Computational Aspects of the Finite Element Method, Imperial College, London, England, September 8-9, 1975.
167. Hobbs, D. W., C. D. Pomeroy, and J. B. Newman. "Design Stresses for Concrete Structures Subject to Multi-Axial Stresses." The Structural Engineer, Vol. 55, No. 5, April 1977, pp. 151-164.
168. Kotsovos, M. D. "A Mathematical Description of the Strength Properties of Concrete under Generalized Stress," Magazine of Concrete Research, Vol. 31, No. 108, Sept. 1979, pp. 151-158.
169. Link, J., "Eine Formulierung des Zweiaxialen Verformungs und Bruchverhaltens von Beton und deren Anwendung auf die wirklichkeitsnahe Berechnung von Stahlbeton platten." Deutscher Ausschuss für Stahlbeton, Heft 270, Berlin, Germany, 1976.
170. Ottosen, N. S. "A Failure Criterion for Concrete." Journal of the Engineering Mechanics Division, ASCE, Vol. 103, No. EM4, Proc. Paper 13111, August 1977, pp. 517-535.
171. William, K. J., and E. P. Warnke. "Constitutive Model for the Triaxial Behaviour of Concrete." International Association of Bridge and Structural Engineers Seminar on Concrete Structures Subjected to Triaxial Stresses; Paper III-1, Bergamo, Italy, May 17-19, 1974.
172. Wastiels, J. "Failure Criteria for Concrete under Multiaxial Stress States." Colloquium on Plasticity in Reinforced Concrete, International Association for Bridge and Structural Engineering, Lyngby, Denmark, May 1979, pp. 3-10.
173. Hsieh, S. S., E. C. Ting, and W. F. Chen. "A Plastic-Fracture Model for Concrete." Intl. J. Solids Structures, Vol. 18, No. 3, pp. 181-197, 1982.
174. Hegemier, G. A. "Mixture Theories with Microstructure for Wave Propagation and Diffusion in Composite Materials." SM Archives, Vol. 3, 1978.
175. Hegemier, G. A., H. Murakami, and A. Maewal. "On Construction of Mixture Theories for Composite Materials by the Method of Multi-variable Asymptotic Expansion." Proceedings, Third International Symposium on Continuum Models of Discrete Systems, Freudenstadt, Germany, 1979.

176. Somayaji, S., and S. P. Shah. "Bond Stress Versus Slip Relationship and Cracking Response of Tension Members." ACI Journal, May-June, 1981.
177. Somayaji, S. "Composite Response, Bond Stress-Slip Relationships and Cracking in Ferrocement and Reinforced Concrete." Ph.D. Dissertation, University of Illinois at Chicago Circle, 1979.
178. Morito, S. and T. Kaku. "Local Bond Stress-Slip Relationship Under Repeated Loading." IABSE Symposium on Resistance and Ultimate Deformability of Structures, Lisbon, 1973. The Reports of the Working Commission, Vol. 13, pp. 221-227.
179. Hegemier, G. A., R. O. Nunn, and S. K. Arya. "Behavior of Concrete Masonry Under Biaxial Stresses." Proceedings of North American Masonry Conference, University of Colorado, Boulder, Colorado, August 1978.
180. Lade, P. V. "Three Parameter Failure Criterion for Concrete." Journal of the Engineering Mechanics Division, ASCE (accepted for publication).

DISTRIBUTION LIST

DEPARTMENT OF DEFENSE

Assist to the Secy of Defense, Atomic Energy
ATTN: Executive Assistant

Defense Advanced Rsch Proj Agency
ATTN: Defense Sciences Office

Defense Communications Agency
ATTN: Code J300
ATTN: WSE
ATTN: 900, D. Israel

Defense Intelligence Agency
ATTN: DB-4C2
ATTN: RTS-2A, Tech Library
ATTN: RTS-2B

Defense Nuclear Agency
ATTN: RAEV
ATTN: STNA
ATTN: STSP
4 cys ATTN: SPSS
4 cys ATTN: STTI-CA

Defense Technical Information Center
12 cys ATTN: DD

Field Command, DNA, Det 2
Lawrence Livermore National Lab
ATTN: FC-1

DNA PACOM Liaison Office
ATTN: J. Bartlett

Field Command, Defense Nuclear Agency
ATTN: FCPR
ATTN: FCTO
ATTN: FCTT
ATTN: FCTT, W. Summa
ATTN: FCTXE

Field Command Test Directorate
ATTN: FCTBE, L. Ashbaugh

Joint Chiefs of Staff
ATTN: GD10, J-5 Nuc & Chem Div

Joint Strat Tgt Planning Staff
ATTN: JLK, DNA Rep
ATTN: JLKC
ATTN: JPPFM
ATTN: JPPFN
ATTN: JPST
ATTN: JPTM

Under Secy of Def for Rsch & Engrg
2 cys ATTN: Strat & Space Sys (OS)

DEPARTMENT OF THE ARMY

BMD Advanced Technology Center
ATTN: ATC-T

BMD Systems Command
ATTN: BMDSC-HW
ATTN: BMDSC-LEE, R. Webb

DEPARTMENT OF THE ARMY (Continued)

Harry Diamond Laboratories
ATTN: SLCHD-NW-P

US Army Ballistic Research Lab
ATTN: AMXBR-TBD, R. Raley
ATTN: DRDAR-BLA-S, Tech Library
ATTN: DRDAR-BLT, J. Keefer

US Army Concepts Analysis Agency
ATTN: CSSA-ADL, Tech Library

US Army Corps of Engineers
ATTN: DAEN-ECE-T
ATTN: DAEN-RDL

US Army Engineer Ctr & Ft Belvoir
ATTN: DT-LRC

US Army Engineer Dist Omaha
ATTN: MROED-D, C. Distefano

US Army Engineer Div Huntsville
ATTN: HNDED-SR
3 cys ATTN: C. Huang

US Army Engineer Div Ohio River
ATTN: ORDAS-L, Tech Library

US Army Engr Waterways Exper Station
ATTN: D. Banks
ATTN: Doc Con Off for DOC, J. Day
ATTN: H. Wilson
ATTN: J. Warringer
ATTN: Library
ATTN: P. Mlakar
ATTN: WESSD, J. Jackson
ATTN: WESSE
ATTN: WESSS, J. Ballard

US Army Information Systems Cmd
ATTN: B. Kappas
ATTN: Tech Reference Division

US Army Material Command
ATTN: DRXAM-TL, Tech Library

US Army Nuclear & Chemical Agency
ATTN: Library

DEPARTMENT OF THE NAVY

Chief of Naval Operations
ATTN: OP-943

Naval Postgraduate School
ATTN: Code 1424 Library

Naval Research Laboratory
ATTN: Code 2627, Tech Library

Naval Surface Weapons Center
ATTN: Tech Library & Info Svcs Br

Naval War College
ATTN: Code E-11, Tech Service

DEPARTMENT OF THE NAVY (Continued)

Ofc of the Dep Ch of Naval Ops
ATTN: NOP 981

Space & Naval Warfare Systems Cmd
ATTN: PDE-110-X1, B. Kruger

Strategic Systems Programs (PM-1)
ATTN: NSP-43, Tech Library

Submarine Force
ATTN: A. Stough

DEPARTMENT OF THE AIR FORCE

Air Force Institute of Technology
ATTN: Library

Air Force Office of Scientific Rsch
ATTN: J. Allen
ATTN: L. Hendrickson
ATTN: W. Best

Air Force Systems Command
ATTN: DLWM
ATTN: XRT

Air Force Weapons Laboratory
ATTN: D. Cole
ATTN: NTE, M. Plamondon
ATTN: R. Galloway
ATTN: SUL

Air University Library
ATTN: AUL-LSE

Assist Ch of Staff, Intelligence
ATTN: IN

Assist Ch of Staff, Studies & Analysis
ATTN: AFCSA/SAMI

Ballistic Missile Office/DAA
ATTN: CC-1
ATTN: CC-3
ATTN: EN
ATTN: ENS, W. Weisinger
ATTN: ENSN
ATTN: MGEN, E. Furbee
ATTN: SYB, L. Pothier
ATTN: SYBU, Lt Michael
3 cys ATTN: ASMS

Dep Ch of Staff, Rsch, Dev, & Acq
ATTN: AF/RDQI
ATTN: AFRD
ATTN: AFRD-M, A. Ravgiala

Strategic Air Command
ATTN: DEPM
ATTN: DOM
ATTN: INAO
ATTN: NRI/STINFO
ATTN: XOKM
ATTN: XPFC
ATTN: XPFS
ATTN: XPQ

Foreign Technology Division
ATTN: NIIS Library

DEPARTMENT OF THE AIR FORCE (Continued)

Secretary of the Air Force
ATTN: SAFAL, S. Gold

DEPARTMENT OF ENERGY

Department of Energy
Office of Military Application, GTN
ATTN: OMA, DP-22

University of California
Lawrence Livermore National Lab
ATTN: G. Smith
ATTN: H. Heard
ATTN: L-47, D. Oakley
ATTN: Tech Info Dept Library

Los Alamos National Laboratory
ATTN: C. Watson
ATTN: D 446, B. Killian
ATTN: J. Neudecker
ATTN: L. Germaine
ATTN: MS P364 Reports Library
ATTN: O. Hart
ATTN: T. Dey

Oak Ridge National Laboratory
ATTN: Central Rsch Library

Sandia National Laboratories
ATTN: Library & Sec Classification Div

Sandia National Laboratories
ATTN: Org 7111, L. Hill
ATTN: Tech Library 3141

OTHER GOVERNMENT AGENCIES

Central Intelligence Agency
ATTN: OSWR/NED

Department of the Interior
Bureau of Mines
ATTN: Tech Library

Department of the Interior
US Geological Survey
ATTN: D. Roddy

Office of Technology Assessment
ATTN: R. Staffin

US Geological Survey
ATTN: B. Carroll
ATTN: W. Twenhofel

DEPARTMENT OF DEFENSE CONTRACTORS

Aerospace Corp
ATTN: Library Acquisition M1/199

Agbabian Associates, Inc
ATTN: C. Bagge
ATTN: D. Vandillen
2 cys ATTN: M. Agbabian

Analytic Services, Inc (ANSER)
ATTN: K. Baker

DEPARTMENT OF DEFENSE CONTRACTORS (Continued)

Applied Research Associates, Inc
ATTN: N. Higgins

Applied Research Associates, Inc
ATTN: S. Blouin

Applied Research Associates, Inc
ATTN: D. Piepenburg

Applied Research Associates, Inc
ATTN: R. Frank

Applied Theory, Inc
ATTN: J. Trulio

AVCO Systems Division
ATTN: Library A83C

BDM Corp
ATTN: Corporate Library
ATTN: T. Neighbors

BDM Corp
ATTN: E. Bultmann
ATTN: F. Leech
ATTN: M. Garcia

Bell Aerospace Textron
ATTN: C. Berninger
ATTN: R. Gellatly

Boeing Co
ATTN: Aerospace Library
ATTN: H. Leistner
ATTN: M/S 42/37, K. Friddell
ATTN: T. Berg
2 cys ATTN: J. Wooster

California Institute of Technology
ATTN: D. Anderson

California Research & Technology, Inc
ATTN: K. Kreyenhagen
ATTN: Library
ATTN: S. Schuster

California Research & Technology, Inc
ATTN: F. Sauer

California Research & Technology, Inc
ATTN: Tech Library

Calspan Corp
ATTN: Z. Zudans

Calspan Corp
ATTN: Library

Carpenter Research Corp
ATTN: H. Carpenter

University of Denver
ATTN: Sec Officer for J. Wisotski

EG&G Was Analytical Svcs Ctr, Inc
ATTN: Library

Electro-Mech Systems, Inc
ATTN: R. Shunk

DEPARTMENT OF DEFENSE CONTRACTORS (Continued)

Foster-Miller Inc
ATTN: J. Hampson for E. Foster

GTE Communications Products Corp
ATTN: E. Courier
ATTN: R. Sullivan

H & H Consultants, Inc
ATTN: E. Cording
ATTN: J. Haltiwanger
ATTN: J. Hendron
ATTN: S. Paul

IIT Research Institute
ATTN: Documents Library
ATTN: M. Johnson
ATTN: R. Welch

Institute for Defense Analysis
ATTN: Classified Library

Kaman Sciences Corp
ATTN: Library

Kaman Sciences Corp
ATTN: Library
ATTN: R. Keefe

Kaman Sciences Corp
ATTN: E. Conrad

Kaman Tempo
ATTN: DASIAC

Kaman Tempo
ATTN: DASIAC

Lockheed Missiles & Space Co, Inc
ATTN: J. Bonin
ATTN: Tech Info Center

Martin Marietta Denver Aerospace
ATTN: J. Gliozzi
ATTN: R. Haymen

Massachusetts Inst of Technology
ATTN: W. Brace

Merritt CASSES, Inc
ATTN: D. Burgess
ATTN: J. Merritt

Mitre Corp
ATTN: Tech Report Center

University of New Mexico
ATTN: N. Baum

University of New Mexico
ATTN: M. Ostrower

City College of New York
ATTN: C. Miller

Pacific-Sierra Research Corp
ATTN: A. Laupa
ATTN: D. Wilson
ATTN: H. Brode, Chairman SAGE

DEPARTMENT OF DEFENSE CONTRACTORS (Continued)

Northern University
ATTN: T. Belytschko

Pacific-Sierra Research Corp
ATTN: D. Gormley

Pacifica Technology
ATTN: G. Kent

Patel Enterprises, Inc
ATTN: M. Patel

Physics International Co
ATTN: E. Moore

R & D Associates
ATTN: C. Lee
ATTN: C. Knowles
ATTN: D. Oberste-Lehn
ATTN: D. Simons
ATTN: J. Lewis
ATTN: P. Haas
ATTN: R. Mesic
ATTN: Tech Info Center

R & D Associates
ATTN: G. Ganong

Rand Corp
ATTN: P. Davis

Rand Corp
ATTN: B. Bennett

S-CUBED
ATTN: C. Archembeam
ATTN: D. Grine
ATTN: K. Pyatt
ATTN: Library
ATTN: R. Duff
2 cys ATTN: G. Hegemier
2 cys ATTN: L. Hageman
2 cys ATTN: K. Cheverton
2 cys ATTN: P. Lade

Science Applications Intl Corp
ATTN: H. Pratt
ATTN: M. McKay
ATTN: Tech Library

Science Applications Intl Corp
ATTN: W. Layson

Science Applications, Inc
ATTN: Tech Library

DEPARTMENT OF DEFENSE CONTRACTORS (Continued)

Southwest Research Institute
ATTN: A. Wenzel
ATTN: W. Baker

SRI International
ATTN: B. Holmes
ATTN: G. Abrahamson
ATTN: J. Bruce

Structural Mechanics Associates, Inc
ATTN: R. Kennedy

Terra Tek, Inc
ATTN: Library
ATTN: S. Green

Texas A & M University System
ATTN: J. Handin
ATTN: Sec Officer for A. Rychlik

TRW Electronics & Defense Sector
ATTN: B. Balachandra
ATTN: N. Lipner
ATTN: P. Huff
ATTN: R. McFarland
ATTN: Tech Info Center

TRW Electronics & Defense Sector
ATTN: B. Keltner
ATTN: D. Randell
ATTN: E. Wong
ATTN: L. Woodruff
ATTN: O. Lev
ATTN: P. Dai
ATTN: R. St Clair
ATTN: S. Rindskopf

Universal Analytics, Inc
ATTN: E. Field

Weidlinger Assoc, Consulting Engrg
ATTN: T. Deevy

Weidlinger Assoc, Consulting Engrg
ATTN: I. Sandler
ATTN: M. Baron

Weidlinger Assoc, Consulting Engrg
ATTN: J. Isenberg

William Perret
ATTN: W. Perret

END

Dtic

5-86